Volume 14, Number 10, 2023 ISSN 1847-6996

FERIT
FACULTY OF ELECTRICAL ENGINEERING, COMPUTER SCIENCE AND INFORMATION TECHNOLOGY **OSIJEK**

IJECES International Journal of Electrical and Computer Engineering Systems

International Journal of Electrical and Computer Engineering Systems

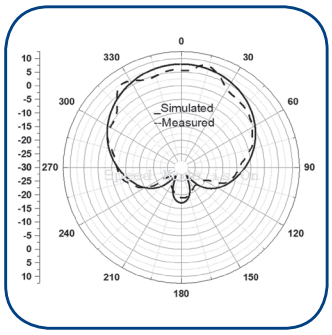

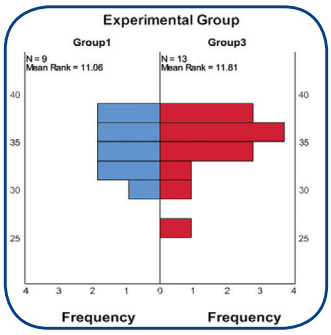

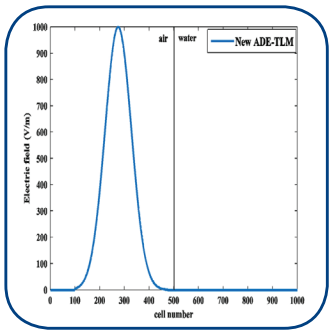

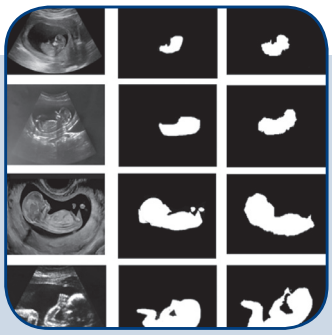

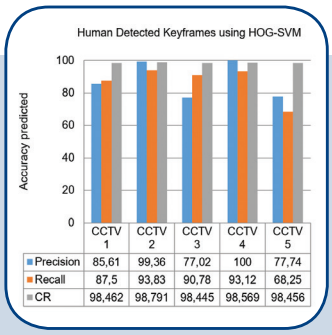

ISSN: 1847-6996

INTERNATIONAL JOURNAL OF ELECTRICAL AND COMPUTER ENGINEERING SYSTEMS

Published by Faculty of Electrical Engineering, Computer Science and Information Technology Osijek, Josip Juraj Strossmayer University of Osijek, Croatia

Osijek, Croatia | Volume 14, Number 10, 2023 | Pages 1087 - 1202

The International Journal of Electrical and Computer Engineering Systems is published with the financial support of the Ministry of Science and Education of the Republic of Croatia

CONTACT

International Journal of Electrical and Computer Engineering Systems (IJECES)

Faculty of Electrical Engineering, Computer Science and Information Technology Osijek,
Josip Juraj Strossmayer University of Osijek, Croatia
Kneza Trpimira 2b, 31000 Osijek, Croatia
Phone: +38531224600, Fax: +38531224605
e-mail: ijeces@ferit.hr

Subscription Information

The annual subscription rate is 50€ for individuals, 25€ for students and 150€ for libraries.
Giro account: 2390001 - 1100016777,
Croatian Postal Bank

Journal is referred in:

- Scopus
- Web of Science Core Collection (Emerging Sources Citation Index - ESCI)
- Google Scholar
- CiteFactor
- Genamics
- Hrčak
- Ulrichweb
- Reaxys
- Embase
- Engineering Village

Bibliographic Information

Commenced in 2010.
ISSN: 1847-6996
e-ISSN: 1847-7003
Published: quarterly
Circulation: 300

IJECES online

https://ijeces.ferit.hr

TABLE OF CONTENTS

Multi-Head CNN based Software Development Risk Classification 1087
Original Scientific Paper
Ayesha Ziana M. | Charles J.

Empirical Validation of Variable Method Interaction Cohesion Metric (VMICM) for Enhancing Reusability of Object-Oriented (O-O) Software 1097
Original Scientific Paper
Bharti Bisht | Parul Gandhi

Semi-automated Software Requirements Categorisation using Machine Learning Algorithms 1107
Original Scientific Paper
Pratvina Talele | Siddharth Apte | Rashmi Phalnikar | Harsha Talele

Improving Scientific Literature Classification: A Parameter-Efficient Transformer-Based Approach 1115
Original Scientific Paper
Mohammad Munzir Ahanger | M. Arif Wani

The New ADE-TLM Algorithm for Modeling Debye Medium.....1125
Original Scientific Paper
El hadi El ouardy | Hanan El Faylali

Estimating Egyptsat -1 Radiometric Coefficient using Cross Calibration with Spot4 and Spot5 1133
Original Scientific Paper
Sayed Abdo | Ibrahim Ziedan | Asmaa Elyamany

FOE NET: Segmentation of Fetal in Ultrasound Images Using V-NET 1141
Original Scientific Paper
Eveline Pregitha R. | Vinod Kumar R. S. | Ebbie Selvakumar C.

Significance of handcrafted features in human activity recognition with attention-based RNN models 1151
Review Paper
Sonia Abraham | Rekha K. James

A Four Slot Dual Feed and Dual Band Reconfigurable Antenna for Fixed Satellite Service Applications 1165
Original Scientific Paper
T. Venkata Suri Apparao | G. Karunakar

Parameter Estimation and Predictive Speed Control of Chopper-Fed Brushed DC Motors.....1173
Original Scientific Paper
Son Nguyen Thanh | Tuan Pham Van | Tu Pham Minh | Anh Hoang

Artificial Intelligent Maximum Power Point Controller based Hybrid Photovoltaic/Battery System 1183
Original Scientific Paper
Aymen Kadhim Mohaisen

Active and Reactive Power loss Minimization Along with Voltage profile Improvement for Distribution Reconfiguration 1193
Original Scientific Paper
Ola Badran | Jafar Jallad

About this Journal
IJECES Copyright Transfer Form

Multi-Head CNN based Software Development Risk Classification

Original Scientific Paper

Ayesha Ziana M.
Department of Computer Science, Noorul Islam Centre for Higher Education,
Kumaracoil 629180, Tamil Nadu, India
zianamicas@yahoo.com

Charles J.
Department of Software Engineering, Noorul Islam Centre for Higher Education,
Kumaracoil 629180, Tamil Nadu, India
jebapillaicharles@gmail.com

Abstract *– Agile methodology for software development has been in vogue for a few decades, notably among small and medium enterprises. The omission of an explicit risk identification approach turns a blind eye to a range of perilous risks, thus dumping the management into strenuous situations and precipitating dreadful issues at the crucial stages of the project. To overcome this drawback a novel Agile Software Risk Identification using Deep learning (ASRI-DL) approach has been proposed that uses a deep learning technique along with the closed fishbowl strategy, thus assisting the team in finding the risks by molding them to think from diverse perspectives, enhancing wider areas of risk coverage. The proposed technique uses a multi-head Convolutional Neural Network (Multihead-CNN) method for classifying the risk into 11 classes such as over-doing, under-doing, mistakes, concept risks, changes, differences, difficulties, dependency, conflicts, issues, and challenges in terms of producing a higher number of risks concerning score, criticality, and uniqueness of the risk ideas. The descriptive statistics further demonstrate that the participation and risk coverage of the individuals in the proposed methodology exceeded the other two as a result of applying the closed fishbowl strategy and making use of the risk identification aid. The proposed method has been compared with existing techniques such as Support Vector Machine (SVM), Multi-Layer Perceptron (MLP), Generalized Linear Models (GLM), and CNN using specific parameters such as accuracy, specificity, and sensitivity. Experimental findings show that the proposed ASRI-DL technique achieves a classification accuracy of 99.16% with a small error rate with 50 training epochs respectively.*

Keywords*: closed fishbowl strategy, explicit risk identification, structured brainstorming, multi-head convolutional neural network*

1. INTRODUCTION

Worldwide circumstances reveal that the success of software development projects highly depends on appropriate planning and an inclination toward minimizing possible risks [1]. Systematic methods for risk management processes and mechanisms are scarce in an agile software development environment [2, 3]. Agile processes perform risk management in an implicit mode by incorporating techniques that handle risks innately. By including time limits and changing requirements, the processes act as risk mitigation techniques, and transparency to the customer improves managing his requirements while also performing risk mitigation [4]. However, the implicit approach is threatening and suitable only as an initial phase and further improvements are needed for sure since a lack of identification of the right risks can lead to poor mitigation, monitoring, and controlling of risks. Explicit risk management strategies that adhere to agile principles are important in agile processes [5,6].

Following explicit risk management strategies in Agile methodology has produced several positive outcomes, like improvements in communication, team efficiency, and product quality [7, 8]. To achieve a certain level of efficiency in Agile Risk Management, an easy methodology that ensures respect for the Agile Manifesto is required [9]. To avoid project failure due to risk traversal, it is necessary to capture and manage risks earlier in the software development process [10]. Recognizing and acknowledging the risks of a project is not always free of complications [11,12].

The ISO/IEC 31000 standard recommends brainstorming as one of the most strongly suitable tools for risk identification and subsequent steps [13]. Brain-

storming is suitable for new or substandard procurement tasks since it encourages different and innovative thinking [14]. However, because of its unsystematic nature, there is a chance for potential risks to be overlooked, and the procedure takes more time to obtain the results and arrive at a conclusion [15,16].

Creative teams with diversity in expertise are the key to success in brainstorming [17]. However, they must give up intentional ignorance for team collaboration to be effective [18]. As a result, risk identification assistance tools must consider the above constraints and facilitate communication and collaboration among participants [19-23]. Keeping this in mind, we continue our research to propose a novel Agile Software Risk Identification using the Deep Learning (ASRI-DL) approach [24-27]. The major contributions of the paper are organized as follows.

- The proposed method uses a deep learning technique along with the closed fishbowl strategy, thus assisting the team in finding the risks by molding them to think from diverse perspectives and enhancing wider areas of risk coverage.
- The proposed technique uses a multi-head Convolutional Neural Network (Multihead-CNN) method for classifying the risk into 11 classes in terms of producing a higher number of risks concerning score, criticality, and uniqueness of the risk ideas.
- The effectiveness of the suggested method has been assessed in terms of specific parameters such as accuracy, specificity, and sensitivity.

The remainder of the paper is structured as shown below. The literature review is discussed in Section II. The details of the proposed ASRI-DL scheme are described in Section III. Results and discussion are covered in Section IV. The conclusion and future work are discussed in Section V.

2. LITERATURE REVIEW

In 2018, E. E. Odzaly, [28] highlighted that risk identification was found to be the most difficult process in terms of effort, and people issues are the most crucial ones in Agile software projects; however, automated risk management was not fully achieved through the solution.

In 2018, A. Nadali, et al. [29] proposed a Structured What If Technique (SWIFT), a systematic risk identification study, which clearly illustrates the sources of identified risks, along with their impact, treatment, and countermeasures. The full potential of the model, however, was not investigated.

In 2020, T. E. Abioye, et al. [30] proposed the ontology-based proactive approach towards managing risks by Abioye et al. Though the risk identification process was carried out using multiple techniques this technique was good enough at unearthing almost all risks in the risk identification approach.

In 2020, M. Sousa, [31] proposed a modern board game-based framework that aimed to offer solutions for small enterprises via simple games to stimulate brainstorming sessions. However, the approach requires more time to be spent initially learning the games and then implementing them in the brainstorming sessions, which is a tedious process.

In 2021, M. Nabawy et al. [32], proposed a Risk Breakdown Structure (RBS) a risk identification framework and database, which classifies the risks into threats and opportunities. They present the usage of RBS in systematically identifying and assessing the risks through risk categories.

In 2021, M. Khalilzadeh et al. [33] proposed a fuzzy Delphi method, a combination of the Delphi technique and fuzzy set theory for handling uncertainty, which was used as a risk identification technique to filter the risks previously identified through documentation analysis.

In 2017, M. Zavvar et al. [34] proposed a Support Vector Machine (SVM) to model risk classification in software development projects. According to the experimental results, the proposed method exhibits superior CAR and AUC.

In 2022, M. Yang et al. [35] proposed a multi-layer perceptron model that can predict risks in software development. The experimental findings show that the prediction accuracy is 83.11%, which is higher than that of typical machine learning models.

In 2015 B. Esmaeili et al. [36] investigated the validity of applying these fundamental risk factors to predict safety outcomes. The modeling technique consists of two steps: (1) doing principle components analysis to minimize dimensionality and (2) using principal components as generalized linear models to describe the probability of various risk categories.

In 2022, Q. Wang et al. [37] presented a convolutional neural network (CNN)-based automated technique for identifying software vulnerabilities. CNN is used to classify vulnerabilities automatically. The suggested approach outperformed the competition in macro recall, macro precision, and macro F1 score in experimental comparison and analysis.

Roughly more than 500 risks from various studies were utilized for the objective, some of which are included here in Table 1, we can identify the implicit and explicit risk identification strategies applied in Agile software development projects. As far as we have reviewed from the literature, the fishbowl strategy has not been utilized in software engineering practices, in the risk identification process of brainstorming in Agile software enterprises. This influenced our ideology in applying the ASRI-DL technique to acquire the desired outcome.

Table 1. Practices for Risk Identification in Agile Projects

Practices	References
Daily Standup Meetings	[10, 28]
Sprint Planning	[10, 3, 23, 11]
Brainstorming	[23, 22, 9]
Checklist	[22]
Weekly Sprint Meetings	[16]
Increment	[17]
Prototype	[17]
Product backlog refinement meeting	[17, 28, 4]
Weekly risk meeting	[17]
Technical specification	[17]
Risk Identification Meetings	[23]
Sprint backlog	[28]
Sprint review	[14, 3, 4, 18]
Sprint Retrospective	[3]

3. AGILE SOFTWARE RISK IDENTIFICATION USING DEEP LEARNING (ASRI-DL) FRAMEWORK

The proposed Agile Software Risk Identification using Deep Learning (ASRI-DL) approach incorporates systematic brainstorming for risk identification.

To soar the partaking of the participants in the discussion, the Closed Fishbowl Strategy was lodged, then, the deep learning technique, multi-head CNN takes the input such as human, organizational, technical, non-technical, and capabilities from the fishbowl strategy and classifies it into 11 categories for efficient risk classification.

The block diagram for the proposed ASRI-DL technique is depicted in Fig 1.

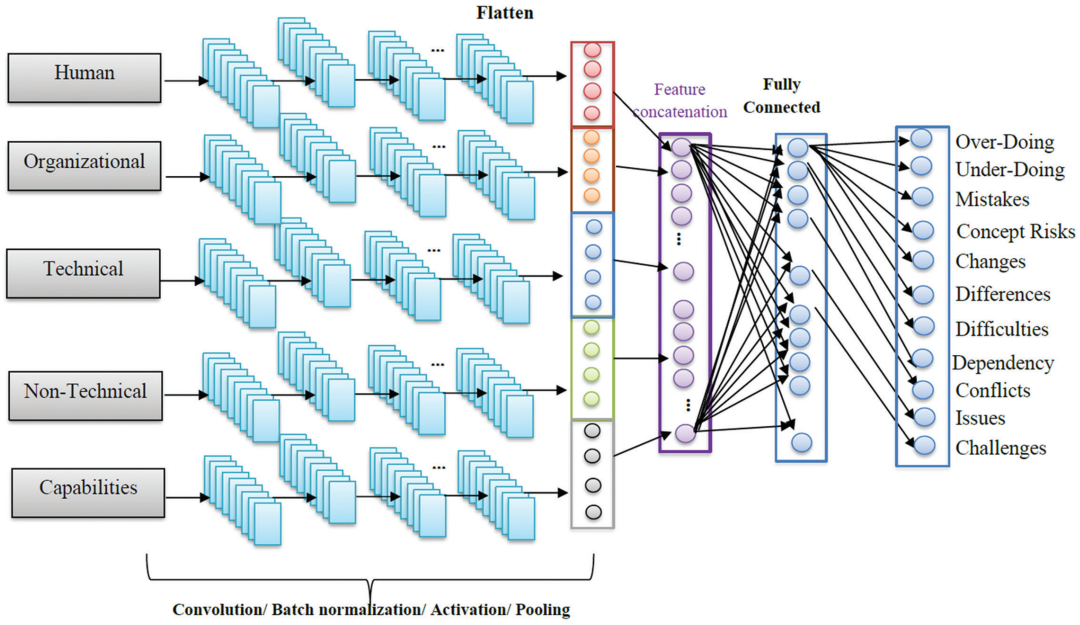

Fig. 1. Architecture of the Proposed ASRI-DL Multi-faceted Taxonomy Assistance for Risk Identification

3.1. MULTI-HEAD CONVOLUTIONAL NEURAL NETWORK

Multi-head convolution (MHCNN) is a CNN in which each time series is handled by a different convolution known as a convolutional head. The proposed method takes data such as humans, organizational, technical, non-technical, and capabilities as input. The three categories *Human*, *Organizational*, and *Technical*, were affixed to the taxonomy for identifying the risk. The Non-technical category is ascended with the Environmental, Marketing, and Legal subcategories. The proposed architecture uses a sliding window to process the test case. The network recovers features based on each phase using window-based time series processing. Convolution is defined as follows:

$$O = \sum_{x=1}^{L} \sum_{y=1}^{W} z(x,y) f(x,y) \quad (1)$$

Where O is the output from $z(x,y)$ and the filter $f(x,y)$ with the length (L) and width (W) respectively. Each temporal sequence receives its own feature map. Equation (2) calculates the number of characteristics in each layer of a typical MHCNN.

$$G = f_m * f_z * d + bias \quad (2)$$

In this case, f_m denotes the number of filters, f_z the filter size, and d the final dimension of the resultant vector from the preceding layer. Each convolution head in MH-CNN requires a 4-dimensional input, which is calculated as follows:

$$I = (n_s, W_s, W_l, n_c) \quad (3)$$

where n_s denote the number of samples in the batch, and n_c refers to the number of channels. The total number of windows is calculated as follows:

$$W_n = \frac{D_p - W_l}{W_t} + 1 \quad (4)$$

The total number of data points in the time series is denoted by D_p, the window length by W_l, and the window step by W_t. As a result, the suggested technique

may collect useful information from the local to the global levels. A loss function is cross entropy and the cross-entropy loss function is calculated as follows:

$$loss = -\frac{1}{S}\sum_{n=1}^{N}[y_t \log \hat{y}_t + (1 - y_t)\log(1 - \hat{y}_t)] \quad (5)$$

where S denotes the number of samples and y_t is the probability of a true label, $\hat{y}_t$ is the probability of the predicted label. The proposed method will classify the risk into 11 classes such as over-doing, under-doing, mistakes, concept risks, changes, differences, difficulties, dependency, conflicts, issues, and challenges.

The proposed *Risk Nature* facet is much more stipulated towards investigating the type of risk focusing on the causation. We used a few more attributes to the facet termed *Changes*, *Differences*, *Challenges*, and *Dependency*. Over-Doing (OD) risks arise as a consequence of adding blameworthy elements to the process. The exclusion of obligatory features gives birth to Under-Doing (UD) risks. Erroneous execution of the right concept is the main reason for Mistakes (M) to arise. Conceptual Problems (C) indicate risks originating from an invalid treatment.

We realized the significance of changes since they can occur at any point in time throughout the project cycle and play a huge part in the winning or losing moments of a software project. The significance of *differences*, otherwise known as non-congruence, and software failure is listed as one of its consequences. The measure of *congruence* is computed by the difference between expectations and requirements. In other words, *dependency* may be a cause for dissimilarities or differences. This precipitated us to move the two attributes, difference and dependency, to the Risk Nature facet under the assumption that they might induce risks. *Challenges* allude to coming across new circumstances, ideas that induce cognitive discrepancies, or the catalyst for thriving and development.

Concerning the suitability of the complexity science theory in project management, *complexity* also known as *difficulty*, is a major factor in the failure of big projects. Furthermore, sudden unexpected events, complexities, and clashes were encountered as risks in the literature, which impelled us to categorize them appropriately under the nature of *issues*, *difficulties*, and *conflicts*. To validate the technique, we implemented the Utility Demonstration approach through quasi-experimental research and classifying the risks, which in turn was used as the training material in the experimental session.

4. RESULTS AND DISCUSSION

4.1. SAMPLING

Two small and medium enterprises, C1 and C2, which follow a hybrid methodology of software development, were chosen for the experiment, and the choice was based on the availability and willingness of the participants. Three groups were chosen with unequal sample sizes of 8, 10, and 12, respectively, excluding the facilitators, and a minimum sample size of 30 altogether was ensured. Each group had unique participants. It should be noted that Groups 2 and 3 are from the same company. The number of participants was purely based on the availability of samples from both companies. We ensured that we got at least 30 samples altogether before the experiments, excluding the facilitators, to produce statistically significant results.

Regarding the disparity in each group,

i. Our group 1 initially contained 9 available samples, including the facilitator during the training sessions. However due to a sudden dropout on the day of the experiment, one of the authors was made the facilitator, and the size was reduced to 8.

ii. (Our Group 2 and Group 3 are from the same company, and we were given 24 samples, including 2 facilitators. Among those 22 participant samples available, since our proposed closed fishbowl strategy requires at least four participants in the inner circle along with the facilitator and the remaining must be in the outer circle, we thought 12 participants and 1 facilitator would be ideal for conducting the session in three rounds for our Group 3. Thus, the group was allotted the remaining participants.

4.2. EXPERIMENTAL PROCEDURE

Initially, all three groups were instilled with the basics of Agile methodology and the significance of risk identification in Agile enterprises through oral and visual presentations. Before the final experiment, Groups 1 and 3 acquired a training session with the fishbowl strategy and the proposed ASRI-DL methodology, respectively, which included training with the solved material, hands-on training, and trial experiments. Group 2 was exempt from training as it was our control group. However, a trial experiment was carried out ahead of time.

4.3. EXPERIMENTAL SESSIONS ILLUSTRATION

Three different project scenarios were given as inputs to the three groups to capture the risks. Sessions 1 and 3 were held uninterrupted for around 40 minutes, as scheduled. Session 2 lasted approximately 33 minutes, while the actual planned session was approximately 40 minutes. The reason for this is that the participants felt that enough ideas had been generated and that their ability to discover new risks had slowed to the point where we had no choice but to end the session.

The facilitators were given the goal of directing their team towards yielding as many risks as possible for the given project scenarios, which in turn were evaluated in terms of novelty and their prominence in the project, otherwise termed Score and Criticality. The outcomes of the three experiments were evaluated by eight experts with significant working experience, from the company C2 using a 5-point Likert scale that took the ordinal values of "Very low, Low, Medium, High, and Very high" to

assess both the Score and Criticality. The demographic details of the eight experts are given in Table 2.

Table 2. Demographic details of the eight experts

EMPID	Designation	Experience	Evaluated group
EMP1	Technical Architect	2.3 yrs	1
EMP2	Senior Developer	4.8 yrs	1
EMP3	Senior business analyst	3.7 yrs	1,2
EMP4	Module lead	5.2 yrs	2
EMP5	Senior Developer	6.8 yrs	2
EMP6	Senior business analyst	2.8 yrs	3
EMP7	Senior Developer	4.9 yrs	3
EMP8	Senior Developer	4.4 yrs	3

4.4. STATISTICAL ANALYSIS

At the juncture of the actual experiments, Group1 spotted 126 risks; Group2 figured out 83 ideas, and finally, the experiments were put to an end by Group3 by ascertaining 226 risks. For quantitative analysis, the IBM SPSS Statistics Version 26 was used. The values of the ordinal variables 'category', 'subcategory', and 'risk nature' were computed from the median and mode of the ranks imparted by three of our evaluation experts. According to the results, the *Organizational* category tops the list, followed by Human and Capability categories. To eliminate the bias, the two pivotal dependent variables, '*actualscore*' and '*actualcriticality*' for each identified risk is employed by using the formula below:

$$actualscore=uniqueness/totalscores \quad (6)$$

$$actualcriticality=(category*subcategory*risknature)*uniqueness/totalcriticality \quad (7)$$

where category, subcategory, and risk nature denote the recoded rank values proffered by the experts. The total scores and total criticality for each identified risk are computed by summing up the marks allotted by the experts.

4.5. PROPOSITIONS

The narration of the propositions formulated for the study is as follows.

4.5.1. Proposition 1

Null Hypothesis: There is no difference in the distribution of unique ideas with good scores among the three groups.

Alternate Hypothesis: There is a difference in the distribution of unique ideas with high scores among the three groups.

We tested the normality of the distribution by the Shapiro-Wilk test and derived the significance value as 0.000 less than 0.05, and the hypothesis of normality was rejected. The Kruskal Wallis test was conducted to examine the hypothesis, and the result shows that the null hypothesis is rejected since the significance value is 0.000 less than 0.05, which is shown in Table 3. There was also no significant difference between Groups 1 and 2, as assured by the significance value of 0.345 greater than 0.05.

Table 3. Pairwise Comparisons of Experimental Groups for Actual Scores of Identified Risks

Sample1-Sample2	Test-Statistic	Std.Error	Std.Test Statistic	Sig.	Adj.Sig.
Group1-Group2	-15.653	16.579	-.944	.345	1.000
Group1-Group3	-61.565	13.039	-4.722	.000	.000
Group2-Group3	-45.912	15.052	-3.050	.002	.007

4.5.2. Proposition 2

Null Hypothesis: There is no difference in the distribution of unique ideas with good criticality among the three groups.

Alternate Hypothesis: There is a difference in the distribution of unique ideas with good criticality among the three groups.

Table 4. Pairwise Comparisons of Experimental Groups for Actual Criticality of Identified Risks

Sample1-Sample2	Test-Statistic	Std. Error	Std. Test Statistic	Sig.	Adj. Sig.
Group2-Group1	1.798	16.616	.108	.914	1.000
Group2-Group3	-57.819	15.086	-3.833	.000	.000
Group1-Group3	-56.021	13.068	-4.287	.000	.000

Scrutinizing the Kruskal Wallis test results interprets in favor of the alternative hypothesis by rejecting the null hypothesis as the significance value is 0.000 less than 0.05, which is shown in Table 4.

4.6. OTHER FINDINGS

The frequency with which participants engendered their viewpoints in their respective sessions is depicted by the graphical illustration in Fig. 2. It is pretty obvious that the graph tends to be more or less uniform among the participants of Group 3, in contrast to the rest of the groups.

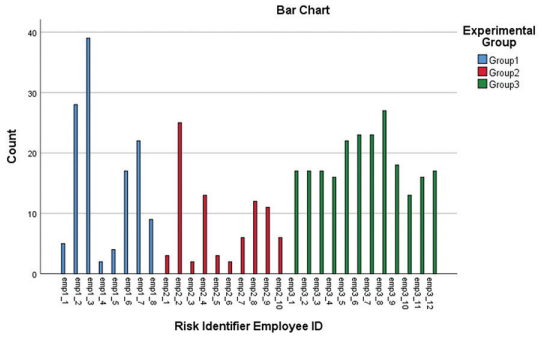

Fig. 2. Bar Chart representing the frequency of participation among the samples across the three groups

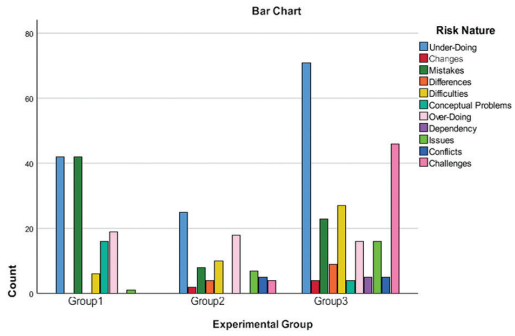

Fig. 3. Bar Chart representing the 'Risk Nature' of the identified risks among the three groups

The cross-tabulation exemplified via the bar chart in Fig. 3 exhibits the rendering of risks under the 'Risk Nature' facet by the 3 groups during their respective brainstorming sessions. Group 3 was the only one to accomplish ideas under every nature of risk. This is a positive sign concerning our proposed methodology.

4.7. FEEDBACK ASSESSMENT

For feedback assessment, a short questionnaire was fabricated and supplied to the participants of the treatment groups at the end of sessions 1 and 3, including the facilitator and one of the dropouts from session 1.

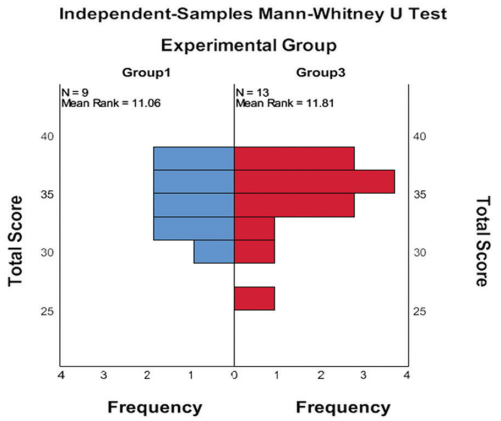

Fig. 4. Mann-Whitney U Test for comparing the mean ranks of the Total Scores in Feedback among Groups 1 and 3

The 'Total Score' is computed by summing up the variables aforementioned. The Mann-Whitney U Test in Fig. 4 reveals the inference of a similar distribution of Total Scores among the 2 groups through the significance value of 0.794 greater than 0.05, thus accepting the null hypothesis.

4.8. RELIABILITY AND VALIDITY ANALYSIS

The reliability analysis for the experiment was attained by the statistical test using Cronbach's Alpha test, as manifested in Tables 5 and 6. As a result of the Cronbach's Alpha values of 0.753 greater than 0.6 and 0.767 greater than 0.6, our experiment is acknowledged to be reliable.

Table 5. Reliability Statistics for Criticality of Risks

Cronbach's Alpha	Cronbach's Alpha Based on Standardized Items	N of Items
.753	.761	3

Table 6. Reliability Statistics for Score of Risks

Cronbach's Alpha	Cronbach's Alpha Based on Standardized Items	N of Items
.767	.803	3

The correlation analysis was performed using Spearman's correlation coefficient which is given in Table 7 which indicates a positive correlation between *risk nature* and *actual criticality*.

Table 7. Construct Validity Analysis using Spearman's Rho correlations

Risk types	Risk Nature	Actual Criticality
Correlation Coefficient	1.000	.180
Sig.(2-tailed)	.	.000
N	435	435
Correlation Coefficient	.180	1.000
Sig.(2-tailed)	.000	.
N	435	435

4.9. PERFORMANCE ANALYSIS

In Fig. 5, the accuracy graph is estimated with the 50 epochs and accuracy range. The proposed Multihead-CNN obtains a high accuracy of 99.16% with a small error rate with 50 training epochs in the identification of risks.

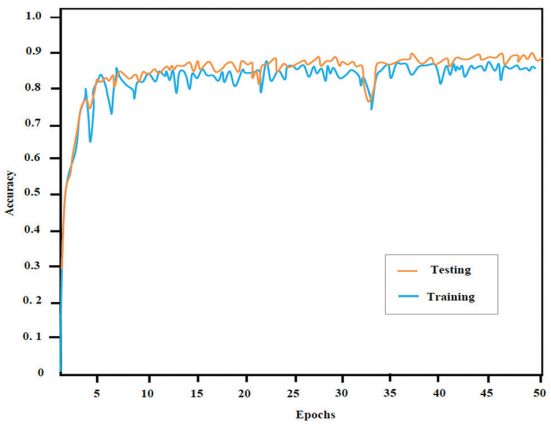

Fig. 5. Training and testing accuracy of the proposed Multihead-CNN model

The proposed multi-head CNN network has been compared with existing techniques such as SVM [34], MLP [35], GLM [36], and CNN [37] using specific parameters such as accuracy, specificity, and sensitivity which are shown in Fig 6. From the figure, it is clear that the proposed method achieves better accuracy than existing techniques.

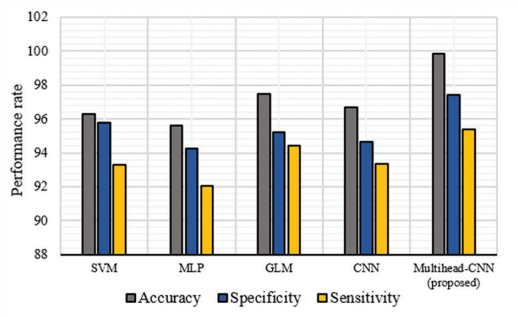

Fig. 6. Performance comparison of the proposed method with existing techniques

The proposed multi-head CNN network has been compared with existing techniques such as SVM [34], MLP [35], GLM [36], and CNN [37] using specific parameters such as accuracy, specificity, and sensitivity which are shown in Fig. 6. From the figure, it is clear that the proposed method achieves better accuracy than existing techniques.

5. CONCLUSION

In this paper, a novel well-defined proactive ASRI-DL methodology method was proposed for risk management, which employs a closed fishbowl strategy and multihead-CNN technique for the risk identification process of Agile software projects. The proposed method has been compared with existing techniques such as SVM, MLP, GLM, and CNN using specific parameters such as accuracy, specificity, and sensitivity. Experimental findings show that the proposed ASRI-DL technique achieves a classification accuracy of 99.16% with a small error rate with 50 training epochs respectively. On this note, we conclude the paper with the future intention of steering the research towards further phases of risk assessment, including risk analysis and prioritization.

6. REFERENCES

[1] M. Esteki, T. J. Gandomani, H. K. Farsani, "A risk management framework for distributed scrum using PRINCE2 methodology", Bulletin of Electrical Engineering and Informatics, Vol. 9, No. 3, 2020, pp. 1299-1310.

[2] B. Prakash, V. Viswanathan, "Distributed cat modeling based agile framework for software development", Sadhana, Vol. 44, No. 7, 2019, pp. 1-11.

[3] C. R. Nelson, G. Taran, L. D. L. Hinojosa, "Explicit Risk Management in Agile Processes", Proceedings of the International Conference on Agile Processes and Extreme Programming in Software Engineering, 2008, pp.190-201.

[4] M. Vieira, J. C. R. Hauck, S. Matalonga, "How Explicit Risk Management is Being Integrated into Agile Methods: Results from a Systematic Literature Mapping", Proceedings of the 19th Brazilian Symposium on Software Quality, Association for Computing Machinery, Vol. 15, 2020, pp. 1-10.

[5] G. P. Gasca-Hurtado, M. C. Gómez-Alvarez, M. Muñoz, A. Peña, "A gamified proposal for software risk analysis in agile methodologies", Proceedings of the European Conference on Software Process Improvement, 2019, pp. 272-285.

[6] S. Patil, R. Ade, "A software project risk analysis tool using software development goal modeling approach", Information Systems Design and Intelligent Applications, 2015, pp. 767-777.

[7] J. T. Marchewka, "A framework for identifying and understanding risks in information technology projects", Journal of International Technology and Information Management, Vol. 19, No. 1, 2010, p. 2.

[8] S. Chaouch, A. Mejri, S. A. Ghannouchi, "A framework for risk management in Scrum development process", Procedia Computer Science, Vol. 164, 2019, pp. 187-192.

[9] B. G. Tavares, M. Keil, C. E. S. da Silva, A. D. de Souza, "A risk management tool for agile software development", Journal of Computer Information Systems, Vol. 61, No. 6, 2021, pp. 561-570.

[10] B. G. Tavares, C. E. S. da Silva, A. D. de Souza, "Practices to improve risk management in agile projects", International Journal of Software Engineering and Knowledge Engineering, Vol. 29, No. 03, 2019, pp. 381-399.

[11] N. Anand, S. Pujar, S. Rao, "A heutagogical interactive tutorial involving Fishbowl with Fish Battle and Round Robin Brainstorming: A novel syndicate metacognitive learning strategy", Medical Journal Armed Forces India, Vol. 77, 2021, pp. S73-S78.

[12] S. de Souza Lopes, R. C. G. de Souza, A. D. G. Contessoto, A. L. de Oliveira, R. T. V. Braga, "A Risk Management Framework for Scrum Projects", Proceedings of the 23rd International Conference on Enterprise Information Systems, Vol. 2, pp. 30-40.

[13] S. Grishunin, S. Suloeva, T. Nekrasova, E. Burova, "Development of Risk Controlling Mechanism and

Tools for Agile Projects in Telecommunications", Proceedings of Internet of Things, Smart Spaces, and Next Generation Networks and Systems, 2020, pp. 270-284.

[14] I. Ermiwin, S. R. Mertosono, Z. Hasyim, "Applying fishbowl technique to improve students speaking skill", E-Journal of ELTS (English Language Teaching Society), Vol. 7, No. 3, 2019.

[15] S. Filyppova, I. Bashynska, B. Kholod, L. Prodanova, L. Ivanchenkova, Ivanchenkov, V, "Risk Management Through Systematization: Risk Management Culture", International Journal of Recent Technology and Engineering, Vol. 8, No. 3, 2019, pp. 6047-6052.

[16] P. Marnada, T. Raharjo, B. Hardian, A. Prasetyo, "Agile project management challenge in handling scope and change: A systematic literature review", Procedia Computer Science, Vol. 197, 2022, pp. 290-300.

[17] M. Nabawy, G. Ofori, M. Morcos, C. Egbu, "Risk identification frame-work in construction of Egyptian mega housing projects", Ain Shams Engineering Journal, Vol. 12, No. 2, 2021, pp. 2047-2056.

[18] O. Ņikiforova, K. Babris, J. Kristapsons, "Survey on Risk Classification in Agile Software Development Projects in Latvia", Applied Computer Systems, Vol. 25, No. 2, 2020, pp. 105-116.

[19] M. Shameem, R. R. Kumar, M. Nadeem, A. A. Khan, "Taxonomical classification of barriers for scaling agile methods in global software development environment using fuzzy analytic hierarchy process", Applied Soft Computing, Vol. 90, No. 6, 2020, p. 106122.

[20] S. V. Shrivastava, U. Rathod, "A Goal-driven Risk Management Approach for Distributed Agile Development Projects", Australasian Journal of Information Systems, Vol. 23, 2019.

[21] J. Sithambaram, M. H. N. B. M. Nasir, R. Ahmad, "Issues and challenges impacting the successful management of agile-hybrid projects: A grounded theory approach", International Journal of Project Management, Vol. 39, No. 5, 2021, pp. 474-495.

[22] C. Tam, E. J. da Costa Moura, T. Oliveira, J. Varajao, "The factors influencing the success of on-going agile software development projects", International Journal of Project Management, Vol. 38, No. 3, 2020, pp. 165-176.

[23] A. A. Mohamed, N. R. Darwish, H. A. Hefny, "Multiple Linear Regression for Determining Critical Failure Factors of Agile Software Projects", International Journal of Intelligent Engineering and Systems, Vol. 12, No. 3, 2019.

[24] E. D. Canedo, A. P. M. do Vale, R. M. Gravina, R. L. Patrão, L. C. de Souza, V.E. dos Reis, F. L. L. de Mendonça, R. T. de Sousa Jr, "An Applied Risk Identification Approach in the ICT Governance and Management Macroprocesses of a Brazilian Federal Government Agency", Proceedings of the International Conference on Enterprise Information Systems, 2022, pp. 272-279.

[25] D. Kasap, M. Kaymak, "Risk Identification Step of the Project Risk Management", Proceedings of the Portland International Conference on Management of Engineering & Technology, Portland, OR, USA, 5-9 August 2007, pp. 2116-2120.

[26] I.A. Kiral, Z. Kural, S. Comu, "Risk Identification in Construction Projects: Using the Delphi Method", Proceedings of the 11th International Congress on Advances in Civil Engineering, Istanbul, Turkey, 2014.

[27] A. Kobo-Greenhut, H. Reuveni, I. B. Shlomo, R. Megnezi, "Unstructured brainstorming is not enough: structured brainstorming based on four verification and validation questions yields better hazard identification in health care", International Journal for Quality in Health Care, Vol. 31, No. 7, 2019, pp. 16-21.

[28] E. E. Odzaly, D. Greer, D. Stewart, "Agile risk management using software agents", Journal of Ambient Intelligence and Humanized Computing, Springer, Vol. 9, No. 23, 2018, pp. 823-841.

[29] A. Nadali, A. Grilo, A. Zutshi, "A conceptual framework of risk identification for scale up companies in transition period", Proceedings of the International Conference on Industrial Engineering and Operations Management, 2018, pp. 2346-2357.

[30] T. E. Abioye, O. T. Arogundade, S. Misra, A. T. Akinwale, O. J. Adeniran, "Toward ontology-based risk management framework for software projects: An empirical study", Journal of Software: Evolution and Process, Vol. 32, No. 12, 2020, p. e2269.

[31] M. Sousa, "Fast Brainstorm techniques with modern board games adaptations for daily uses in business and project managing", Proceedings of the International Conference of Applied Business and Management, 2020, pp. 508-524.

[32] L. M. Khodeir, M. Nabawy, "Identifying key risks in infrastructure projects-Case study of Cairo Festival City project in Egypt", Ain Shams Engineering Journal, Vol. 10, No. 3, 2019, pp. 613-621.

[33] M. Khalilzadeh, H. Shakeri, S. Zohrehvandi, "Risk identification and assessment with the fuzzy DEMATEL-ANP method in oil and gas projects under uncertainty", Procedia Computer Science, Vol. 181, 2021, pp. 277-284.

[34] M. Zavvar, A. Yavari, S. M. Mirhassannia, M. R. Nehi, A. Yanpi, M. H. Zavvar, "Classification of risk in software development projects using support vector machine", Journal of Telecommunication, Electronic and Computer Engineering, Vol. 9, No. 1, pp. 1-5.

[35] M. Yang, M. K. Lim, Y. Qu, X. Li, D. Ni, "Repair missing data to improve corporate credit risk prediction accuracy with multi-layer perceptron", Soft Computing, Vol. 26, No. 18, 2022, pp. 9167-9178.

[36] B. Esmaeili, M. R. Hallowell, B. Rajagopalan, "Attribute-based safety risk assessment. II: Predicting safety outcomes using generalized linear models", Journal of construction engineering and management, Vol. 141, No. 8, 2015, p. 04015022.

[37] Q. Wang, Y. Li, Y. Wang, J. Ren, "An automatic algorithm for software vulnerability classification based on CNN and GRU", Multimedia Tools and Applications, Vol. 81, No. 5, 2022, pp. 7103-7124.

Empirical Validation of Variable Method Interaction Cohesion Metric (VMICM) for Enhancing Reusability of Object-Oriented (O-O) Software

Original Scientific Paper

Bharti Bisht
Research scholar, School Of Computer Applications, MRIIRS
Faridabad, India
onebharti@gmail.com

Parul Gandhi
Professor, School Of Computer Applications, MRIIRS
Faridabad, India
parul.fca@mriu.edu

Abstract *– Any object-oriented (O-O) module's primary goal is to build classes with a high level of coherent interaction between variables and methods. To increase the quality of O-O (Object-Oriented) software, various metrics emphasizing cohesiveness have been established so far. These metrics operate on both the design and the code levels. However, these metrics still fall short of fully measuring the cohesion of object-oriented (O-O) software. Based on several concepts of cohesive interlinkages between variables and procedures, the study proposed an enhanced cohesion metric. The four forms of cohesive linkages (VMRv, VMMv, VMRTv, and VMOv) between variables and procedures were the focus of this study. The axiomatic frame of reference was employed for theoretical validation, and univariate logistic regression was applied in the MATLAB environment for empirical validation. The approach of univariate logistic regression has been adopted because it provides incredibly accurate data and can even be applied to datasets that can be linearly separated. The proposed metric exhibits high cohesion, which is the ultimate perspective of a highly reusable Object-Oriented (O-O) module, as evidenced by the testing phase and even training the real dataset with reusability prediction in terms of high values of precision, recall, R2, and low value of RSME of VMICM metric. The study results demonstrated that the proposed metric can act as a measure for predicting the reusability of the Object-Oriented (O-O) system.*

Keywords*: cohesion, cohesive linkages, logistic regression, reusable, validation*

1. INTRODUCTION

The importance of software applications has increased in recent years, and the wide variety of advantages offered by them is drawing a large global audience [1, 2]. Any software development phase involves a variety of intricate [3] tasks that must be efficiently managed if high-quality software is to be produced. It is possible to reduce the work needed for similar procedures by using the enhanced software generated after careful monitoring of various activities at various stages, and this will also assist in increasing the overall quality of newly developed software [4]. Measurement supports an institution's efforts to enhance the overall software development process and even improve the product's overall quality. Additionally, this would assist programmers in addressing the complexity of a particular software component at a very early stage of the process.

Building high-quality software, and Object-Oriented- based techniques are still quite popular [5]. Good modular designs maximize cohesion. The attributes of high cohesion classes are not shared with other classes, and they can be reused.

Therefore, by reducing complexity, a high level of cohesion promotes reusability. To assess software modules concerning cohesion, many scholars have developed numerous Object-Oriented (O-O) metrics [6]. However, in several situations, such measures do not take into account cohesion properly and thus have only a limited view of measuring it. To accurately measure cohesiveness, there is therefore a need to develop cohesion met-

rics that vary given the idea of cohesive interactions. This study presents the following contributions:

- Proposing a new cohesion metric called VMICM that emphasizes variable-method interactions.
- Validating the proposed metric empirically using a univariate logistic regression approach and studying correlation with other cohesion-based metrics.
- Analyzing the relationship between metric and degree of inheritance.

The framework of this work is further organized as Section II provides a detailed literature analysis of various studies. Section III details about designing phase of the proposed metric i.e. VMICM metric and a case study. The validation (theoretically and empirically) of the proposed metric is discussed in Section IV. Section V finally outlines the conclusion drawn from the study.

2. LITERATURE ANALYSIS

In the Object-Oriented (O-O) model, cohesion measures the relatedness between variables as well as methods of a particular class [6, 7]. Relatedness depicts the similarity between variable-method interactions. Cohesion can be categorized into a range from highly desirable i.e. functional cohesion to very low desirable i.e. coincidental cohesion. Cohesion can be maximized by effective as well as efficient O-O (Object-Oriented) based systems. The complexity of particular software can increase due to the low value of cohesion which in turn increases bugs during the development phase. Any class with a low value of cohesion can be further segmented into many subclasses [7] that would help to increase the value of cohesion.

The requirements of common instance variable usage by method pairs serve as the foundation for cohesion. measurements of Tight Class Coherence (TCC) and Loose Class Cohesion (LCC) provided by Bieman et al. [8] The authors suggested that the two methods are considered related if they use or refer to the same instance variable either directly or indirectly. The fact that variable A occurs in the body of method M indicates that variable A is being used directly by M. While a direct reference to variable A by a method M' that is either directly or indirectly invoked by method M qualifies as an indirect use of variable A by method M. TCC is defined as the proportion of method pairs that are directly connected, whereas LCC is defined as the proportion of method pairs that are either directly connected or indirectly connected.

Kakkar et al. [9] developed a SCOM metric that emphasizes interlinkage intensity in addition to taking weight into account. The ratio of the number of shared variables between two techniques to the greatest number of variables that any method can access is used to determine how strongly two methods are interconnected. The weight component is determined by dividing the total number of variables in a certain class by the number of variables that are shared by the method pair. SCOM value is the sum of the products of the weight and interlinkage intensities of all potential method pairs. Kansal et al. [10] in their study do not consider criteria based on similarity but focus on interlinkage patterns between various methods to compute cohesion. A class's protected or private meth-ods never access any of the variables found in that class. If protected or private methods are invoked by 2 public methods then we can say that they are interconnected to each other. Khajenoori et al. [11] suggested the first-class-based cohesion metric, LCOM (Lack of Cohesion in methods). This metric computes several method pairs that do not share any variable. It also represents the count of methods having zero similarity minus the count of methods not having zero similarity. If there are several pairs of comparable method definitions, the class is more cohesive. If none of a class's method pairs employ instance attributes, then there is no similarity between them, and the LCOM metric's value will be zero. The LCOM metric value is a measurement of the distinctiveness of the various method pairings that are present in the class.

Rasool et al. [12] discussed cohesive interlinkages between variables used by methods. They have proposed 3 types of cohesive interlinkages and then categorized them based on the ranking as well as weights. Both theoretical and empirical validation have been carried out. Pearson analysis and logistic regression are used to carry out experiments. Alsarraj et al. [13] introduced AECC which measures the degree of interconnectedness between distinct methods via variable-variable linkage as well as the invocation of methods in a specific class while taking the size of the cohesive fragment into account. even correlation experimentation of this metric with previously proposed class-based cohesion metrics was completed in this study. The comparison of related studies on cohesion-based metric approaches for reusability enhancement conducted by various scholars is shown in Table 1.

Table 1. Comparative Analysis of Various Frameworks related to reusability enhancement

Ref. No.	Motive	Metric used for Study	Conclusion
[4]	Developers of Object-Oriented software can identify flaws in class design and LSCC metric	LSCC metric	The findings imply that the cohesion metric which takes into consideration the level of interaction between each pair of methods, can more effectively explain the class quality
[14]	High Precision Cohesion Measure (HPCM), a new cohesion metric that aims to address the shortcomings of the preceding metrics	HPCM Metric	One of the desirable characteristics of a good object-oriented design is a class with high cohesiveness. A class that works well together is less likely to make mistakes and is simple to create and keep up with

[15]	Variable Frequency-Inverse Method Frequency (VF-IMF) metric is proposed to evaluate the degree of cohesion in modules and to group module methods to foster high cohesion	VF-IMF metric	To make it easier for a developer to create a module that ensures code reuse, the variables in this study are grouped using the VF-IMF metric to show what level of cohesion exists in a module among three low, high, and medium cohesions
[16]	Proposed a new method of measuring the cohesion of object-oriented software at the module level, where modules initially denote a single class and then a group of classes in later sections	UPBC metric	The suggested method aims to increase the object-oriented software's cohesion iteratively and repeatedly, calculating the cohesion score and using it to do clustering up until there is no longer a meaningful increase in the system's overall cohesion
[17]	The method devised in this study offers a technique to gauge cohesiveness measures at the class level	CSM metric, ACSM metric	Very cohesive classes must be designed with a strong coupling between their methods and a coherent internal description

3. MATERIAL AND METHODS

One of the most crucial aspects of an object-oriented (O-O) module is its high cohesiveness, which even aids in identifying the most reusable module. This section summarises the methodology of the proposed VMICM metric by anticipating high cohesiveness between variable-method interlinkages.

3.1. PROPOSED METRIC- VARIABLE METHOD INTERACTION COHESION METRIC (VMICM)

The majority of cohesion metrics that have been developed so far focus either on the use of methods within a class or their similarity due to the sharing of instance attributes. A new class cohesiveness metric, which takes into account the interlinking of variable methods from various contexts, has been proposed in this study. To better understand the variable methods interlinkages, this study has concentrated on four distinct coherent linkages between variables and methods. Considering variable $vi \in V$ and method $mn \in Md$ of class F, this study elucidated four types of cohesive interlinkages in the following manner:

i. Received (CRv) [17, 20]: ($V \times Md$) such that vi*CRv*mn, if $vi \in V$ is received as a parameter to a particular method $mn \in Md$.

ii. Manipulated (CMV) [17, 20]: ($V \times Md$) such that vi *CMv *mn, if $vi \in V$ is manipulated by method $mn \in Md$. This computation could be done either mathematically or it could be in the form of a function call [17, 20].

iii. Returned ($CRtv$) [20]: ($V \times Md$) such that vi*$CRtv$* mn, if the value of $vi \epsilon V$ is returned by method mn ϵ Md.

iv. Override (COv): ($V \times Md$) such that vi*COv*mn, if the scope of vi is overridden by method $mn \epsilon Md$.

3.1.1. Defining Proposed Metric- Variable Method Interaction Cohesion Metric (VMICM)

This proposed metric describes the MMI definition [20], which serves as the foundation for the widely acknowledged class-based cohesion features as indicated in [21], and this even has the potential to be utilized as a signal for the reconstruction of classes with weak cohesion. Non-inherited methods (both private as well as public) have been taken into consideration for the study. Eq.(1) represents the combination of several cohesive interlinkages in Class F as:

$$\sum CIv = \left(\begin{pmatrix} (CRi1 \cup CMi1 \cup CRti1 \cup VMOi1)\ldots \\ \cup (CRin \cup CMin \cup CRtin \cup COin) \end{pmatrix} \right) \quad (1)$$

where CIv represents the union of all proposed cohesive interlinkages between different variables and methods of Class F.

The two interconnected methodologies shown by VMICM are AVU (Average Variable Usage) and CSv (Cohesive Strength). AVU (Average Variable Usage) as defined in Eq. (2) denotes the average count of all variables used by all methods included in Class F:

$$\text{AVU} = \frac{\sum \text{CIv}}{\text{Md}} \quad (2)$$

where Md represents the total methods present in a Class F.

The total count of common variables between various methods pairs is represented by Eq. (3) as:

$$\text{CVv} = |\, \text{VM1} \cup \text{VM2} \cup \text{VM3} \ldots \cup \text{VMn} \,| \quad (3)$$

Based on the count of shared variables between method pairs, Cohesive Strength (CSv) represents the degree of [21, 22] cohesive interlinkages between them. Cohesive Strength is defined by Eq. (3) as:

$$\text{CS}_\text{v} = \begin{cases} \dfrac{\text{CV}_\text{v}}{\text{AVU}} & \text{if } \text{CV}_\text{v} <= \text{AVU} \\ 1 & \text{if } \text{CV}_\text{v} > \text{AVU} \end{cases} \quad (4)$$

Where:

CVv = Total count of common variables between various method pairs of Class F

AVU = Average count of all variables used by all methods included in Class F

$VMICM$ represents the average of cohesive strength (CSv) between variables and methods available in a particular class.

In the same way as an AVU analysis is carried out, it will take account of both privately and publicly inherited methods, and then their cohesive strength is added up. So, $VMICM$ proposed by this study is represented by Eq.(5) as follows:

$$\text{VMICM} = \frac{\text{CSv}}{\text{Md} * \frac{\text{Md} - 1}{2}} \quad (5)$$

3.2. RESEARCH METHODOLOGY

In this section, the process flow of the proposed metric $VMICM$ (Variable Method Interaction Cohesion Metric) is discussed. The research methodology used in this work was carried out in various phases as shown in Fig. 1. Different phases of the research flow are as follows:

- Initially, various metrics from the online $MAVEN$ repository were assimilated.
- To examine interlinkages between variable methods and their interaction with the reusability factor, cohesion metrics derived from the $MAVEN$ repository have been applied as input.
- The concept of the MMI was used as a foundation to create more coherent interlinkages.
- The next phase was the creation of a proposed metric $VMICM$ outline using 2 methodologies - AVU (Average Variable Usage) and CSv (Cohesive Strength).
- Theoretical validation has been performed using an axiomatic frame of reference. Alternative measurement hypotheses relating to the length, size, coupling, complexity, and unity of the software are analyzed using a base of reference for axioms in this model.
- Univariate logistic regression has been used in the MATLAB environment for empirical verification. This method was used to assess both the efficiency of the proposed $VMICM$ metric as well as those from the previous studies. It also demonstrates how the proposed metric contributes significantly to the reusability of Object-Oriented (O-O) software systems.
- Open-source JAVA-based classes were used as data sets in the testing and training phases.
- After repeated repetition of the training data set, the work was able to achieve high precision, recall, $R2$, and low $RSME$ values for the proposed metric.

Thus, this paper demonstrated that the proposed metric shows high cohesion and can act as a measure for predicting the reusability of Object-Oriented (O-O) classes.

4. RESULTS AND DISCUSSION

The theoretical and empirical validation of the proposed metric $VMICM$ using several techniques and approaches is discussed in this section.

4.1. THEORETICAL VALIDATION OF PROPOSED METRIC VMICM

This study incorporated the framework suggested by Briand for validating the proposed metric $VMICM$ theoretically. In this work, an axiomatic frame of reference for different software properties such as length, size, coupling, complexity, and cohesion are used to examine the various measurement parameters. To determine cohesion and verify that the $VMICM$ metric complies with the abovementioned benchmarks, there are several properties applied in this framework:

- Non-negativity[14-16]: $VMICM$ is calculated with the help of the modulus of the union of four types of cohesive interlinkages CRv, CMv, $CRtv$, and COv and the resultant value of $VMICM$ obtained was not less than
- Normalization [14]: When there are no cohesive interlinkages between the methods and the variable, $VMICM$ acquires 0 (i.e., the minimum value), and when there are all cohesive interlinkages, it reaches 1 (i.e., the maximum value). So, the value of the $VMICM$ metric falls between the range [0-Max].
- Cohesive modules [14, 15]: This property states that if two unrelated components are combined, the cohesiveness of the combined component will not increase. $VMICM$ metric satisfies this property.
- Monotonicity [14, 15]: Any cohesive interlinkages added to the proposed framework means that either $|CRv|$,$|CMv|$, $|CRtv|$, or $|COv|$ increases by 1. Consequently, the value of the $VMICM$ metric would be either increased or not affected at all.
- Null value [23]: The $VMICM$ metric shall be 0 if there is no cohesion among variables and methods of a particular class used in the analysis, such as CRv, CMv, $CRtv$, or Cov

All the properties suggested by Briand are met by the proposed $VMICM$ metric. Thus $VMICM$ metric is proven to be a valid cohesion metric.

4.2. EMPIRICAL VALIDATION OF PROPOSED METRIC VMICM

We have empirically tested the proposed metric $VMICM$ in this section to assess reusability for an Object-Oriented (O-O) module. This study produces a highly cohesive metric that contributes towards the high reusability of Object-Oriented(O-O) software systems.

4.2.1. Experimental Set-up

The analysis in the above study was carried out using JAVA-based classes from an online $MAVEN$ Repository. They were relatively different from each other in terms of methods pairs used in particular classes, due to the differences in size between the classes chosen for this study.

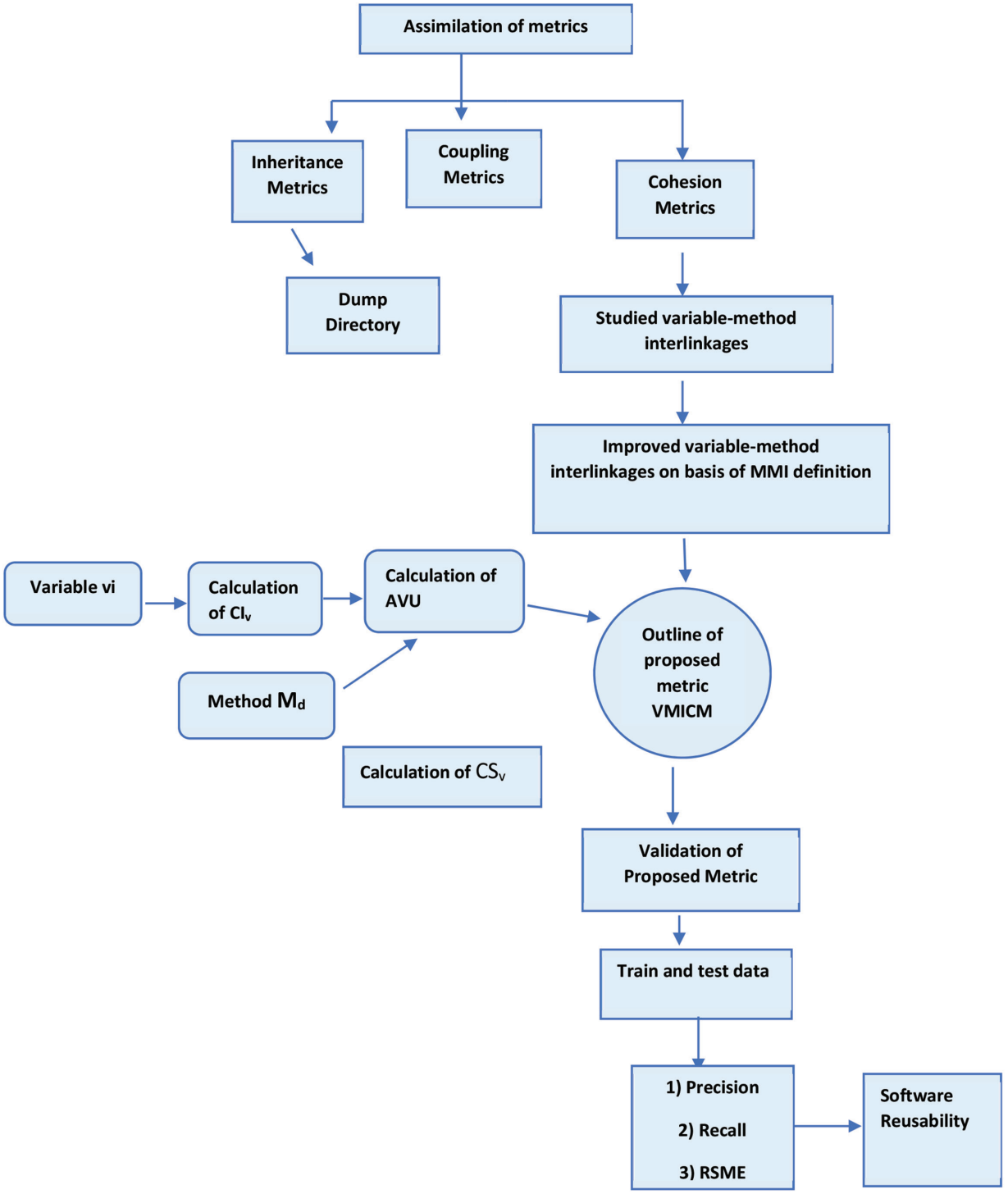

Fig. 1. Research Methodology Flowchart

Table 2 depicts the datasets used for this study.

Table 2. Datasets

Class Name	MD	CRV	CMV	CRtv	COv	Civ	AVU
Loan	3	3	3	3	1	10	3.3333
BMI	2	1	3	3	1	8	4
Employee	2	4	4	2	2	11	5.5
Course	3	2	1	1	1	5	1.6667
Box	2	4	4	2	1	12	6
Stack	3	1	1	1	1	4	1.3333

Complex	2	3	1	1	1	6	3
Shopping Cart	3	4	4	4	2	14	4.6667
Account	2	1	1	3	1	6	3
Lottery	3	4	4	4	1	13	4.3333
Person	3	2	2	2	2	8	2.6667
Triangle	3	3	2	3	2	10	3.3333
Stack of Integers	4	2	2	1	1	6	1.5
Car	3	3	3	3	3	12	4
Rectangle	2	2	1	2	1	6	3
Queue	5	3	1	1	3	8	1.6
Tax	2	2	2	2	2	8	4
Compute Change	6	4	4	5	2	12	2
Circle	3	1	1	4	1	4	1.3333
Calendar	2	2	2	6	2	8	4

After collecting the dataset from open-source projects, the proposed VMICM metric value is computed for the input classes. Earlier proposed cohesion metric values are also computed for the same input classes. Table 3 lists the calculated values of the VMICM metric and other cohesion-based metrics for each input class.

Table 3. Values of Proposed VMICM metric and other cohesion-based metrics of input classes used for the study

CNO	Class Name	CC	LAMCC	VMICM
CN1	Loan	0.67	0.34	3.3333
CN2	BMI	1.45	0.62	4
CN3	Employee	0.74	0.75	5.5
CN4	Course	0.48	0.45	1.6667
CN5	Box	0.457	0.356	6
CN6	Stack	1.22	0.833	1.3333
CN7	Complex	0.75	0.93	3
CN8	Shopping Cart	0.345	0.225	4.6667
CN9	Account	0.98	0.73	3
CN10	Lottery	0.35	0.26	4.3333
CN11	Person	0.350	0.456	2.6667
CN12	Triangle	0.451	0.382	3.3333
CN13	Stack of Integers	0.777	0.775	1.5
CN14	Car	0.25	0.38	4
CN15	Rectangle	0.65	0.52	3
CN16	Queue	0.90	0.82	1.6
CN17	Tax	0.83	0.73	4
CN18	Compute Change	0.35	0.28	2
CN19	Circle	0.534	0.486	1.3333
CN20	Calendar	0.76	0.50	4

To assess how the proposed VMICM metric can be adapted to the reusability of these classes, values for the proposed VMICM metric and all cohesion metrics are shown in the table above.

4.2.2. Data Selection

- Context Selection: This paper aims to demonstrate the fact that the proposed metric can act as a measure for the reusability of Object-Oriented (O-O) classes.
- Variable Selection: This work considers cohesion as an independent attribute and reusability measure as a dependent attribute.

4.2.3. Result Analysis

The univariate logistic regression technique [24, 25] is used in this study. The effectiveness of the proposed metric VMICM as well as currently utilized metrics from earlier studies have been independently examined using this method. It also demonstrates how the proposed metric contributes significantly to the reusability of Object-Oriented (O-O) software systems. Table 4 compares the proposed VMICM metric with existing cohesion-based metrics.

Table 4. Descriptive Analysis Results

Metric	Min.	Max.	Mean	Median	Standard Deviation
LCOM1	0.0	7875	89.45	20.0	336.7
LCOM2	0.0	7875	69.61	9.0	314.3
LCOM3	0.0	11.0	1.32	1.0	0.90
LCOM4	0.0	11.0	1.31	1.0	0.89
LCOM5	0.0	2.0	0.76	0.82	0.26
TCC	0.0	1.0	0.42	0.37	0.35
DCD	0.0	1.0	0.45	0.42	0.31
CAMC	0.0	1.0	0.39	0.39	0.16
NHD	0.0	1.0	0.64	0.67	0.16
LAMCC	0.0	0.9	0.54	0.51	0.22
VMICM	0.0	0.6	0.27	0.25	0.15

A graphical representation of a comparison of existing cohesion-based metrics and the proposed metric VMICM is shown in Fig. 2.

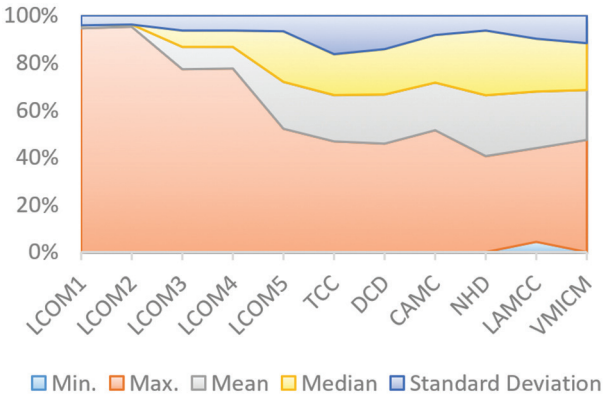

Fig. 2. Analysis of Proposed Metric VMICM and other metrics

In comparison to the existing metrics, according to the above analysis, the proposed VMICM metric has low mean and median values.

This lower value suggests that this study did not take into account an increased inheritance level. Increased level of inheritance leads to less reusable Object-Oriented (O-O) modules. Various statistics have been reported in this study for the evaluation of the proposed metric VMICM. These statistics are as follows:

- Precision [23-25]: This depicts the ratio between the counts of classes that are least reusable to the total count of reusable classes.
- Recall [23-25]: This depicts the ratio between the counts of classes that are reusable to the total count of actual classes [25] that are highly reusable.
- R2 [23-25]: This is one of the techniques of goodness-of-fit. It represents the percentage of the variance of the dependent attribute to the percentage of the variance of the independent attribute.
- RSME [23-25]: It represents the average magnitude of overall errors [24, 25]. This focus is on a relatively large count of errors.

The results of the above statistics evaluated for the study are shown below with the help of Table 5.

Metric	Precision	Recall	R2	RMSE
LCOM1	0.645	0.545	0.514	0.181
LCOM2	0.827	0.750	0.100	0.211
LCOM3	0.729	0.659	0.210	0.208
LCOM4	0.577	0.721	0.012	0.208
LCOM5	0.567	0.785	0.010	0.198
TCC	0.562	0.800	0.007	0.200
DCD	0.691	0.800	0.101	0.194
CAMC	0.553	0.752	0.221	0.208
NHD	0.589	0.660	0.013	0.219
LAMCC	0.823	0.875	0.414	0.210
VMICM	1.00	1.00	0.977	0.172

The observations that can be analyzed from the table are:

- High values of precision, recall, and R2 for the proposed metric VMICM demonstrate that it exhibits high cohesion, which is the ultimate perspective of a highly reusable Object-Oriented (O-O) module.
- The low RSME value of the proposed metric VMICM shows that it is the most suitable cohesion metric among those previously proposed and that it causes fewer errors, which results in a highly reusable module.

From the above analysis, we can conclude that our proposed metric VMICM is the best cohesion metric that contributes to a highly reusable Object-Oriented (O-O) system which is the main objective of this study. Fig. 3 shows a graphical comparison of the proposed metric VMICM and other cohesion metrics.

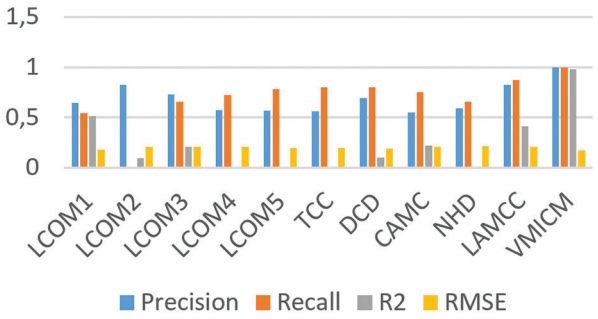

Fig. 3. Comparison of Univariate Statistics Results of Proposed Metric VMICM and other metrics

5. THREATS TO VALIDITY

Researchers suggest that there are various threats to the validity of any experimental analysis. We attempted to discuss the following threats in this section:

- Construct Validity [25]: This study deals with the measurement of variables used for this purpose. If these variables (dependent as well as independent) are accurately measured, we can say that they are valid constructively. This study even ensures the construct validity of dependent attributes.
- Internal Validity [25]: This deals with the relationship between cause and effect of both dependent attribute and independent attribute. If a particular study can establish effectively this relationship, we can conclude that it is valid internally.
- External Validity [25]: JAVA is used to implement the data set, i.e. all classes that are being considered. Applicability of the proposed cohesion metric should not be confined to one platform only, it should also apply to other Object-Oriented languages such as C++.

6. CONCLUSION AND FUTURE STUDY

This work has addressed the shortcomings of earlier proposed cohesiveness measurements. The study pro-

poses a new class-based cohesion metric VMICM that accounts for four different types of cohesive interlinkages CRv, CMv, CRtv, and COv between variables and methods. Using theoretical and empirical analysis, the quality of the metric is also validated against several modules. The results showed that the proposed metric VMICM is the most appropriate cohesion-based metric contributing towards the highly reusable Object-Oriented (O-O) system. The theoretical validation of the proposed metric VMICM conforms with all the properties suggested by Briand, proving it to be a valid cohesion-based metric.

In the future, the proposed metric will be taken as an input dataset and then a hybrid data mining algorithm will be applied to uncover relationships between metrics values and different levels of reusability of a given class.

7. REFERENCES:

[1] K. Zozas, A. Ampatzoglou, S. Bibi, A. Chatzigeorgiou, P. Avgeriou, I. Stamelos, "REI: An integrated measure for software reusability", Journal of Software: Evolution and Process, Vol. 31, No. 8, 2019, pp. 1-18.

[2] Y. Zhou, Y. Mi, Y. Zhu, L. Chen, "Measurement and refactoring for package structure based on the complex network", Applied Network Science, Vol. 5, No. 50, 2020, pp. 1-20.

[3] Q. Sun, J. Wu, K. Liu, "Toward understanding students' learning performance in an object-oriented programming course: The perspective of program quality", IEEE Access, Vol. 8, No. 4, 2020, pp. 37505-37517.

[4] A. Gosain, G. Sharma, "Dynamic Metrics for Object-oriented Software Systems", IEEE Access, Vol. 7, No. 5, pp. 244-249.

[5] B. Mehboob, Y. Chun, "A metadata-driven process assessing for assessing stability and reusability based on the risk of change of software systems", Journal of Software: Practice and Experience, Vol. 53, No. 5, 2023, pp. 1218-1248.

[6] D. Singh, H. J. S. Sidhu, "Optimizing the software metrics for UML structural and behavioral diagrams using metrics tool", Asian Journal of Computer Science and Technology, Vol. 7, No. 2, 2018, pp. 11-17.

[7] A. M. Altaie, "Designing and implementing a tool for measuring cohesion and coupling of Object-Oriented Systems", Journal of Software: Practice and Experience, Vol. 13, No. 2, 2022, pp. 368-375.

[8] G. Rasool, Z. Arshad, "A review of code smell mining techniques", Journal of Software: Practice and Experience, Vol. 27, No. 11, 2015, pp. 867-895.

[9] J. Pantiuchina, M. Lanza, G. Bavota, "Improving Code: The (Mis) Perception of Quality Metrics", Proceedings of IEEE International Conference on Software Maintenance and Evolution, Madrid, Spain, 23-29 September 2018, pp. 80-91.

[10] T. M. Meyers, D. Binkley, "An empirical study of slice-based cohesion and coupling metrics", ACM Transactions on Software Engineering and Methodology, Vol. 17, No. 1, 2007, pp. 1-27.

[11] B. Mehboob, C. Y. Chong, S. P. Lee, J.M.Y. Lim, "Reusability affecting factors and software metrics for reusability: A systematic literature review", Journal of Software: Practice and Experience, Vol. 51, No. 6, 2021, pp. 1416-1458.

[12] S. Manhas, R. Vashisht, P. S. Sandhu, N. Neeru, "Reusability evaluation model for procedure-based software systems", International Journal of Computer and Electrical Engineering, Vol. 2, No. 6, 2010, pp. 1107-1111.

[13] S. Mal, K. Rajnish, "New class cohesion metric: An empirical view", International Journal of Multimedia and Ubiquitous Engineering. Vol. 9, No. 5, 2014, pp. 367-376.

[14] W. Schäfer, R. Prieto-Diaz, M. Matsumoto, "Software Reusability", 2nd Edition, Ellis Horwood, 1994.

[15] J. C. Esteva, R. G. Reynolds, "Identifying reusable software components by induction", International Journal of Software Engineering, Vol. 1, No. 4, 1991, pp. 271-292.

[16] G. Maheswari, K. Chitra, "Enhancing reusability and measuring performance merits of software component", International Journal of Innovative Technology and Exploring Engineering, Vol. 8, No.6, 2019, pp. 1577-1583.

[17] R. M. Andrianjaka, H. Razafimahatratra, T. Mahatody, M. Ilie, S. Ilie, R.N. Raft, "Automatic generation of software components of the Praxeme methodology from ReLEL", Proceedings of 24th International Conference on System Theory, Control, and Computing, Lunago, Spain, 24-28 November 2020, pp. 843-849.

[18] S. Khajenoori, D. G. Linton, C. A. Morris, "Enhancing software reusability through effective use of the essential modeling approach," Information and Software Technology, Vol. 36, No. 11, 1994, pp. 495-501.

[19] D. Kansal, T. Aher, R. K. Joshi, "Sensitivity and Monotonicity in Class Cohesion Metrics", Proceedings of the 12th Innovations on Software Engineering Conference, New York, USA, 10-15 February 2019, pp. 1-5.

[20] P. Kakkar, M. Sharma, P. Sandhu, "Modeling of Reusability of Procedure based Software Components using Naive Bayes Classifier Approach", International Journal of Computer Applications, Vol. 55, No. 5, 2012, pp. 12-17.

[21] P. Gandhi, P. K. Bhatia, "Estimation of generic reusability for object-oriented software an empirical approach", ACM SIGSOFT Software Engineering Notes, Vol. 36, No. 3, 2011, pp. 1-4.

[22] A. Sharma, E. Al, "Maintainability Evaluation for Object-Oriented Software Metrics Using Tool Cohesion Inheritance (COIN)", International Journal of Software Engineering, Vol. 12, No. 4, 2021, pp. 233-238.

[23] M. Alzahrani, S. Alqithami, A. Melton, "Using Client-Based Class Cohesion Metrics to Predict Class Maintainability", Proceedings of IEEE 43rd Annual Computer Software and Applications Conference, New York, NY, USA, 15-20 June 2019, pp. 72-80.

[24] B. Bisht, P. Gandhi, "Software Reusability of Object-Oriented Systems using Data Mining Techniques", International Journal of Recent Technology and Engineering, Vol. 7, No. 4, 2020, pp. 48-53.

[25] R. G. Alsarraj, A. M. Altaie, A. A. Fadhil, "Designing and implementing a tool to transform source code to UML diagrams", Periodicals of Engineering and Natural Sciences, Vol. 9, No. 4, 2021, pp. 430-440.

8. APPENDIX

1	0.86	0.34	0.92	0.86	0.75	0.86	0.75	0.86	0.86
2	0.8428	0.3332	0.9016	0.8428	0.735	0.8428	0.735	0.8428	0.8428
3	0.825944	0.326536	0.883568	0.825944	0.7203	0.825944	0.7203	0.825944	0.825944
4	0.809425	0.320005	0.865897	0.809425	0.705894	0.809425	0.705894	0.80942512	0.80942512
5	0.793237	0.313605	0.848579	0.793237	0.691776	0.793237	0.6917761	0.793236618	0.793236618
6	0.777372	0.307333	0.831607	0.777372	0.677941	0.777372	0.6779406	0.777371885	0.777371885
7	0.761824	0.301186	0.814975	0.761824	0.664382	0.761824	0.6643818	0.761824448	0.761824448
8	0.746588	0.295163	0.798675	0.746588	0.651094	0.746588	0.6510942	0.746587959	0.746587959
9	0.731656	0.289259	0.782702	0.731656	0.638072	0.731656	0.6380723	0.731656199	0.731656199
10	0.717023	0.283474	0.767048	0.717023	0.625311	0.717023	0.6253108	0.717023075	0.717023075
11	0.702683	0.277805	0.751707	0.702683	0.612805	0.702683	0.6128046	0.702682614	0.702682614
12	0.688629	0.272249	0.736673	0.688629	0.600549	0.688629	0.6005485	0.688628962	0.688628962
13	0.674856	0.266804	0.721939	0.674856	0.588538	0.674856	0.5885375	0.674856382	0.674856382
14	0.661359	0.261468	0.707501	0.661359	0.576767	0.661359	0.5767668	0.661359255	0.661359255
15	0.648132	0.256238	0.693351	0.648132	0.565231	0.648132	0.5652315	0.64813207	0.64813207
16	0.635169	0.251113	0.679484	0.635169	0.553927	0.635169	0.5539268	0.635169428	0.635169428
17	0.622466	0.246091	0.665894	0.622466	0.542848	0.622466	0.5428483	0.62246604	0.62246604
18	0.610017	0.241169	0.652576	0.610017	0.531991	0.610017	0.5319913	0.610016719	0.610016719
19	0.597816	0.236346	0.639525	0.597816	0.521351	0.597816	0.5213515	0.597816385	0.597816385
20	0.58586	0.231619	0.626734	0.58586	0.510924	0.58586	0.5109245	0.585860057	0.585860057
21	0.34	0.63	0.75	0.15	0.75	0.34	0.75	0.34	0.34
22	0.3332	0.6174	0.735	0.147	0.735	0.3332	0.735	0.3332	0.3332
23	0.326536	0.605052	0.7203	0.14406	0.7203	0.326536	0.7203	0.326536	0.326536
24	0.320005	0.592951	0.705894	0.141179	0.705894	0.320005	0.705894	0.32000528	0.32000528
25	0.313605	0.581092	0.691776	0.138355	0.691776	0.313605	0.6917761	0.313605174	0.313605174
26	0.307333	0.56947	0.677941	0.135588	0.677941	0.307333	0.6779406	0.307333071	0.307333071
27	0.301186	0.558081	0.664382	0.132876	0.664382	0.301186	0.6643818	0.301186409	0.301186409
28	0.295163	0.546919	0.651094	0.130219	0.651094	0.295163	0.6510942	0.295162681	0.295162681
29	0.289259	0.535981	0.638072	0.127614	0.638072	0.289259	0.6380723	0.289259428	0.289259428
30	0.283474	0.525261	0.625311	0.125062	0.625311	0.283474	0.6253108	0.283474239	0.283474239
31	0.277805	0.514756	0.612805	0.122561	0.612805	0.277805	0.6128046	0.277804754	0.277804754
32	0.272249	0.504461	0.600549	0.12011	0.600549	0.272249	0.6005485	0.272248659	0.272248659
33	0.266804	0.494372	0.588538	0.117708	0.588538	0.266804	0.5885375	0.266803686	0.266803686
34	0.261468	0.484484	0.576767	0.115353	0.576767	0.261468	0.5767668	0.261467612	0.261467612
35	0.256238	0.474794	0.565231	0.113046	0.565231	0.256238	0.5652315	0.25623826	0.25623826
36	0.251113	0.465299	0.553927	0.110785	0.553927	0.251113	0.5539268	0.251113495	0.251113495
37	0.246091	0.455993	0.542848	0.10857	0.542848	0.246091	0.5428483	0.246091225	0.246091225
38	0.241169	0.446873	0.531991	0.106398	0.531991	0.241169	0.5319913	0.241169401	0.241169401
39	0.236346	0.437935	0.521351	0.10427	0.521351	0.236346	0.5213515	0.236346012	0.236346012
40	0.231619	0.429177	0.510924	0.102185	0.510924	0.231619	0.5109245	0.231619092	0.231619092
41	0.15	0.63	0.75	0.86	0.75	0.34	0.5	0.63	0.63
42	0.34	0.15	0.92	0.34	0.75	0.86	0.75	0.34	0.86
43	0.3332	0.147	0.9016	0.3332	0.735	0.8428	0.735	0.3332	0.8428
44	0.326536	0.14406	0.883568	0.326536	0.7203	0.825944	0.7203	0.326536	0.825944
45	0.320005	0.141179	0.865897	0.320005	0.705894	0.809425	0.705894	0.32000528	0.80942512
46	0.313605	0.138355	0.848579	0.313605	0.691776	0.793237	0.6917761	0.313605174	0.793236618
47	0.307333	0.135588	0.831607	0.307333	0.677941	0.777372	0.6779406	0.307333071	0.777371885
48	0.301186	0.132876	0.814975	0.301186	0.664382	0.761824	0.6643818	0.301186409	0.761824448
49	0.295163	0.130219	0.798675	0.295163	0.651094	0.746588	0.6510942	0.295162681	0.746587959
50	0.34	0.05	0.75	0.63	0.75	0.63	0.75	0.63	0.63

Semi-automated Software Requirements Categorisation using Machine Learning Algorithms

Original Scientific Paper

Pratvina Talele
Department of Computer Engineering and Technology,
Dr. Vishwanath Karad MIT World Peace University,
Pune, India
pratvina.talele@mitwpu.edu.in

Siddharth Apte
Department of Computer Engineering and Technology,
Dr. Vishwanath Karad MIT World Peace University,
Pune, India
sidapte.01@gmail.com

Rashmi Phalnikar
Department of Computer Engineering and Technology,
Dr. Vishwanath Karad MIT World Peace University,
Pune, India
rashmi.phalnikar@mitwpu.edu.in

Harsha Talele
Department of Computer Engineering,
Pimpri Chinchwad College of Engineering,
Pune, India
harshatalele19@gmail.com

Abstract *– Requirement engineering is a mandatory phase of the Software development life cycle (SDLC) that includes defining and documenting system requirements in the Software Requirements Specification (SRS). As the complexity increases, it becomes difficult to categorise the requirements into functional and non-functional requirements. Presently, the dearth of automated techniques necessitates reliance on labour-intensive and time-consuming manual methods for this purpose. This research endeavours to address this gap by investigating and contrasting two prominent feature extraction techniques and their efficacy in automating the classification of requirements. Natural language processing methods are used in the text pre-processing phase, followed by the Term Frequency – Inverse Document Frequency (TF-IDF) and Word2Vec for feature extraction for further understanding. These features are used as input to the Machine Learning algorithms. This study compares existing machine learning algorithms and discusses their correctness in categorising the software requirements. In our study, we have assessed the algorithms Decision Tree (DT), Random Forest (RF), Logistic Regression (LR), Neural Network (NN), K-Nearest Neighbour (KNN) and Support Vector Machine (SVM) on the precision and accuracy parameters. The results obtained in this study showed that the TF-IDF feature selection algorithm performed better in categorising requirements than the Word2Vec algorithm, with an accuracy of 91.20% for the Support Vector Machine (SVM) and Random Forest algorithm as compared to 87.36% for the SVM algorithm. A 3.84% difference is seen between the two when applied to the publicly available PURE dataset. We believe these results will aid developers in building products that aid in requirement engineering.*

Keywords*: Natural Language Processing, Machine Learning, Software Engineering, Supervised Machine Learning*

1. INTRODUCTION

In system engineering, the software development life cycle (SDLC) or application development life cycle is a process utilised to plan, test, and deploy software projects. The SDLC is a standardised procedure that tries to guarantee the accuracy of the shipped software in accordance with the client's requirements. A crucial stage in SDLC is requirement engineering, which involves establishing, documenting, and managing system requirements [1]. Requirement elicitation, which is a component of requirement engineering, is the process of collecting software requirements by communicating with stakeholders. The methods used for requirement elicitation include task analysis, interviews, and brainstorming.

There are two main types of requirements: Functional and Non-Functional. Functional requirements are mandatory requirements that must be implemented in the software system. It defines what a system must do and its features and functions. Non-functional requirements are not mandatory but desirable attributes that specify how a system should function. They can be considered as quality attributes of the software systems.

Another aspect of requirement engineering is requirement prioritisation. After identifying functional and non-functional requirements, priorities are to be assigned to streamline and order the development of software. Requirement prioritisation is a continuous process encompassing multifaceted and critical decision-making events that simplify high-quality software development. This process ensures that the ordering of both functional and non-functional requirements specified by software stakeholders is correct for implementation [2].

These requirements are ordered as per their significance, such as conflict, penalty, and price [3]. Given the rising demand for software functionality, many software solutions have a wide range of requirements. Implementing various requirements in a limited amount of time with limited availability of resources and budget is challenging. Hence, software products are delivered in stages. With each new release, features can be added. However, this prioritisation of shipping the critical requirements earliest and proceeding with the less crucial aspects makes requirement engineering a challenging process. Accurate requirement classification is critical to a software project's success. There are significant risks associated with the incorrect classification of requirements [4]. These risks can entail the project being over budget, going overtime, or even failing. According to research, 71% of errors result from an unclear understanding and classification of requirements [5]. The CHAOS report by the Standish Group outlined the causes of IT project failure in the United States. It revealed that just 16.2% of IT projects were successful; the rest failed [6]. The current manual methods for classifying software requirements are labour and time-intensive and require subject-matter specialists. Additionally, manual techniques can also lead to inaccuracy and misrepresentation. Our purpose in undertaking this research is to provide a modern automated solution that will aid the process of requirement engineering by improving accuracy while reducing the time taken.

Significant research is being conducted in the field of applying machine learning models and techniques in classifying text [7] from documents and other natural language processing techniques. Based on several studies [3, 8, 9] and comparative analysis, in this paper, TF-IDF and Word2Vec techniques have been employed for feature selection and several machine learning algorithms, which are Decision tree, Random Forest, Linear regression, Neural network, KNN (K – nearest neighbours), SVM (Support vector machines) for text categorisation.

This paper is organised as follows: The literature review is covered in section two. The research methodology and techniques employed are thoroughly described in section three. Experimental results are discussed in section four. In section five, the conclusion is presented, and future scope is discussed in section six.

2. LITERATURE REVIEW

Using machine learning, researchers have employed many techniques to classify software requirements (functional and nonfunctional). The j48 decision tree is implemented with pruned and unpruned being the two types of trees to create a total of four models; model 1 handles 'authentication authorization' type of security requirements, model 2 deals with 'access control' requirements, model 3 defines 'cryptography-encryption' requirements and model 4 is concerned with 'data integrity' requirements. Out of which, model 4 gives the maximum accuracy [10]. The use of algorithms such as MNB, Gaussian Naïve Bayes (GNB), KNN, Decision tree, Support Vector Machine (SVM), and Stochastic Gradient Descent SVM (SVM SGD) was done. Of these, SVM and SGD performed better than all the algorithms with GNB performing the worst [11]. The author has used KNN, SVM, Logistic regression, and MNB. SVM and Linear regression both have shown high precision values in classifications of functional and non-functional requirements [12]. In this paper, the authors have used Multinomial Naïve Bayes, KNN, Sequential Minimal Optimization (SMO). SMO performed the best with an accuracy of 0.729 [13]. A series of support vector machine (SVM) is used along with lexical features to achieve recall and precision on 0.92 [10]. It is observed that the modified version of decision tree, Multiple Correlation based decision tree, used to classify software requirements performs better when using TF-IDF as a feature extraction method [14]. MNB and Logistic regression are employed to obtain an accuracy of 95.55% and 91.23% respectively [15]. Naïve Bayes and decision tree were employed on a dataset comprising crowdsourced software requirements with accuracy results for Naïve Bayes being 92.7% and Decision tree being 84.2% [16]. The study investigated two types of models CNN (convolutional neural network) and ANN (Artificial neural network) by varying the hyperparameters i.e., Training epoch, Batch size, Number of filters, Embedding Dimension for CNN and Training Epochs, Alpha, Hidden Neurons for ANN having achieved an accuracy of 82% to 90% for the ANN model and 82% to 94% for the CNN models [17]. A semi-supervised learning approach is described for NFR classification. This approach with EM strategy (expectation maximisation) shows an improvement in classification accuracy as compared to supervised naïve bayes, KNN and TF-IDF in terms of its accuracy. In accordance with the percentage increase of labelled requirements, the accuracy achieved ranges from 80% to higher 90's [18]. In this approach, the BoW (bag of words) is used as a text vectorization technique in combination with two machine learning algorithms, SVM and KNN. The results are presented in three types. Firstly, the classification of FR/NFR having a precision of 90% and 82%, secondly, the classification of subcategories of NFR with an accuracy of 68% and 56% and lastly, the classification of subcategories of NFR and FR with a precision of 73% and 67% respectively, for SVM and KNN algorithms [19]. Researchers applied the TF-IDF

preprocessing technique to a dataset containing SRS document phrases with functional and non-functional requirements and were able to achieve an accuracy of 78.57% for the SVM algorithm whereas decision tree performed the worst with an accuracy of 61.42% [20].

The studies mentioned had to preprocess and extract important features to manually achieve this goal. With the rise of powerful deep learning algorithms, cheaper computational power, and other advancements facilitating the use of such algorithms, it was observed that end-to-end methods could be built to do this work. The authors in [21] employed the use of Bidirectional Gated Recurrent Neural Networks (BiGRU) to classify requirements using raw text, using word and character sequence as tokens. The accuracy range for the Word sequence ranged from 76% to 87% whereas for the character sequence ranged from 56% to 70% for binary classification and multiclass multilabel classification. The results were 69% for word vector and 64% for character sequence. The authors have examined the possibility of combining standard feature selection with 9 different kinds of deep learning predictors. They have used different types of Max–Min ratio (MMR) approaches, which have shown an improvement in performance by 1 to 5% when tested on the PROMISE dataset [22].

The research gap that we identified in the reviewed publications is that they do not consider all types of software requirements (functional/non-functional) [10, 11, 13] as well as a wide array of existing machine learning algorithms have not been evaluated [10, 15, 16, 19]. To overcome this drawback, machine learning algorithms such as DT, RF, LR, NN, KNN, and SVM are considered, and feature extraction techniques, TF-IDF and Word2Vec are evaluated in this study. This will assist researchers in developing the software framework.

3. METHODOLOGY

To classify software requirements, many researchers have suggested various requirement classification strategies. Since each stakeholder has a unique viewpoint on the software, this process takes a long time to complete. This calls for automating the requirement identification process. Different machine learning (ML) techniques are utilised to automate the requirements classification. As these requirements are stated in natural language, the text pre-processing phase is necessary to turn the text into vectors. These vectors can be used as input for ML algorithms. The steps in the conduct of this research are mentioned in Fig.1.

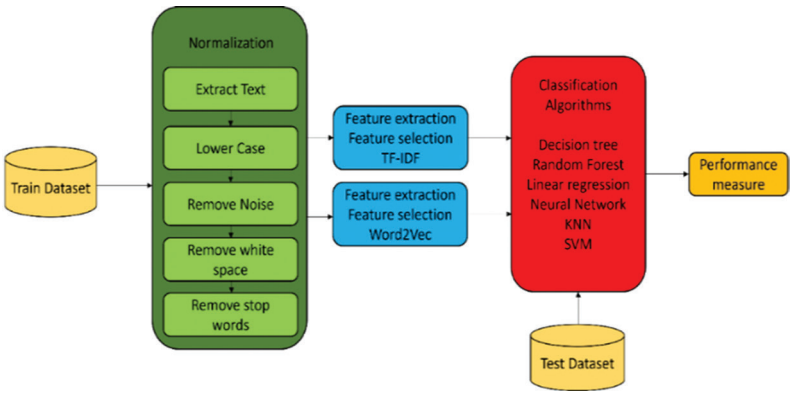

Fig. 1. Proposed Architecture for Automation of Classifying Requirements

3.1. TEXT PREPROCESSING

Natural language processing (NLP) is a branch of Machine learning that deals with teaching computers to process data that is specified in human-readable language. The raw text is cleaned by feature extraction and text preprocessing techniques, which then supply the features to machine learning algorithms. Training on supervised learning algorithms becomes easier when raw text is processed. The text preprocessing methods are as follows:

- Extract text: This method uses Python libraries to extract the text from documents in PDF or CSV formats to give the outputs in paragraphs.
- Lowercase: All uppercase characters are converted to lowercase, as having some uppercase characters might lead to incorrect feature extraction caused by duplication.
- Removal of noise: meaningless symbols that do not carry any specific meaning, such as ! $@$%&*(^$#@ {}[]:"><,.}]| are removed.
- Removal of white space: extra white space occurring between two words is removed for preprocessing.
- Removal of stop words: certain words in grammar such as "the", "a", "on", "is", "all" do not carry any information of significance and hence are removed.

3.2. EXTRACTION TECHNIQUE

Based on the literature survey, two techniques, Term Frequency – Inverse Document Frequency and Word-2Vec are used to extract features.

Term Frequency – Inverse Document Frequency (TF-IDF) – is a method to compute words in a set of documents. It quantifies the frequency of a term in a

document while considering its rarity across the entire collection, aiding in information retrieval and text analysis. It is calculated by:

$$tfidf_{w,d} = tf_{w,d} \times idf_w \quad (1)$$

where Term Frequency (TF) is simply a frequency counter for a word (w) in document(d).

$$tf_{w,d} = \frac{n_{w,d}}{Number\ of\ words\ in\ the\ document} \quad (2)$$

Inverse Document Frequency measures the informativeness of word (w). It is calculated by

$$idf_w = log\left(\frac{number\ of\ documents}{number\ of\ documents\ with\ word\ w}\right) \quad (3)$$

Word2Vec – Word2Vec's objective is to align the vectors of words with similar meanings in the vector space. It searches for mathematical similarities. Word2Vec automatically distributes numerically and vectorizes word characteristics, such as the context of specific words.

3.3. CLASSIFICATION ALGORITHMS

- Decision Tree (DT): A Decision Tree is a non-parametric algorithm for classification and regression. It organises data into a tree-like flowchart, using if-else tests on features to recursively partition the dataset. The leaves of the tree provide final predictions. Measures like Entropy, Gini Index, and Chi-Square Test guide the selection of important features, aiding in decision-making and prediction accuracy.
- Random Forest (RF): It is an ensemble method, which means that a random forest model is composed of numerous decision trees, known as estimators, each of which generates a separate set of predictions. The estimators' predictions are combined by the random forest model to yield a more precise prediction.
- Logistic Regression (LR): It is an ML Algorithm used for binary classification by predicting whether something happens or not. It uses a Sigmoid function (Logistic function) to give the probability output which is then compared to a pre-defined threshold and further labelled into one of the two categories accordingly.
- Neural Network (NN): It is an ML Algorithm used to diagnose the relationships in a set of features through a process inspired by the behaviour of the human brain. Several nodes comprise a neural network layer that can have multiple layers.
- K-nearest neighbours (KNN): It is a type of supervised learning classifier that groups individual data points together which are in close proximity (k closest relatives). It assumes that points lying near one another are similar. The class label is decided based on the class labels assigned to the surrounding points; this is referred to as "majority voting". Its performance is lower than SVM and Multinomial Naïve Bayes.
- Support Vector Machines (SVM): are a set of supervised machine learning algorithms employed for classification and regression. In an n-dimensional space, where n represents the number of features, data items are plotted, and a hyperplane is identified. This hyperplane effectively separates the coordinates into positive and negative classes, classifying the data items. SVM is less suitable for large datasets due to extended training times.

4. EXPERIMENTAL RESULTS

To the best of our knowledge, a comparison between Word2Vec and TF-IDF feature extraction techniques has yet to be performed on the PURE dataset.

4.1. EXPERIMENTAL SETTINGS

These experiments were carried out on a local computer running 64-bit Windows 11 equipped with 8GB RAM. These experiments were carried out on a local Jupyter Notebook environment with the Python3 programming language.

4.2. DESCRIPTION OF THE DATASET

Table 1. Categories of Requirements

PURE dataset [23]			
1.	Functional Requirement (FR)	11.	Quality attribute requirements
2.	Qualitative attributes	12.	Availability requirement
3.	Help module	13.	Maintainability requirement
4.	Support module	14.	Other requirements
5.	Audit module	15.	Safety requirement / Security requirement
6.	Access module	16.	Usability requirements
7.	Ease of use	17.	Portability requirements
8.	Usability	18.	Testability requirements
9.	System Availability	19.	Other nonfunctional requirements
10.	Performance and scalability / Performance requirement	20.	Software quality attributes

The publicly available dataset PURE (PUblicREquirement) used is a compendium of 79 different documents in PDF and HTML formats. These are SRS (Software Requirement Specification) documents that represent real-world requirements taken from academia, industry, etc., and contain 20 different functional and nonfunctional requirements written in natural language. These documents would be representative of the client's requirements, typically presented to the software developers. Table 1 provides an overview of the number of requirements present in the dataset [23].

4.2. RESULTS

This study uses the PURE dataset, which contains 79 SRS documents. Two text preprocessing techniques,

Word2Vec and TF-IDF, are employed. A total of 2153 feature instances were extracted, representing 20 distinct feature categories within the dataset. The results are as follows. A comparison of the results using the TF-IDF technique and the Word2Vec technique is discussed below.

Using the TF-IDF preprocessing technique, which calculates how relevant a word in a series or corpus is to a text/document [24], in our study, all of the algorithms were able to identify Functional, Access module, Maintainability requirements, other requirements, Performance requirements, software quality attributes, Usability, and software qualitative attributes, as illustrated in Fig. 2.

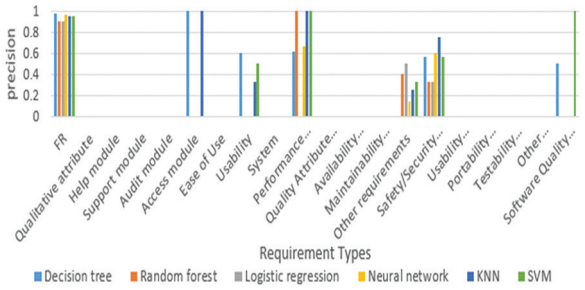

Fig. 2. Comparison of ML Algorithms Using TF-IDF (Precision)

Only Decision Tree was able to identify the Audit Module, and only Neural Network was able to identify Portability Requirements. The Help module, support module, Ease of use, Availability, Usability requirements, Testability, and Other nonfunctional requirements were all not identified by any of the algorithms. However, some algorithms, while able to correctly identify the requirements, are not in all cases able to correctly map those requirements to the corresponding test dataset, as shown in Table 2. '0' indicates that it is identified but not mapped, whereas '-' indicates it is not identified at all.

Fig. 3 shows the accuracy technique for the various algorithms. SVM (support vector machine) performs the best with an accuracy of 91.20%, followed by 90.10% for the KNN algorithm. Decision Tree, Logistic Regression, Random Forest, and Neural Network all have accuracies of 88.46%, 87.91%, 87.36%, and 84.06% respectively.

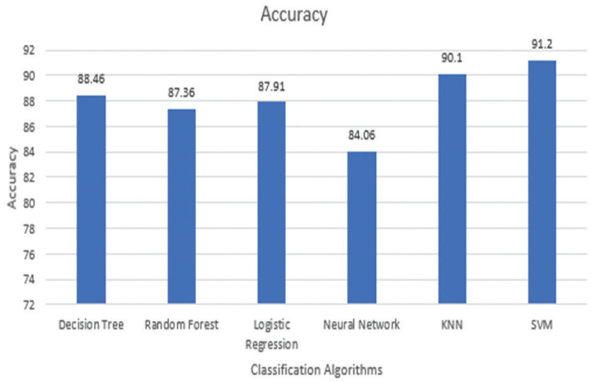

Fig. 3. Comparison of ML Algorithms Using TF-IDF (Accuracy)

Table 2. Comparison of Precision Value for ML Algorithms Using TF-IDF

	Precision									
ML algorithm	FR	Qualitative attribute	Help module	Support module	Audit module	Access module	Ease of Use	Usability	System Availability	Performance Requirements
Decision tree	0.98	0	-	-	0	1	-	0.60	0	0.62
Random forest	0.91	0	-	-	-	0	-	0	-	1
Logistic regression	0.90	0	-	-	-	0	-	0	-	0
Neural network	0.97	0	-	-	-	0	-	0	-	0.67
KNN	0.95	0	-	-	-	1	-	0.33	-	1
SVM	0.95	0	-	-	-	0	-	0.50	-	1

ML algorithm	Quality Attribute Requirements	Availability Requirements	Maintainability Requirements	Other Requirements	Safety/Security Requirements	Usability Requirements	Portability Requirements	Testability Requirements	Other Nonfunctional Requirements	Software Quality Attributes
Decision tree	-	-	0	0	0.57	-	-	-	-	0.5
Random forest	-	-	0	0.4	0.33	-	-	-	-	0
Logistic regression	-	-	0	0.5	0.33	-	-	-	-	0
Neural network	0	-	0	0.14	0.60	-	0	-	-	0
KNN	-	-	0	0.25	0.75	-	-	-	-	0
SVM	-	-	0	0.33	0.57	-	-	-	-	1

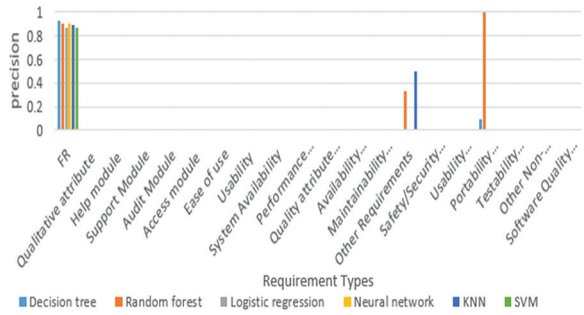

Fig. 4. Comparison of ML Algorithms Using Word2Vec (Precision)

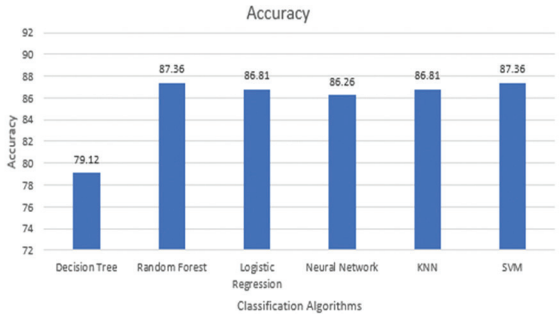

Fig. 5. Comparison of ML Algorithms Using Word2Vec (Accuracy)

	Precision									
ML algorithm	**FR**	**Qualitative attribute**	**Help module**	**Support module**	**Audit module**	**Access module**	**Ease of Use**	**Usability**	**System Availability**	**Performance Requirements**
Decision tree	0.93	0	0	-	-	0	-	0	-	-
Random forest	0.90	0	0	-	-	0	-	0	-	-
Logistic regression	0.87	0	-	-	-	0	-	0	-	-
Neural network	0.90	0	-	-	-	0	-	0	-	-
KNN	0.89	0	-	-	-	0	-	0	-	-
SVM	0.87	0	-	-	-	0	-	0	-	-

ML algorithm	**Quality Attribute Requirements**	**Availability Requirements**	**Maintainability Requirements**	**Other Requirements**	**Safety/Security Requirements**	**Usability Requirements**	**Portability Requirements**	**Testability Requirements**	**Other Nonfunctional Requirements**	**Software Quality Attributes**
Decision tree	-	0	0	0	0	0	0.1	-	0	0
Random forest	-	0	0	0.33	0	0	1	-	0	0
Logistic regression	-	-	0	0	0	0	0	-	0	0
Neural network	-	-	0	0	0	0	0	-	0	0
KNN	-	-	0	0.5	0	0	0	-	0	0
SVM	-	-	0	0	0	0	0	-	0	0

The Word2Vec learns representations by predicting word contexts in a given dataset. This enables efficient encoding of semantic similarities and differences, facilitating tasks like natural language processing and machine learning [25]. In our research, all the algorithms were able to identify Functional requirements, Qualitative attributes, Access module, Usability, Maintainability, other requirement, Safety/Security Requirements, Usability requirements, Portability, other nonfunctional requirements, and software quality attributes. Only random forest and decision tree can classify the Help module and Availability requirements; all other requirements were unidentified by any of the algorithms. However, some algorithms, while able to correctly identify the requirements, are not in all cases able to correctly map those requirements to the corresponding test dataset, as illustrated in Table 3. '0' indicates that it is identified but not mapped whereas '-' indicates it is not identified at all.

5. CONCLUSION

Through this work, we have provided a systematic comparison of several ML algorithms (DT, Random Forest, LR, NN, KNN, and SVM) used to identify and categorise a number of functional and non-functional requirements. The dataset undergoes preprocessing which includes extracting the text, conversion to lowercase, removal of noise, white space, and stop words after which the feature selection technique of TF-IDF and Word2Vec is employed. The performance of the ML algorithms is measured by the test dataset.

79 separate SRS documents in PDF and HTML formats that depict actual client requests were employed in the second phase of our research. In this, the feature selection techniques are compared while the pre-processing methods stay the same. The study was carried out using the Word2Vec and TF-IDF approaches. When

compared to the Word2Vec technique, it has been found that the TF-IDF feature selection technique produces better outcomes in subsequent algorithmic evaluations. 91.20% (for the SVM and Random Forest algorithm) as compared to 87.36% (for the SVM algorithm), a 3.84% difference is seen between the two. We are sure that these techniques will assist developers in automating the task of software requirement categorisation, thus saving time, money, and other vital resources in the SDLC while being able to ship the most suitable product tailored to the stakeholder's requirements. Additionally, it can assist industry experts in choosing the appropriate algorithm that offers the most significant degree of accuracy in the categorisation process.

6. FUTURE SCOPE

To facilitate the widespread adoption of ML algorithms in requirement engineering, the future scope entails extending the research to ensure practical applicability and scalability. The focus should be on optimising the proposed methods for large-scale projects. Additionally, there is a need to explore integration with popular development tools, thereby facilitating adoption by development teams and streamlining the software engineering process.

7. REFERENCES:

[1] P. Talele, R. Phalnikar, "Software requirements classification and prioritization using machine learning", Machine Learning for Predictive Analysis, Lecture Notes in Networks and Systems, Springer, Vol. 141, 2021, pp. 257-267.

[2] P. Talele, R. Phalnikar, "Automated Requirement Prioritisation Technique Using an Updated Adam Optimisation Algorithm", International Journal of Intelligent Systems and Applications in Engineering, Vol. 11, No. 3, 2023, pp. 1211-1221.

[3] R. Phalnikar, D. Jinwala, "Analysis of Conflicting User Requirements in Web Applications Using Graph Transformation", ACM SIGSOFT Software Engineering Notes, Vol. 40, No. 2, 2015, pp. 1-7.

[4] H. Alrumaih, A. Mirza, H. Alsalamah, "Toward Automated Software Requirements Classification", Proceedings of the 21st Saudi Computer Society National Computer Conference, Riyadh, Saudi Arabia, 25-26 April 2018, pp. 1-6.

[5] "Fixing the Software Requirements Mess", https://www.cio.com/article/255253/developer-fixing-the-software-requirements-mess.html (accessed: 2023)

[6] The Standish Group Report, "Chaos report", https://simpleisbetterthancomplex.com/media/2016/10/chaos-report.pdf (accessed: 2023)

[7] R. Pawar, S. Ghumbre, R. Deshmukh, "Developing an Improvised E-Menu Recommendation System for Customer", Recent Findings in Intelligent Computing Techniques, Advances in Intelligent Systems and Computing, Vol. 708, Springer, Singapore.

[8] M. Binkhonain, L. Zhao, "A review of machine learning algorithms for identification and classification of non-functional requirements", Expert Systems with Applications: X, Vol. 1, 2019.

[9] A. Khan, B. Baharudin, L. H. Lee, K. Khan, "A Review of Machine Learning Algorithms for Text-Documents Classification", Journal of Advances in Information Technology, Vol. 1, No. 1, 2010, pp. 4-20.

[10] R. Jindal, R. Malhotra, A. Jain, "Automated classification of security requirements", Proceedings of the International Conference on Advances in Computing, Communications and Informatics, Jaipur, India, 21-24 September 2016, pp. 2027-2033.

[11] M. A. Haque, M. Abdur Rahman, M. S. Siddik, "Non-Functional Requirements Classification with Feature Extraction and Machine Learning: An Empirical Study", Proceedings of the 1st International Conference on Advances in Science, Engineering and Robotics Technology, Dhaka, Bangladesh, 3-5 May 2019, pp. 1-5.

[12] E. D. Canedo, B. C. Mendes, "Software Requirements Classification Using Machine Learning Algorithms", Entropy, Vol. 22, No. 9, 2020 p. 1057.

[13] P. Talele, R. Phalnikar, "Classification and Prioritisation of Software Requirements using Machine Learning – A Systematic Review", Proceedings of the 11th International Conference on Cloud Computing, Data Science & Engineering, Noida, India, 28-29 January 2021, pp. 912-918.

[14] P. Talele, R. Phalnikar, "Multiple correlation based decision tree model for classification of software requirements", International Journal of Computational Science and Engineering, Vol. 26, No. 3, 2023, pp. 305-315.

[15] A. A. A. Althanoon, Y. S. Younis, "Supporting Classification of Software Requirements system Using Intelligent Technologies Algorithms", Technium, Vol. 3, No. 11, 2021, pp. 32-39.

[16] S. Taj, Q. Arain, I. Memon, A Zubedi. "To apply Data Mining for Classification of Crowd sourced Software Requirements", Proceedings of the 8th International Conference on Software and Information Engineering, New York, NY, USA, 2019, pp. 42-46.

[17] C. Baker, L. Deng, S. Chakraborty, J. Dehlinger, "Automatic Multi-class Non-Functional Software Requirements Classification Using Neural Networks", Proceedings of the IEEE 43rd Annual Computer Software and Applications Conference, Milwaukee, WI, USA, 15-19 July 2019, pp. 610-615.

[18] A. Casamayor, D. Godoy, M. Campo, "Identification of non-functional requirements in textual specifications: A semi-supervised learning approach", Information and Software Technology, Vol 52, No. 4, 2010, pp. 436-445.

[19] G. Y. Quba, H. Al Qaisi, A. Althunibat, S. AlZu'bi, "Software Requirements Classification using Machine Learning algorithm's", Proceedings of the International Conference on Information Technology, Amman, Jordan, 14-15 July 2021, pp. 685-690.

[20] S. Apte, Y. Honrao, R. Shinde, P. Talele, R. Phalnikar, "Automatic Extraction of Software Requirements Using Machine Learning", ICT with Intelligent Applications, Lecture Notes in Networks and Systems, Vol. 719, Springer, Singapore.

[21] O. Al Dhafer, I. Ahmad, S. Mahmood, "An end-to-end deep learning system for requirements classification using recurrent neural networks", Information and Software Technology, Vol. 147, 2022, p. 106877.

[22] S. Saleem, M. N. Asim, L. Van Elst, A. Dengel, "FNReq-Net: A hybrid computational framework for functional and non-functional requirements classification", Journal of King Saud University - Computer and Information Sciences, Vol. 35, No. 8, 2023.

[23] "Natural Language Requirements Dataset", http://nlreqdataset.isti.cnr.it/ (accessed: 2023)

[24] Y. Xu, C. Zhang, W. Song, "Prioritizing Customer Requirements for Science and Technology Service Platform Based on Improved TF-IDF and Sentiment Analysis", Proceedings of the IEEE International Conference on Industrial Engineering and Engineering Management, Kuala Lumpur, Malaysia, 7-10 December 2022, pp. 210-214.

[25] S. J. Putra, M. N. Gunawan, A. A. Hidayat, "Feature Engineering with Word2vec on Text Classification Using The K-Nearest Neighbor Algorithm", Proceedings of the 10th International Conference on Cyber and IT Service Management, Yogyakarta, Indonesia, 20-21 September 2022, pp. 1-6.

Improving Scientific Literature Classification: A Parameter-Efficient Transformer-Based Approach

Original Scientific Paper

Mohammad Munzir Ahanger
University of Kashmir
Faculty of Applied Sciences, Department of Computer Sciences, Srinagar, India
munzir.scholar@kashmiruniversity.net

M. Arif Wani
University of Kashmir
Faculty of Applied Sciences, Department of Computer Sciences, Srinagar, India
awani@uok.edu.in

Abstract *– Transformer-based models have been utilized in natural language processing (NLP) for a wide variety of tasks like summarization, translation, and conversational agents. These models can capture long-term dependencies within the input, so they have significantly more representational capabilities than Convolutional Neural Networks (CNN) and Recurrent Neural Networks (RNN). Nevertheless, these models require significant computational resources in terms of high memory usage, and extensive training time. In this paper, we propose a novel document categorization model, with improved parameter efficiency that encodes text using a single, lightweight, multiheaded attention encoder block. The model also uses a hybrid word and position embedding to represent input tokens. The proposed model is evaluated for the Scientific Literature Classification task (SLC) and is compared with state-of-the-art models that have previously been applied to the task. Ten datasets of varying sizes and class distributions have been employed in the experiments. The proposed model shows significant performance improvements, with a high level of efficiency in terms of parameter and computation resource requirements as compared to other transformer-based models, and outperforms previously used methods.*

Keywords*: deep learning, document categorization, text classification, scientific literature classification*

1. INTRODUCTION

An ever-increasing amount of textual information in the form of research articles, books, conference proceedings, patents, and theses is produced and published every year. PubMed, a biomedical and life science literature search engine, lists more than 30,000 journals and more than 35 million citations [1]. As far back as 2009, the number of published journal articles surpassed 50 million [2] The value and utility of scientific literature depends upon the automatic organization and categorization into different subjects, domains, and themes. Text classification has proven to be an indispensable tool for the organization, curation, and retrieval of such textual data repositories.

Deep learning algorithms such as Convolution neural network (CNN) [3-6] and Recurrent neural network (RNN) [7, 8] based models have been used for text classification. The applications of these supervised deep learning models are numerous and varied, ranging from biometrics such as face recognition [9] and fingerprint recognition [10] to medical science [11, 12] and time series forecasting [13].

Recently more complex, transformer-based models have been applied [14-19]. These models outperform the other simpler models for tasks involving text classification. However, the performance improvements are at the cost of increased model size and complexity. Such complex models are required for good results in tasks such as translation and summarization. However, these models are inefficient when used in comparatively simpler tasks such as text classification. This inefficiency and model complexity result in issues such as higher computational demands, complex fine-tuning, model space complexity, interpretability issues, latency, and data requirements. Besides they may not be suitable for small datasets, consume substantial resources, and lack transparency.

In this study, we address the efficiency and model complexity issues associated with the transformer-based models in dealing with the text classification problem. The architecture choices for the transformer-based model are reconsidered to achieve parameter efficiency for text classification. A new efficient model is proposed and evaluated on the task of Scientific Literature Classification (SLC) and is compared with previously used models.

2. RELATED WORK

Deep learning has been applied in a variety of different applications of supervised learning [20]. Different approaches have been employed in text classification tasks [3-8]. Convolutional Neural network (CNN) based models apply filters of varying sizes on the input text to extract useful features. Such models vary in input representation, the number of CNN layers, and the number and size of filters in each layer. The model Text-CNN [3] trains a CNN over text represented as a matrix comprising pre-trained word vectors. The model uses both finetuned as well as pre-trained word embeddings. The authors in [21] demonstrate the advantages of using pre-trained word embeddings in text classification tasks. Multi-group norm constraint CNN [22] uses multiple such word embeddings to improve the performance of CNN-based algorithms. The authors apply the model to text classification tasks such as sentiment analysis, irony detection, and question type detection. Self-attention mechanisms can be used to achieve improvements for such algorithms [23]. Inspired by the success of large models used in image classification tasks, a deeper CNN network that uses a character-based input text representation is employed by some authors [24, 25]. The model VDCNN [25] uses up to 30 layers to extract features from the input text. For text classification, the use of such deep models is costly and not necessary [26]. Set-CNN employs semantic extension and multi-channel convolution to improve classification performance [27].

Recurrent neural network-based models have been used in text classification tasks [7, 28]. Enhanced recurrent models such as BLSTM-2DCNN try to combine the best features of CNN and RNNs to obtain a better input representation [7, 8].

Hybrid models that combine CNN and RNN in different ways have been proposed, as those used in [29, 30, 31]. These models use a CNN layer to extract useful features followed by an RNN layer to obtain an enriched contextual representation. The authors in [29] use BiGRU (Bidirectional Gated Recurrent unit), a gated RNN while [31] uses LSTM (Long Short-Term Memory). An alternate approach is to use RNN followed by CNN. This approach has been employed by [7, 32]. The authors in [7] use two-dimensional max-pooling to the output of LSTM. The model BiLSTM-C uses two layers of LSTM followed by a layer of CNN [32]. In such models, the LSTM layer outputs token representations based on the previously seen tokens. This representation is input into the convolutional layer(s) for feature extraction. Similar models are used in [33, 34, 35]. The authors in [36] propose enhancing RNN models by modifying the activation functions used.

To address the problems associated with CNN and RNN-based methods, specifically, the lack of interpretability and intuition, Attention-based models were proposed in [37]. Attention-based models have been employed for machine translation [37], visualizing important parts of a text [38]. HAN (Hierarchical Attention Network) proposed in [38] encodes a sentence by focusing on the constituent words differentially. Another encoder is used to encode the whole document by attending to the constituent sentence representations [39]. Transformer-based models similar to the original transformer model [15] such as BERT (Bidirectional Encoder Representation for Text) [14] use a stack of attention-based encoders. Similar variations have been proposed. These include the models proposed in [16-19]. These models have been applied for tasks such as translation [40], summarization [41] as well as text categorization [42].

This paper proposes a new multi-headed attention-based model for text classification that reconsiders the architectural choices in transformer-based models when used for tasks involving text classification. The model demonstrates that significantly more parameter-efficient models can be designed and used for such tasks. This reduces memory requirements as well as training and inference times. Besides the carbon footprint associated with large pre-trained language models is also minimized [43]. The paper applies the model to the task of classifying scientific literature. The model outperforms previously applied methods.

3. PROPOSED MODEL

3.1. OVERVIEW

Transformer-based models such as BERT [14] have the drawback of having large parameter spaces (BERT-base has 108 M parameters), making them slow to train and run. For relatively simple NLP tasks such as text classification, this makes their use inefficient. The proposed model addresses this by reconsidering the architectural choices in such large and complex transformer-based models.

We employ a single efficient and lightweight encoder block with 12 attention heads. The encoder block consists of a Self-Attention subunit and a fully connected neural network (FCN) subunit. Our experiments show that this simplification of the architecture of the encoder block suffices to capture textual semantics without a significant loss in performance.

3.2. DETAILED DESCRIPTION OF THE PROPOSED MODEL

This subsection presents a detailed description of the proposed approach and explains the different steps involved using mathematical equations.

3.2.1. Embeddings Block

The proposed model (Fig. 1) uses two types of embeddings, word embedding and positional embedding. We use token embeddings of size 100 initialized using GloVe [44]. The word embedding outputs a dense word representation as a linear projection of one-hot encoded words as shown in (Eq. 1).

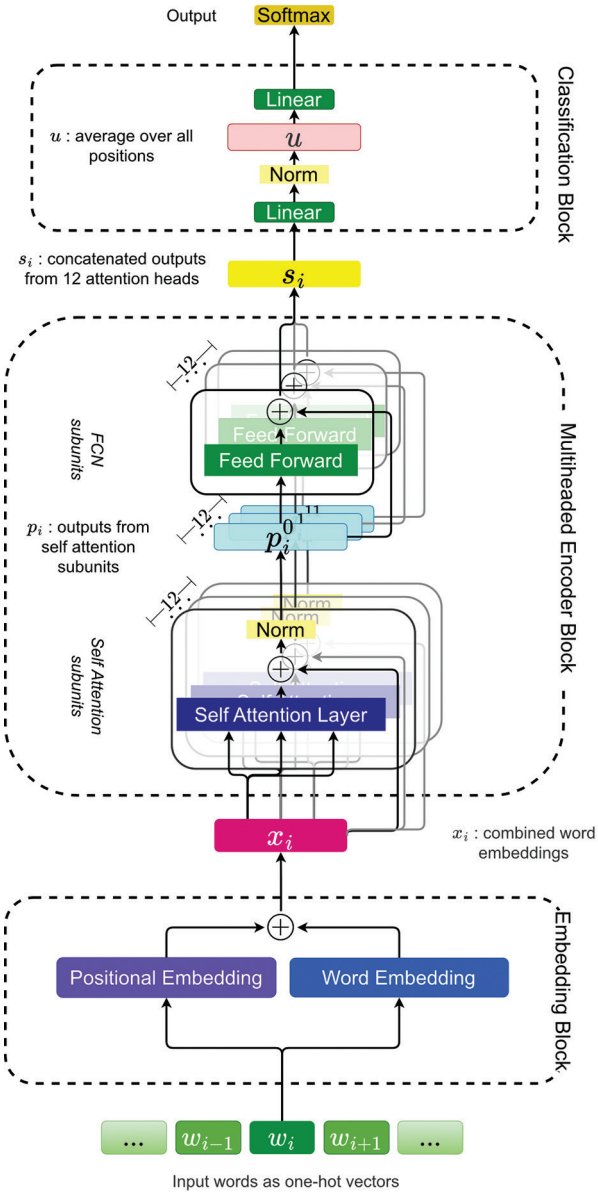

Fig.1. Proposed model architecture

$$x_i^{word} = W^{word} \times w_i^T \tag{1}$$

Here x_i^{word} is the dense word vector for the i^{th} word in the input, w_i. W^{word} is the word embedding matrix initialized using GloVe [44].

The positional embedding learns to encode the order of tokens in the input text as a linear transformation of the position within the input text as shown in (Eq. 2).

$$x_i^{pos} = W^{pos} \times w_i^T \tag{2}$$

Here x_i^{pos} is the positional embedding vector corresponding to the k^{th} word in the input, w_i. W^{pos} is the positional embedding matrix. The positional embedding matrix is initialized as used in [15].

The two embeddings are combined to obtain a better, position-aware word embedding. The combined word embeddings are obtained by calculating the sum of the corresponding word and positional embeddings as shown in (Eq. 3).

$$x_i = x_i^{word} + x_i^{pos} \tag{3}$$

Here, x_i is the combined word vector.

3.2.2. Light Weight encoder block

The proposed model approach uses a single efficient and lightweight encoder block to obtain token representations using the mechanism of self-attention. We project the word embeddings, to three different dense vector spaces using three projections – Query, Key, and Value which are linear transformations of the combined word vector (Eq. 3). This is shown in (Eq. 4), (Eq. 5), and (Eq. 6).

$$q_i = W_q \times x_i^T \tag{4}$$

$$k_i = W_k \times x_i^T \tag{5}$$

$$v_i = W_v \times x_i^T \tag{6}$$

Here, v_i is the key vector corresponding to the i^{th} word in the input text, x_i is the combined word embedding vector and W_v is the value projection matrix.

The encoder outputs an attention-based representation with the capability to attend to a specific piece of information from a potentially infinitely large context. The scaled dot product (a_{ij}) of a query vector (q_i) (representing the word being encoded) with a key vector (k_j) (representing another word) is treated as the attention score assigned to the keyword when interpreting the query word as shown in (Eq. 7).

$$a_{ij} = q_i^T k_j \tag{7}$$

$$score(q_i, k_j) = \frac{a_{ij}}{\sqrt{n}} \tag{8}$$

here, q_i is the query word (one that is being encoded) and k_j is a keyword (one of the words in the input) whose attention score against q_i is to be calculated. n is the length of the query and key vectors.

Next, *softmax* is applied over scores for all key vectors for a query vector. This scaled set of scores (α_i) is used to scale each value vector v_j. The scaled value vectors are added together to obtain z_i, the representation of the i^{th} word in the input text. This operation is shown in (Eq. 9).

$$z_i = \sum_j (\alpha_{i,j} \otimes v_j) \tag{9}$$

We use residual connections [45] across the attention mechanism in the proposed model, allowing gradients to travel through them directly. The unattended representations (x_i) are added to the representation obtained as a result of the attention mechanism (z_i) to obtain the input for the next step, layer normalization ($n_i \in R^{\text{embedding\_dim}}$). This is shown in (Eq. 10).

$$n_i = z_i + x_i \tag{10}$$

The proposed model uses layer normalization as a means of regularization to reduce training time [46]. This can be represented as shown in (Eq. 11)

$$p_i = \mathrm{LN}_{\gamma_1,\beta_1}(n_i) \quad (11)$$

The normalized word representations are input to two successive fully connected neural network layers to generate the attention head output. The output vectors obtained from multiple attention heads are concatenated together and are subjected to a linear transformation layer to output a combined multiheaded word representation. A residual connection is used that bypasses the output i.e., p_i is added to r_i to obtain a combined output s_i as shown in (Eq. 12).

$$s_i = p_i + r_i \quad (12)$$

3.2.3. Classification Block

The combined output from all the heads is passed to a single linear transformation layer, followed by a normalization layer that generates the normalized vectors t_i, as shown in (Eq. 13).

$$t_i = \mathrm{LN}_{\gamma_2,\beta_2}(W_0 \times s_i^T) \quad (13)$$

Finally, the average overall positions represent the entire text as shown in (Eq. 14).

$$\mathrm{u} = \frac{\sum_i^n t_i}{n} \quad (14)$$

The feature vector, u, is finally input into a *softmax* activated fully connected layer of neurons whose outputs are treated as class probabilities as shown in (Eq. 15) and (Eq. 16).

$$\mathrm{v} = W_{out} \times u^T \quad (15)$$

$$\mathrm{out_i} = \mathrm{softmax}(v_i) = \frac{e^{v_i}}{\sum_{j=1}^{nClasses} e^{v_j}} \quad (16)$$

4. EXPERIMENTS AND RESULTS

The proposed model was applied to ten different datasets. For comparison, seven other deep-learning-based text classification models were also tested on the task. The following subsections describe the datasets and the model evaluation method used.

4.1. DATASETS

In this study, we used ten datasets comprising abstracts of scientific papers. Three Web of Science (WOS) datasets created and used by [6] were employed. In addition to these, seven new SLC datasets were created and used. We used Python libraries like Urllib, Lxml, and Beautiful Soup to obtain data. The datasets contain labeled abstracts with their associated categories and subcategories.

The three *WOS* datasets [6] include abstracts from 46958 publications and are categorized into 134 categories and 7 domains. The three *COR* datasets are derived from the *ArXiv* metadata repository released by Cornell University. The *ArXiv* dataset was gathered from the *ArXiv* [47]. The collection is divided into seven domains and contains 146 areas. The *Nature* dataset was gathered from the scientific paper repository - *Nature* [48]. It is divided into eight domains and contains 102 areas. The *Springer* dataset comprises metadata about 116230 published papers available from *Springer* [49]. The collection is divided into 24 domains and contains 117 areas. The *Wiley* dataset was gathered from the *Wiley Online Library* [50]. There are 494 areas in the collection, which are divided into 74 categories.

Table 1 describes the features of the datasets used in the study. These datasets vary in the number of domains, training and testing samples, mean number of words and characters per sample, and vocabulary size. These characteristics can impact the performance of text classification models trained on these datasets. The larger and more diverse the dataset, the better the model's performance is likely to be. Table 2 lists the classes within each dataset.

Table 1. Summary of datasets used

Dataset	Dataset characteristics						
	Number of Domains	Number of Abstracts	Training samples	Testing samples	Words/sample (Mean)	Chars/sample (Mean)	Vocabulary Size
WOS5376	3	5736	4588	1148	209.03	1386.13	42306
WOS11967	7	11967	8017	3950	201.43	1340.19	57875
WOS46985	7	46985	31479	15506	205.27	1375.76	125968
ArXiv	7	40060	32048	8012	148.21	978.67	112452
Nature	8	49782	24891	24891	175.20	1206.56	84228
Springer	24	116230	92984	23246	167.92	1128.41	22254
Wiley	74	179953	143962	35991	170.26	1150.62	113534
COR-8883	3	8883	7106	1777	135.705	889.15	28836
COR-61033	4	61033	48826	12207	127.545	782.714	52053
COR-233962	6	233962	187169	46793	148.247	971.305	172954

Table 2. Classes in datasets

	Number	Labels
WOS5376	3	Elec. & Comm. Eng., Psychology, Biochemistry
WOS11967, WOS46985	7	Comp. Sci., Elec. & Comm. Eng., Psychology, Mech. & Aero Eng., Civil, Medical, Biochemistry
ArXiv	7	Comp Sci, Economics, EE&SS, Math, Physics, Q Biology, Q Finance
Nature	8	Bio Sci, Bus & Comm, Earth & Env Sci, Health Sci, Humanities, Phys Sci, Sci Community & Society, Soc Sci
Springer	24	Biomedicine, Bus. & Mgmt., Chemistry, Comp Sci., Earth Sci., Economics, Education, Engineering, Environment, Geography, History, Law, Life Sci., Literature, Mat. Sci., Math, Med. & Pub. Health, Pharmacy, Philosophy, Physics, Poli. Sci. & Intl. Relations, Psychology, Social Sci., Statistics
Wiley	74	Accounting, Agriculture, Allergy & Clin. Immunology, Analytical Chem., Anatomy & Physiology, ..., Religion & Theology, Social Policy & Welfare, Space & Planetary Sci., Statistics, Veterinary Medicine
COR-8883	3	Economics, Chaotic Dynamics, Algebraic Geometry
COR-61033	4	HEP - Experiment, HEP - Lattice, Nuclear Exp, Quantitative Finance
COR-233962	6	Gen. Relativity & Quantum Cosmology, Stats, Elec. Eng. & Sys. Science, Nuclear Theory, Math Physics, Quant. Biology

4.2. EXPERIMENTAL SETUP

This subsection describes the experimental setup used in this study. The experiments were performed using Python v3.9.1 [51] using Keras v2.3.1 [52] API for Tensorflow 2.0 [53]. Python libraries such as the lxml v4.6.4 [54], and beautiful soup v4.10.0 [55] were utilized to acquire some of the datasets from websites such as ArXiv, Wiley, Springer, and Nature

The datasets were cleaned by filtering out special characters. Tokenization was then done using a dictionary size of 20000. A constant length of 250 words was ensured using padding and truncation as needed. The datasets underwent a random shuffle to eliminate any ordering bias, and subsequently, a standard (80-20) rule was used to split them into training and testing subsets. In the proposed model, we utilized the Adam optimizer, with a learning rate of 0.01 and a batch size of 16. All the models were trained for 20 epochs. (Fig. 2) shows the training graphs for the proposed model on two different datasets.

4.3. RESULTS

We compare the performance of the proposed model with previously applied deep learning-based text classification methods based on classification accuracy percentages. This subsection presents the results of the experiments conducted to assess the efficacy of the proposed model and to compare its performance against other deep learning-based models that have previously been applied to the task of SLC.

Table 3 compares the accuracy of the proposed model with state of art models on seven different datasets. The performance can be depicted visually as shown in (Fig. 3). Model training times are listed in Table 4.

Table 3. Comparison with previously used models on classification accuracy (%) metrics

	Models							
Datasets	**TextCNN [3]**	**MGNCNN [22]**	**CharCNN [24]**	**RCNN [28]**	**VDCNN [25]**	**HDLTEX- CNN [6]**	**HDLTEX – RNN [6]**	**Proposed Model**
Parameters (M)	25.6	33.7	11.5	16.9	14.35	34.9	11.32	11.9
WOS-5736	49.46	97.41	88.48	97.07	82.9	96.47	97.82	99.13
WOS-11967	16.55	92.94	25.45	92.94	67.64	93.52	93.98	96.17
WOS-40896	31.13	89.33	76.59	88.2	75.76	88.67	90.45	95.71
ArXiv	26.26	85.35	80.53	83.32	66.11	85.84	84.26	87.11
Springer	27.7	100	61.6	85.0	63.0	99.98	100	100
Nature	33.79	57.23	51.23	52.21	53.44	60.12	61.83	61.56
Wiley	8.15	52.04	7.82	62.10	49.50	50.81	43.39	72.24
COR-8883	88.74	91.64	97.97	91.87	67.24	93.35	92.90	94.25
COR-61033	90.06	90.66	93.38	92.38	28.16	94.67	92.46	93.41
COR-233962	87.23	91.93	90.725	92.31	56.44	90.2	91.55	93.37

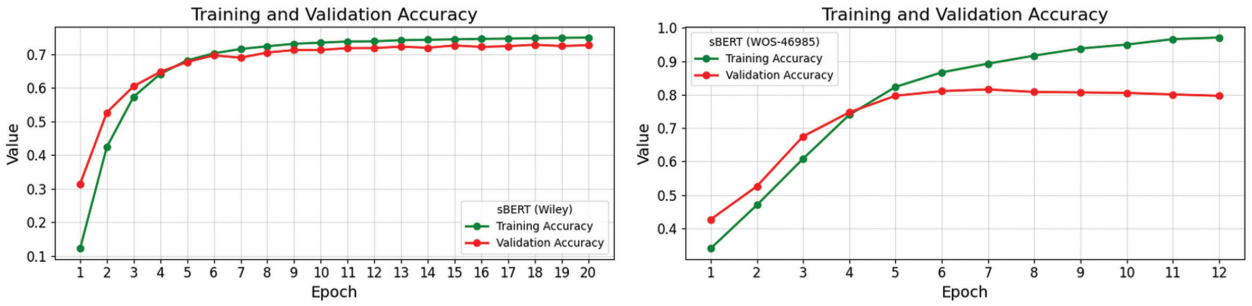

Fig. 2. Training graphs of the proposed model on two datasets WOS- 46985 and Wiley

Table 4. Comparison with training times with previously used models (in seconds)

	TextCNN	MGNCNN	CharCNN	RCNN	VDCNN	HDLTEX-CNN	HDLTEX – RNN	sBERT
WOS5736	73.15214	3631.116	158.1202	501.49	269.139	140.4653	166.1034	157.2688
WOS11967	106.2313	5498.224	221.2821	716.46	405.123	206.5897	708.5794	286.5306
WOS46985	333.4941	10805.61	771.9043	2644.6	1267.18	482.8745	2948.638	604.8373
arXiv	341.4121	15226.54	450.2403	771.23	687.927	330.3308	831.7495	500.1951
Nature	243.1619	10844.71	386.2782	532.34	407.972	271.8696	639.7405	361.6975
Springer	776.393	34626.14	880.3642	2096.1	788.691	549.7363	2251.08	721.5509
Wiley	1222.111	54504.59	1077.362	3002.8	8974.24	1845.265	3309.169	1333.135
COR-8883	94.99683	4236.737	186.051	457.67	555.342	127.8164	696.8934	179.0956
COR-61033	464.6511	20722.85	670.7038	1324.9	1891.57	434.1656	906.9122	527.6036
COR-233962	1509.796	67334.97	1773.456	4780.1	8909.46	1510.261	2864.248	1493.209

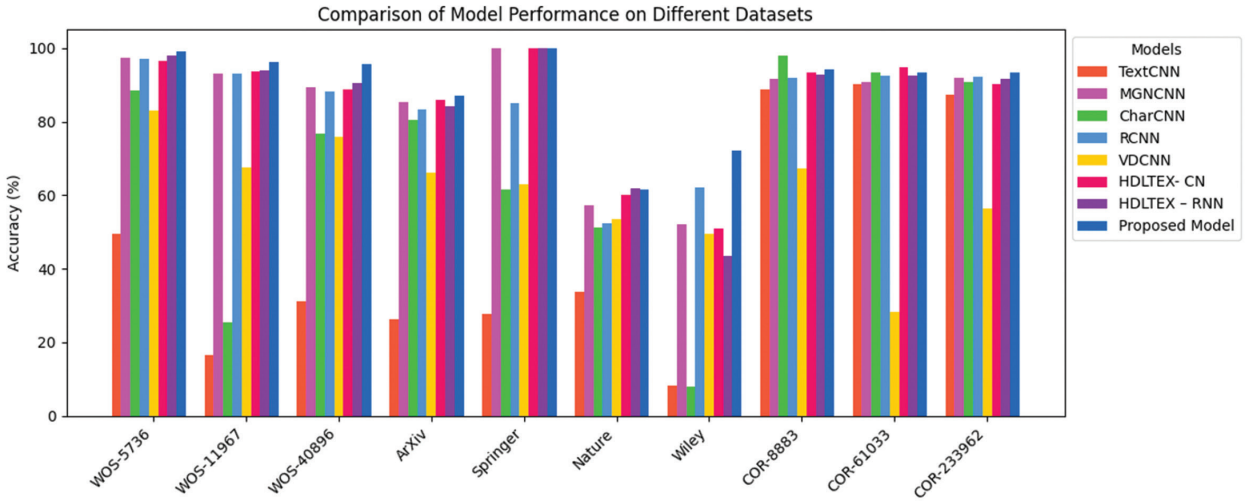

Fig. 3. Classification accuracy performance of different models

5. DISCUSSION

This section provides an analysis and discussion of the experimental results, comparing and contrasting the performance of the various models under consideration From the experimental results, it follows that models such as TextCNN capture local n-gram features and ignore long-range dependencies within the input, resulting in poor performance on the task. Models such as HDLTex CNN use a deeper network architecture with a wider range of filter sizes. Although this improves the results, the models still do not capture long-range dependencies within the text.

Models like VDCNN and CharCNN detect character n-grams rather than words and phrases within the text. The models need to be deeper, which increases the time required to train and infer. Models such as RCNN treat text as a sequence of tokens and attempt to capture long-range dependencies within the text by finding contextual representations. This is limited by the problem of vanishing gradients. HDLTex RNN uses LSTM to maintain an internal cell state and a system of gates to maintain information over an extended number of timesteps. These models are slow to train and infer because of their sequential nature.

Transformer-based models make it possible to attend to a potentially infinitely long context while encoding a given position within a text. These models, however, suffer from a large parameter space, leading to inefficiency in tasks like text classification.

The proposed model employs a single, parameter-efficient encoder block. The parameter efficiency achieved facilitates faster training and utilization. Moreover, the model significantly reduces resource requirements, making it feasible to train and deploy in low-resource environments. The proposed model outperforms previously used methods on the task.

6. CONCLUSION

Text classification, particularly in scientific literature, holds significant importance. While Transformer-based models have revolutionized NLP, applying them to text classification results in parameter-inefficient models with considerable space and time complexities. The proposed model addresses these issues by re-evaluating the architectural choices of Transformer-based models while prioritizing parameter efficiency. As a result, the model surpasses the performance of previously employed deep learning-based methods in the task of SLC, with only a fraction of the parameter space required by Transformer-based models like BERT. However, it is essential to recognize that our approach's applicability extends beyond scientific literature classification. To gauge its full potential and limitations, future research should involve its evaluation in other related tasks such as sentiment analysis, toxicity detection, and similar domains. Assessing the model's performance in diverse contexts will provide a comprehensive understanding of its capabilities and guide further refinements.

7. REFERENCES

[1] PubMed, "List of All Journals Cited in PubMed", nlm.nih.gov/bsd/serfile_addedinfo.html (accessed: 2022)

[2] M. Ware, M. Mabe, "The STM Report: An overview of scientific and scholarly journal publishing", International Association of Scientific, Technical and Medical Publishers, 2015.

[3] Y. Kim, "Convolutional neural networks for sentence classification", Proceedings of the Conference on Empirical Methods in Natural Language Processing, Doha, Qatar, October 2014, pp. 1746-1751.

[4] S. V. Georgakopoulos, S. K. Tasoulis, A. G. Vrahatis, V. P. Plagianakos, "Convolutional Neural Networks for Toxic Comment Classification", Proceedings of the 10th Hellenic Conference on Artificial Intelligence, New York, NY, USA, July 2018, pp. 1-6.

[5] M. Hughes, I. Li, S. Kotoulas, T. Suzumura, "Medical Text Classification Using Convolutional Neural Networks", Studies in Health Technology and Informatics, Vol. 235, 2017, pp. 246-250.

[6] K. Kowsari, D. E. Brown, M. Heidarysafa, K. Jafari Meimandi, M. S. Gerber, L. E. Barnes, "HDLTex: Hierarchical Deep Learning for Text Classification", Proceedings of the 16th IEEE International Conference on Machine Learning and Applications, Cancun, Mexico, 18-21 December 2017, pp. 364-371.

[7] P. Zhou, Z. Qi, S. Zheng, J. Xu, H. Bao, B. Xu, "Text classification improved by integrating bidirectional LSTM with two-dimensional max pooling", Proceedings of the 26th International Conference on Computational Linguistics: Technical Papers, Osaka, Japan, 11-17 December 2016, pp. 3485-3495.

[8] B. McCann, J. Bradbury, C. Xiong, R. Socher, "Learned in translation: Contextualized word vectors", Proceedings of the 31st International Conference on Neural Information Processing Systems, Red Hook, NY, USA, December 2017, pp. 6297-6308.

[9] M. A. Wani, F. A. Bhat, S. Afzal, A. I. Khan, "Supervised Deep Learning in Face Recognition", Studies in Big Data, Vol. 57, 2020, pp. 95-110.

[10] M. A. Wani, F. A. Bhat, S. Afzal, A. I. Khan, "Supervised Deep Learning in Fingerprint Recognition", Studies in Big Data, Vol. 57, 2020, pp. 111-132.

[11] M. L. Tlachac, R. Flores, E. Toto, E. Rundensteiner, "Early Mental Health Uncovering with Short Scripted and Unscripted Voice Recordings", Deep Learning Applications, Vol. 4, 2023, pp. 79-110.

[12] X. W. Gao et al. "Identification of Human Papillomavirus from Super-Resolution Microscopic Images Generated Using Deep Learning Architectures", Deep Learning Applications, Volume 4, Advances in Intelligent Systems and Computing, Springer Nature, 2023, pp. 1-20.

[13] K. Agarwal, L. Dheekollu, G. Dhama, A. Arora, S. Asthana, T. Bhowmik, "Deep Learning-Based Time Series Forecasting", Proceedings of the 19th IEEE International Conference on Machine Learning and Applications, December 2020, pp. 859-864.

[14] J. Devlin, M. W. Chang, K. Lee, K. Toutanova, "BERT: Pre-training of deep bidirectional transformers for language understanding", Proceedings of the Conference of the North American Chapter of the Association for Computational Linguistics: Human Language Technologies, Minneapolis, MN, USA, June 2019, pp. 4171-4186.

[15] A. Vaswani et al. "Attention Is All You Need", Proceedings of the 31st Conference on Neural Information Processing Systems, Long Beach, CA, USA, June 2017.

[16] Z. Yang, Z. Dai, Y. Yang, J. Carbonell, R. Salakhutdinov, Q. V. Le, "XLNet: Generalized autoregressive pretraining for language understanding", Proceedings of the 33rd International Conference on Neural Information Processing Systems, Red Hook, NY, USA, 2019, pp. 5753-5763.

[17] Y. Liu et al. "RoBERTa: A robustly optimized BERT pretraining approach", arXiv:1907.11692, 2019.

[18] Z. Lan, M. Chen, S. Goodman, K. Gimpel, P. Sharma, R. Soricut, "ALBERT: A Lite BERT for Self-supervised Learning of Language Representations", Proceedings of the 8th International Conference on Learning Representations, Addis Ababa, Ethiopia, 26-30 April 2020.

[19] V. Sanh, L. Debut, J. Chaumond, T. Wolf, "DistilBERT, a distilled version of BERT: smaller, faster, cheaper and lighter", arXiv:1910.01108, 2020.

[20] M. A. Wani, F. A. Bhat, S. Afzal, A. I. Khan, "Advances in Deep Learning, Vol. 57", Studies in Big Data, Vol. 57, 2019.

[21] A. Mandelbaum, A. Shalev, "Word Embeddings and Their Use in Sentence Classification Tasks", arXiv:1610.08229, 2016.

[22] Y. Zhang, S. Roller, B. C. Wallace, "MGNC-CNN: A Simple Approach to Exploiting Multiple Word Embeddings for Sentence Classification", Proceedings of the Conference of the North American Chapter of the Association for Computational Linguistics: Human Language Technologies, San Diego, CA, USA, June 2016, pp. 1522-1527.

[23] H. L. Xin Wu, Yi Cai, QingLi, Jingyun Xu, "Combining Contextual Information by Self-attention Mechanism in Convolutional Neural Networks for Text Classification", Web Information Systems Engineering - WISE 2013 Workshops, Vol. 8182, 2014, pp. 453-467.

[24] X. Zhang, J. Zhao, Y. LeCun, "Character-level Convolutional Networks for Text Classification", Advances in Neural Information Processing Systems, 2015, pp. 649-657.

[25] A. Conneau, H. Schwenk, Y. le Cun, L. Barrault, "Very deep convolutional networks for text classification", Proceedings of the 15th Conference of the European Chapter of the Association for Computational Linguistics: Volume 1, April 2017, pp. 1107-1116.

[26] R. Johnson, T. Zhang, "Convolutional Neural Networks for Text Categorization: Shallow Word-level vs. Deep Character-level", arXiv:1609.00718, 2016.

[27] Y. Zhou, J. Li, J. Chi, W. Tang, Y. Zheng, "Set-CNN: A text convolutional neural network based on semantic extension for short text classification", Knowledge-Based Systems, Vol. 257, 2022, p. 109948.

[28] S. Lai, L. Xu, K. Liu, J. Zhao, "Recurrent convolutional neural networks for text classification", Proceedings of the National Conference on Artificial Intelligence, January 2015, pp. 2267-2273.

[29] S. Gonçalves, P. Cortez, S. Moro, "A Deep Learning Approach for Sentence Classification of Scientific Abstracts", Lecture Notes in Computer Science, 2018, pp. 479-488.

[30] D. Jin, P. Szolovits, "Hierarchical Neural Networks for Sequential Sentence Classification in Medical Scientific Abstracts", Proceedings of the Conference on Empirical Methods in Natural Language Processing, August 2018, pp. 3100-3109.

[31] A. Hassan, A. Mahmood, "Convolutional Recurrent Deep Learning Model for Sentence Classification", IEEE Access, Vol. 6, 2018, pp. 13949-13957.

[32] Y. Senarath, U. Thayasivam, "DataSEARCH at IEST 2018: Multiple Word Embedding based Models for Implicit Emotion Classification of Tweets with Deep Learning", Proceedings of the 9th Workshop on Computational Approaches to Subjectivity, Sentiment and Social Media Analysis, Brussels, Belgium, October 2018, pp. 211-216.

[33] Y. Li, X. Wang, P. Xu, "Chinese Text Classification Model Based on Deep Learning", Future Internet, Vol. 10, No. 11, Nov. 2018, p. 113.

[34] T. Kim, J. Yang, "Abstractive text classification using sequence-to-convolution neural networks", arXiv:1805.07745, 2018.

[35] T. Liu, S. Yu, B. Xu, H. Yin, "Recurrent networks with attention and convolutional networks for sentence representation and classification", Applied Intelligence, Vol. 48, No. 10, 2018, pp. 3797-3806.

[36] W. Chen, J. Jin, D. Gerontitis, L. Qiu, J. Zhu, "Improved Recurrent Neural Networks for Text Classification and Dynamic Sylvester Equation Solving", Neural Processing Letters, Vol. 55, 2023, pp. 8755-8784.

[37] D. Bahdanau, K. H. Cho, Y. Bengio, "Neural machine translation by jointly learning to align and translate", Proceedings of the 3rd International Conference on Learning Representations, ICLR 2015, San Diego, CA, USA, May 2015, pp. 1-15.

[38] Z. Yang, D. Yang, C. Dyer, X. He, A. Smola, E. Hovy, "Hierarchical Attention Networks", Proceedings of NAACL-HLT, June 2016, pp. 1480-1489.

[39] X. Zhou, X. Wan, J. Xiao, "Attention-based LSTM network for cross-lingual sentiment classification", Proceedings of the Conference on Empirical Methods in Natural Language Processing, Austin, TX, USA, 2016, pp. 247-256.

[40] X. Wu, Y. Xia, J. Zhu, L. Wu, S. Xie, T. Qin, "A study of BERT for context-aware neural machine translation", Machine Learning, Vol. 111, No. 3, 2022, pp. 917-935.

[41] S. Abdel-Salam, A. Rafea, "Performance Study on Extractive Text Summarization Using BERT Models", Information, Vol. 13, No. 2, No. 2, 2022.

[42] M. Khadhraoui, H. Bellaaj, M. Ben Ammar, H. Hamam, M. Jmaiel, "Survey of BERT-Base Models for Scientific Text Classification: COVID-19 Case Study", Applied Sciences, Vol. 12, No. 6, 2022.

[43] J. Dodge et al. "Measuring the Carbon Intensity of AI in Cloud Instances", Proceedings of the ACM International Conference Proceeding Series, Vol. 22, June 2022, pp. 1877-1894.

[44] J. Pennington, R. Socher, C. D. Manning, "GloVe: Global vectors for word representation", Proceedings of the Conference on Empirical Methods in Natural Language Processing, Doha, Qatar, October 2014, pp. 1532-1543.

[45] K. He, X. Zhang, S. Ren, J. Sun, "Deep Residual Learning for Image Recognition", Proceedings of the IEEE conference on computer vision and pattern recognition, Las Vegas, NV, USA, 27-30 June 2016, pp. 770-778.

[46] L. J. Ba, J. R. Kiros, G. E. Hinton, "Layer Normalization", arXiv:1607.06450, 2016.

[47] Arxiv, arxiv.org (accessed: 2020)

[48] Nature, Latest research and news by subject, www.nature.com/subjects (accessed: 2020)

[49] Springer, link.springer.com (accessed: 2020)

[50] Wiley, onlinelibrary.wiley.com (accessed: 2020)

[51] Python 3 Reference Manual, docs.python.org/3.9 (accessed: 2020)

[52] Keras, keras.io/api (accessed: 2020)

[53] Tensorflow, "A system for large-scale machine learning", www.tensorflow.org/api_docs (accessed: 2020)

[54] S. Behnel, M. Faassen, I. Bicking, "lxml: XML and HTML with Python", lxml.de (accessed: 2020)

[55] Beautifulsoup, "python library for HTML and XML", crummy.com/software/BeautifulSoup (accessed: 2020)

The New ADE-TLM Algorithm for Modeling Debye Medium

Original Scientific Paper

El hadi El ouardy
Ibn Tofail University,
Faculty of Sciences, Department of physics,
Laboratory of Electronic Systems Information Processing Mechanics and Energetics
University Campus,Pbox 133, Kenitra, Morocco
abdelhadi.elouardy@gmail.com

Hanan El Faylali
Ibn Tofail University,
Faculty of Sciences, Department of physics,
Laboratory of Electronic Systems Information Processing Mechanics and Energetics
University Campus,Pbox 133, Kenitra, Morocco
wh_elfaylali@yahoo.fr

Abstract *– In this paper, we present a novel approach to simulating the interaction between electromagnetic waves and a Debye medium utilizing a Transmission Line Matrix (TLM) algorithm with the symmetrical condensed node (SCN-TLM) technique. The proposed method utilizes the polarization current within the media and incorporates the auxiliary differential equation (ADE) technique to handle scattering following the conventional discretization process. The averaged approximation is employed to utilize the polarization current density J and the electric voltage. By reducing the number of operations required per iteration, the New ADE-TLM method has successfully decreased the computational time compared to time convolution techniques. Despite this reduction in computational time, the New ADE-TLM method maintains a numerical accuracy that is comparable to that of time convolution techniques. The efficiency and precision of this approach are confirmed by the agreement between the results obtained and those predicted by the analytic model.*

Keywords*: Auxiliary Differential Equation (ADE), Symmetrical Condensed Node (SCN), Transmission line matrix (TLM) approach, Debye medium*

1. INTRODUCTION

The Transmission Line Matrix (TLM) approach was designed as a simple analogy between the principles of electromagnetic wave propagation and those of electrical currents and voltages in a network of continuous transmission lines. This network, representing the discretization of the physical environment to be studied, is formed by interconnected transmission lines, which constitute the basic elements called nodes.

The TLM approach is immediately derived from Maxwell's equations using the centered derivative approximation [1], shares similarities with the finite difference model. This suggests that the TLM approach offers a similar level of accuracy and efficiency in representing and solving electromagnetic problems, making it a viable choice for modeling such systems.

For example, it has been shown that the equations of the extended TLM node model can be transformed into the finite difference equations used by Brodwin and Taflove [2, 3].

The TLM technique can be considered either as a mathematical representation obtained from Maxwell's equations using the finite difference approach or a physical representation based on the Huygens principle for modeling transmission line networks.

In recent years, several approaches based on the FDTD model [4, 5] have been presented to analyze problems related to the propagation of electromagnetic wave fields in linear media [6, 7] and to predict the gain, absorption, and scattering in a nonlinear medium [8].

The technique, which depends on the auxiliary differential equation (ADE-FDTD), has been effectively used in modeling nonlinear media [9, 10].

The TLM approach effectively simulated the performance of electromagnetic waves in nonlinear and

linear media [11, 12], allowing the resolution of three-dimensional problems as well as the treatment of inhomogeneous, anisotropic and dispersive waves [13].

In recent years, we report a many TLM-based approaches for the analysis of a dispersive medium. We find that : the use of equations characterizing the conductive medium in terms of equivalent node sources [14], the use of Constant Recursive Convolution (CRC) [15], which was later improved to the Current Density Recursive Convolution (CDRC-TLM) technique [16], and the Piecewise Linear Current Density Recursive Convolution (PLCDRC-TLM) technique [17] ,which are applied to magnetized plasma, the application of the Z-transform approach [18] to characterize the electric properties of the dispersive media, and the other technique includes the JE-TLM with voltage sources [19] which is applied to model isotropic plasma.

The auxiliary differential equation (ADE-TLM) approach is employed to simulate the chiral media [20], this is achieved by utilizing the ADE approximation, and employed to model Cole-Cole media [21].

In this paper, we propose the new ADE-TLM algorithm in terms of polarization current density and the constitutive relations between the voltage V and the polarization current density J, which are presented in [22], to simulate the propagation of EM wave in the Debye medium. Therefore, we will discuss the formulation of this technique in detail.

The New ADE-TLM algorithm is based on the SCN-TLM by using 12 principal ports to model the free space and modeling the properties of the Debye medium by using 3 additional ports as voltage sources.

In contrast, the derivation of our new ADE-TLM algorithm, which utilizes the centered derivative approximation, is simpler in comparison to the derivation of the ADE-TLM algorithm discussed in [23].

When comparing the ADE schemes to the RC and PLRC schemes [16, 17], it is found that the ADE schemes require a smaller number of variables to be stored and involve fewer arithmetic operations. As a result, the ADE schemes significantly reduce the computational complexity involved in the calculations, making them a more efficient option. Also, the derivation of our proposed method is simpler compared to the derivation of the JE-TLM method [19]. However, it typically leads to enhanced accuracy.

This new ADE-TLM method is examined and validated by calculations of the reflection coefficient of a Gaussian pulse incident at the air-water interface. An excellent agreement has been found between the new proposed ADE-TLM calculation and the analytical solutions for the reflection coefficient.

The present paper is organized in the following sections: In Section 2, we present the theoretical formulations and equations related to the Debye model. In Section 3, we introduce the derivation of the New ADE-TLM algorithm, which is used for calculating sources. The efficiency and validity of this algorithm are demonstrated in the frequency domain, and the results are detailed in Section 4. In conclusion, section 5 presents our final remarks.

2. FORMULATIONS AND EQUATIONS

In the Debye medium, the polarization current density is described by Maxwell equations as follows:

$$\nabla \times H = \varepsilon_0 \varepsilon_\infty \frac{\partial E}{\partial t} + J \tag{1}$$

$$\nabla \times E = -\mu_0 \frac{\partial H}{\partial t} \tag{2}$$

Where H represents the magnetic field strength, E defines the electric field strength, ε_0 is the permittivity of vacuum, ε_∞ is the relative permittivity at infinite frequency, μ_0 is the magnetic permeability of vacuum, and $J = \sum_{p=1}^{p} J_p$ defines the polarization current density with multiple poles, where J represents the polarization current density and p is the number of poles.

In the frequency domain, we express the relative permittivity of the Debye media as [24]:

$$\varepsilon(\omega) = \varepsilon_\infty + (\varepsilon_s - \varepsilon_\infty) \sum_{p=1}^{p} \frac{G_p}{1 + j\omega\tau_p} \tag{3}$$

τ_p is the relaxation time for the p_{th} pole, the amplitude for each pole is: $\Delta\varepsilon_p = \varepsilon_s - \varepsilon_\infty$. Where ε_s is the static permittivity. With [24]: $\sum_{p-1}^{p} G_p = 1$.

In the frequency domain, the polarization current density caused by one pole is given as [25, 26]:

$$\tilde{J}_p = (\varepsilon_s - \varepsilon_\infty) \times G_p \times \varepsilon_0 \left(\frac{j\omega}{1 + j\omega\tau_p} \right) \times \tilde{E} \tag{4}$$

An efficient means to obtain $\tilde{J}_p$ from Eq. (4) is to first multiply both sides of this equation by $(1+j\omega\tau_p)$. This gives:

$$\tilde{J}_p + jw\tau_p \tilde{J}_p = (\varepsilon_s - \varepsilon_\infty) \times \varepsilon_0 \times G_p jw\tilde{E} \tag{5}$$

We obtain by applying the inverse Fourier transform to each term in equation (5):

$$J_p + \tau_p \frac{\partial J_p}{\partial t} = (\varepsilon_s - \varepsilon_\infty) \times \varepsilon_0 \times G_p \frac{\partial E}{\partial t} \tag{6}$$

3. ADE-TLM ALGORITHM

We obtain by using the finite difference time in Eq. (6) at time step n+1:

$$\left(\frac{J_p^{n+1} + J_p^n}{2} \right) + \tau_p \left(\frac{J_p^{n+1} - J_p^n}{\Delta t} \right) = (\varepsilon_s - \varepsilon_\infty) \times \varepsilon_0 \times G_p \left(\frac{E^{n+1} - E^n}{\Delta t} \right) \tag{7}$$

The updated equation is:

$$J_p^{n+1} = a_d J_p^n + b_d \left(\frac{E^{n+1} - E^n}{\Delta t} \right) \tag{8}$$

With the coefficients:

$$\begin{aligned} a_d &= \frac{2\tau_p - \Delta t}{2\tau_p + \Delta t} \\ b_d &= \frac{2(\varepsilon_s - \varepsilon_\infty) \times \varepsilon_0 \times G_p \times \Delta t}{2\tau_p + \Delta t} \end{aligned} \tag{9}$$

The time discretization centered at step $n + 1/2$ of Eq. (1) gives:

$$E^{n+1} = E^n + \frac{\Delta t}{\varepsilon_0 \varepsilon_\infty} \left(\nabla \wedge H^{n+\frac{1}{2}} - J^{n+\frac{1}{2}} \right) \tag{10}$$

From Eq. (8), we obtain the polarization current centered at step $n + 1/2$ by:

$$J_p^{n+\frac{1}{2}} = \frac{1}{2} \left(J^{n+1} + J^n \right) \tag{11}$$

We convert the electric field to a voltage utilizing the following equation:

$$E^n = \frac{V^n}{\Delta l} \tag{12}$$

Where Δl represents the space step as well as V defines the electric voltage.

By substituting Eq. (12) in Eq. (8) and Eq. (10) respectively, we find:

$$J_p^{n+1} = a_d J_p^n + b_d \left(\frac{V^{n+1} - V^n}{\Delta t \Delta l} \right) \tag{13}$$

$$V^{n+1} = V^n + \frac{\Delta t \Delta l}{\varepsilon_0 \varepsilon_\infty} \left(\nabla \wedge H^{n+\frac{1}{2}} - J^{n+\frac{1}{2}} \right) \tag{14}$$

We first update Eq. (13) to improve the efficiency of ADE-TLM, and we find by utilizing the average approximation defined in [27]:

$$V^n = \frac{V^{n+1} + V^{n-1}}{2} \tag{15}$$

We obtain by substituting Eq. (15) into Eq. (13):

$$J_p^{n+1} = a_d J_p^n + b_d \left(\frac{V^n - V^{n-1}}{\Delta t \Delta l} \right) \tag{16}$$

We find by utilizing the SCN-TLM method [28] to Eq. (2):

$$\begin{pmatrix} \nabla \wedge H_x^{n+\frac{1}{2}} \\ \nabla \wedge H_y^{n+\frac{1}{2}} \\ \nabla \wedge H_z^{n+\frac{1}{2}} \end{pmatrix} = \tag{17}$$

$$\begin{pmatrix} \frac{\varepsilon_0}{2\Delta t \Delta l} \left[\left(V_1^i + V_2^i + V_9^i + V_{12}^i \right)^{n+1} - (V_1^r + V_2^r + V_9^r + V_{12}^r)^n \right] \\ \frac{\varepsilon_0}{2\Delta t \Delta l} \left[\left(V_3^i + V_4^i + V_8^i + V_{11}^i \right)^{n+1} - (V_3^r + V_4^r + V_8^r + V_{11}^r)^n \right] \\ \frac{\varepsilon_0}{2\Delta t \Delta l} \left[\left(V_5^i + V_6^i + V_7^i + V_{10}^i \right)^{n+1} - (V_5^r + V_6^r + V_7^r + V_{10}^r)^n \right] \end{pmatrix}$$

Applying the charge conservation's laws:

$$\begin{pmatrix} V_1^r + V_2^r + V_9^r + V_{12}^r \\ V_3^r + V_4^r + V_8^r + V_{11}^r \\ V_5^r + V_6^r + V_7^r + V_{10}^r \end{pmatrix}^n = \begin{pmatrix} V_1^i + V_2^i + V_9^i + V_{12}^i \\ V_3^i + V_4^i + V_8^i + V_{11}^i \\ V_5^i + V_6^i + V_7^i + V_{10}^i \end{pmatrix}^n + \begin{pmatrix} V_{sx} \\ V_{sy} \\ V_{sz} \end{pmatrix}^n \tag{18}$$

Replacing Eq. (17) in Eq. (14), utilizing Eq. (18), and employing the Symmetrical Condensed Node (SCN), the total voltage is written as follows:

$$\begin{pmatrix} V_x^{n+1} \\ V_y^{n+1} \\ V_z^{n+1} \end{pmatrix} = \begin{pmatrix} \frac{2}{4+Y_{ox}} \\ \frac{2}{4+Y_{oy}} \\ \frac{2}{4+Y_{oz}} \end{pmatrix} \begin{pmatrix} \left[V_1^i + V_2^i + V_9^i + V_{12}^i + \frac{1}{2} V_{sx} \right]^{n+1} \\ \left[V_3^i + V_4^i + V_8^i + V_{11}^i + \frac{1}{2} V_{sy} \right]^{n+1} \\ \left[V_5^i + V_6^i + V_7^i + V_{10}^i + \frac{1}{2} V_{sz} \right]^{n+1} \end{pmatrix} \tag{19}$$

Y_{ox}, Y_{oy}, and Y_{oz} indicate the normalized admittances.

The normalized admittances Y_{ox}, Y_{oy}, and Y_{oz} can be written after comparing between Eq. (14) and Eq. (19) as follows:

$$Y_{ou} = 4 \left(\varepsilon_\infty - 1 \right) \tag{20}$$

And the voltage sources V_{ox}, V_{oy}, and V_{oz} are :

$$V_{su}^{n+1} = -V_{su} - 4 \left[\frac{\Delta t \Delta l}{2\varepsilon_0} \sum_{p=1}^{p} \left(J_{pu}^{n+1} + J_{pu}^n \right) \right] \tag{21}$$

With: $u \in \{x, y, z\}$.

The ADE-TLM algorithm procedure in the Debye medium is as follows:

1. We start by conserving values from V^n, V^{n-1} and J_p^n , and J_p^{n-1}.
2. We update J_p^{n-1} made by Eq. (16), and we introduce the obtained values of J_p^{n-1} in the voltage Sources employing Eq. (21).
3. According to Eqs. (20) and (21), we update the V^{n+1} characterized in Eq. (19) using normalized admittance and voltage sources.
4. The reflected pulses are simulated by using the conserved values of V^{n+1}, employing the scattering matrix.
5. At the end, the connection matrix is used to simulate the propagation to neighboring nodes.

The flow chart of the New ADE-TLM algorithm for Debye dispersive media is proposed in Fig. 1.

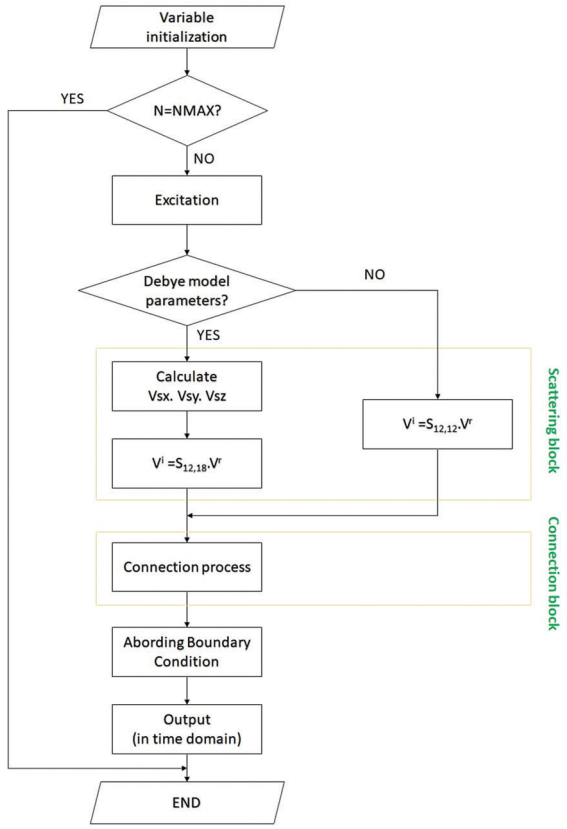

Fig. 1. Flowchart of New ADE-TLM process for Debye Dispersive Media

4. RESULTS AND DISCUSSION

To evaluate the efficiency and validity of the newly presented ADE-TLM algorithm, which includes voltage sources for the Debye medium. A simulation is performed to study the interaction between an electromagnetic wave and a Debye slab. We simulate the reflection coefficient of an interface between air and water (Debye medium) employing a one-dimensional, the results obtained are compared to the analytical solutions to validate and make comparisons.

A Gaussian plane wave is incident from air to a Debye media. First the TLM network is partitioned in (1,1,1000)Δl with the space step: Δl=37.5μm and the time step: Δt=0.0625 ps.

We partitioned the one-dimensional computational space into 1000 cells, with 500 cells represented to simulating air and the remaining 500 cells representing water.Similar to [29], the following parameters describe the simulated Debye media in the structure:

$$\varepsilon_s = 81,\ \varepsilon_\infty = 1.8 \text{ and } \tau_0 = 9.4\times10^{-12}\,s\,.$$

The wave source was defined in the form of :

$$E(t)_s = 1000e^{-\frac{(t-t_0)^2}{T^2}} \text{ with } T = 152\Delta t$$

and t_0=400Δt . The simulations are programmed to run 5000 iterations.

After being reflected from the air-water interface (cell 499), the Gaussian pulse propagates across it.

Figs. 2-6 show the total electric field along the x-axis after different time steps: 750, 1300, 1500, 1800, and 3000. These figures clearly indicate the presence of dispersion and attenuation effects.

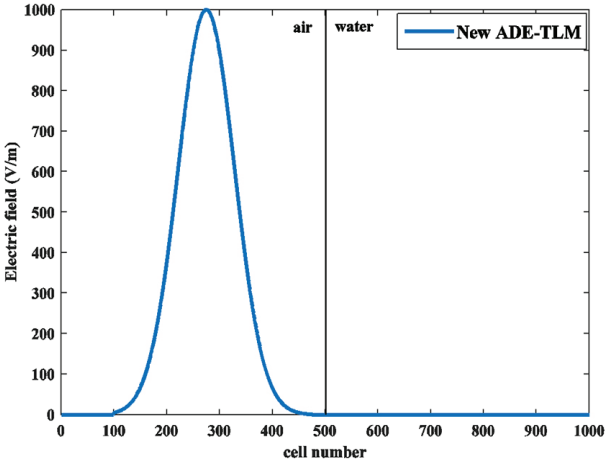

Fig. 2. The incidence Gaussian signal after 750 time steps

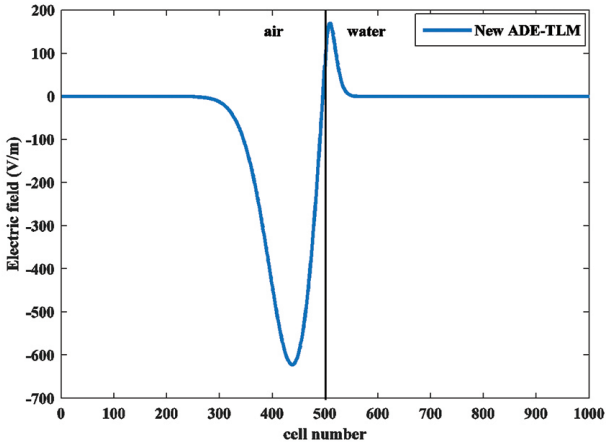

Fig. 3. The total electric field versus position after 1300 time steps

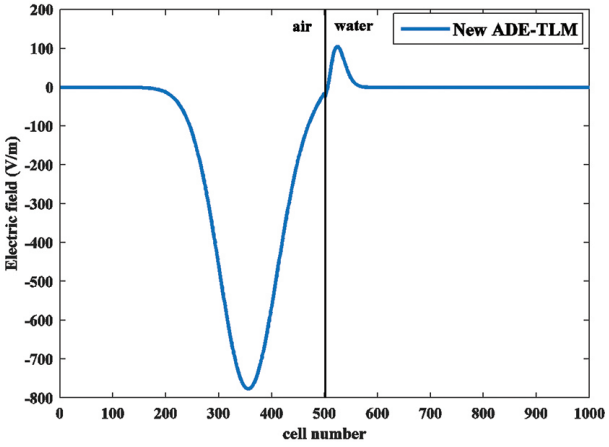

Fig. 4. The total electric field versus position after 1500 time steps

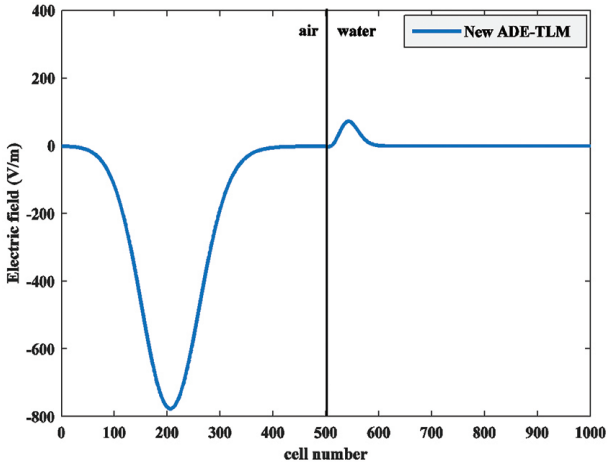

Fig. 5. The total electric field versus position after 1800 time steps

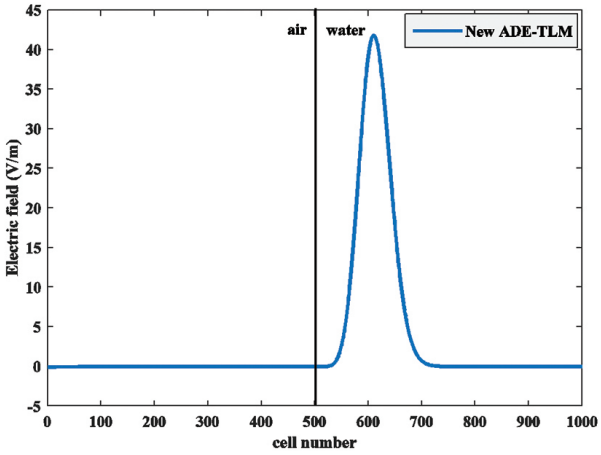

Fig. 6. The total electric field versus position after 3000 time steps

For the ADE-TLM approach, we simulate the air-water interface reflection coefficient, which is calculated by subtracting the Fourier transform of the incident field from the Fourier transform of the reflected field.

We calculate the analytical solution for the reflection coefficient, utilizing the next formulation [30]:

$$\left|\Gamma(\omega)\right| = \left|\frac{\sqrt{\varepsilon_0} - \sqrt{\varepsilon^*(\omega)}}{\sqrt{\varepsilon_0} + \sqrt{\varepsilon^*(\omega)}}\right| \tag{22}$$

Where $\varepsilon^*(\omega)$ is the complex permittivity.

Fig. 7. shows the results of the reflection coefficient simulation at the air-water interface.

An efficient agreement was noted between the simulation results obtained employing the new ADE-TLM method, the ADE-TLM method described in [23] and the analytical results for the reflection coefficient at different frequencies as defined by Eq. (22).

This agreement is excellent and is consistent with the findings presented in [29].

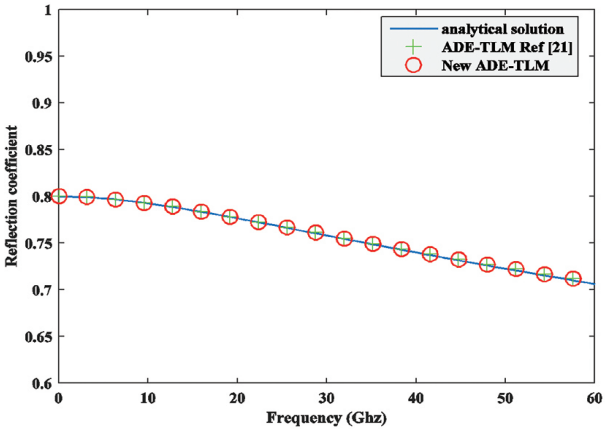

Fig. 7. Comparison of the new ADE-TLM calculated with the analytical solution (eq.22) for the magnitude of the reflection and the ADE-TLM method described in [23]

5. CONCLUSION

In this work, the New ADE-TLM algorithm was effectively used to analyze various polarization formulations and Maxwell's equations, allowing the simulation of reflected optical pulses propagation in a Debye media. This method utilizes the connection between centered derivatives approximations, electrical voltage, and polarization current density *J*.

In our approach, we included voltage sources that model linear characteristics and utilized the principle of variable admittance. In general, the proposed model offers simplicity as an advantage, as it avoids the need to handle convolution products, which are required in recursive convolution methods. This simplicity results in notable performance improvements when compared to other methods like RC, PLRC, and JE.

The results obtained using our new ADE-TLM approach are in excellent agreement with both the analytical values of the reflection coefficient and the ADE-TLM method described in [23], demonstrating the efficiency and validity of the suggested method.

Future work will integrate the new ADE-TLM algorithm into Kerr and Raman nonlinear dispersive media.

6. REFERENCES:

[1] P. B. Johns, "On the Relationship Between TLM and Finite-Difference Methods for Maxwell's Equations", IEEE Transactions on Microwave Theory and Techniques, Vol .35, No. 1, 1987, pp. 60-61.

[2] M. C. Marcysiak, W. K. Gwarek, "Generalized TLM Algorithms with Controlled Stability Margin and Their Equivalence with Finite-Difference Formulations for Modified Grids", IEEE Transactions on Microwave Theory and Techniques, Vol. 43, No. 9, 1995, pp. 2081-2090.

[3] A. Taflove, M. E. Brodwin, "Numerical Solution of Steady-State Electromagnetic Scattering Problems Using the Time-Dependent Maxwell's Equations", IEEE Transactions on Microwave Theory and Techniques, Vol. 23, 1975, pp. 623-630.

[4] K. S. Yee, "Numerical Solution of Initial Boundary Value Problems Involving Maxwell's Equations in Isotropic Media", IEEE Transactions on Antennas and Propagation, Vol.14, 1966, pp. 302-306.

[5] S. D. Gedney, "An Anisotropic Perfectly Matched Layer-Absorbing Medium for the Truncation of FDTD Lattice", IEEE Transactions on Antennas and Propagation, Vol. 44, 1996, pp. 1630-1639.

[6] T. Kashiwa, I. Fukai, "A Treatment by the FDTD Method of the Dispersive Characteristics Associated with Electronic Polarization", Microwave and Optical Technology Letters, Vol. 3, 1990, pp. 203-205.

[7] J. L. Young, "Propagation in Linear Dispersive Media: Finite Difference Time Domain Methodologies", IEEE Transactions on Antennas and Propagation, Vol. 43, 1995, pp. 422-426.

[8] S. C. Hagness, R. M. Joseph, A. Taflove, "Subpicosecond Electrodynamics of Distributed Bragg Reflector Microlasers: Results From Finite Difference Time Domain Simulations", Radio Science, Vol. 31, No. 4, 1996.

[9] P. M. Goorjian, A. Taflove, "Direct Time Integration of Maxwell's Equations in Nonlinear Dispersive Media for Propagation and Scattering of Femtosecond Electromagnetic Solitons", Optics Letters, Vol. 17, 1992, pp. 180-182.

[10] A. S. Nagra, R. A. Cork, "FDTD Analysis of Wave Propagation in Nonlinear Absorbing and Gain Media", IEEE Transactions on Antennas and Propagations, Vol. 46, 1998, pp. 334-340.

[11] M. I. Yaich, M. Khalladi, "The Far-Zone Scattering Calculation of Frequency Dependent Materials Objects Using the TLM Method", IEEE Transactions on Antennas and Propagations, Vol. 50, 2002, pp. 1605-1608.

[12] R. Abrini, M. I. Yaich, M. Khalladi, "Efficient Modelling of Isotropic Cold Plasma Media Using JE-TLM Method", IEICE Electronic Express, Vol. 4, 2007, pp. 492-497.

[13] P. Naylor, R. A. Desay, "New Three dimensional Symmetrical Condensed Lossy Node for Solution of Electromagnetic Wave Problems by TLM", Electronics Letters, Vol. 27, No. 26, 1990, pp. 492-494.

[14] L. R. A. X. De Menezes, W. J. R. Hoefer, "Modeling of general constitutive relationships in SCN TLM", IEEE Transactions on Microwave Theory and Techniques, Vol. 44, No. 6, 1996, pp. 854-861.

[15] M. I. Yaich, M. Khalladi, I. Zekik, J. Morente, "Modeling of frequency dependent magnetized plasma in hybrid Symmetrical condensed TLM method", IEEE Microwave and Wireless Components Letters, Vol. 12, 2002, pp. 293-295.

[16] S. E. Adraoui, M. Khalid, A. Zugari, M. Yaich, M. Khalladi, "Novel CDRC-TLM algorithm for the analysis of magnetized plasma", Optik, Vol. 125, 2014, pp. 276-279.

[17] K. Mounirh, S. El Adraoui, M. Charif, M. I. Yaich, M. Khalladi, "Modeling of anisotropic magnetized plasma media using PLCDRC-TLM method", Optik, Vol. 126,2015, pp.1479-1482.

[18] N. Doncov, T. Asenov, Z. Stankovic, J. Paul, B. Milovanovic, "TLM Z-Transform Method, Modelling of Lossy Grin MTM with Different Refractive Index Profiles", SER: Electrical Energy, 2012, pp.103-112.

[19] R. Abrini, M. I. Yaich, M. Khalladi, "Efficient modeling of isotropic cold plasma media using JE-TLM method", IEICE Electronics Express, Vol. 4, No. 15, 2007, pp. 492-497.

[20] K. Mounirh, S. El Adraoui, Y. Ekdiha, M. I. Yaich, M. Khalladi, "Modeling of dispersive chiral media using the ADE-TLM method", Progress in Electromagnetics Research, Vol. 64, 2018, pp. 157-166.

[21] M. Kanjaa, K. Mounirh, S. El Adraoui, O. Mrabet, M. Khalladi, "An ADE-TLM modeling of biological tissues with cole-cole dispersion model", Progress in Electromagnetics Research M, Vol. 89, 2020, pp. 161-166.

[22] A. Attalhaoui, H. Bezzout, M. Habibi, H. El Faylali, "A New ADE-TLM for Lorenz dispersive medium", Journal of Russian Laser Research, Vol. 42, No. 2, 2021, pp. 237-242.

[23] M. Kanjaa et al. "An ADE-TLM Algorithm for Modeling Wave Propagation in Biological Tissues with

Debye Dispersion", Advanced Electromagnetics, Vol. 9, No. 3, 2020, pp. 1-5.

[24] A. Taflove, S. C. Hagness, "Computational Electrodynamics: The Finite-Difference Time-Domain Method", Artech House, 1995.

[25] S. J. Huang, "Exponential time differencing algorithm for Debye medium in FDTD", Journal of Infrared, Millimeter, and Terahertz Waves, Vol. 28, 2007, pp. 1025-1031.

[26] A. Taflove, S. C. Hagness, "Computational Electrodynamics: The Finite-Difference Time-Domain Method", 3rd Edition, Artech House, 2005.

[27] H. Jin, R. Vahldieck, "Full-wave analysis of coplanar waveguide discontinuities using the frequency domain TLM method", IEEE Transactions on Microwave Theory and Techniques, Vol. 41, No. 9, 1993, pp. 1538-1542.

[28] C. Christopoulos, "The Transmission-Line Modeling Method (TLM)", IEEE Series on Electromagnetic Wave Theory, New York, 1995.

[29] R. J. Luebbers et al. "A frequency-dependent finite-difference time-domain formulation for dispersive materials", IEEE Transactions on Electromagnetic Compatibility, Vol. 32, 1990, pp. 222-227.

[30] O. P. Gandhi, B. Q. Gao, J. Y. Chen, "A frequency-dependent finite difference time-domain formulation for general dispersive media", IEEE Transactions on Microwave Theory and Techniques, Vol. 41, 1993, pp. 658-665.

Estimating Egyptsat -1 Radiometric Coefficient using Cross Calibration with Spot4 and Spot5

Original Scientific Paper

Sayed Abdo
National Authority for Remote Sensing and Space Science 23
Josef Tito, New Nozha Cairo, Egypt
Sayed.abdo@narss.sci.eg

Ibrahim Ziedan
Zagazig University, Faculty of Engineering, Department of Computer and Systems Engineering
Zagazig, Egypt
ieziedan@gmail.com

Asmaa Elyamany
Zagazig University, Faculty of Engineering, Department of Computer and Systems Engineering
Zagazig, Egypt
eng.a.elyamany@gmail.com

Abstract *– The pre-processing of satellite data is a vital step in harnessing the full potential of remote sensing pictures. EgyptSat-1, Egypt's first satellite for observing the Earth from a distance, encountered a major obstacle as a considerable amount of the images it captured could not be used since the necessary radiometric coefficients were missing. This study utilises a cross-calibration methodology, taking advantage of the spectral similarity between Spot 4 and Spot 5 as reference satellites, in order to retrieve these difficult-to-obtain coefficients. The analysis demonstrates that the selection of window size in the cross-calibration process is crucial in determining the outcomes. In general, smaller window sizes tend to produce better results. However, there are certain cases when larger windows are more successful, such as in the scenario of EgyptSat-1's band 3 and its cross-calibration with Spot 5. In contrast to a previous study, the new methodology produces much diminished uncertainty factors, indicating a remarkable enhancement in accuracy. The cross-calibration results highlight the significance of selecting the appropriate window size and satellite for accurate calibration, especially for the Near-Infrared (NIR) band, which is highly responsive to these parameters. Moreover, there are differences in the computations of offset and gain between Spot 4 and Spot 5, which further highlight the intricacies involved in radiometric calibration. The results of this study lead to the determination of improved calibration coefficients for EgyptSat -1, with the specific aim of maximising the accuracy of the results and minimising any errors.*

Keywords*: information security, information system, security awareness, user behavior*

1. INTRODUCTION

It is well known that the satellites orbiting the earth are subjected to mechanical or electrical effects, as well as UV radiation. These effects can alter the way sensors on board operate, resulting in inaccurate results from satellite image processing. This is why satellite sensors must be calibrated on a regular basis. The calibration is basically the comparison of the measured instrument to an absolute reference, standard reference or a well-known accuracy this later one is called cross calibration. In cross calibration the comparison is made between the sensor to be calibrated and a well-known sensor. Egypt has lunched Egyptsat -1 since 2007, a huge amount of data has been sent to the ground station since then. the missing calibration coefficients made it hard to use those data. In 2012, cross calibration is made between Egyptsat -1 and Spot 4 to retrieve the missing radiometric calibration coefficients of Egyptsat -1 [1]. In 2016, Using simultaneously collected Landsat-8 OLI data, the Gaofen-1 WFV cameras were cross calibrated, and the findings showed that the newly calibrated reflectance exhibited a modest difference (5%) with the calibrated OLI (Operational Land Imager) reflectance for the four spectral bands over a large reflectance range [2]. In 2017, the 8 corresponding spectral bands of the Sentinel-2 MSI (MultiSpectral Instrument) cross calibrated with the well-calibrated Landsat 8 OLI as a reference and the results showed

that the radiometric difference of the 7 corresponding bands are consistent to OLI within 1% or better, except on cirrus band [3]. In 2018, Landsat and Sentinel-2 cross calibration resulted in stable radiometric calibration for each instrument and consistency to ~2.5% between the instruments for all the spectral bands that the instruments have in common [4]. In 2019, the GF-1 wide coverage multi-spectral camera cross calibrated with MODIS and the results used to correct the side swing angle [5]. The findings of the calibration coefficients from the 2019 GF-1 satellite cross-calibration with MODIS and Landsat 8 showed that the suggested strategy can obtain excellent calibration accuracy, and the total calibration uncertainties of PMS using MODIS as reference sensor are less than 6% [6]. In 2019, FORMOSAT-5 satellite was both vicarious and cross-calibrated with Landsat 8, the results showed a decaying optical sensitivity, which resulted in rapid changes (6%–24% in radiometric coefficient) during the first year after [7] launch . In 2020, the GF-6/WFV is cross-calibrated with Landsat-8/OLI, Sentinel-2/MSI and Terra/MODIS, the uncertainty analysis showed that the total uncertainty is 3.35% for the blue band, 3.56% for the green band, 4.23% for the red band and 4.60% for the NIR band, all less than 5% [8]. In2020, a 4-angle BRDF normalization model was used for Cross Calibration and Validation between Landsat 8 and Sentinel 2A, the findings indicated that there was good potential for normalization in the longer wavelength bands but less promise in the blue and coastal aerosol bands. [9]. in 2021, a new cross-calibration approach using extended pseudo invariant calibration sites (EPICS) over North Africa used to evaluated the gain for Landsat 7/8 and Sentinel 2A/B, with the results showing that the sensors are calibrated within 2.5% (within less than 8% uncertainty) or better for all sensor pairs [10]. In2021, HJ-1A CCD1 and Terra MODIS data was cross calibrated on long term for gains calculation and the results are validated by the field calibration results, the gain difference between the site calibration and cross-calibration is less than 3%. The long-term cross-calibration results further indicate the attenuation rate has reached 23.51%, 21.89%, 8.11%, and 13.37%, respectively by the end of 2019 based on the cross-calibration results [11]. This study addresses the critical challenge of missing radiometric coefficients in EgyptSat-1's acquired imagery by employing a cross-calibration approach with reference to Spot 4 and Spot 5. The key contributions of this research are:

- Improved comprehension of the influence of various window widths on radiometric calibration, yielding valuable observations for enhancing the accuracy of satellite photography.
- Enhanced calibration precision, rendering Egyptsat -1 data more reliable and valuable for research and practical purposes.
- The introduction of updated calibration coefficients, specifically tailored to each band, guarantees low inaccuracies and maximizes the quality of the data.

Therefore, the rest of this paper is organized as follows, literature review of the presented problem in section 2. Detailed data descriptions are presented in Section 3. In section 4, description of the study area and region of interest. The proposed approach is illustrated in a detailed manner in Section 5. The detailed presentation of the results is presented in Section 6. Finally, the conclusion is discussed in section 7.

2. DATA DESCRIPTION

The study uses data from Egyptsat -1 while data from Spot4 and Spot 5 is used as reference. Egyptsat -1 is Egypt's first Earth remote sensing satellite. This satellite was jointly built by Egypt's National Authority for Remote Sensing and Space Sciences (NARSS) together with the Yuzhnoye Design Bureau in Ukraine and was launched on board a Dnepr rocket from the Baikonur Cosmodrome. On 23 October 2010, the National Authority for Remote Sensing and Space Sciences announced that control and communication with the satellite had been lost since July 2010 [12, 13].

SPOT-4 (Satellite pour l'Observation de la Terre) is a public Earth-imaging satellite launched in 1998 by the French National Centre for Space Studies (CNES) to provide worldwide crop monitoring for environmental research. [14], SPOT 5 was a commercial Earth-imaging satellite launched by CNES (Centre National d'Études Spatiales), the French Space Agency. Launched on 4 May 2002, it terminated operations in March 2015 due to a technical failure [15]. In this study, the first three bands' spectral range similarities were used to select a reference coefficient for cross-calibration retrieval of the missing coefficient. Table 1 lists the characteristics of the three satellites, while Table 2 lists the spectral resolutions.

Table 1. Characteristic of Egyptsat-1, Spot4 and Spot5

	Egyptsat -1	Spot4	Spot5
Lunch date	17 April 2007	24 March 1998	4 May 2002
altitude	668 Km	832 Km	832 Km
orbit	sun synchronous	sun synchronous	sun synchronous
Swath width	46 Km	120 Km	120 Km
Instrument	Push broom	Push broom	Push broom
Repeat cycle	~ 57 days	26 days	26 days
viewing capability	±35° about nadir	± 27° about nadir	± 27° about nadir

Table 2. Spectral resolutions of Egyptsat -1, Spot4 and Spot5

Bands	Description	Egyptsat -1	Res.	Spot 4	Res.	Spot5	Res.
Band1	Green	0.51-0.59	7.8 m	0.51-0.59	20 m	0.50-0.59	10m
Band 2	Red	0.61-0.68	7.8 m	0.61-0.68	20 m	0.61-0.68	10m
Band3	NIR	0.79-0.89	7.8 m	0.79-0.89	20 m	0.78-0.89	10m
Band4	Pan	0.50-0.89	7.8 m	0.61-0.68	10 m	0.48-0.71	5m
Band 5	SWIR	1.55 - 1.7	39 m	1.58 - 1.75	40 m	1.58-1.75	20m

3. STUDY AREA

The optical images selected for usage in the study area (Southern Egypt) must be cloud-free and collected on dates that are close together. The images used in this study are from the area of Aswan Egyptsat -1 Feb., 23, 2010 Spot4 Feb., 9, 2010 Spot5. Feb.,5, 2010 Fig. 1., these dates are the best that could be and the gap can be ignored as the ROI (Region Of Insert) is stable and doesn't contain much urban as well the method used uses only the homogeneous areas. The image contains water, desert and vegetation cover to consider both "bright" and "dark" target sites to allow better characterization across each sensor's dynamic range. To minimize the deference brought on by the sun's position change, the calibration target should be nearly Lambertian in nature and constant in terms of radiometric response and atmospheric conditions. Some of these qualities, such as a steady environment, radiometric response, and spatial uniformity, are present in desert sites, making them a good target for cross-calibration [16].

Fig. 1. (a)map of Egypt indicating the study Area ROI (b) Egyptsat -1, (c) Spot4, (d) Spot5

As the regions of interest (ROI must be in the same size and resolution and perfectly aligned together as the process uses sliding window to extract the points of interest and Calibration errors are introduced by any incorrect registration between the images acquired by the two sensors. The images used in this paper is in the DN form but registered to each other. As noticed that the resolution of the images is different so a preprocessing is a must first to proceed to the cross calibration the Egyptsat -1 is subjected to upsampling process using cubic convolution and Spot 4 MS (multispectral) bands was fused with the panchromatic band to resample the MS bands to 10 m while the Spot5 left as it is.

4. METHODS

Typically, the first stage in cross calibration is Spectral Adjustment, which eliminates the discrepancy between the spectral response of the target sensor and that of the reference sensor using spectral band adjustment factors (SBAF) [17], however the spectral response of Egyptsat -1 is unavailable that's why Spot 4 and Spot5 is chosen for the similarity in the spectral range (Table 2) Egyptsat -1's manufacturer did not provide generic calibration data, so it is considered to be missing. Consequently, Egyptsat -1 sensor calibration data is estimated using the output pixel Digital Numbers (DNs), and the missing radiometric coefficient is obtained through relative calibration relationships between the DNs of Egyptsat -1 and the source. Fig.2. shows the flow chart of the cross-calibration procedure used in this paper.

Step1: a sliding window goes over the image to extract the points of interest by selecting the center point of the window if its CV (coefficient of variation calculated by dividing the standard deviation by the mean value) of the master image (in this case the Spot image) is < 1%, as the surface in this window could be considered as homogenous. The size of the window is taken to be 15x15, 5x5 and 3x3.

Step 2: A list of matched point from the master (Spot) image and slave (Egyptsat -1) image is used to apply linear regression on the points to find the relation between the master and slave images> the list is divided to two parts 70% for the training and 30% for testing. Equation 1 shows the relation between the $DN_{Egyptsat}$ and DNS_{pot}

$$DN_{Spot} = A.DN_{Egptsat} + B \quad (1)$$

From this relation the gain and offset be determined the gain and offset of Egyptsat -1 as follows:

$$Given: L = Gain_{Spot}\, DN_{Spot} + Offset_{Spot} \quad (2)$$

From equation (1)

$$L = Gain_{spot}(A \cdot DN_{Egyptsat} + B) + Offset_{Spot} \quad (3)$$

$$L = A \cdot Gain_{Spot}\, DN_{Egyptsat} + B \cdot Gain_{Spot} + Offset_{Spot} \quad (4)$$

From that

$$Gain_{Egyptsat} = A \cdot Gain_{Spot} \quad (5)$$

$$Offest_{Egyptsat} = B \cdot Gain_{Spot} + Offset_{Spot} \quad (6)$$

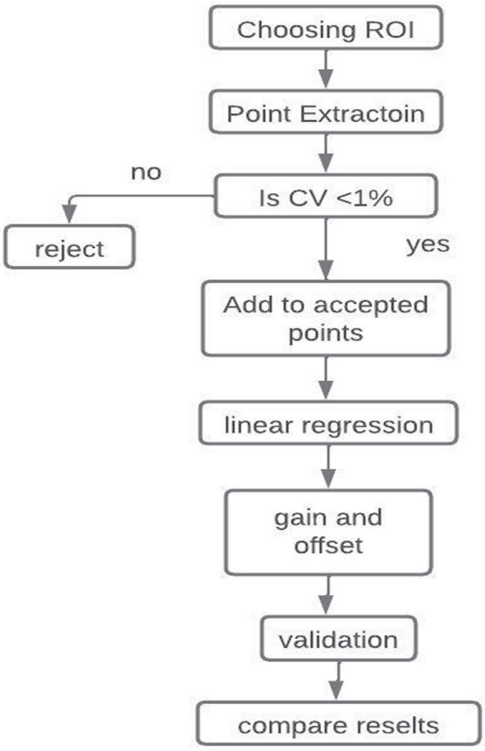

Fig. 2. The work flow of the cross-calibration process

Step 3: Using the obtained coefficients from the cross calibration with Spot 4 to retrieve Egyptsat -1 level 2A image and compare it to Spot 5 level 2A image, Likewise Using the obtained coefficients from the cross calibration with Spot 5 to retrieve Egyptsat -1 level 2A image and compare it to Spot 4 level 2A image. The compare process is done by computing the RMSE (Root Mean Square Error) and normalizing the result by dividing it by the range of the DN of the images (in this case 0-255).

5. RESULTS AND DISCUSSION

Table 3 shows the gain of Spot4 and Spot 5 from the metadata files while the offset for both satellites is 0.0.

Table 3 gain of Spot4 and Spot5

Satellite	Band1	Band2	Band3
Spot4	0.85857	0.78700	1.34100
Spot5	0.830500	0.800678	1.313315

After applying the previous algorithm and equations (5, 6) the results are shown in Tables 4 and 5, along with the uncertainty degree calculated from the normalized RMSE.

Table 4. The calibration coefficients due to cross calibration with spot 4

15x15 window			
Band	**Gain**	**Offset**	**Uncertinity**
1	2.2022	-14.0150	25.06%
2	1.3463	-6.7689	16.15%
3	1.4357	5.9256	18.7%
5x5 window			
Band	**Gain**	**Offset**	**Uncertinity**
1	2.8486	-61.6575	22.13%
2	1.5203	-25.0393	14.99%
3	1.4876	-0.1991	18.57%
3x3 window			
Band	**Gain**	**Offset**	**Uncertinity**
1	3.0921	-79.1228	21.5%
2	1.7706	-51.6968	12.91%
3	1.8168	-46.0309	14.95%

Table 5 The calibration coefficients due to cross calibration with spot 5

15x15 window			
Band	**Gain**	**Offset**	**Uncertinity**
1	2.1487	-73.4105	19.53%
2	1.4341	-57.5250	12.34%
3	0.8430	30.0816	11.9%
5x5 window			
Band	**Gain**	**Offset**	**Uncertinity**
1	2.0602	-66.7629	19.36%
2	1.3454	-48.3277	11.49%
3	0.8732	24.9954	12.25%
3x3 window			
Band	**Gain**	**Offset**	**Uncertinity**
1	2.0523	-66.1413	19.18
2	1.3215	-45.8055	11.54%
3	0.9437	15.2819	12.71%

The findings displayed were produced using an average of 400 points for the 3x3 window, while 8000 and 34,000 points, respectively, were used for the 5x5 and 15x15 windows. Figs. 3, 4 represent the scatter plot of Egyptsat -1 DN versus Spot 4 and Spot 5. plotted by MATLAB. It is evident that the points tend to form vertical lines. In order to investigate this issue, a histogram plot was drawn for Egyptsat -1 bands in Fig. 5., which reveals voids in the histogram for all three bands. This indicates that the vertical lines in Fig. 3, 4 are the result of Egyptsat -1 poor quantization. It is evident from Fig. 3, 4, that the line generated is satisfactory and fairly depicts the relationship between Egyptsat -1 points and Spot points. Spot 4 results (Table 4) shows that the uncertainty factor is decreasing with decrease of the window size, it is also noticeable that the gain fluctuates around the average with no more than 20% declines to 15% in the case of band 2 and 3, whereas the offset results are so widely dispersed from the average.

In the other hand Spot 5 results (Table 5) shows that with the decreasing of the window size the uncertainty factor decrease with the exception of band 3 (NIR) the uncertainty factor increase with decreasing the window size. By examining the findings, it can be found that the gain fluctuates around the average with no more than 6% in band 2 and 3, falling to 3% in the case of band 1,and that the offset results fluctuate by 7% in band 1, 14% in band 2, and 35% in band 3. Table 5 lists the outcomes of an earlier attempt to determine the messing coefficient of Egyptsat1 and was obtained via 13 points of cross-calibration between Egyptsat1 and Spot4 [17].

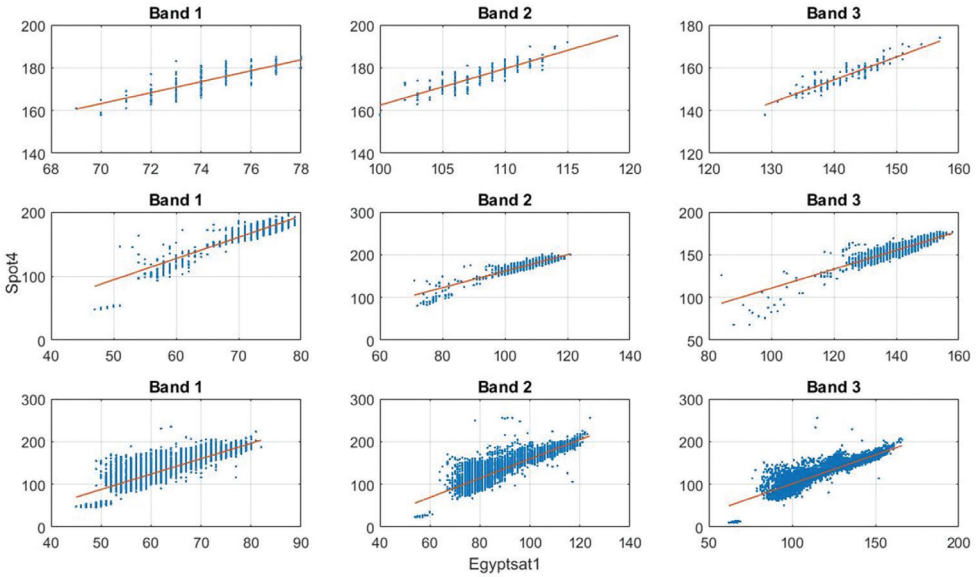

Fig. 3. Scatter plot of Spot 4 and Egyptsat -1 DN's

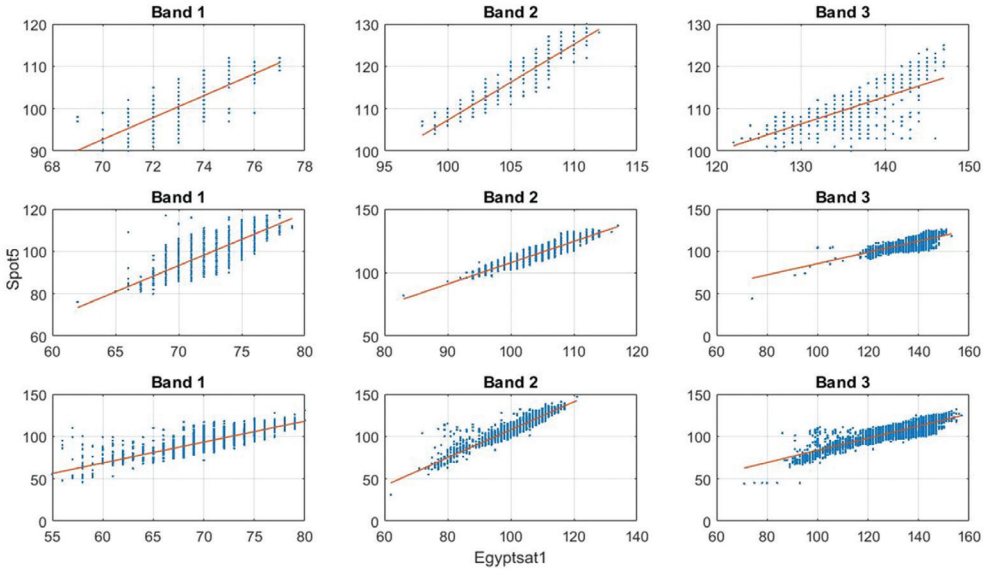

Fig. 4. Scatter plot of Spot 5 and Egyptsat -1 DN's

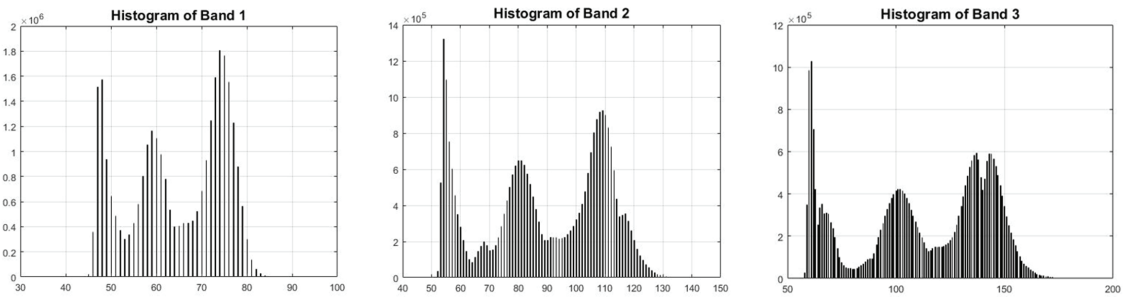

Fig. 5. A histogram for the bands of the Egyptsat -1 image in Fig. 1.(b)

It is apparent that the Spot 4 results are similar to those previously acquired in the case of gain, particularly in the window sizes of 5 and 3, while the results are very different in the case of offset.

The outcome of applying the coefficient in Table 6 to the Egyptsat-1 image to generate a level 2A image and comparing it to a level 2A image from Spot 4 is shown in Table 7.

Table 6. The finding of the prior study

Egyptsat-1	Band1	Band2	Band3
Gain [W/(m2 sr µm)]	3.032477	1.462634	1.458202
Offset [W/(m2 sr µm)]	-32.1473	-9.89971	-27.8724

Table 7. The uncertainty factor of the prior finding

Band	Uncertinty
1	38.29%
2	18.85%
3	7.06%

6. CONCLUSIONS

By stdying the cross-calibration results between Egyptsat -1 and Spot 4/5, it is evident that the smaller the window size the better the result.with except in the case of Egyptsat -1 and Spot 5 band 3 the bigger the window size the better the results

With the exception of band 3, where the earlier study's results are superior with an uncertainty factor of 7.06%, the results of the cross calibration of Egyptsat -1 with Spot 4/5 reveal that the new study has a low uncertainty factor.

The data indicate that switching from Spot4 to Spot5 and adjusting the window size has a slight impact on the gain. However, the window size in Spot 4 cross-calibration has a significant impact on the offset computation. In the case of Spot5, changing the window size from 5 to 3 has a negligible impact on the results, except for the NIR band (band 3). The NIR band is typically very sensitive to window size changes. While the offset varies between Spot4 and Spot5, band 3 varies greatly when the window is altered. In the case of the offset calculation, the results vary greatly, whereas the gain calculation yields very similar values. The uncertainty factor in the case of Spot 4 is varying from 25.06% to 21.5% in the case of band 1 while in the case of spot 5 it varies from 19.53% to 19.18% in case of band 1.

From all the previous results the calibration coefficients can be considered as follows:

Table 8. The estimated calibration coefficient of Egyptsat1

Egyptsat-1	Band1	Band2	Band3
Gain [W/(m2 sr µm)]	2.0523	1.345	1.458202
Offset [W/(m2 sr µm)]	-66.1413	-48.3277	-27.8724

These results are chosen in the light of the uncertainty factor to achieve the best results with minimum error. Band 1 coefficients are chosen from the cross calibration results with Spot5 with window size 3x3 with uncertainty of 19.18%. Band 2 calibration coefficients are chosen from the cross calibration with Spot5 with window size 5x5 with uncertainty of 11.49%.Band 3 best results obtained by applying the calibration coefficients of the prior study with uncertainty 7.06%.

7. ACKNOWLEDGMENT

The authors are grateful to the National Authority for Remote Sensing and Space Sciences (NARSS) in Egypt for supporting this study.

8. REFERENCES:

[1] A. Nasr, B. El Leithy, H. Badr, J. Centeno, "Estimation of Radiometric Calibration Coefficients of EGYPTSAT-1 Sensor", The International Archives of the Photogrammetry, Remote Sensing and Spatial Information Sciences, Vol. 39, 2012, pp. 139-143.

[2] J. Li, L. Feng, X. Pang, W. Gong, X. Zhao, "Radiometric cross calibration of gaofen-1 wfv cameras using landsat-8 oli images: A simple image-based method", Remote Sensing, Vol. 8, No. 5, 2016, p. 411.

[3] S. Li, S. Ganguly, J. L. Dungan, W. Wang, R. R. Nemani, "Sentinel-2 MSI radiometric characterization and cross-calibration with Landsat-8 OLI", Advances in Remote Sensing, Vol. 6, No. 02, 2017, p. 147.

[4] J. A. Barsi et al. "Sentinel-2A MSI and Landsat-8 OLI radiometric cross comparison over desert sites", European Journal of Remote Sensing, Vol. 51, No. 1, 2018, pp. 822-837.

[5] Y. Xie, Z. Tao, W. Shao, J. J. Qu, H. Huan, C. Tian, "Radiation Cross Calibration Based on GF-1 Side Swing Angle", Journal on Internet of Things, Vol. 1, No. 1, 2019, p. 9.

[6] Q. Liu, T. Yu, H. Gao, "Radiometric cross-calibration of GF-1 PMS sensor with a new BRDF model", Remote Sensing, Vol. 11, No. 6, 2019, p. 707.

[7] T.-H. Lin et al. "Radiometric variations of On-Orbit FORMOSAT-5 RSI from vicarious and cross-calibration measurements", Remote Sensing, Vol. 11, No. 22, 2019, p. 2634.

[8] A. Yang et al. "Radiometric cross-calibration of the wide field view camera onboard GaoFen-6 in multispectral bands", Remote Sensing, Vol. 12, No. 6, 2020, p. 1037.

[9] M. Farhad, M. Kaewmanee, L. Leigh, D. Helder, "Radiometric cross calibration and validation using 4 angle BRDF model between landsat 8 and sentinel 2A", Remote Sensing, Vol. 12, No. 5, 2020, p. 806.

[10] P. Khakurel, L. Leigh, M. Kaewmanee, C. T. Pinto, "Extended Pseudo Invariant Calibration Site-Based Trend-to-Trend Cross-Calibration of Optical Satellite Sensors", Remote Sensing, Vol. 13, No. 8, 2021, p. 1545.

[11] L. Liu, T. Shi, H. Gao, X. Zhang, Q. Han, X. Hu, "Long-term cross calibration of HJ-1A CCD1 and Terra MODIS reflective solar bands", Scientific Reports, Vol. 11, No. 1, 2021, p. 7386.

[12] Y. G. Moustafa, F. A. Farrag, A. A. Abdelhafiz, A. M. Abd Elwahed, "The Potentials of Satellite Images for Map Updating with Emphasizes on Egypt Sat-1 Images", JES. Journal of Engineering Sciences, Vol. 40, No. 4, 2012, pp. 989-1003.

[13] A. R. Elshehaby, L. G. E.-d. Taha, "Assessment of cartographic potential of EgyptSat-1 satellite image (case study in flat areas)", Applied Geomatics, Vol. 3, 2011, pp. 159-169.

[14] M. Magnusson, J. E. Fransson, "Combining airborne CARABAS-II VHF SAR data and optical SPOT-4 satellite data for estimation of forest stem volume", Canadian Journal of Remote Sensing, Vol. 30, No. 4, 2004, pp. 661-670.

[15] W. Fu, J. Ma, P. Chen, F. Chen, "Remote sensing satellites for digital earth", Manual of Digital Earth, 2020, pp. 55-123.

[16] S. Kabir, L. Leigh, D. Helder, "Vicarious methodologies to assess and improve the quality of the optical remote sensing images: A critical review", Remote Sensing, Vol. 12, No. 24, 2020, p. 4029.

[17] Q. Zhou, L. Tian, J. Li, Q. Song, W. Li, "Radiometric cross-calibration of Tiangong-2 MWI visible/NIR channels over aquatic environments using MODIS", Remote Sensing, Vol. 10, No. 11, 2018, p. 1803.

FOE-NET: Segmentation of Fetal in Ultrasound Images using V-NET

Original Scientific Paper

Eveline Pregitha R.
Research Scholar, Department of Electronics and Communication Engineering,
Noorul Islam Centre for Higher Education,
Tamil Nadu, India
epregitha@gmail.com

Vinod Kumar R. S.
Professor & Head, Department of Electronics and Communication Engineering,
Noorul Islam Centre for Higher Education,
Tamil Nadu, India
rsvinodkumar69@yahoo.co.in

Ebbie Selvakumar C.
Assistant Professor, Department of Electrical and Electronics Engineering,
Rohini College of Engineering and Technology,
Tamil Nadu, India
ebbieve@gmail.com

Abstract *– Ultrasound is a non-invasive method to diagnose and treat medical conditions. It is becoming increasingly popular to use portable ultrasound scanning devices to reduce patient wait times and make healthcare more convenient for patients. By using ultrasound imaging, you will be able to obtain images with better quality and also gain information about soft tissues. The interference caused by tissues reflected in ultrasound waves resulted in intensified speckle sound, complicating imaging. In this paper, a novel Foe-Net has been proposed for segmenting the fetal in ultrasound images. Initially, the input US images are noise removal phase using two different filters Adaptive Gaussian Filter (AGF) and Adaptive Bilateral Filter (ABF) used to reduce the noise artifacts. Then, the US images are enhanced using CLAHE and MSR for smoothing to enhance the image quality. Finally, the denoised images are input to the V-net is used to segment the fetal in the US images. The experimental outcomes of the proposed Multi-Scale Retinex (MSR) is an image enhancement technique that improves image quality by adjusting its illumination and enhancing details. Foe-Net was measured by specific parameters such as specificity, precision, and accuracy. The proposed Foe-Net achieves an overall accuracy of 99.48%, specificity of 98.56 %, and precision of 96.82 % for segmented fetal in ultrasound images. The proposed Foe-Net attains better pre-processing outcomes at low error rates and, high SNR, high PSNR, and high SSIM values.*

Keywords*: Ultrasound images, Adaptive Gaussian Filter, Adaptive Bilateral Filter, CLAHE, Multi-scale retinex, V-net*

1. INTRODUCTION

Ultrasound (US) image mechanism is considered an important medical imaging method that is used for visualizing the growth and pathology of the fetus in the womb of a mother. The ultrasound scan sends high-frequency waves through the abdomen into the uterus. This wave gets reflected by the baby and reaches the scanner [1]. Ultrasonic waves are used at frequencies ranging from 2 MHz to 15 MHz Ultrasonic waves reflected by body tissues after traveling through an organ are struck. To create US images, the echoes that reflect are analyzed, and the scattered echoes are referred to as speckle noise [2]. Speckle noise reduces the clarity and contrast of US images. It is extremely difficult for radiologists to diagnose diseases accurately due to speckle noise. The structural analysis of the US images is distorted by speckle noise [3]. Speckle noise reduces the quality of the images, resulting in low-quality images for the US. Many denoising techniques have been developed to minimize noise, including total variation, wavelet-based filtering techniques, median filtering, nonlocal means, and various other techniques [4].

In recent years, deep learning has been applied to medical image analysis, bringing about a revolutionary impact on the existing diagnostic techniques [5].

US images commonly contain two types of noise due to the technology used to obtain ultrasonic images and the presence of various organs and tissues within the imaging area [6]. The quality and contrast of a US image drastically deteriorate, making medical diagnosis challenging. The Adaptive Gaussian Filter (AGF) is an image analysis method that improves the conventional Gaussian filter by varying its regional visual factors that reduce distortion while maintaining borders and patterns. ABF enhances bilateral filters changing their characteristics to regional image features. The AGF and ABF are more effective compared to different techniques for reducing the level of noise in the original image. CLAHE technique is used for enhancing images to improve spatial brightness and features by breaking an illustration into tiny segments. Histogram equalization [7] is implemented for each segment and limiting contrast enhancement to prevent noise activation. In Multi-scale Retinex (MSR), the illumination and details of an image are adjusted to improve its quality. The CLAHE and MSR are more effective compared to different techniques for enhancing the quality of the original image. The segmentation process simplifies the analysis of images by making them more understandable. when compared to segnet [8], Alexnet [9], and U-Net [10], the proposed V-net achieves better accuracy. As a result, despeckling ultrasound images is critical, and numerous research have been conducted to enhance image quality using noise filtering algorithms and segmentation results.

The main contribution of the research summarised as,

- The main objective of the work is to represent a novel Foe-Net that has been proposed for segmenting the fetal in ultrasound images. Initially, the input US images are noise removal phase using two different filters AGF and ABF used to remove the noise artifacts.
- Then, the US images are enhanced by CLAHE and MSR for smoothing to enhance the image quality. The proposed Foe-Net technique is evaluated based on denoising filters PSNR, MSE, SNR, and SSIM.

The following five divisions were developed for the remaining components of this investigation. The involved works are specified in Section 2, the proposed foe-net is reviewed in Section 3, findings and analysis are reported in Section 4, and a conclusion and recommendations for further study are provided in Section 5.

2. LITERATURE SURVEY

In recent days some methods and techniques remained presented by researchers mainly to detect the fetus efficiently. This section provides a brief overview of the most recent studies.

In 2019 Sobhaninia et al. [11] developed a multitasking deep network for 2D ultrasound image calculation of the fetal head circumference based on a Link-Net architecture with multiscale inputs. A completely linked network-based Ellipse Tuner formed part of the organized system.

In 2020 Qiao et al. [12] employed 2D prenatal ultrasound images to propose a DL semantic segmentation network in fetal HC segmentation. A squeeze-and-excitation (SE) block was added to the jump connection, and an advanced convolutional layer was added after the last encoder.

In 2022 Ashkani Chenarlogh et al. [13] developed a novel fast, and accurate U-Net-based architecture for the problem of segmenting medical images. The encoder-decoder path consists of four blocks. Dice and Jaccard coefficients for the dataset using the suggested precise model were 97.62% and 95.43%, respectively.

In 2021 Singh, et al. [14] created an innovative deep-learning method for automatically segmenting the foetal cerebellum from 2D US images. By integrating the residual block (Res), adding extended convolution to the final two slices, and using U-Net as the basis model, able to distinguish the cerebellum (c) from the noisy US image.

In 2023 Cengiz et al. [15] proposed an improved segmentation quality assessment methodology (FUSQA) to automatically classify the quality of a fetal ultrasound segmentation model on unseen data. They contrasted the various designs, attaining over 90% classification accuracy when separating high- and low-quality segmentation masks from a dataset that was unidentified.

In 2022 Cammarasana et al. [16] developed a deep learning system for denoising US pictures in real-time. The most effective method for preserving morphological features and enhancing edges is Weighted Nuclear Norm Minimization (WNNM), which was determined after a comparison of state-of-the-art denoising approaches.

In 2021 Dong et al. [17] a Feature-guided CNN for image denoising using portable ultrasonography equipment was developed. To achieve high-quality denoising outcomes for clinical images, a feature masking layer was utilized to power a tiered denoising system.

From the comprehensive study of the existing works, the observed all existing work has some sort of pitfalls. Therefore, the proposed method focuses on denoising and segmenting the fetal US images using a novel Foe-Net method, a combination of denoising filters and segmenting the US images of fetal.

3. PROPOSED FOE-NET

In this section, a novel Foe-Net for segmenting the fetal in ultrasound images. AGF and ABF are used to remove noise artifacts from US input images. To enhance the quality of the US images, CLAHE and MSR are applied for smoothing. Pre-processed US images are given as input to the deep-learning based V-net for the segmentation of fetal. The overall flow diagram of the proposed method is illustrated in Fig. 1.

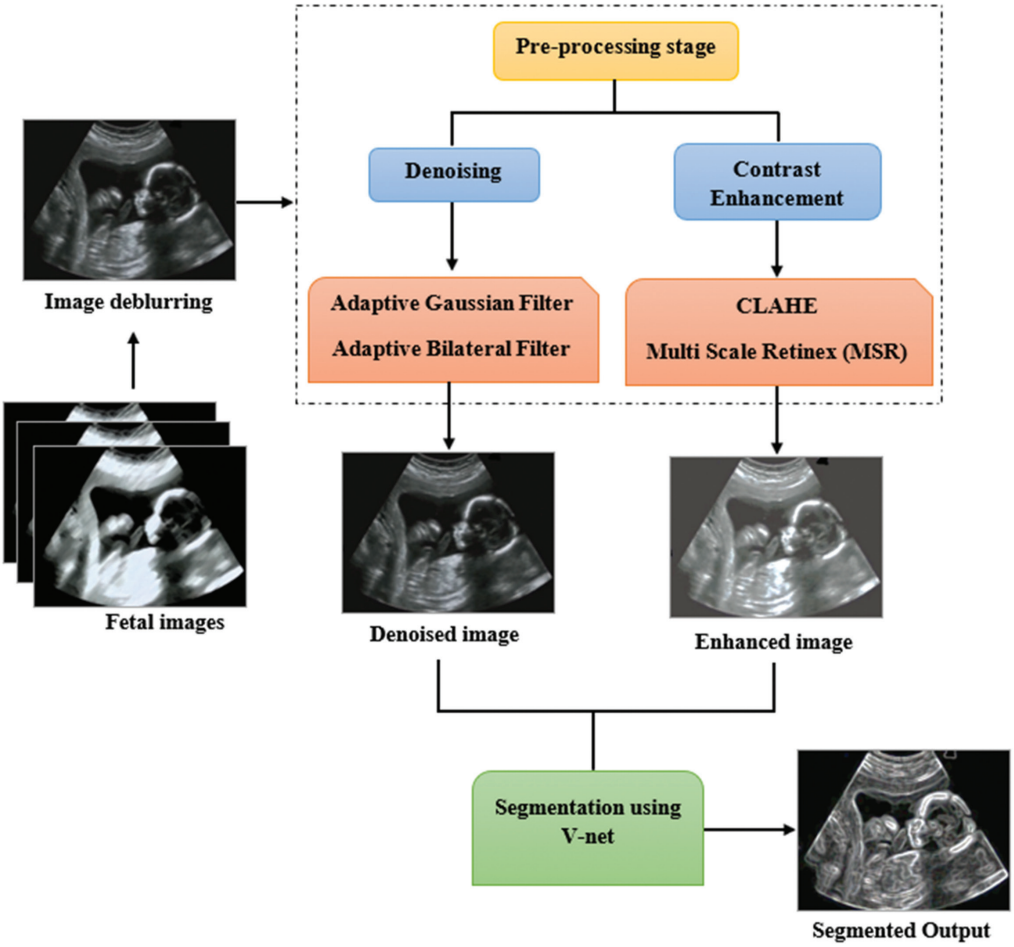

Fig. 1. Schematic representation of proposed methodology

3.1. IMAGE DEBLURRING

Image deblurring techniques have developed recently in response to the pressing demands of numerous businesses for image clarity, and these techniques are currently in use.

If the image destruction process is assumed to be spatially constant, the mathematical method can be expressed in equation (1)

$$f(y,z)=g(y,z)\otimes h(y,z)+m(y,z) \quad (1)$$

It is generally assumed that the process of image degradation is represented by $f(y,z)$ the interaction of spatial motion invariant functions $g(y,z)\otimes h(y,z)$ with additional noise. The following equation (2) can be used to describe the process of image degradation:

$$f(y,z)=G([h(y,z)]+m(y,z) \quad (2)$$

In the formula from equation (3) the function G is a linear system that satisfies,

$$G[bh_1(y,z)+ch_2(y,z)]=bG[h_1(y,z)]+cG[h_2(y,z)] \quad (3)$$

where b and c are arbitrary values, function G is a linear system, and $h_1(y,z)$ and $h_2(y,z)$ are optional depicts of the same size in equation (4).

$$G[h(y-\alpha, z-\beta)]=f(y-\alpha, z-\beta) \quad (4)$$

The system has space shift invariance $y-\alpha$, $z-\beta$ at that point, it is typically said in equation (4). It demonstrates how a point's output is only influenced by its input and not by its geographical position within the system. According to the procedure representation in the frequency domain $F(v,w)$, can be denoted in equation (5)

$$(v,w)=G(v,w)H(v,w)+M(v,w) \quad (5)$$

From the above equation (7) (v,w) the denoted coefficients of the image frequency. The image deblurring approach M is improved and simplified using the below equation (6):

$$F = GH+M \quad (6)$$

The absolute evaluation approach, which is distingué by evaluation scales by international standards and is the most often applied technique for image deblurring, is immediately categorized based on vision. The results of the evaluation will differ due to the impact of other testers and evaluating situations on image quality, but this method can best capture the impact of image restoration.

3.2. PRE-PROCESSING STAGE

In this phase, the US images are pre-processed in two phases namely denoising using AGF & ABF filtering techniques and enhancement using CLAHE & MSR techniques. Initially, the AGF filter automatically adjusts flattening using localized image features to minimize

distortion while keeping edge patterns in fetal images. Along with suppressing distortion after AGF, the ABF also maintains boundaries by adapting filter variables to localized image qualities. Afterward, the CLAHE effectively improves contrast in images by enhancing the dynamic range of pixel intensity levels. Next, the MSR analyses images at multiple resolutions to eliminate poor illumination and improve the clarity of the image.

3.2.1. Image Denoising

(a) Adaptive Gaussian Filter (AGF)

The image is deformed but the noise is smoothed out when using an adaptive Gaussian filter to reduce the noise. The following terms can be used to express the two-dimensional digital Gaussian filter in equation (7):

$$G(y,z) = \frac{1}{\sqrt{2\pi\sigma}} exp(-\frac{y^2+z^2}{2\sigma^2}), \quad (7)$$

Where σ^2 is the Gaussian filter's variance, and the size of the filter kernel $k(-k \leq y, z \geq k)$ is frequently calculated by excluding values that are smaller than the kernel's maximum value. The expression for the one-dimensional Gaussian filter $G(y)$ is denoted in equation (8),

$$G(y) = \frac{1}{\sqrt{2\pi\sigma}} exp\ (-\frac{y^2}{2\sigma^2}) \quad (8)$$

When the Gaussian filter is used to reduce noise, a high filter variance is successful at reducing noise, but it also distorts the areas of the image where there are sharp fluctuations in pixel brightness. The adaptive filter variance $\sigma^2(y)$ is defined in equation (9):

$$\sigma^2(y) = \frac{2\varepsilon}{|E''(y)|}, \quad (9)$$

Where ε is the step of predefined error brought on by a Gaussian filter. $E''(x)$ is determined using a complex regression-based method from the noisy, distorted signal.

The goal of the adaptive Gaussian filtering problem is to minimize the mean square error while ensuring that the filter variance does not significantly shift from pixel to pixel. Let G and E stand for the image and the two-dimensional Gaussian filter, respectively.

(b) Adaptive Bilateral Filter (ABF)

For removing noise artifacts, images are pre-processed using adaptive bilateral filters. The adaptive bilateral filter is a new sharpening and smoothing technique (ABF). Where $[x_t, y_t]$ and $\Omega_{x_t y_t}$ are defined as before, and the normalization factor, the suggested shift-variant ABF's response at $[x_t, y_t]$ to an impulse at $[x, y]$ at the bottom is given by equation (10),

$$r_{x_t y_t} = \sum_{x=x_t-M}^{x_t+M} \sum_{y=y_t-M}^{y_t+M} exp\left(-\frac{(x-x_t)^2+(y-y_t)^2}{2\sigma_{d^2}}\right) \times exp\left(-\frac{(f[x,y]-f[x_t,y_t]-\zeta[x_t,y_t])^2}{2\sigma_{r^2}[x_t,y_t]}\right) \quad (10)$$

ABF includes two significant modifications but maintains the basic structure of a bilateral filter. ABF is first given an offset ζ. Second, the ABF's locally adaptable parameters include both the width and ζ of the range filter.

ABF is a fixed low-pass Gaussian domain filter. *If* =0 and r is fixed, the ABF transforms into a normal bilateral filter (BL). The domain filter of the ABF is a fixed low-pass Gaussian filter. The BL smooths and sharpens when combined with a locally adaptive ζ and σ_r. Let $\Omega_{x_t y_t}$ denote the group of pixels in the window of pixels (2M+1) × (2M+1) cantered at $[x_t, y_t]$.

The initial threshold value is calculated by using the following equation (11) and considering the brightness d_u and dv of pixels e_i and e_j

$$SB = Z \times \sum_{e=0}^{255} \frac{d_u+d_v}{2} \quad (11)$$

where Z stands for the Laplacian second-order differential equation used to isotopically distribute pixels across the blood smear images. The equation (12) is to calculate Z.

$$Z = \frac{\partial^2 Z}{\partial e_i} + \frac{\partial^2 Z}{\partial e_j} \quad (12)$$

The pre-processed image has been blurred, the edges may not have been retained, and the image will look flattened even though the pre-processing is complete and the image is noise-free.

3.2.2. Image Enhancement

(a) CLAHE

CLAHE improves adaptive histogram equalization. The image appears more natural due to the limitation on the amplification of noise in the image, which overcomes the problems possessed by AHE. In addition to producing an optimal equalization, it seems to be an effective algorithm for obtaining a good-quality ultrasound fetal image. It raises the brightness level to a particular range, making it easier to compare various portions of an image. CLAHE works by partitioning the image into many nonoverlapping regions that have almost equal sizes and HE is applied to each one. The CLAHE filter method was primarily created for medical imaging, and it aims to reduce the noise produced by homogeneous areas. When pre-processing digital photos, the procedure can be used to improve the image by removing noise. Rather, than using the complete image, CLAHE works on discrete areas of the image called tiles. CLAHE is an improved form of HE (Histogram Equalization), a quick and efficient technique for enhancing images that can improve the contrast by reducing the grayscale. If colored images are utilized, the input images are greyed out and CLAHE suggests the three channels. The effects of CLAHE processing on images are in Fig. 2.

(b) MSR

The MSR technique is used for pre-processing, which has become more popular in recent years. It is commonly known as MSR for enhancing fetal ultrasound images. Numerous researchers have developed a variety of Retinex-based image enhancement algorithms, including the single-scale Retinex algorithm, multi-scale Retinex algorithm, and multi-scale Retinex algorithm with colour restoration.

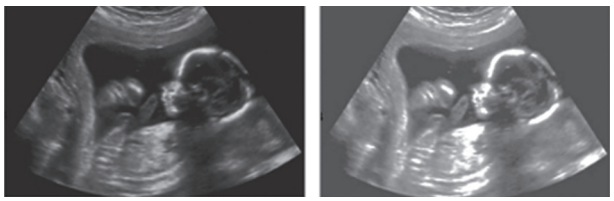

(a) (b)

Fig. 2. (a) Original image, and (b) Image enhanced using CLAHE

Then, averaging and adding the results of the filtering on different scales can maintain the image's high quality, reduce its dynamic range, and achieve colour improvement and consistency. The algorithm of the Multi-Scale Retinex (MSR) is as follow in equation (13) and (14):

$$S(j) = R_v(j).\sum_{m=1}^{M} \omega_m\{log\, Y(j) - log[g(j) \otimes Y(j)]\} \quad (13)$$

$$R_v(j) = \beta\{log[\alpha Y(j)] - log\,[\sum_{j=1}^{n} Y(j)]\} \quad (14)$$

R_v stands for the color parameter of the *v-th* channel, which is used to modify the ratio of the color of the three channels, where $S(j)$ is enhanced output for MSR, $Y(j)$ is the input image, and $g(j)$ is the filter function, β is a gain contrast and α controls the nonlinear strength, $n = 3$ represents the three channels of RGB.

3.3. V-NET

The V-net network framework contains encoders and decoders. V-Net is an advanced neural network designed for efficient image segmentation in medical images. V-Net is useful for complex frameworks and 3D medical images. Additionally, it reduces fading gradients problems enhances training reliability, and enables more modern performance in segmentation than other traditional networks. The encoder comprised numerous phases, each of which had a different resolution. Finally, after a long decompression process, the decoder can provide an output image with the same size as the original image. Additionally, V Net uses Res Net's short-circuit connection method to learn the residual function simultaneously like every phase's input and output. When waiting, the cross-entropy loss function is replaced with the dice reduction rate to increase the susceptibility of the desired segment area. used a V Net network where the encoder part extracted global features of the decoder component and generated a full-resolution result from the source visual. It is suggested that the V net's fundamental structure is for segmenting fetal tissue. The architecture diagram of the V net is shown in Fig. 3.

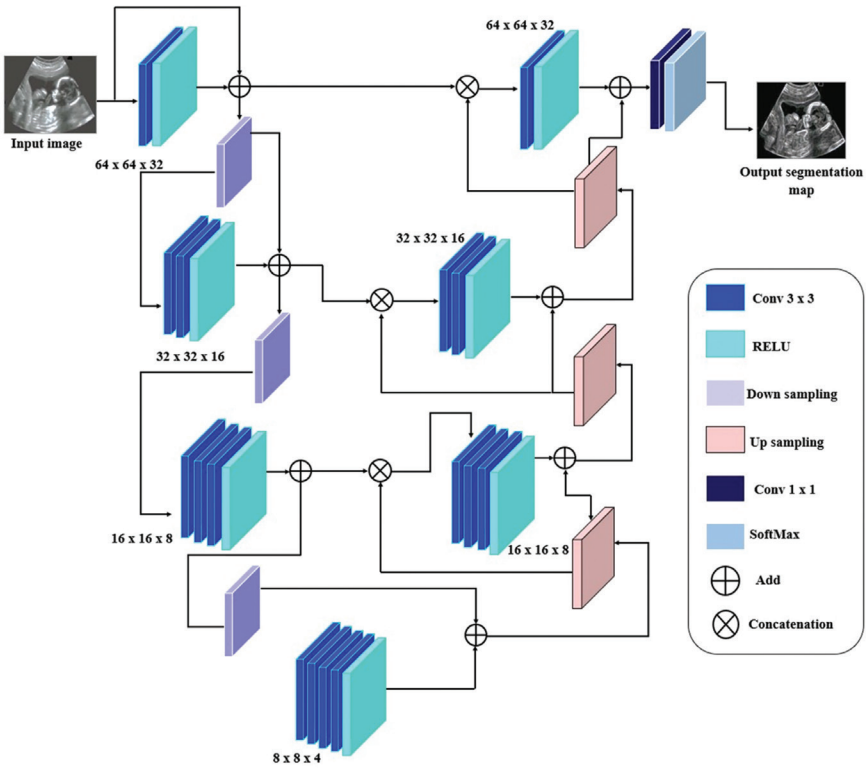

Fig. 3. V-net architecture

Fig. 3 displays the structure of V-Net, which holds the properties of the encoder/decoder structure. The entire network consists of convolutional blocks, non-convolutional blocks, and a final layer of convolutional outputs. Each convolution block consists of 32 convolution kernels, 32 regularization functions, and 32 ReLU activation functions.

These convolution blocks extract features using the convolution kernel's 4, 8, 16, 32, and 64 channels while reaching phase 1. Compression is employed to reduce the quantity of memory needed during training by replacing the pooling process in the down-sampled phase with a kernel of convolution and a variable duration overlap.

The size of the output feature map matches the input and is determined by a remnant pooling engine that includes pooling layers, convolution layers, and remnant structures. Then a suitable stage is inserted, followed by the data supplied for the following level. To create a photo with the exact size as the data input, the last layer of convolution applies an efficient convolution base. It is a widely used loss function in the field of medical image segmentation and is perfect for balancing backdrop and background information.

4. RESULT AND DISCUSSION

In this section, the efficiency of the Proposed Foe-Net is estimated using Matlab-2019b. This work was evaluated and compared with a database of 100 fetal images from subjects between 6 and 20 weeks of maturation. The database images were collected using a variety of scanning techniques, including the THI

Siemens machine, the Wipro GE Logic 400, the Toshiba color Doppler tests, and others. There are 100 images gathered from different ultrasound institutions in the Kanyakumari District of Tamil Nadu, India. This dataset consisted of 80% training images, 10% testing images, and 10% validation images. The performance of the Proposed Foe-Net is estimated through the validation of denoising metrics like MSE, SNR, SSIM, and PSNR of standard processing metrics. The competence of the proposed Foe-Net is assessed by the SSIM, PSNR, and MSE. The PSNR is a frequently used metric to determine the image quality and SSIM is utilized to measure the similarity value between the ground truth and the produced output of the proposed network. There is a comprehensive comparison between the reference and altered images. MSE is a measure of the error ratio between the original and inpainted images. MSE values are used to evaluate the effectiveness of a model with a lower error rate considered more effective. The evaluation of the parameters is given below,

Data analysis results show the effectiveness of this method using maximum PSNR and SSIM in equation (15).

$$PSNR = 10.log_{10}(\frac{MAX_I^2}{MSE}) \quad (15)$$

The ratio of signal power to background noise is called the SNR. It is explained in equation (16).

$$SNR = \frac{D_s}{\hat{\sigma}_m} \quad (16)$$

Where DS is the estimated image signal density and $\hat{\sigma}_m$ is the estimated image noise standard deviation.

Mean Squared Error (MSE) is a measure of the total squared error between the denoised image and the raw image. It is calculated in equation (17):

$$MSE = \sum_{U,V} \frac{[m_1(u,v)-m_2(u,v)]^2}{U*V} \quad (17)$$

where the dimensions of the image are U and V and m_1 (u, v) is the original image. m_2 (u, v) is an approximate version of the filtered image.

The SSIM measures the structural similarity between the original and denoised images. It's described as equation (18):

$$SSIM\ (y,z) = \frac{(2\mu_y\mu_z+a_1)(\sigma_{yz}+a_2)}{(\mu_y^2+\mu_z^2+a_1)(\sigma_y^2+\sigma_z^2+a_2)} \quad (18)$$

where, μy and μz the average values and, σy and σz are the image's standard deviations.

The dice index (DI) uses both a reproducibility validation metric and an index of spatial overlap of the fetal images. DI is calculated to determine the exact ratio of the true region (fetal) to pixels. The predicted fetal pixels and background pixels are calculated in equation (19). Jaccard index (JI) measures the similarity between two finite samples by dividing intersection sizes by union sizes. JI is determined which measures the similarity between actual fetal pixels and predicted fetal pixels.

$$DI = \frac{2T_{pos}}{F_{pos}+2T_{pos}+F_{neg}} \quad (19)$$

$$JI = \frac{T_{pos}}{T_{pos}+F_{neg}+F_{pos}} \quad (20)$$

Where T_{pos} and T_{neg} means true positives and negatives of the sample images, F_{pos} and F_{neg} specifies false positives and negatives of the sample images. The performance analyzed by these metrics is shown in Table.1.

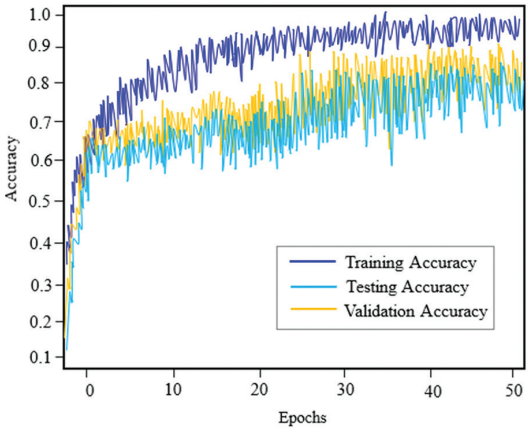

Fig 4. Training and testing accuracy of the proposed method

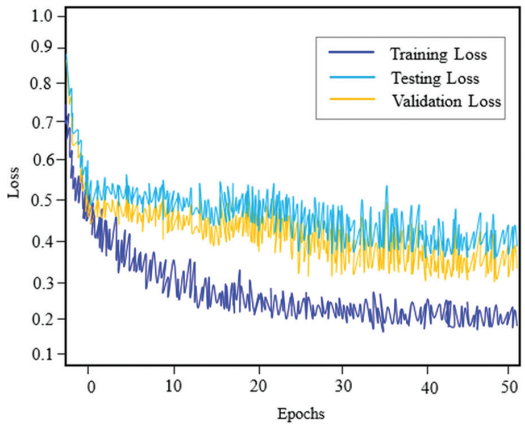

Fig 5. Training and testing loss of proposed method

Figs. 4 and 5 show the results of 100 completed training epochs that were used to test the accuracy and loss of the model. Additionally, the test dataset utilized for each of these techniques was filled with images that were collected from the dataset. Epochs and accuracy for the suggested strategy are correlated in Fig. 4. It is evident that when the epoch value is raised, the model's performance improves. The epochs and loss curves in Fig. 5 show that the model loss will decrease as the number of epochs increases. Therefore, the proposed model was highly reliable for the accurate prediction of fetal in ultrasound images.

The denoised output of the pre-processing filters is shown in Fig. 6

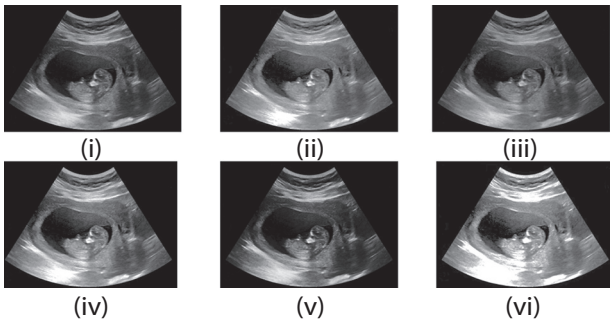

Fig. 6. Denoised output of the pre-processing filters: (i) Original image, (ii) Median filter, (iii) gaussian filter, (iv) bilateral filter, (v) wiener filter, and (vi) Proposed AGF and ABF filters

Fig. 6 expresses the denoised images produced by the pre-processing filters. The fetal input image from the acquired dataset is displayed in section (i). The median filter classified image is shown in section (ii), the Gaussian filter noise reduction images are shown in portion (iii), the bilateral filter pre-processed image is shown in section (iv), the wiener filter enhanced image is shown in portion (v), and the proposed AGF and ABF filter image is demonstrated in portion (vi).

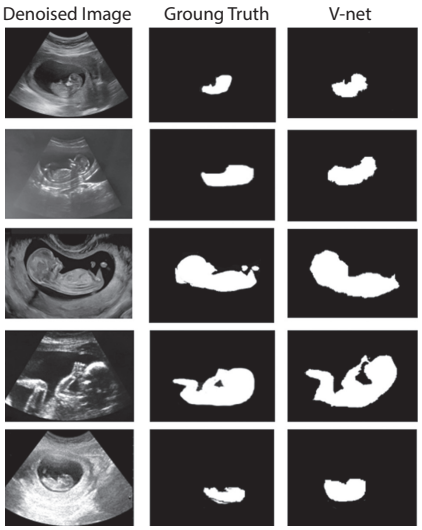

Fig. 7. The experimental segmented results of the proposed model

Fig. 7 shows the results of the proposed Foe-Net obtained from the dataset. Denoising the input fetal images using AGF and ABF filters followed by CLAHE and MSR filters are applied to enhance the quality of images as depicted in column 1. The segmented ground truth images are shown in column 2. Then, the V-net approach for segmenting the input images in column 3. The segmentation result reveals (Fig. 7) that the V-net performs faster and attains the best results based on the Jaccard index and dice index.

Table 1. Performance evaluation of the proposed method using denoising metrics

AUTHOR	METHODS	ACCURACY
Sobhaninia et al. [11]	Link-Net	88.96%
Ashkani Chenarlogh et al. [13]	U-Net	97.62%
Cengiz et al. [1]	FUSQA	90%
Proposed method	Foe-Net	99.48%

Table 1 shows the performance analysis of different image de-noising techniques such as median filter, gaussian filter, and bilateral filter. The proposed Foe-Net achieves MSE values of 0.28, 0.36, and 0.26 for noise rates of 1%, 3% and 5%, respectively. The proposed Foe-Net achieves SSIM values of 0.65, 0.66, and 0.58 for signal-to-noise ratios of 1%, 3%, and 5%, respectively. The proposed Foe-Net achieves SNR values of 32.53, 28.17, and 32.14 at signal-to-noise ratios of 1%, 3%, and 5%, respectively. Then the proposed Foe-Net obtains PSNR values of 68.52, 73.52, and 73.48 for noise rates of 1%, 3%, and 5%, respectively. From the analysis, the proposed Foe-Net gives the minimum MSE, PSNR, SNR, and SSIM compared to other denoising techniques.

4.2. COMPARATIVE ANALYSIS

The comparative analysis section analyzes the performance of existing and proposed models. Table 2 shows the comparison of existing deep learning networks and the proposed Foe-Net for segmenting the fetal in ultrasound images. The accuracy achieved by the proposed Foe-Net is 99.48%, which is better than the accuracy of existing deep learning networks. The proposed method performance is compared with the different deep learning networks such as Ghost Net, AlexNet, and U-net.

Table 2. Comparison of different deep learning networks

Networks	Accuracy	Specificity	Precision	Jaccard index	Dice index
Ghost Net [21]	95.48	94.34	93.26	94.32	81.74
Alex Net [22]	96.32	95.59	94.27	90.48	80.53
U-net [23]	98.46	96.18	95.08	89.51	78.73
V-net	99.48	98.56	96.82	96.67	85.82

From Table 2., the comparison was made between various segmentation algorithms in terms of the performance metrics. The segmentation performance is evaluated in terms of the accuracy, precision, specificity, recall, f1 score, dice score, and Jaccard index as shown in table.2. The V-net increases the overall Jaccard index by 2.43%, 6.84%, and 7.40% better than Ghost Net [21], Alex Net [22], and U-net [23] respectively. The V-net increases the overall Dice index by 4.75%, 6.16%, and 8.26% better than Ghost Net [21], Alex Net [22], and U-net [23] respectively. However, the classic segmentation networks did not perform well compared to the V-net.

Table 3. The comparison between the proposed Foe-Net and state-of-the-art models

Noise Ratio	Performance Metrics	De-noising techniques			
		Median filter [18]	Gaussian filter [19]	Bilateral filter [20]	Proposed
1%	PSNR	43.25	38.16	54.24	68.52
	MSE	0.72	0.56	0.43	0.28
	SSIM	0.26	0.43	0.56	0.65
	SNR	11.04	19.54	24.68	32.53
3%	PSNR	50.64	56.25	64.28	73.52
	MSE	0.86	0.63	0.59	0.36
	SSIM	0.46	0.57	0.64	0.66
	SNR	14.3	20.62	25.06	28.17
5%	PSNR	49.42	58.79	67.81	73.48
	MSE	0.68	0.45	0.38	0.26
	SSIM	0.24	0.34	0.43	0.58
	SNR	24.7	28.61	30.5	32.14

Table 3 demonstrates how our novel network works better than the earlier methods. Several metrics are used to compare existing models with high classification accuracy. In comparison to Link-Net, U-Net, and FUSQA the Proposed Foe-Net increases overall accuracy by 10.5%, 1.90%, and 9.52%, respectively. The proposed Foe-Net results are therefore particularly trustworthy for glaucoma identification.

5. CONCLUSION

This paper proposed a novel Foe-Net for segmenting the fetal in ultrasound images. Initially, the input US images are noise removal phase using two different filters AGF and ABF, to reduce the noise artifacts. Then, the US images are enhanced using CLAHE and MSR for smoothing to enhance the quality of the image. The efficiency of the proposed Foe-Net was evaluated through the validation of denoising metrics like MSE, SNR, SSIM, and PSNR. The proposed Foe-Net gives an overall accuracy of 99.48% achieved for segmented fetal in ultrasound images. In comparison to Link-Net, U-Net, and FUSQA the Proposed Foe-Net increases overall accuracy by 10.5%, 1.90%, and 9.52%, respectively. The proposed Foe-Net achieves MSE values of 0.28, 0.36, and 0.26 for noise rates of 1%, 3% and 5%, respectively. The experimental outcomes show the PSNR, MSE, SNR, and SSIM of the proposed method which is significant compared to other techniques. In future research, the network performance will be examined using greater data sets directly from several fetal individuals. In addition, we'll look for and categorize structural deviations in the fetal heart.

6. ACKNOWLEDGMENT

The author would like to express his heartfelt gratitude to the supervisor for his guidance and unwavering support during this research for his guidance and support.

7. REFERENCES:

[1] K. Niha, S. Amutha, B. Surendiran, "Deep Learning Techniques for Foetal and Infant Data Processing in a Medical Context", Healthcare Industry, Vol. 4, 2023, pp. 19-50.

[2] A. Jegatheesh, N. Kopperundevi, M. A. Sahaya Infant Tinu, "Brain aneurysm detection via firefly optimized spiking neural network", International Journal of Current Bio-Medical Engineering, Vol. 01, No. 01, 2023, pp. 23-29.

[3] R. Ren, Z. Guo, Z. Jia, J. Yang, N. K. Kasabov, C. Li, "Speckle noise removal in image-based detection of refractive index changes in porous silicon microarrays", Scientific Reports, Vol. 9, No. 1, 2019, p. 15001.

[4] A. Nithya, A. Appathurai, N. Venkatadri, D. R. Ramji, C. A. Palagan, "Kidney disease detection and segmentation using artificial neural network and multikernel k-means clustering for ultrasound images", Measurement, Vol. 149, No. 106952, 2020, p. 40.

[5] E. Fenil, G. Manogaran, G. N. Vivekananda, T. Thanjaivadivel, S. Jeeva, "Real time violence detection framework for football stadium comprising of big data analysis and deep learning through bidirectional LSTM", Computer Networks, Vol. 151, 2019, pp. 191-200.

[6] P. G. Sreelekshmi, P. L. Babu, P. J. Shermila, "Leukemia classification using a fusion of transfer learning and support vector machine", International Journal of Current Bio-Medical Engineering, Vol. 1, No. 1, 2023, pp. 1-8.

[7] Dakshina, D. R. Valiaveetil, A. Bindhu, "Alzheimer disease detection via deep learning-based shuffle network", International Journal of Current Bio-Medical Engineering, Vol. 1, No. 1, 2023, pp. 9-15.

[8] A. Saood, I. Hatem, "COVID-19 lung CT image segmentation using deep learning methods: U-Net versus SegNet", BMC Medical Imaging, Vol. 21, No. 1, 2021, pp. 1-10.

[9] K. Rasheed, F. Junejo, A. Malik, M. Saqib, "Automated fetal head classification and segmentation using ultrasound video", IEEE Access, Vol. 9, 2021, pp. 160249-160267.

[10] M. Amiri, R. Brooks, H. Rivaz, "Fine-tuning U-Net for ultrasound image segmentation: different layers, different outcomes", IEEE Transactions on Ultrasonics, Ferroelectrics, and Frequency Control, Vol. 67, No. 12, 2020, pp. 2510-2518.

[11] Z. Sobhaninia, S. Rafiei, A. Emami, N. Karimi, K. Najarian, S. Samavi, S. R. Soroushmehr, "Fetal ultrasound image segmentation for measuring biometric parameters using multi-task deep learning", Proceedings of the 41st Annual International Conference of the IEEE Engineering in Medicine and Biology Society, Berlin, Germany, 23-27 July 2019, pp. 6545-6548.

[12] D. Qiao, F. Zulkernine, "Dilated squeeze-and-excitation U-Net for fetal ultrasound image segmentation", Proceedings of the IEEE Conference on Computational Intelligence in Bioinformatics and Computational Biology, Via del Mar, Chile, 27-29 October 2020, pp. 1-7.

[13] V. A. Chenarlogh, M. G. Oghli, A. Shabanzadeh, N. Sirjani, A. Akhavan, I. Shiri, H. Arabi, M. S. Taheri, M. K. Tarzamni, "Fast and accurate U-net model for fetal ultrasound image segmentation", Ultrasonic Imaging, Vol. 44, No. 1, 2022, pp. 25-38.

[14] V. Singh, P. Sridar, J. Kim, R. Nanan, N. Poornima, S. Priya, G. S. Reddy, S. Chandrasekaran R. Krishnakumar, "Semantic segmentation of cerebellum in 2D fetal ultrasound brain images using convolutional neural networks", IEEE Access, Vol. 9, 2021, pp. 85864-85873.

[15] S. Cengiz, I. Almakk, M. Yaqub, "FUSQA: Fetal Ultrasound Segmentation Quality Assessment", arXiv:2303.04418, 2023.

[16] S. Cammarasana, P. Nicolardi, G. Patanè, "Real-time denoising of ultrasound images based on deep learning", Medical & Biological Engineering & Computing, Vol. 60, No. 8, 2022, pp. 2229-2244.

[17] G. Dong, Y. Ma, A. Basu, "Feature-guided CNN for denoising images from portable ultrasound devices", IEEE Access, Vol. 9, 2021, pp. 28272-28281.

[18] G. Yang, W. Feng, J. Jin, Q. Lei, X. Li, G. Gui, W. Wang, "Face mask recognition system with YOLOV5 based on image recognition", Proceedings of the IEEE 6th International Conference on Computer and Communications, Chengdu, China, 11-14 December 2020, pp. 1398-1404.

[19] K. M. Jaeger, M. Nissen, R. Richer, S. Rahm, A. Titzmann, P. A. Fasching, B. M. Eskofier, H. Leutheuser, "Machine Learning-based Detection of In-Utero Fetal Presentation from Non-Invasive Fetal ECG", Proceedings of the IEEE-EMBS International Conference on Biomedical and Health Informatics, Ioannina, Greece, 27-30 September 2022, pp. 1-4.

[20] M. Elhoseny, K. Shankar, "Optimal bilateral filter and convolutional neural network based denoising method of medical image measurements", Measurement, Vol. 143, 2019, pp. 125-135.

[21] I.A. Kazerouni, G. Dooly, D. Toal, "Ghost-UNet: an asymmetric encoder-decoder architecture for semantic segmentation from scratch", IEEE Access, Vol. 9, 2021, pp. 97457-97465.

[22] S. Lu, Z. Lu, Y. D. Zhang, "Pathological brain detection based on AlexNet and transfer learning", Journal of computational science, Vol. 30, 2019, pp. 41-47.

[23] X. X. Yin, L. Sun, Y. Fu, R. Lu, Y. Zhang, "U-Net-Based medical image segmentation", Journal of Healthcare Engineering, Vol. 2022, 2022.

Significance of handcrafted features in human activity recognition with attention-based RNN models

Original Scientific Paper

Sonia Abraham
Department of Computer Science, Cochin University of Science and Technology,
Kochi, India
sonianidhi@gmail.com

Rekha K James
Division of Electronics, School of Engineering, Cochin University of Science and Technology,
Kochi, India.
rekhajames@cusat.ac.in

Abstract *– Sensors incorporated in devices are a source of temporal data that can be interpreted to learn the context of a user. The smartphone accelerometer sensor generates data streams that form distinct patterns in response to user activities. The human context can be predicted using deep learning models built from raw sensor data or features retrieved from raw data. This study analyzes data streams from the UCI-HAR public dataset for activity recognition to determine 31 handcrafted features in the temporal and frequency domain. Various stacked and combination RNN models, trained with attention mechanisms, are designed to work with computed features. Attention gave the models a good fit. When trained with all features, the two-stacked GRU model performed best with 99% accuracy. Selecting the most promising features helps reduce training time without compromising accuracy. The ranking supplied by the permutation feature importance measure and Shapley values are utilized to identify the best features from the highly correlated features. Models trained using optimal features, as determined by the importance measures, had a 96% accuracy rate. Misclassification in attention-based classifiers occurs in the prediction of dynamic activities, such as walking upstairs and walking downstairs, and in sedentary activities, such as sitting and standing, due to the similar range of each activity's axis values. Our research emphasizes the design of streamlined neural network architectures, characterized by fewer layers and a reduced number of neurons when compared to existing models in the field, to design lightweight models to be implemented in resource-constraint gadgets.*

Keywords*: Attention mechanism, deep learning, Gated Recurrent Units*

1. INTRODUCTION

Human activity recognition (HAR) is a widely researched area due to the availability of cutting-edge technologies and miniature devices incorporating various sensors capable of transmitting time-series data forming patterns that help users monitor motion. Of the available sensors, tri-axial accelerometer and gyroscope sensors are commonly used in determining human context. Various activities ranging from simple motion to highly complex activities can be accurately determined from the sensor data.

Studies carried out a decade ago utilized the potential of machine learning classifiers. With the advent of deep learning models, features are automatically extracted from raw sensor data for classifying the activities. The more the number of layers and hidden neurons, the more time for training. Another pitfall is that the data collected from sensors forms a spare matrix as the continuous signal flow is disturbed due to the subtle movement of the sensor, resulting in less well-labeled data and an imbalanced class [1]. Data augmentation techniques help in the formation of synthetic data computed from the available annotated data blocks, which reduces overfitting in models with fewer well-labeled data. Of the experimented data augmentation strategies, the moving average smoothing and exponential smoothing, the latter increased the accuracy of the RNN models considerably when applied to temporal data.

The recurrent neural network variants, Long Short-Term Memory (LSTM) and Gated Recurrent Unit (GRU), exhibit high-performance accuracy for time-series classification problems [2]-[4]. When subtle movements

are to be considered, deep learning networks fail to capture the context information required for generalization from a domain with an unbalanced class distribution, in particular. Simplified and context-based attention is applied to hidden layers in a two-stacked GRU architecture concatenated and applied to fully connected layers to learn weights for features automatically computed from attention. When the layers of these networks are enhanced with an attention mechanism, the accuracy improves with the benefit of reduced model parameters [5].

Later studies extracted temporal and frequency dimension features from time-series data and proved that the deep learning models trained with these features give comparable accuracies. A total of 202 temporal and frequency domain features extracted from raw accelerometer and gyroscope data stream with selected base classifiers recognized human motion in a context-aware scenario employing an incremental learning model [6]. An ensemble model updated through weighted majority voting when run with user and position-independent streaming data generates personalized context recognition applications.

To understand the decision taken by a model in classification, the knowledge of features is required. To learn the impact of each feature on the performance of a supervised learning model, a technique called feature importance ranking is used in deep learning models. The existence of irrelevant features in the input may breach the generalization of a learning system. An optimal subset of features results in better model performance with optimum resources. In this regard, binary and multi-class classification is conducted using features selected based on their correlation diversity from different activities [7]. Pair-wise correlation between temporal features extracted from the raw accelerometer and gyroscope sensors of each activity is determined and extended to compare binary subsets. Classification using top-ranked features gave comparable performance against all with much reduction in data space. The study in [8] correctly separates dynamic activities using bidirectional LSTM architecture, deploying a grid search strategy for the selection of layers and their depth.

This work uses LSTM and GRU models to classify human context using features computed from raw accelerometer sensor data available in UCI-HAR, a public dataset with 6 activities. The contributions of the study include the following:

- The construction of single and two stacked recurrent neural network variants with attention added to the RNN layer before the fully connected layer. The input to the models is 31 temporal and frequency domain statistical features extracted from raw accelerometer sensor data.
- The work delves into feature selection, a critical task to optimize model performance and efficiency.
- The choice of optimal features from the handcrafted features computed from accelerometer sensor data, employing feature importance ranking measures.
- The comparison of the accuracy of models trained with all features and optimal features. The evaluation shows that training the attention-based classifiers with significant features improved model performance.
- GRU models' performance is better than LSTM models considering the accuracy metric.

Following is the structure of the remaining paper: Section 2 describes the related literature in time-series classification using deep learning models. Section 3 gives a detailed explanation of various architecture, attention mechanisms and feature importance measures. Section 4 gives an insight into the proposed method, while experiments and results are discussed in Section 5.

2. RELATED WORKS

An extensive study on various deep learning architectures apropos speed, accuracy and memory is conducted in [9] using accelerometer and gyroscope sensor data to determine human context. The models employed hidden units in the range of 100 to 600 that span across three layers. The article concluded that CNN captures sensor correlations and temporal dependencies efficiently. The model proposed in [10] used two stacked LSTM with 64 neurons connected to two convolution layers with 64 and 128 filters and a global average pooling layer which reduced model parameters to a great extent without compromising recognition rates. The performance effect of filter count, optimizers and batch size are investigated and the final model is trained utilizing the selected optimal hyper-parameters.

According to a multi-input CNN-GRU model introduced in [11], the same input is fed into three heads with convolution layers having various filter sizes, allowing the model to collect feature vectors with local correlations at various scales. Two GRU layers that automatically extract features from the input dataset and categorize activity data are applied after the convolution layers. To distinguish between everyday activities and accidents involving falls, this study [4] used independent GRU models with forward and backward cells that each had 200 hidden units of data gathered from a mobile phone accelerometer sensor.

A hierarchical framework constructed with an SVM classifier on 12 statistical features from time and frequency domain differentiated coarse-level activities as a GRU network input with RSSI data discriminated fine-level similar activities [12]. The RSSI data was acquired from sensors mounted at different locations in two different environments utilizing the sniffer technique, thereby creating a low-cost, device-free HAR system. Accelerometer and angular velocity signal values from

the Shimmer platform are gathered to build low-energy wearable devices for fall and activity recognition [13]. These values are then subjected to a compressed sensing method. Machine learning classifiers are used to extract and analyze 44 temporal characteristics. According to the study, the use of compressed sensing algorithms led to an increase in battery life of 2.55 times the higher duration without sacrificing precision.

Fall and non-fall events are categorized using four recurrent networks, and their performance is analyzed using an embedded device [14]. The advantage of these wearable fall detectors apropos energy consumption is provided in the paper. The findings demonstrate that when implemented in a real-time microcontroller that runs on small batteries, a single RNN is capable of differentiating multi-class falls.

The model proposed in [15] compared a linear and a nonlinear dimension reduction and feature selection technique using LSTM in binary and multiclass classification for monitoring malicious activity in a network. The calculation of the mutual information score helped select those features from among the 53 available features that had the most significant impact in training the model. A novel dimensionality reduction technique that randomly organizes a small number of feature vectors from each class is proposed in [16]. The selection of features is determined based on the Euclidean distance of feature vectors that fall in a specific range. The proposed method chose 11% of features, and the classification techniques resulted in good accuracy and low response time, paving the way to low computational cost.

The LSTM architecture's inception is covered in detail [17], along with a potential fix for the vanishing gradient issue that involves maintaining a constant error flow by controlling internal cell states. The potential of LSTM in overcoming the vanishing gradient problem substantiated by its performance in a handful of domains is portrayed [18]. The review covers in detail the main components of the network, their interaction and the determination of the weight matrix using a gradient-based method. When the input is sparse dataset, a data-driven model like LSTM is utilized to simulate flood flow by analyzing sequential data streams and identifying long-term dependencies [19]. The study in [20] examined whether memristor-based LSTM might be used as a solution to the low speed of these models caused by their parallel structure and sequential behavior.

GRU networks with weighted averaging, which give more weights to the middle range, determine representations using handcrafted features extracted from raw input vectors, thereby minimizing the need for expert-level knowledge in feature design [21]. A real-time model that recognizes complex activities is designed [2] by concatenating multiple convolution kernels with different scaling and max-pooling layers. Four such Inception-like network is connected with two GRU layers, enabling the model to extract sequential temporal dependencies. The classification performance of gated recurrent units in emotion recognition is examined [22] using clean speech data overlay with various environmental noises. According to the research, GRU produced results similar to LSTM while taking 18.6% less time to run. Network intrusions can be effectively identified using a single or bi-directional GRU with 128 hidden units followed by three layers of multilayer perceptron with 48 hidden nodes and softmax regression. According to the study [3] BGRU can do better in related domains. The work in [5] suggests that augmenting convolution models with LSTM moderately improves the performance of time-series datasets. The refinement phase that iterates with change in learning rate and batch size improved model accuracy although with increased computational complexity.

This study applies different RNN variants with attention to time and frequency domain features that are extracted from raw accelerometer sensor data to identify human activity. These features are ranked according to relevance, and the best features are used to train the model.

3. BACKGROUND

Recurrent neural networks (RNN) set themselves apart from other types of neural networks by having a memory structure that uses earlier input data to influence current input and output and finds use in ordinal or temporal problems involving sequential data. The units in each layer share the same weight parameters and leverage the backpropagation algorithm to determine the gradients that appropriately fit the model parameters. This process may result in smaller gradients, which ceases the network's ability to learn by generating insignificant weight parameters through constant updates. Long short-term memory (LSTM) and Gated recurrent units (GRU) mitigate the short-term memory problem of RNN models. Internal gating mechanisms in these variants control information flow, eliminate unnecessary input, and retain what is necessary for accurate prediction.

3.1. LONG SHORT-TERM MEMORY (LSTM)

Long short-term memory (LSTM) networks are well suited for more general sequence learning tasks like activity identification because they can learn from sequences of data through recurrent processing, where the input at the present step influences the output at subsequent time steps. The gates in LSTM regulate the control flow by learning throughout the training procedure what is significant and what can be allowed on the cell state [23]. To learn which data should be retained and which ought to be removed based on relevance, gates integrate sigmoid activations that push values between 0 and 1 rendering them suited for backpropagation [24].

The output of the LSTM is decided by the current long-term memory of the network, the cell state, the prior hidden state, and the input data at the current time step. The forget gate, f_t, determines which part of

the long-term memory should be deleted or retained at this time, given the prior hidden state and the current data point in the sequence.

$$f_t = \sigma\left(W_i[h_{t-1}, x_t] + b_f\right) \quad (1)$$

Given the previous hidden state and the new input data, the new memory network and input gate, i_t, decide what new information should be added to the network's long-term memory. The tanh-activated neural network, which squishes values between -1 and 1, creates a vector that indicates how much to update each component of the cell state given the new data.

$$i_t = \sigma\left(W_i\left[h_{t-1}, x_t\right] + b_i\right) \quad (2)$$

$$\check{c} = \tanh\left(W_c\left[h_{t-1}, x_t\right] + b_c\right) \quad (3)$$

The output from the input gate is used to update the cell state, c_t, to new values that the neural network deems appropriate.

$$c_t = f_t * c_{t-1} + i_t * \check{c}_t \quad (4)$$

The output gate, o_t, which is applied to the newly updated cell state, is a filter that accepts the same input as the forget gate along with a sigmoid activation to ensure that only necessary information is output. Hence, the output gate determines the next hidden state, which aids in prediction.

$$o_t = \sigma\left(W_i\left[h_{t-1}, x_t\right] + b_o\right) \quad (5)$$

$$h_t = o_t * \tanh(c_t) \quad (6)$$

where W_x, gate(x) neuron weights, h_{t-1}, the output of prior block, x_t, input at current time step, b_x, gate(x) biases, c_t, cell state at time step(t) and $\check{c}$, candidate for cell state at time step (t). The following time step is subsequently updated with the new hidden state and cell states.

3.2. GATED RECURRENT UNITS (GRU)

A gated recurrent unit (GRU) is designed similarly to LSTM and, for the most part, yields results that are just as good. Two vectors - update and reset gates – decide information transfer and the model trains relatively quickly with fewer parameters.

The update gate, z_t, assists the model in determining how much of the past information should be transmitted into the future, thereby eliminating the possibility of the vanishing gradient problem.

$$z_t = \sigma\left(W^{(z)} x_t + U^{(z)} h_{t-1}\right) \quad (7)$$

The model uses the reset gate, r_t, to decide how much of the past information to forget.

$$r_t = \sigma\left(W^{(r)} x_t + U^{(r)} h_{t-1}\right) \quad (8)$$

The candidate activation, $\hat{h}_t$, which uses the reset gate to store the apposite information from the past is computed.

$$\hat{\mathrm{h}}_t = \tanh(W x_t + r_t \odot U h_{t-1}) \quad (9)$$

Finally, the activation at time t, which contains the information for the current unit is determined and transmitted to the network.

$$h_t = z_t \odot h_{t-1} + (1 - z_t) \odot \hat{\mathrm{h}}_t \quad (10)$$

where h_{t-1}, the output of the prior vector, x_t, the input vector, h_t, the output vector, W and U, weight matrices and $\odot$, the Hadamard product.

3.3. ATTENTION MECHANISM FOR ACTIVITY RECOGNITION

The attention mechanism enhances the accuracy of time series classification models by emphasizing the more pertinent temporal features produced by recurrent neural networks through a weighted combination of all hidden state vectors to focus the models's attention on the most significant part of the input sequence. The hierarchical context-based attention mechanism employs an adaptive focusing technique to produce a context vector capable of utilizing a hierarchy of time-dependent features in the sensor data.

Alignment scores, weights, and the context vector are computed iteratively as part of the attention process. The alignment score, e_{ij}, computed using hidden state, h_j, and previous output, s_{i-1}, indicates how closely the parts of the input sequence match with the current output.

$$e_{ij} = a\left(s_{i-1}, h_j\right) \quad (11)$$

where a(.) represents the alignment model of a feedforward neural network.

A softmax function is applied to the previously computed alignment scores to determine the weights.

$$\alpha_{ij} = \frac{e^{(e_{ij})}}{\sum_{k=1}^{T_x} e^{(e_{ik})}} \quad (12)$$

The weighted sum of the hidden states then decides the context vector, c.

$$c_i = \sum_{j=1}^{T_x} \alpha_{ij} h_j \quad (13)$$

Incorporating attention to the layer before the dense layer in a single RNN and on layers of a stacked network improves accuracy, reduces the computational cost and helps to learn the decision process.

3.4. FEATURE IMPORTANCE

3.4.1. CORRELATION AMONG FEATURES:

Algorithms for predictive modeling need data adequately representational of the target domain. Identifying and extracting discriminating features helps construct a model that not only performs effectively but also lessen the likelihood that decisions will be based on outliers. The selection of appropriate features can be determined statistically using correlation analysis techniques like Pearson product-moment correlation and Spearman rank-order correlation.

Pearson's correlation coefficient concisely summarises the relationship between two data points. It is calculated by dividing the covariance of the two points by the product of their respective standard deviation. For a given feature variable, x, and target variable, y, the Pearson coefficient, ρ_{xy}, is defined as:

$$\rho_{xy} = \frac{\sum_{i=1}^{n}(x-\bar{x})(y-\bar{y})}{\sqrt{\sum_{i=1}^{n}(x-\bar{x})^2}\sqrt{\sum_{i=1}^{n}(y-\bar{y})^2}} \quad (14)$$

where $\bar{x} = \frac{\sum_{i=1}^{n} x_i}{n}$, $\bar{y} = \frac{\sum_{i=1}^{n} y_i}{n}$

Spearman's correlation coefficient is a good measure when the nature of the distribution and relationship between the data points remain unclear. For the given variables, the Spearman correlation, σ_{xy}, is calculated as:

$$\sigma_{xy} = 1 - \frac{6\sum_{i=1}^{n} d_i^2}{n(n^2-1)} \quad \textbf{(15)}$$

where d_i is the difference between the ranks of the data points. Fast Fourier Transform's first and third components are most correlated from among the 31 features calculated on the UCI-HAR dataset, with correlation values of -0.803 and 0.622 respectively, Fig. 1.

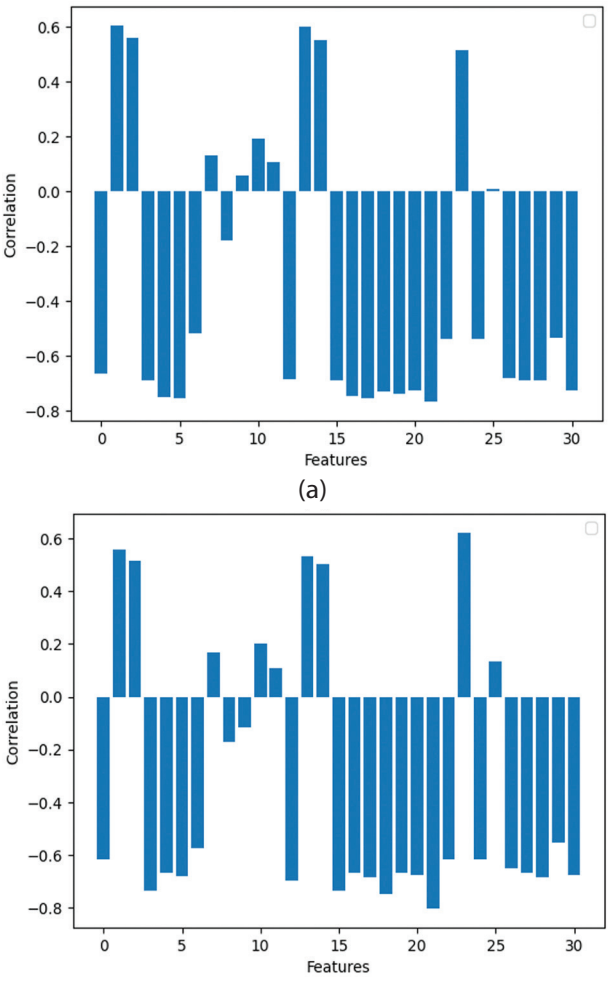

Fig. 1. Correlation between feature and target data points in UCI-HAR dataset (a) Pearson Correlation (b) Spearman's rank

3.4.2. Permutation Feature Importance:

Permutation feature importance inspects the estimator by randomly shuffling one feature and the feature's importance is determined by calculating the model's prediction error. Suppose the model error increased after permuting the feature, in that case, it indicates that the feature contributed to prediction and if the error did not increase, it implies that the feature is not significant.

Compute the score, $s_{n,j}$, of a fitted predictive model, m, on a feature matrix, F, using a scoring argument that accepts multiple scores (like RMSE) for each iteration n from 1 to N and for each feature, f_j, permuted randomly.

The computation of importance, i_j, for a given feature, f_j, is defined as:

$$i_j = s - \frac{1}{N}\sum_{n=1}^{N} s_{n,j} \quad (16)$$

Feature importance gives a reasonable interpretation of how the model will behave, provided the original prediction is accurate. It requires that features be uncorrelated since highly correlated features reduce the importance of the feature in question by spreading the importance between both features.

3.4.3 Shapley Values

The contribution of a feature in a prediction is given by the Shapley value, which evaluates the relevance of a feature by including and excluding it in the prediction. More precisely, understanding how the model behaves for every potential combination of features is necessary to calculate Shapley values. The Shapley value, $\emptyset_i(v)$, for a given feature is calculated as:

$$\emptyset_i(v) = \frac{1}{|N|!}\sum_R [v(P_i^R \cup \{i\}) - v(P_i^R)] \quad (17)$$

where R, is the permutation order of features, $v(P \cup \{i\})$, is the contribution of features to the outcome including the ith feature and $v(P)$, is the contribution of features on the outcome excluding the ith feature. This calculates each feature's average contribution by adding the marginal contribution of an individual feature to the result of all possible permutations of the order of the features.

4. PROPOSED METHOD

The study predicts human context using data acquired from smartphone accelerometer sensors. The raw signals are analyzed to extract several temporal and frequency domain features, which are then applied to deep learning models with an attention mechanism added to the layers before the dense layer. The model interpretability is studied using the permutation feature importance and shapely values.

4.1 DATASET DESCRIPTION

The public dataset, Smartphone-based Recognition of Human Activities and Postural Transitions Data Set (UCI-HAR https://archive.ics.uci.edu/dataset/240) [25], is used to evaluate the recurrent neural network variants.

Tri-axial accelerometer and gyroscope data from 30 users between the ages of 19 and 48 were collected at a constant rate of 50 Hz for the samples in a semi-controlled environment. The signal data is available for 6 activities, three sedentary activities (*Sitting, Standing, and Lying*), three dynamic activities (*Walking, Walk Upstairs and Walk Downstairs*) and postural transitions.

The dataset contains an equal proportion of representative samples from all activities.

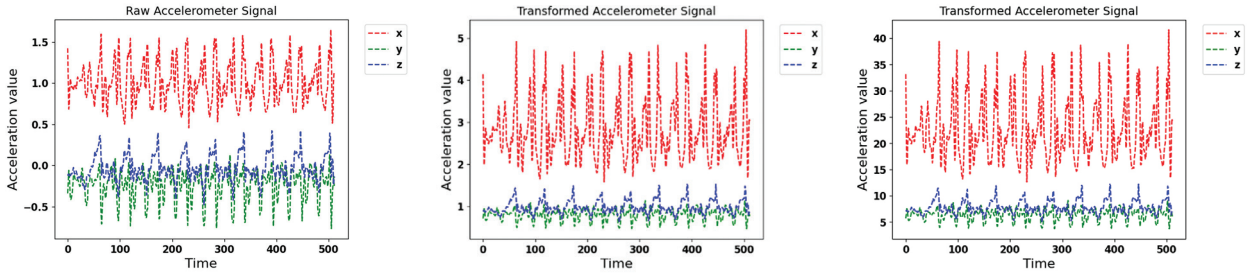

(a) (b) (c)

Fig. 2. Accelerometer Signal Transformation (a) Raw signal (b) e^x of axis values (c) Fibonacci (e^x) for n=4

4.2. DATA PREPROCESSING

The accelerometer sensor data is considered a three-dimensional vector, $A_i=(a_{x_i}, a_{y_i}, a_{z_i}) \in R^3$, where A_i represents the ith signal data. The raw signal data is smoothened using a simple exponential window function.

$$A_k = \alpha A_k + (1-\alpha) A_{k-1} \text{ where } \alpha=0.001$$

The continuous stream data is divided into blocks of 128 sample points, called an example. The raw values are transformed to a larger range by first computing the exponent of each axis value, $y=e^x$, and then by generating the Fibonacci series with the initial value obtained from the earlier step for $n = 4$. The transformations are applied in succession to separate linearly inseparable values; see Fig. 2. 31 temporal and frequency domain features are computed from a 50% overlapped window. The complete feature list is given in Table 1. The standard deviation indicates how far the signal deviates from its mean value. Skewness quantifies the dispersion of a signal around the mean value and is computed as the ratio of average deviation from the mean cubed by the standard deviation cubed. The availability of peaks in a normal distribution is measured by kurtosis. It is the fourth central moment divided by the square of the variance.

Table.1. Temporal and frequency domain feature list

No	Feature
1 – 3	Mean along each axes
4 – 6	Standard Deviation along each axes
7 – 9	Skewness of the component signal
10 – 12	Kurtosis of the component signal
13 – 15	Root Mean Square of ith acceleration vector
16 - 18	Mean Absolute Deviation
19 – 21	Range of each axes
22 – 25	Fast Fourier Transformation components of block
26	Mean of magnitude vector
27	Standard deviation of magnitude vector
28	RMS of Standard Deviation along each axes
29	Standard Deviation magnitude in the horizontal plane
30	RMS of axes data in the horizontal plane
31	Maximum peak-to-peak acceleration amplitude

Root Mean Square (RMS) determines the signal amplitude and energy in the time domain.

$$RMS(\vec{a}[k]) = \sqrt{a_x^2[k] + a_y^2[k] + a_z^2[k]} \quad (18)$$

The mean absolute deviation is the average distance between each data point, a_{k_i}, and the mean, μ.

$$MAD = \sum \frac{(a_{ki}-\mu)}{N}; k \in (x, y, z) \quad (19)$$

The range is calculated as the difference between maximum and minimum axes value. Fast Fourier Transform is applied to blocks to determine the amplitude spectrum. The standard deviation of the magnitude vector is determined as

$$M(\vec{a}[k]) = \sqrt{\sigma_x^2[k] + \sigma_y^2[k] + \sigma_z^2[k]} \quad (20)$$
$$\text{with } \sigma_i = std(\vec{a}[k])$$

The standard deviation of the horizontal plane and RMS of axes data in the horizontal plane is computed with data points in the x, a_{k_x}, and z, a_{k_z}, axes.

$$SD_{hor}(\vec{a}[k]) = \sqrt{\sigma_x^2[k] + \sigma_z^2[k]} \quad (21)$$

$$RMS_{hor}(\vec{a}[k]) = \sqrt{a_x^2[k] + a_z^2[k]} \quad (22)$$

Maximum peak-to-peak acceleration amplitude gives the maximum positive or negative signal deviation from its reference level.

$$P_k - P_k = RMS\,(\max(\vec{a}[k]) - \min(\vec{a}[k])) \quad (23)$$

4.3. LSTM AND GRU NETWORKS:

The study uses single and two-layer stacked LSTM and GRU architectures as well as LSTM-GRU combination networks with attention applied to the hidden state output of the layer immediately preceding the dense layer. The proposed model is depicted in Fig. 3.

Single-stacked models used 64 hidden neurons in the LSTM or GRU layer and a fully connected dense layer with 32 neurons. A dropout of 50% is applied after the first layer to aid with the de-correlation of weights

by selectively eliminating neurons, thus forming a better representation of input data.

The rectified linear activation unit (ReLU) that works on a simple calculation that drops the value to 0 for non-positive inputs is employed as the activation function in layers. The final fully connected output layer is applied with a softmax activation to classify human activities. The two stacked variants and the combination models used 64 neurons each in their architecture layers, followed by a dense layer with 32 neurons. The stacked variant model is given in Fig. 4.

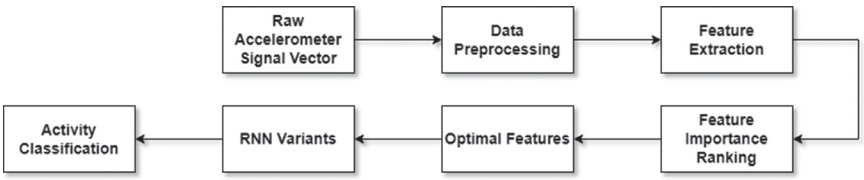

Fig. 3. Proposed Architecture

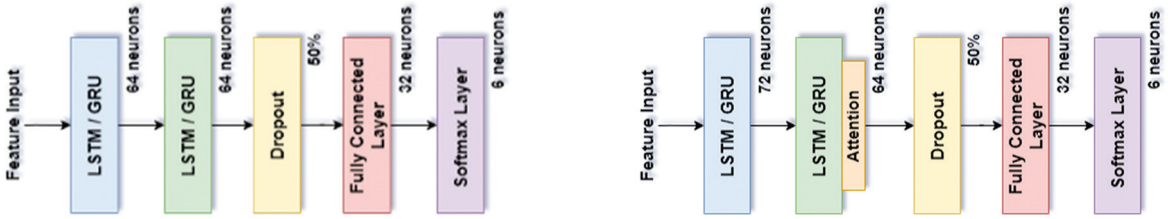

Fig. 4. Two stacked layers model architecture (a) without attention (b) with attention

For LSTM and GRU stacked models, a dropout of 50% is introduced after the stacked layers. However, for the combination model, a dropout of 50% is added to the first layer and 20% to the second layer. All layers except the final fully connected layer used the ReLU activation function. The architecture diagram of the LSTM-GRU combination model is given in Fig. 5.

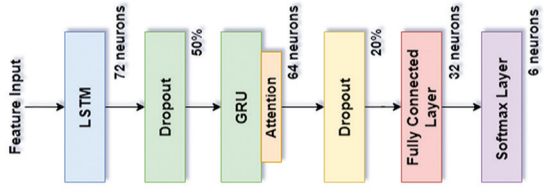

Fig. 5. LSTM-GRU Combination model architecture

In every architecture, an attention mechanism is added to the layer just preceding the dense layer. When computing the weights for single stacked models, the attention mechanism uses the only RNN layer available. For stacked and combination models, weights are computed with the second RNN layer preceding the fully connected layer. All models gave better fit when trained with Adam optimizer and a batch size of 32. The models converged at epochs in the range of 25 to 40 when the early stopping regularization technique was implemented. Validation loss is the monitoring metric to terminate the training based on validation performance. The learning rate is the hyperparameter that determines how much of the model should be changed each time the weights are updated with the estimated error. Single-stacked models performed better by setting the learning rate to 0.0025, while stacked models worked with a value of 0.001.

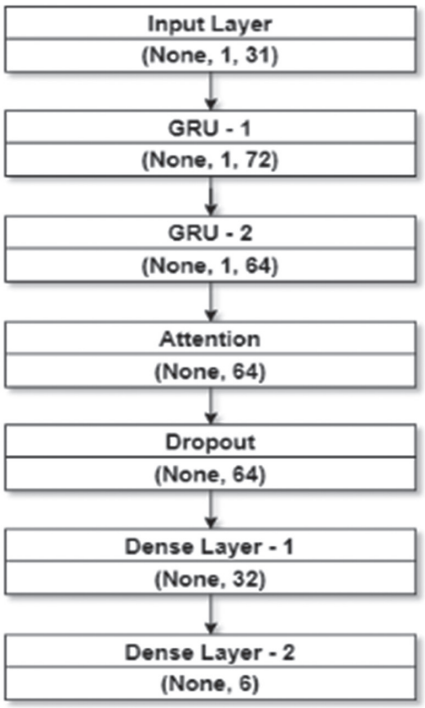

Fig. 6. Network architecture diagram of the two stacked GRU model

The input sequence to the network in Fig. 6 is the features vector computed from each example of the transformed accelerometer signal. The GRU layers process the sequential data and capture temporal dependencies. The attention mechanism added to the second GRU layer focuses on specific elements of the sequence. The dense layers process the output from the GRU layers and classify the activities.

5. EXPERIMENTS AND RESULTS

The proposed models in the activity recognition domain are evaluated using the UCI-HAR public dataset. The metrics used in evaluating the model classification performance are accuracy, the ratio of correct predictions to total predictions; precision, a measure of the accuracy of positive predictions; recall, a measure of the completeness of positive predictions and F1-score, the harmonic mean of precision and recall.

$$Accuracy = \frac{TP+TN}{TP+FN+TN+FP} \quad (24)$$

$$Precision = \frac{TP}{TP+FP} \quad (25)$$

$$Recall = \frac{TP}{TP+FN} \quad (26)$$

$$F1-score = \frac{2 \times Precision \times Recall}{Precision+Recall} \quad (27)$$

5.1. EVALUATION OF MODELS USING ALL COMPUTED FEATURES

The two stacked GRU architectures exhibited the highest accuracy of 99% when the model is trained with attention, compared to 98% when the attention mechanism is not used. Table 2 compares the recognition rate for models with and without attention when trained with all 31 features extracted from the raw accelerometer signal.

Table. 2. Recognition rate of classifiers in the UCI-HAR dataset

Model Architecture	Performance (Accuracy)	
	Model without Attention	Model with attention
Single Layer LSTM	0.85	0.89
Single Layer GRU	0.89	0.87
Two Stacked LSTM	0.94	0.93
Two Stacked GRU	0.98	0.99
LSTM - GRU	0.96	0.95
GRU - LSTM	0.93	0.93

The performance of stacked GRU architecture, when trained with attention, is given in Table 3. The dynamic activity, walking, and all the sedentary activities achieved the highest scores.

Table. 3. Performance of stacked GRU with attention

Activity	Precision	Recall	F1-Score
Walking	1.00	1.00	1.00
Walk Up	0.94	0.98	0.96
Walk Down	0.98	0.94	0.96
Sitting	1.00	0.99	0.99
Standing	0.99	1.00	1.00
Lying	1.00	1.00	1.00

The confusion matrix for the two stacked GRU models with and without attention are given in Fig. 7. The misclassification of walking upstairs and downstairs is due to the similarity in signal patterns gathered from the accelerometer sensor.

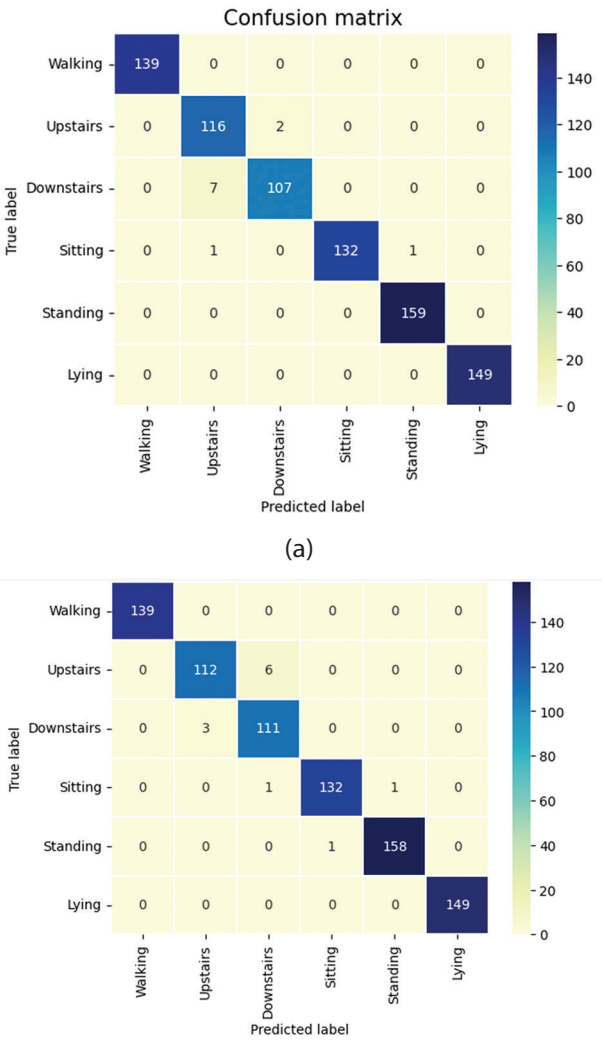

(a)

(b)

Fig. 7. Confusion Matrix for the two stacked GRU architecture (a) Model with attention (b) Model without attention

The raw signal pattern of these activities is given in Fig. 8. The models are trained with fewer parameters as compared to the baseline architectures. The total trainable parameters used in two stacked GRUs with attention is 51519, whereas the model trained without attention used 51454 parameters. There is only a < 1% increase in parameters when trained with attention. Fig. 8 shows that both activities' axis values fall within a similar range, which can cause misclassification when trained with handcrafted features. The factor that makes the proposed model distinct is fewer neurons in the hidden layers and a single dense layer before the output layer. The training time is considerably reduced in training using features extracted rather than the automatically learned features from the accelerometer vector.

To comprehend how and why a complex model reached a particular conclusion, it helps to analyze the importance of various features in the model. The permutation feature importance values are calculated to learn the model's interpretability. Feature importance arranged in increasing order of significance is given in Fig. 9.

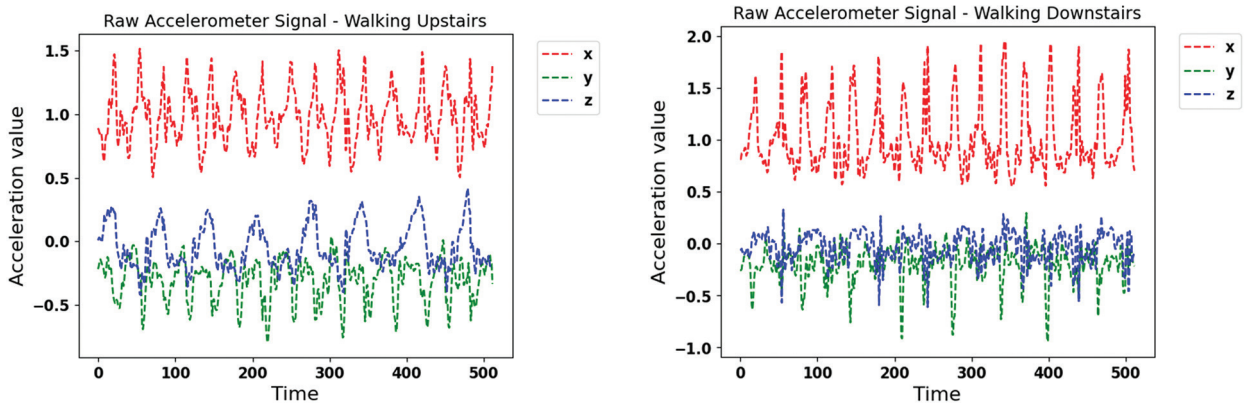

(a) (b)

Fig. 8. Raw accelerometer signal patterns (a) Walking Upstairs (b) Walking Downstairs

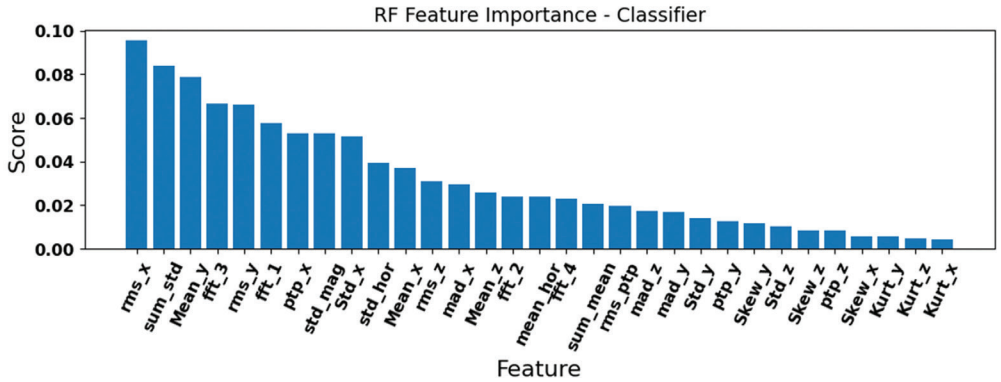

Fig. 9. Permutation feature importance scores in the UCI-HAR dataset

The magnitude vector computed for the x-axes component of the acceleration vector gave the highest score of 0.09565 when feature ranking is performed using the Random Forest Classifier. Permutation feature importance may often lead to misleading interpretations in the presence of strongly correlated features. Figure 1 shows that the features used in the study are correlated. Hence, to determine how a feature contributes to making a prediction, Shapley values, shown in Fig. 10, are a better choice, but their implementation is more expensive. The area of the force plot to the left side from the mean position are the features that helped in prediction, whereas those on the right side would have decreased the likelihood of prediction.

Fig. 10. SHAP explanation force plot for single layer GRU model

The four features with the highest score, namely, magnitude vector along the x-axis, signal mean along the y-axis, root mean square of standard deviation along each axis and fast Fourier transform component, plotted against the activity classes, are shown in Fig. 11.

It is observed that lying (activity 6) in Fig. 11 (a) does not overlap with any other activities for the magnitude vector along the x_axis. This is the most separable activity for all models. The dynamic activities of Walking (activity 1), Walking Upstairs (activity 2) and Walking Downstairs (activity 3), which overlap significantly for all features, make prediction hard. Similar to this, the root mean square of the standard deviation along each axis, Fig. 11 (c), and the fast Fourier transform component, Fig. 11 (d), entirely overlap the sedentary behaviors of Sitting (activity 4) and Standing (activity 5), making classification difficult.

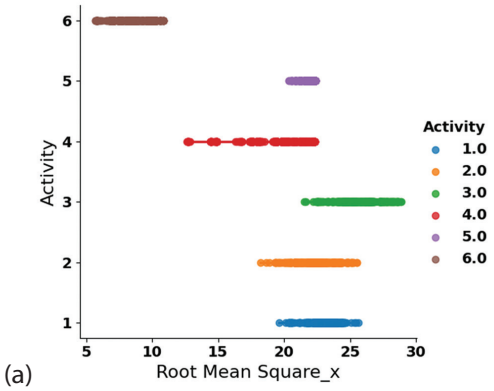

(a)

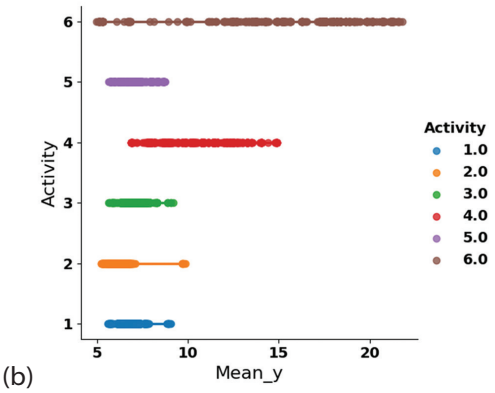

(b)

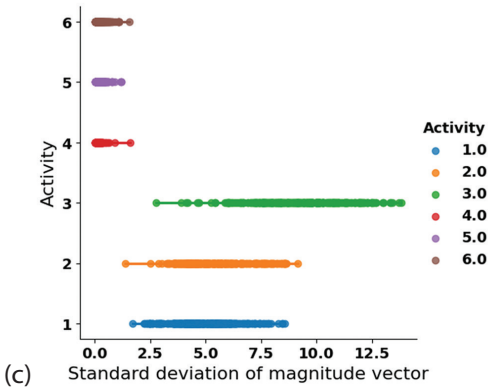

(c)

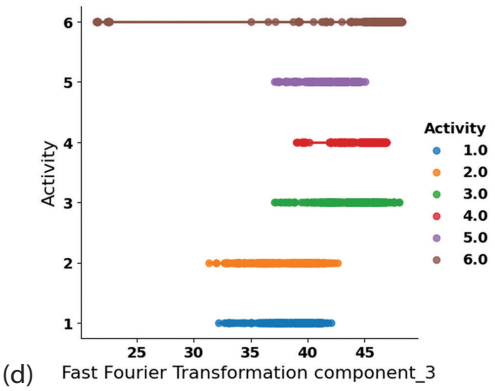

(d)

Fig. 11. Most important feature values against activity classes (a) Magnitude vector along the x-axis (b) Signal mean along the y-axis (c) RMS of standard deviation along each axis (d) Fast Fourier Transform component (Activity: 1 – Walking, 2 – Walking Upstairs, 3 – Walking Downstairs, 4 – Sitting, 5 - Standing, 6 – Lying)

5.2. EVALUATION OF THE MODELS USING OPTIMAL FEATURES

Among the 31 features computed from raw accelerometer sensor data, 23 features representing three-fourths of the total features, arranged according to relevance using permutation feature importance measure, are used to train the models.

Table 4 shows the comparison between recognition rates of classifiers with and without attention mechanism using three-fourths of the highly relevant features. The introduction of the attention mechanism has improved the recognition rates of all models. The accuracy of models trained with GRU shows high performance compared to LSTM architectures. Figure 12 depicts the training and validation accuracy and loss curves for the GRU model having an attention-based stacked layer.

Table. 4. Recognition rate of classifiers using 75% features selected based on feature importance

Model Architecture	Performance (Accuracy)	
	Model without Attention	Model with attention
Single Layer LSTM	0.85	0.88
Single Layer GRU	0.87	0.88
Two Stacked LSTM	0.93	0.93
Two Stacked GRU	0.95	0.97
LSTM - GRU	0.92	0.93
GRU - LSTM	0.92	0.97

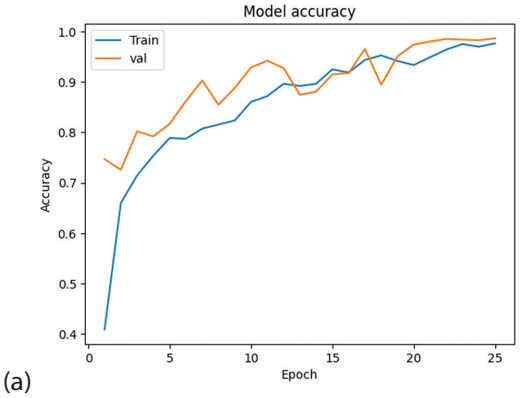

(a)

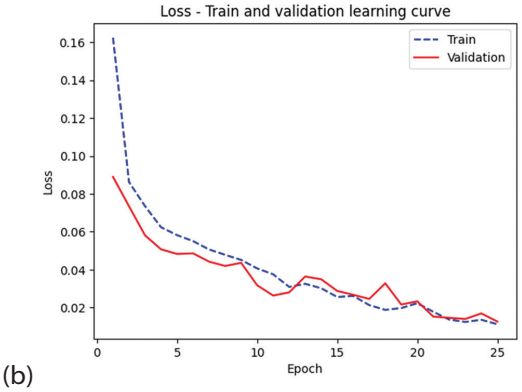

(b)

Fig. 12. Train and validation curve for stacked attention-based GRU model (a) Accuracy curve (b) Loss curve

The training and validation loss decreases with increased epochs and stabilizes at a value without much gap, indicating that the model is a good fit. It is also to be noted that the decrease in the number of features has not affected the performance of the model.

5.3. EVALUATION OF THE MODELS USING FEATURES GIVEN BY SHAPLEY VALUES

The highly ranked features selected by Shapley values, Figure 9, and fast Fourier transform components, making a total of 16 features, are used to train the model. Table 5 shows the recognition rate of classifiers trained with and without attention using half of the total features originally used in the study, selected based on their ranking.

Table. 5. Recognition rate of classifiers using 50% features selected by Shapley values

Model Architecture	Performance (Accuracy)	
	Model without Attention	Model with attention
Single Layer LSTM	0.85	0.96
Single Layer GRU	0.93	0.95
Two Stacked LSTM	0.93	0.96
Two Stacked GRU	0.96	0.96
LSTM - GRU	0.96	0.95
GRU - LSTM	0.96	0.96

Comparing the results obtained from various study using the lists of all significant features reveals that correlated features minimally impact the performance of the classifiers. When trained using 16 features and attention mechanisms, all models performed comparably. The time overhead of the attention mechanism in single-layer models is less than 2 seconds, and in stacked models is less than 10 seconds.

Table. 6. Statistical analysis of classifiers

Model Classifiers	Independent t-test	
	T-statistic	p-value
All features	0.06	0.95
75% features	0.88	0.39
50% features	1.43	0.18

An independent t-test is carried out with a significance threshold set at 0.05 to ascertain whether the observed performance difference between the attention-based approach and the non-attention-based strategy is statistically significant. The T-statistic and p-value obtained in the statistical analysis of the classifiers are given in Table 6.

The Receiver Operating Characteristic (ROC) curve is shown for all models trained with optimal features in Fig. 13, illustrates the classification performance. This measure depicts the model's ability to accurately predict the positive class when the result is positive. The Area Under the Curve (AUC) measure in Fig. 12 indicates that all models are good at discriminating various activities.

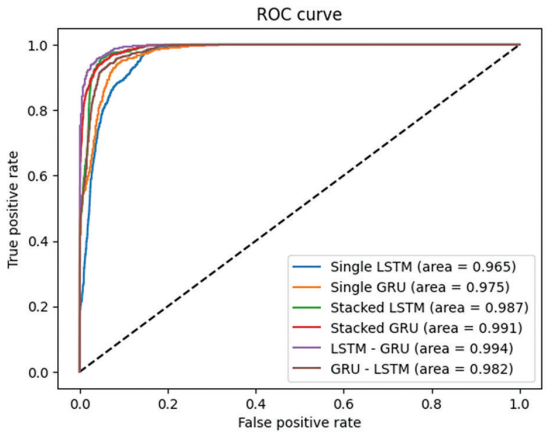

(a)

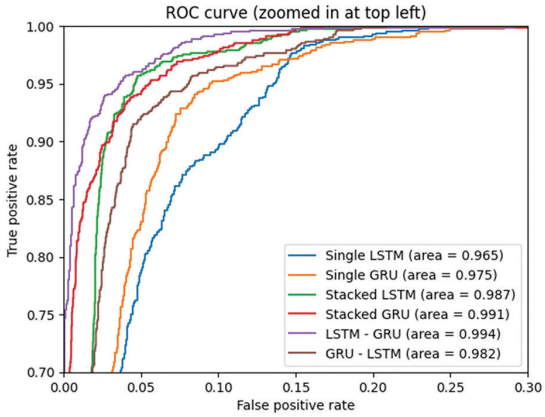

(b)

Fig. 13. ROC analysis (a) models trained with optimal features (b) ROC curve zoomed in at top left

The LSTM-GRU combination model has the highest AUC, followed by the two-stacked GRU model. Less false positives are indicated by smaller values on the plot's x-axis, and greater values on the y-axis show more true positives. Table 7 gives the proposed two stacked GRU models compared with other baseline architectures in the literature on the UCI-HAR dataset. The proposed model used a compact architecture with minimum layers and fewer neurons, thereby reducing the number of parameters, to design a lightweight RNN model.

6. CONCLUSION

In conclusion, we have conducted a comprehensive investigation into the classification of human activities using single and stacked recurrent neural network variants with an attention mechanism built into the layer preceding the fully connected dense layer. The attention mechanism enhanced the classification performance of all models, particularly those trained with GRU. Our approach relies on analyzing temporal and frequency domain features calculated from raw accelerometer signal data, offering a robust foundation for human activity classification. The classifier uses fewer neurons and a single dense layer, distinguishing our studies from others in the field that often employ more complex architectures.

The results obtained in the study are given below.

i. GRU performed better than LSTM with the selected handcrafted features to determine human context.

ii. The attention mechanism, when used with stacked variants, improved the overall accuracy of all models.

iii. The significance of features in prediction is determined using permutation feature ranking measures and shapely values. The model is retrained with optimal features that contributed the most, still attaining comparable accuracies.

iv. The accuracy of the GRU stacked models, which reached 99% when trained with all features, dropped by less than 2% when trained with three-fourths of the optimal features and by 3% when only half of the features were used.

In future work, more feature importance measures to attain the interpretability of models having features with high correlation will be attempted.

Table. 7. Comparison of proposed model with baseline architectures

Paper	Year	Model	Layer	Neurons/ layer	Train example	Test Example	Accuracy
[7]	2020	LSTM-CNN	4	(32,32,64,128)	7319	3069	95.8
[26]	2019	GRU with Attention	2	-	7352	2947	94.16
[27]	2023	GRU-INC	2	(144, 128)	-	-	96.4
[28]	2023	CNN-GRU with Attention	4	(128,128)	-	-	94.19
Proposed Model		Stacked GRU with Attention	2	(64,64)	2092	813	99

- The paper does not report these parameters

7. REFERENCES

[1] L. Alawneh, T. Alsarhan, M. Al-Zinati, M. Al-Ayyoub, Y. Jararweh, H. Lu, "Enhancing human activity recognition using deep learning and time series augmented data", Journal of Ambient Intelligence and Humanized Computing, 12, 2021, 10565 – 10580.

[2] C. Xu, D. Chai, J. He, X. Zhang, S. Duan, "InnoHAR: A Deep Neural Network for Complex Human Activity Recognition", IEEE Access, vol. 7, 2019, pp.9893-9902. https://doi.org/10.1109/ACCESS.2018.2890675

[3] C. Xu, J. Shen, X. Du, F. Zhang, "An Intrusion Detection System Using a Deep Neural Network with Gated Recurrent Units", IEEE Access, vol. 6, 2018, 48697-48707. https://doi.org/10.1109/ACCESS.2018.2867564

[4] T. Alsarhan, L. Alawneh, M. Al-Zinati, M. Al-Ayyoub, "Bidirectional Gated Recurrent Units For Human Activity Recognition Using Accelerometer Data", IEEE SENSORS, Montreal, QC, Canada, 2019, pp.1-4. https://doi.org/10.1109/SENSORS43011.2019.8956560

[5] F. Karim, S. Majumdar, H. Darabi, S. Chen, "LSTM Fully Convolutional Networks for Time Series Classification", IEEE Access, vol. 6, 2018, pp. 1662-1669. https://doi.org/10.1109/ACCESS.2017.2779939

[6] P. Siirtola, J. Röning, "Context-aware incremental learning-based method for personalized human activity recognition", Journal of Ambient Intelligence and Humanized Computing, 12, 2021, 10499–10513. https://doi.org/10.1007/s12652-020-02808-z

[7] A. Tsanousa, G. Meditskos, S. Vrochidis, L. Angelis, "A novel feature selection method based on comparison of correlations for human activity recognition problems", Journal of Ambient Intelligence and Humanized Computing, 11, 2020. https://doi.org/10.1007/s12652-020-01836-z

[8] F. Hernandez, L.F. Suarez, J. Villamizar, M. Altuve, "Human Activity Recognition on Smartphones Using a Bidirectional LSTM Network", in Proceedings of XXII Symposium on Image, Signal Processing and Artificial Vision (STSIVA), Bucaramanga, Colombia, 2019, pp. 1-5. https://doi.org/10.1109/STSIVA.2019.8730249

[9] E.S.R. Montoliu, O.B. Fernández, "A study of deep neural networks for human activity recognition", Computational Intelligence, 36, 2020.

[10] K. Xia, J. Huang, H.Wang, "LSTM-CNN Architecture for Human Activity Recognition", IEEE Access, vol. 8, 2020, 56855-56866. https://doi.org/10.1109/ACCESS.2020.2982225

[11] N. Dua, S.N. Singh, V.B. Semwal, "Multi-input CNN-GRU based human activity recognition using wearable sensors", Computing, 103, 7 (Jul 2021), 1461–1478. https://doi.org/10.1007/s00607-021-00928-8

[12] J.Chen, X. Huang, H. Jiang, X. Miao, "Low-Cost and Device-Free Human Activity Recognition Based on Hierarchical Learning Model", Sensors, 2021, 21(7):2359. https://doi.org/10.3390/s21072359

[13] O. Kerdjidj, N. Ramzan, K. Ghanem, A. Amira, F. Chouireb, "Fall detection and human activity classification using wearable sensors and compressed sensing", Journal of Ambient Intelligence and Humanized Computing, 11(1), 2020, 349-361. https://doi.org/10.1007/s12652-019-01214-4

[14] F. Luna-Perejon, M. Dominguez-Morales, A. Civit, "Wearable Fall Detector Using Recurrent Neural Networks", Sensors, 2019, 19. 4885. https://doi.org/10.3390/s19224885

[15] F. Laghrissi, S. Douzi, K. Douzi, B. Hssina, "Intrusion detection systems using long short-term memory (LSTM)", J Big Data, 8, 65, 2021. https://doi.org/10.1186/s40537-021-00448-4

[16] B.A.M. Hashim, R. Amutha, "Human activity recognition based on smartphone using fast feature dimensionality reduction technique", Journal of Ambient Intelligence and Humanized Computing, 12, 2020, 2365-2374.

[17] R.C. Staudemeyer, E.R. Morris, "Understanding LSTM -- a tutorial into Long Short-Term Memory Recurrent Neural Networks", ArXiv, 2019, arXiv: 1909.09586.

[18] G.V. Houdt, C. Mosquera, G. Nápoles, "A review on the long short-term memory model", Artif Intell Rev, 53, 2020, 5929–5955. https://doi.org/10.1007/s10462-020-09838-1

[19] X. Le, H.V. Ho, G. Lee, S. Jung, "Application of Long Short-Term Memory (LSTM) Neural Network for Flood Forecasting", Water, 2019, 11(7):1387. https://doi.org/10.3390/w11071387

[20] K. Smagulova, A.P. James, "A survey on LSTM memristive neural network architectures and applications", Eur. Phys. J. Spec. Top., 228, 2019, 2313–2324. https://doi.org/10.1140/epjst/e2019-900046-x

[21] R. Zhao, D. Wang, R. Yan, K. Mao, F. Shen, J. Wang, "Machine Health Monitoring Using Local Feature-Based Gated Recurrent Unit Networks", IEEE Transactions on Industrial Electronics, vol. 65, no. 2, 2018, pp. 1539-1548. https://doi.org/10.1109/TIE.2017.2733438

[22] R. Rana, J. Epps, R. Jurdak, X. Li, R. Goecke, M. Breretonk, J. Soar, "Gated Recurrent Unit (GRU) for Emotion Classification from Noisy Speech". ArXiv, 2016, ArXiv abs/1612.07778.

[23] K. Greff, R.K. Srivastava, J. Koutník, B.R. Steunebrink, J. Schmidhuber, "LSTM: A search space odyssey. IEEE transactions on neural networks and learning systems, Vol. 28, No. 10, 2017, pp. 2222-2232.

[24] Y. Yu, X. Si, C. Hu, J. Zhang, "A Review of Recurrent Neural Networks: LSTM Cells and Network Architectures", Neural Computation, vol. 31, no. 7, 2019, pp. 1235-1270. https://doi.org/10.1162/neco_a_01199

[25] Davide Anguita, Alessandro Ghio, Luca Oneto, Xavier Parra and Jorge L. Reyes-Ortiz. A Public Domain Dataset for Human Activity Recognition Using Smartphones. 21th European Symposium on Artificial Neural Networks, Computational Intelligence and Machine Learning, ESANN 2013. Bruges, Belgium 24-26 April 2013.

[26] M.N. Haque, M.T.H. Tonmoy, S. Mahmud, A.A. Ali, M.A.H. Khan, M. Shoyaib, "GRU-based Attention Mechanism for Human Activity Recognition", in Proceedings of 1st International Conference on Advances in Science, Engineering and Robotics Technology (ICASERT), Dhaka, Bangladesh, 2019, pp. 1-6. https://doi.org/10.1109/ICASERT.2019.8934659

[27] T.R. Mim, M. Amatullah, S. Afreen, M.A. Yousuf, S. Uddin, S.A. Alyami, K.F. Hasan, M.A. Moni, "GRU-INC: An inception-attention based approach using GRU for human activity recognition", Expert Systems with Applications, Volume 216, 2023, 119419, ISSN 0957-4174.

[28] U. Verma, P. Tyagi, M.K. Aneja, "Multi-Branch CNN GRU with attention mechanism for human action recognition", Engineering Research Express, vol. 5, 2, 2023.https://doi.org/10.1088/2631-8695/acd98c

A Four Slot Dual Feed and Dual Band Reconfigurable Antenna for Fixed Satellite Service Applications

Original Scientific Paper

T. Venkata Suri Apparao
GITAM University
Department of electrical electronics and communication engineering,
GITAM University, Visakhapatnam, India
vtanakal@gitam.edu

Dr. G. Karunakar
GITAM University
Department of electrical electronics and communication engineering,
GITAM University, Visakhapatnam, India
kgodi@gitam.edu

Abstract *– A dual feed and dual-band reconfigurable antenna is designed, analyzed, and prototyped in this work for fixed satellite service communication applications. The designed model occupies the compact dimension of 24X21X1.2 mm on FR4 substrate and provides an input impedance of 50 ohms at both ports. The proposed model offers additional circular polarization characteristics at both the resonating bands. The PIN diode-based switching conditions, and the frequency reconfigurability analysis in both simulation and measurement are almost match. The combination of dual-band resonance, frequency reconfigurable nature, and compact dimension makes this model an attractive candidate in the specified field with considerable gain (8.5 dB) and efficiency (80%).*

Keywords*: Circular polarization, Dual Band, Dual feed, Reconfigurability, Satellite application*

1. INTRODUCTION

Recently, several advancements have happened in antennas due to their various applications. Emerging technologies came into existence in wireless communication, and the demand for antennas has increased tremendously. An antenna is the central part of any wireless communication application. The advanced antenna design is very much needed these days for their extensive use in all modern gadgets and devices[1-2]. Several antennas are available in the literature for various applications like Bluetooth, LTE, Wi-Fi, wireless LAN and 5G communication [3-8].

One reconfigurable antenna is equivalent to some antennas; the reconfiguration is based on frequency, polarisation, and pattern of the antenna without regard to physical size. For reconfugaration, varactor diodes, field effect transistors, and PIN diodes are commonly used [9]. PIN diodes are symmetrically positioned to retain the antenna's electrical properties [10]. The dual-band antenna is conceivable depending on the feed position and inset size. Different band reconfiguration and modes of operation can achieved by ON and OFF of the PIN diodes [11]

There are several methods to design the antenna using various feeding techniques. The coaxial probe method is traditional, whereas the microstrip line feed method is another alternative and easy feeding method. The coplanar waveguide fed method is another alternative to design the antennas simply with good impedance matching [12-15]. Antenna with circular polarization has advantages over linear polarization. The researchers made several designs to attain circular polarization in the antenna with different feeding techniques and with the combination of meandered slots [16-18]. The researchers extensively use other methods like metamaterials, electromagnetic bandgap structures, frequency-selective surfaces, and artificial magnetic conductors while designing modern communication-based antennas [19-23].

This work is concentrated on the design of a circularly polarised antenna with a dual feeding technique. The Antenna consists of 4 slots in the radiating structure, fed with coaxial probe feeding. The design considerations and the dimensional characterization is provided in the antenna design section.

2. ANTENNA DESIGN:

The designed slot antenna is prototyped on an FR4 substrate with dual feeding. The coaxial feeding has been used here due to its straightforward approach and ease of exciting the patch antenna. Coaxial feeding done by conecting the condcting wire that terminates at the patch. It has been implemented with the center conductor in the coaxial launcher attached to the ground plane at the bottom side. Based on the feed location, the input impedance varies in the probe feeding, and here, the feed location away from the edge of the patch will affect lower input resistance. To obtain good matching with 50-ohm impedance, the condition should be 0.13 λg. Fig. 1 shows the antenna topside as well as the bottom side structure. Table 1 represents the parameter data of antenna design.

Table 1. Antenna design Parameters data

S. No	Parameter	Value
1	Length of patch (Lp)	8.2 mm
2	Width of the patch (Wp)	8.2 mm
3	L1	2 mm
4	Slot cut S1	2mm, 3mm, 4mm, 5mm
5	Length of slot	7.6424
6	Width of slot	0.155 mm
7	Coaxial length	0.425 mm
8	Coaxial width	0.3267 mm
9	Inset_1	3.94 mm
10	Inset_2	3.94 mm

Two separate probes are required to attain dual polarization with dual feeding, and each probe is responsible for corresponding polarization. The narrow bandwidth that is obtained with dual feeding is due to the high cross-polarization Because of the probe radiation and probe inductance.

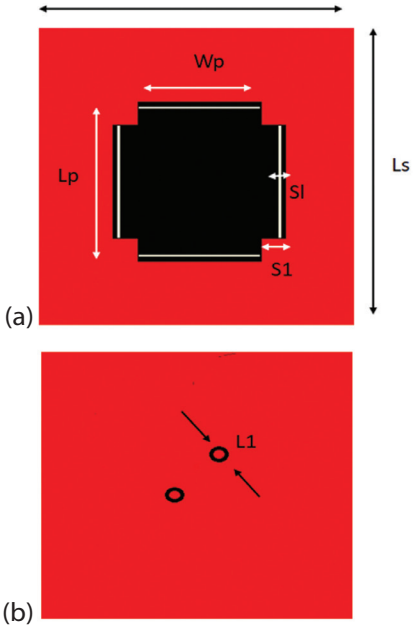

Fig 1. Dual Fed Slot Antenna, (a) Top View, (b) Bottom View

3. RESULTS AND DISCUSSION:

3.1. DUAL FEED SLOT ANTENNA:

Fig. 2 shows S-parameters and VSWR plots for the dual-feed antenna model. Antenna resonating at the dual-band of 9.4 GHz and 13.3 GHz, respectively.

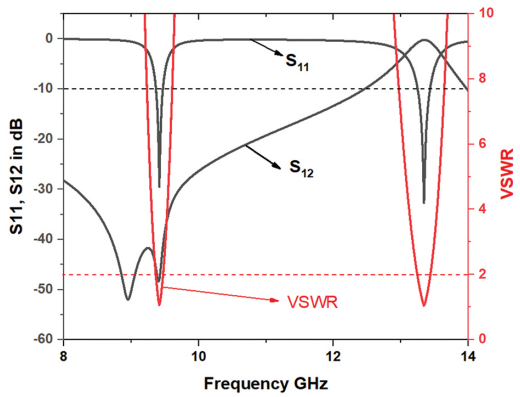

Fig 2. S-Parameters and VSWR Vs Frequency

Antenna showing dual band characteristics with reflection coefficient less than -10 dB and VSWR of 2:1 ratio. The transmission coefficient result indicates a value less than-25 dB at the first resonant band -10 dB at the second resonant band.

The parametric analysis has been done for the slotted monopole antenna and presented the results in Fig. 3. It has been observed that for S1 of 2 mm and L1 of 2 mm, the antenna shows dual band characteristics with good impedance matching.

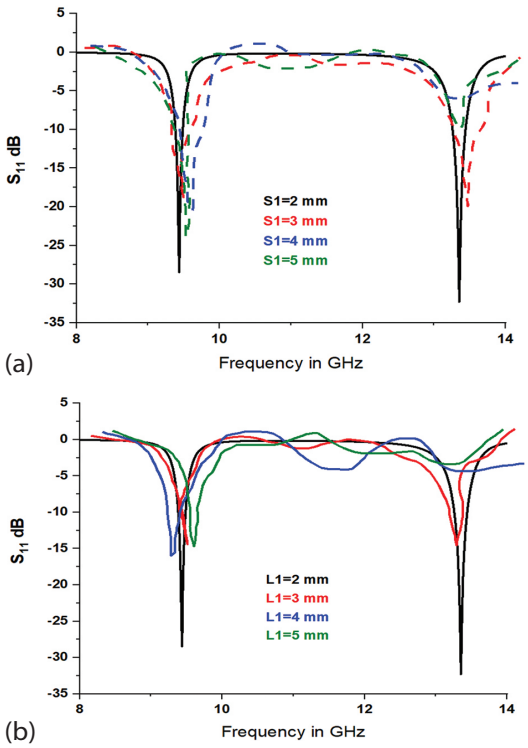

Fig 3. Parametric Analysis, (a) Change in S1, (b) Change in L1

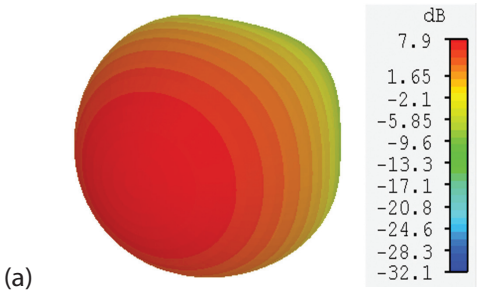

(a)

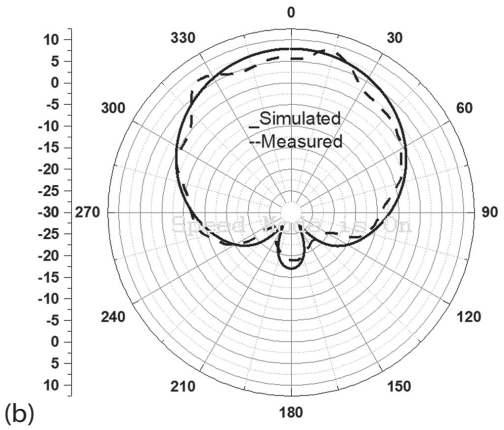

(b)

Fig 4. Radiation Pattern at 9.4 GHz, (a) Three-dimensional, (b) E-Plane Pattern

Fig. 4 and 5 display the slotted monopole antenna's radiation characteristics. A maximum gain of 7.9 dB is attained at 9.4 GHz and a maximum gain of 7.91 dB is attained at 13.3 GHz. Antenna exhibiting low backlobe, monopole-like radiation in the E-plane. A nulling is occurred for 210 degrees at 13.3 GHz and the antenna showing good radiation characteristics at dual band.

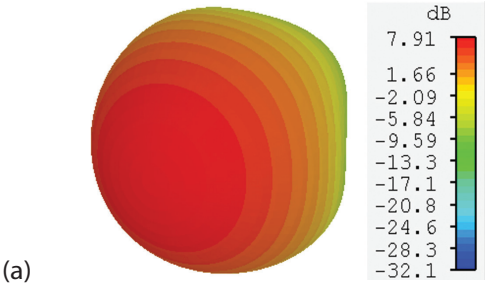

(a)

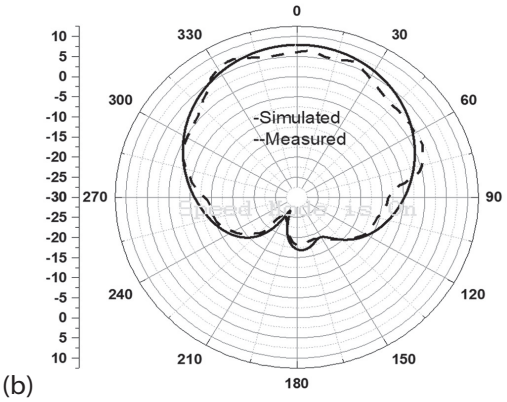

(b)

Fig 5. Radiation Pattern at 13.3 GHz, (a) Three-dimensional, (b) E-Plane Pattern

3.2. RECONFIGURABLE ANTENNA

The slotted monopole antenna is converted into a reconfigurable antenna with the placement of pin diodes at four slots, as shown in Fig. 6. The equivalent circuit model for PIN diode ON and OFF conditions is presented in Fig. 6(c). The parameters like reflection and transmission coefficients concerning the diodes on and off conditions are analyzed and presented in this section.

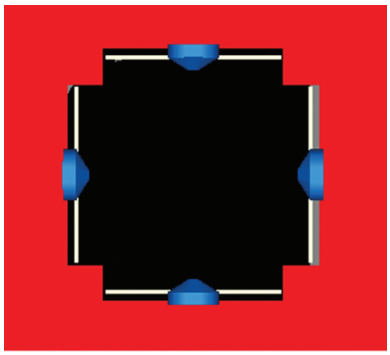

(a)

(b)

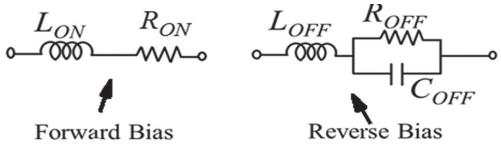

(c)

Fig 6. Reconfigurable Dual Fed Slot Antenna with Diodes, (a) Top View, (b) Bottom View (c) PIN diode equivalent circuit for ON and OFF

The fabrication of the antenna is shown in Fig. 7. Dual feed slot antennas and dual feed slot antennas with diodes are displayed here. The S-parameters are analyzed with diodes ON and OFF condition is presented in Fig. 8 and 9. Four diodes are used in the design to verify the performance characteristics of the antenna in reconfigurable conditions. When four diodes are in an off state, antenna shows dual band characteristics at 9.4 GHz and 13.3 GHz, respectively. Diode 4 in the ON condition and remaining diodes in the OFF condition also provide dual-band characteristics with resonance at 9.6 GHz and 13 GHz, respectively. When diode 3 is in ON condition and the remaining diodes are in OFF condition, providing a single resonance at 9.7 GHz. When diode 2 is in ON condition, the remaining diodes are in OFF condition, providing a single band with resonance at 9.8 GHz.

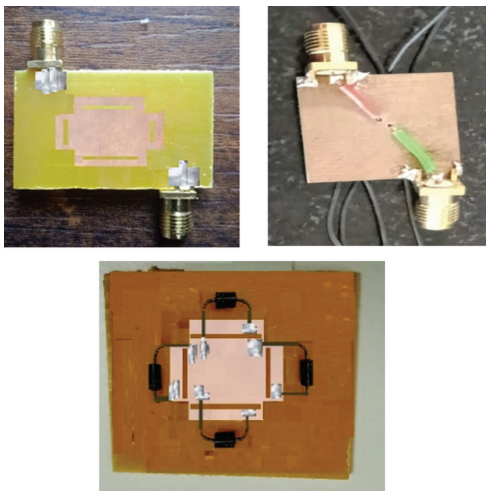

Fig 7. Fabricated a) dual Fed Slot Antenna b) feed line c) Dual Fed Slot Antenna with Diode

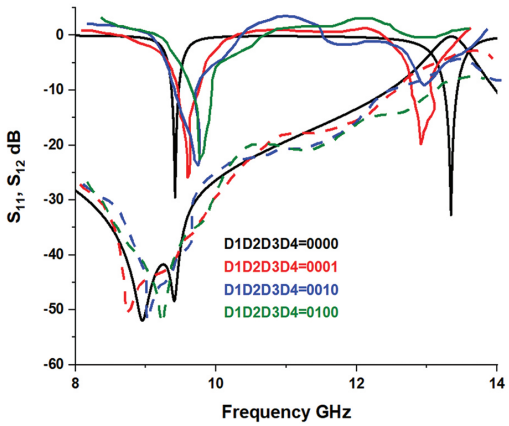

Fig 8. Reconfigurability Conditions 1

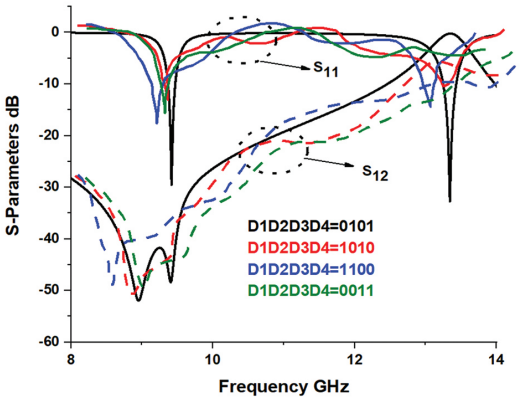

Fig 9. Reconfigurability Conditions 2

The reconfigurable conditions for 0101, 1010, 1100, and 0011 are presented in Fig. 8. When diodes 2 & 4 are in ON condition, and the remaining diodes are in OFF condition, antenna provides dual-band characteristics with resonance at 9.3 GHz and 13.4 GHz, respectively. When diodes 1 & 3 are in ON condition, and the remaining diodes are in OFF condition, antenna provides dual-band characteristics with resonance at 9.1 GHz and 13 GHz, respectively. When diodes 1 & 2 are in ON condition, and the remaining diodes are in OFF condition, antenna provides dual-band characteristics with resonance at 9.4 GHz and 13.1 GHz, respectively. When diodes 3 & 4 are in ON condition and remaining diodes are in OFF condition, the antenna provides single band characteristics with resonance at 9.2 GHz.

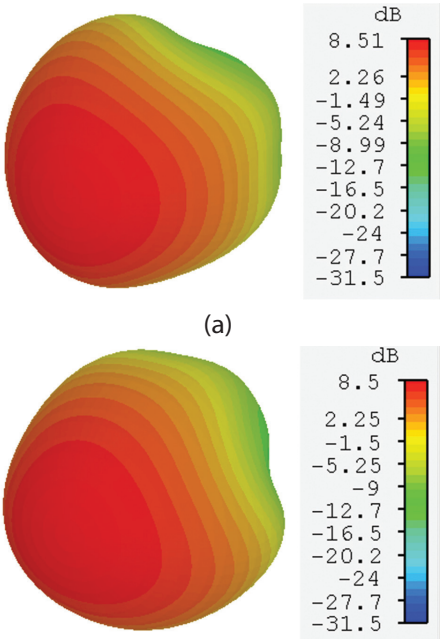

Fig 10. 3D-Radiation pattern, (a) At 1010, (b) At 0101

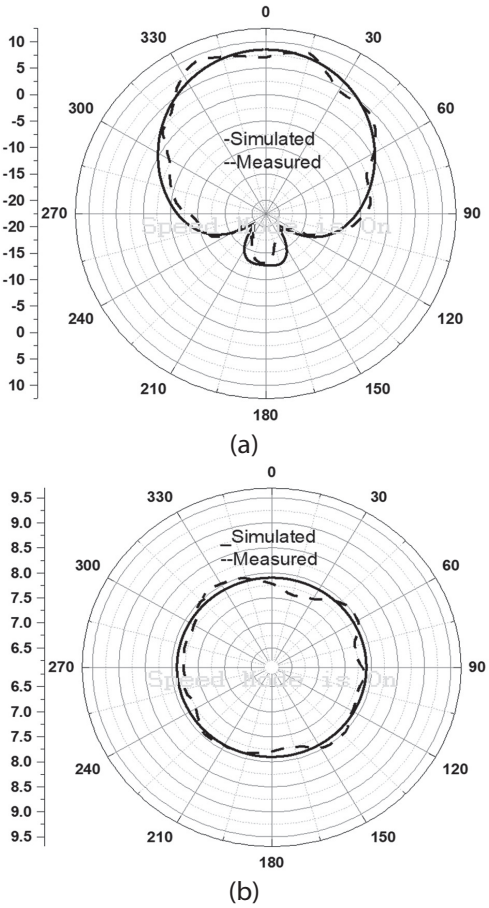

Fig 11. Radiation Pattern in Polar, (a) E-Plane at 1010 Condition, (b) H-Plane at 1010 Condition

Fig. 10. displays the antenna's radiation properties in both 3D and polar coordinates. A peak gain of 8.51 dB at 1010 conditions and 8.5 dB at 0101 conditions can be observed from Fig. 11. The radiation characteristics in polar coordinates are presented in Figs. 10 and 11 for 1010 and 0101 conditions. A directive pattern with low back lobe radiation can be observed from Fig. 11(a) of the E-plane and quasi-omni directional patterns in the H-plane from Fig. 11(b) for 1010. A directive pattern with nulling between 190 to 210 degrees can be observed from Fig. 12(a) of the E-plane and quasi-omni directional patterns in the H-plane from Fig. 12(b) for 0101.

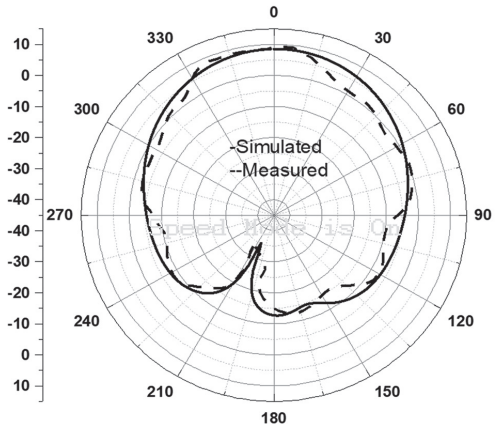

(a)

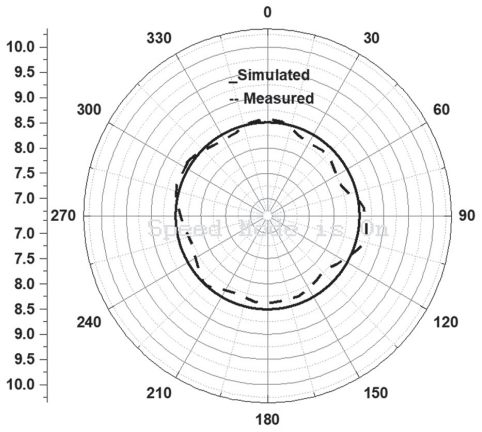

(b)

Fig 12. Radiation Pattern in Polar, (a) E-Plane at 0101 Condition, (b) H-Plane at 0101 Condition

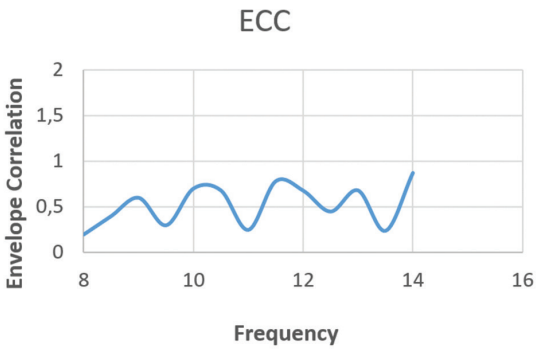

Fig 13. Relation between Envelope correlation to the frequency

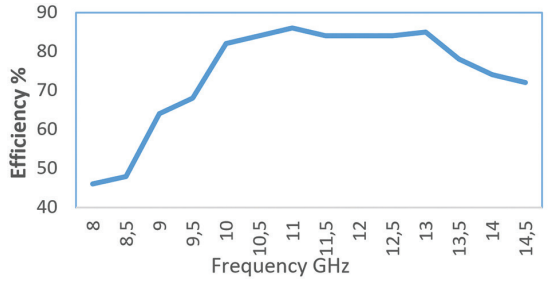

Fig 14. Efficiency of the Dual Fed Slot Antenna w.r.t frequency

Table 2. Comparision of Proposed work with standrad literaure.

S.no	Frequency	Gain	Efficiency
1 [24]	5.45 GHz	7.55dB	-
2 [25]	4.63 GHz	1.02dB	-
3 [26]	6.4GHz	1.87dB	70%
Proposed work gain	9.4 GHz	7.9dB	83%
	13.3 GHz	7.91dB	

Fig. 13. shows the envelope correlation factor with frequency, the maximum value of 0.8 obtained is good enough for a practical case. Fig. 14 represents the antenna's efficiency, which is almost above 80%. Table 2 compares the proposed work with the standard and obtained a maximum gain of 7.91dB

4. CONCLUSION

In this paper, a dual-feed, dual-band, reconfigurable antenna is designed and studied. The designed antenna resonates at 9.4 GHz and 13.3 GHz, respectively, with a gain of more than 8 dB. Antenna shows excellent radiation characteristics with monopole-like radiation in the E-plane and omnidirectional radiation in the H-plane with low cross-polarization. The resonant frequencies are changed concerning the diodes on and off conditions, and a remarkable gain change of 0.5 dB is observed in the reconfigurable antenna. There is a good match between the simulated and measurement results obtained from the prototype antenna with reconfigurable conditions.

5. REFERENCES

[1] V. K. Allam, S. Maloji, "Novel Reconfigurable Bandpass Filtering Antenna for IoT Communication Applications", Progress in Electromagnetics Research C, Vol. 96, 2019, pp. 13-26.

[2] M. L. S. N. S. Lakshmi, H. Khan, P. V. V. Kishore, "A Frequency and Pattern Reconfigurable Asymmetric Ground Antenna on Flexible Polyimide Material for LTE, Wi-Fi, WLAN and Fixed Satellite Applications", Flexible and Printed Electronics, Vol. 5, No. 2, 2020.

[3] B. T. P. Madhav, B. P. Nadh, "Frequency Reconfigurable Split Ring Antenna for LTE And WiMAX Applications", International Journal of Electronics and Telecommunications, Vol. 66, No. 2, 2020, pp. 255-260.

[4] K. V. Vineetha, M. SivaKumar, "SRR based Tri-Mode Resonant Microstrip Bandpass Filter for WLAN Applications", Journal of Engineering Science and Technology, Vol. 15, No. 5, 2020, pp. 3218-3241.

[5] P. Bora, "Design and Analysis of EBG Antenna for Wi-Fi, LTE, and WLAN Applications", ACES Journal, Vol. 35, No. 9, 2020, pp. 1030-1036.

[6] S. Lakrit, A. Nella, S. Das, B. T. P. Madhav, C. M. Krishna, "An integrated three-antenna structure for 5G, WLAN, LTE and ITU band cognitive radio communication", AEU-International Journal of Electronics and Communications, Vol. 139, 2021, p. 153906.

[7] I. H. Nejdi, S. Das, Y. Rhazi, S. Bri, "Mustapha Aitlafkih, "A Compact Planar Multi-Resonant Multi-Broadband Fractal Monopole Antenna for Wi-Fi, WLAN, Wi-MAX, Bluetooth, LTE, S, C, and X Band Wireless Communication Systems", Journal of Circuits, Systems and Computers, 2022.

[8] M. C. Rao, "Flexible bandpass filter with silver conductive layer for GPS, ISM, PCS, LTE and WLAN applications", Materials Technology Proceedings, Vol. 42, No. 2, 2021, pp. 1321-1328.

[9] S. Annamary, A. Jeevakumari, N. Velmurugan. "Dual feed pattern reconfigurable antenna for wireless applications", Wireless Personal Communications, Vol. 99, 2018, pp. 829-837.

[10] Y. Sung, "Dual-band reconfigurable antenna for polarization diversity", International Journal of Antennas and Propagation, Vol. 2018, 2018.

[11] L. Ge, K.-M. Luk, "A band-reconfigurable antenna based on directed dipole", IEEE Transactions on antennas and propagation, Vol. 62, No. 1, 2013, pp. 64-71.

[12] S. Lakrit, S. Das, A. Chowdhury, MoussaLabbadi, "Analysis and Fabrication of a Compact CPW-Fed Planar Printed UWB Antenna Using Isola Tera MT (R) Substrate for Medical Applications, Advanced Energy and Control Systems", Lecture Notes in Electrical Engineering, Vol. 820, 2022.

[13] T. Anusha, T. V. Ramakrishna, A. N. Meena Kumari, "Dual-Band-Notched CPW-Fed Antennas with WiMAX/WLAN Rejection for UWB Communication", Lecture Notes in Electrical Engineering, Vol. 471, 2018, pp. 559-570.

[14] M. Mudaliar, Y. B. Dhanade, K. Sreelakshmi, P. Bora, "Slot Loaded Defected Ground Structured CPW Fed Antenna for ISM Band Applications", Journal of Advanced Research in Dynamical and Control Systems, Vol. 9, No. 14, 2017, pp. 2346-2355.

[15] V. S. Reddy, V. Agarwal, M. S. G. Prasad," A Novel Ultra-Wide Band CPW Fed Printed Antenna for IoT Wireless Applications", International Journal of Engineering and Advanced Technology, Vol. 8, No. 4, 2019, pp. 1817-1823.

[16] M. P. Kishore, S. S. M. Reddy, "Metamaterial Inspired Gain Enhanced Elliptical Curved CPW fed Multiband Antenna for Medical and Wireless Communication Applications", Biomedical & Pharmacology Journal, Vol. 12, No. 2, 2019, pp. 729-737.

[17] S. Lakrit, S. Das, S. Ghosh, "Compact UWB flexible elliptical CPW-fed antenna with triple notch bands for wireless communications", International Journal of RF Microwave Computer Aided Engineering, Vol. 30, No. 7, 2020, p. e22201.

[18] V. S. D. Rekha, P. Pardhasaradhi, Y. U. Devi, "Dual Band Notched CPW Fed Printed Monopole Antenna for UWB Applications", International Journal of Intelligent Engineering Systems, Vol. 13, No. 3, 2020, pp. 26-32.

[19] A. Tirunagari et al. "Analysis of CPW-Fed Modified Z-Shaped Reconfigurable Antenna for Automotive Communications, Electromagnetics and Telecommunications", Lecture Notes in Electrical Engineering, Vol. 655, 2021.

[20] A. B. Devarapalli, T. Moyra, B. T. P. Madhav, "An FSS Based Broadband Elliptical Tree Shaped Antenna with Augmented Gain for Wireless Applications", IETE Journal of Research, 2022. (in press)

[21] A. Badisa, B. T. P. Madhav, S. Das, M. C. Rao, "Design and analysis of varactor-loaded bi-state switchable active artificial magnetic conductor reflector for wearable antenna integration", International Journal of RF and Microwave Computer Aided Engineering, Vol. 32, No. 4, 2022, p. e23047.

[22] Y. Ghazaoui, M. El Ghzaoui, A. El Alami, "A compact high gain wideband millimeter wave 1 × 2 array antenna for 26/28 GHz 5G applications", Circuit World, Vol. 49, No. 4, 2021.

[23] B. Aghoutane, S. Das, M. E. Ghzaoui, B. T. P. Madhav, H. El Faylali, "A novel dual band high gain 4-port millimeter wave MIMO antenna array for 28/37 GHz 5G applications", AEU-International Journal of Electronics and Communications, Vol. 145, 2022, p. 154071.

[24] R. K. Singh, A. Basu, S. K. Koul, "Reconfigurable microstrip patch antenna with polarization switching in three switchable frequency bands", IEEE Access, Vol. 8, 2020, pp. 119376-119386.

[25] A. Bhattacharjee, S. Dwari, "A monopole antenna with reconfigurable circular polarization and pattern tilting ability in two switchable wide frequency bands", IEEE Antennas Wireless Propagation Letters, Vol. 20, No. 9, 2021, pp. 1661-1665.

[26] I. Ahmad et al. "Frequency reconfigurable antenna for multi standard wireless and mobile communication systems", Computers, Materials & Continua, Vol. 68, No. 2, 2021, pp. 2563-2578.

Parameter Estimation and Predictive Speed Control of Chopper-Fed Brushed DC Motors

Original Scientific Paper

Son Nguyen Thanh
Hanoi University of Science and Technology,
School of Electrical and Electronic Engineering
1 Dai Co Viet Street, Hanoi, Vietnam
son.nguyenthanh@hust.edu.vn

Tu Pham Minh
Hanoi University of Science and Technology,
School of Electrical and Electronic Engineering
1 Dai Co Viet Street, Hanoi, Vietnam
tu.phamminh@hust.edu.vn

Tuan Pham Van
Vinh University of Technology Education,
Faculty of Electrical Engineering
117 Nguyen Viet Xuan Street, Vinh City, Vietnam
tuanvp.bk@gmail.com

Anh Hoang
Hanoi University of Science and Technology,
School of Electrical and Electronic Engineering
1 Dai Co Viet Street, Hanoi, Vietnam
anh.hoang@hust.edu.vn

Abstract *– This paper presents an effective speed control method for brushed DC motors fed by a DC chopper using the concept of Finite Control Set-Model Predictive Control (FCS-MPC). As this control algorithm requires the parameters of the controlled object, the estimation of motor parameters is first performed by using two types of data. The first data includes the output speed response corresponding to the step input voltage to obtain the transfer function in the no-load regime. The second data consists of the motor speed and armature current when a load torque is applied to the motor shaft. The discrete-time equation of the motor armature circuit is used to obtain the future values of the armature circuit current and the motor speed. A cost function is defined based on the difference between the reference and predicted motor speed. The optimal switching states of the DC chopper are selected corresponding to the maximum value of the cost function. The performance of the proposed speed control algorithm is validated on an experimental system. The simulation and experimental results obtained show that the MPC controller can outperform the conventional proportional-integral (PI) controller.*

Keywords*: Brushed DC motor, DC chopper, motor parameter estimation, motor speed control, model predictive control*

1. INTRODUCTION

Electric drive systems can be only seen as high-performance drive systems if they can accurately follow specified trajectories regardless of unknown load variations and uncertainties of parameters. An electric drive system is basically formed by an electrical motor, a power electronic converter, and a controller to perform precise mechanical manoeuvres. As brushed DC motors can be controlled over a wide speed range, they are still widely used in various industrial and commercial applications including electric vehicles, robotic manipulators, and precise mechanisms. In addition, brushed DC motors can be known as the most common controlled object for testing and evaluating different proposed control algorithms.

The accurate mathematical model and related parameters of a specific brushed DC motor are usually needed for designing an appropriate controller for the motor. In addition, the exact model of the motor can allow the designer to predict the closed-loop dynamics of the motor control system. This work can be only facilitated if the motor parameters can be estimated. Motor parameter estimation approaches can be divided into two categories: offline estimation methods [1] and online estimation methods [2]. Offline methods require the use of test inputs and the measurement of corresponding parameters using data acquisition (DAQ) devices. Next, coefficients determined by the measurement are used to obtain unknown parameters by an offline computer-based analysis. Meanwhile, online parameter estimation techniques sometimes include power converters and high-speed DAQ devices.

The conventional design of controllers for brushed DC motors often involves the use of constant gains for controllers like proportional-integral-derivative (PID) controllers, which are only useful for the control of a narrow speed range [3, 4]. Recently, brushed DC motor drive control systems have been developed using nonlinear control approaches, such as sliding mode controllers [5, 6], fuzzy logic controllers [7, 8], and artificial neural network controllers [9, 10].

As high-performance brushed DC motor drives frequently need to be adaptable, several studies on motor control have focused on adaptive control methods [11, 12], in which the coefficients of the controller can be adaptive utilising techniques for intelligent inference such as fuzzy logic and artificial neural networks. To increase the robustness of the motor control system, some studies have suggested techniques for estimating the speed of brushed DC motors [13-15] because the use of speed sensors could degrade system reliability and necessitate periodic maintenance. Most speed estimation techniques, however, have been developed using a precise mathematical model of the motor.

With the recent rapid development of powerful and fast microcontrollers, there is increasing attention to the exploration of model predictive control (MPC) for various topologies of power converters [16-18]. The MPC algorithms can eliminate the use of pulse width modulation (PWM) techniques and conventional PID controllers. In addition, the MPC control algorithms can take the nonlinearities of controlled objects into account.

This research focuses on the development of an effective controller for a chopper-fed DC motor drive using the Finite Control Set-Model Predictive Control (FCS-MPC) theory. Specifically, a motor speed predictive control strategy and its practical implementation have been presented in detail. It has been shown that the proposed control method can be used to control the motor speed very effectively. The proposed control method can result in good dynamic responses compared to the use of a conventional PI controller. Moreover, the proposed MPC-based method in this study is simple and easy to implement on low-cost hardware. In this study, the proposed control method is implemented on an STM32F4 Discovery board which is conveniently programmed using MATLAB Simulink. The analysis for obtaining the discrete model can be also used for other controlled objects.

The rest of this paper is divided into subsequent sections. Section 2 provides the concept of MPC for controlling power electronic converters and electric drives. The motor parameter estimation process is described in Section 3. The procedure for designing an MPC controller for a chopper-fed brushed DC motor is described in Section 4. The simulation and experimental results obtained are presented in Section 5. Finally, Section 6 is the conclusion of this research.

2. MODEL PREDICTIVE CONTROL

Model predictive control (MPC) emerged as an advanced process control method in the 1960s. In the future, this control technique will be expected to be very effective for various nonlinear, multiple-input multiple-output (MIMO) systems. In MPC, the model of the controlled object is considered to predict the future behaviours of the variables over a time frame. These predictions are then used for evaluating a cost function and the choice of the optimal action for the system based on the minimum value of the cost function. The MPC has several advantages such as the inclusion of nonlinearities and constraints of control systems. Another advantage of MPC in power converters and electric drives is to take the consideration the inherent discrete nature of power converters. As power converters only have a finite number of switching states, the MPC optimisation problem can be simplified to behaviours of possible switching states of power converters. In every sampling interval, the predicted variables are used to evaluate a cost function. This is also known as the Finite Control Set-Model Predictive Control (FCS-MPC). Therefore, this study only focuses on FCS-MPC for a DC chopper driving a brushed DC motor.

Fig. 1 shows the operating principle of FCS-MPC. The control process of power converters and electric drives can be defined as the determination of an appropriate control action $S(t)$ for the gate signals of power converter switches to obtain a desired system variable x(t) as close as possible to a reference value $x^*(t)$.

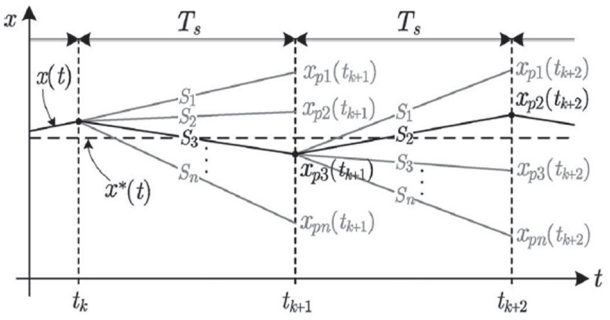

Fig. 1. The FCS-MPC operating principle

In a specific sampling period T_s, the variable $x(t)$ is sampled as $x(t_k)$ for evaluating the cost function with possible control actions of the power converter (S_1,...,S_N). If the action control S_3 is selected, it can be used to predict the future value $x_{p3}(t_k+1)$. Next, the predicted value in the previous sampling period will be used to compute the cost function for selecting the control action S_2 corresponding to the minimum value of the cost function. Similarly, $x_{p2}(t_k+2)$ can be also predicted based on $x_{p3}(t_k+1)$ and the control action S_2. In general, the possible predictive values of the control variable $x(t)$ can be expressed as:

$$x_{pi}\left(t_{k+1}\right) = f_p\left\{x\left(t_k\right), S_i\right\} \qquad i = 1,\ldots,\mathrm{N} \tag{1}$$

where f_p is the prediction function obtained from the controlled model. Then a cost function is defined as:

$$g_i = \left|x^*\left(t_{k+1}\right) - x_{pi}\left(t_{k+1}\right)\right| \qquad i = 1,\ldots,\mathrm{N} \tag{2}$$

The evaluation of the cost function (2) results in N values of the cost function. The control action leading to the minimum value of the cost function is finally selected.

3. PARAMETER ESTIMATION OF BRUSHED DC MOTORS

For brushed DC motors, a DC voltage can be directly applied to the terminal of the armature circuit. Using Kirchhoff's law for the armature circuit gives:

$$V_{dc}(t) = R_a i_a(t) + L_a \frac{di_a(t)}{dt} + K\omega(t) \quad (3)$$

Based on Newton's law, the torque equation can be derived as follows:

$$Ki_a(t) = J\frac{d\omega(t)}{dt} + D\omega(t) + T_L(t) \quad (4)$$

Where K, R_a, L_a, J and D are the back-EMF constant, the armature resistance, the armature inductance, the rotor mass moment of inertia, and the damping constant, respectively. $\omega(t)$, $i_a(t)$, $V_{dc}(t)$ and $T_L(t)$ denote the rotor angular velocity, the armature current, the terminal voltage, and the load torque, respectively.

At the steady-state, equation (3) yields:

$$\omega = \frac{V_{dc}}{K} - \frac{R_a I_a}{K} = \omega_0 - \Delta\omega \quad (5)$$

In which:

$$\omega_0 = \frac{V_{dc}}{K} \quad (6)$$

$$\Delta\omega = \frac{R_a I_a}{K} \quad (7)$$

In equations (6) and (7), $\omega 0$ is the no-load rotor angular velocity and $\Delta\omega$ is the drop of the rotor angular velocity when a load torque is applied to the motor rotor. The back-EMF constant can be determined through the terminal voltage and the no-load rotor angular velocity as follows:

$$K = \frac{V_{dc}}{\omega_0} \quad (8)$$

When a load torque is applied to the motor shaft, the armature current is measured to calculate the armature resistance as follows:

$$R_a = \frac{V_{dc} - K\omega}{I_a} \quad (9)$$

According to equation (9), if V_{dc} is kept being a constant, ω can be measured using a tachometer or an encoder, and I_a can be measured using a DC ammeter, then the value of R_a can be computed.

The Laplace transforms of equations (3) and (4) have the following forms:

$$V_{dc}(s) = R_a I_a(s) + L_a s I_a(s) + K\omega(s) \quad (10)$$

$$Js\omega(s) = KI_a(s) - D\omega(s) - T_L(s) \quad (11)$$

Where s is the Laplace operator. $V_{dc}(s)$, $I_a(s)$, $\omega(s)$ and $T_L(s)$ are the Laplace transforms of the terminal voltage, the armature current, the rotor angular velocity, and the load torque, respectively.

From equations (10) and (11), the relationship between the rotor angular velocity (the system output) and the terminal voltage, and the load torque (the system inputs) can be expressed as follows:

$$\omega(s) = \frac{KV_{dc}(s) - T_L(s)(sL_a + R_a)}{s^2 L_a J + s(R_a J + L_a D) + (R_a D + K^2)} \quad (12)$$

In the no-load regime ($T_L(s) = 0$), equation (12) yields:

$$\omega(s) = \frac{K}{s^2 L_a J + s(R_a J + L_a D) + (R_a D + K^2)} V_{dc}(s) \quad (13)$$

Equation (13) indicates a second-order system and can be shorten as follows:

$$\frac{\omega(s)}{V_{dc}(s)} = \frac{a}{s^2 + sb + c} \quad (14)$$

in which:

$$a = \frac{K}{L_a J} \quad b = \frac{R_a J + L_a D}{L_a J} \quad c = \frac{R_a D + K^2}{L_a J} \quad (15)$$

The coefficients a, b, and c of equation (14) can be obtained by acquiring the start-up motor speed with respect to the step terminal voltage and the MATLAB System Identification Toolbox [19]. According to equation (15), K and R_a can be determined using equations (8) and (9). Three remaining parameters of the motor can be computed as follows:

$$D = \frac{1}{R_a}\left(\frac{cK}{a} - K^2\right) \quad (16)$$

$$L_a = \frac{bK - \sqrt{(bK)^2 - 4aDKR_a}}{2aD} \quad (17)$$

$$J = \frac{K}{aL_a} \quad (18)$$

4. MODEL PREDICTIVE CONTROL OF CHOPPER-FED BRUSHED DC MOTOR

If the sampling interval T_s is small enough, the derivative of the armature current can be approximated as follows:

$$\frac{di_a(t)}{dt} = \frac{i_a(t_k) - i_a(t_{k-1})}{T_s} \quad (19)$$

Fig. 2 shows the principle circuit of a brushed DC motor driven by a DC chopper. Fig. 3. shows the armature circuit when the switch S is closed. The armature circuit of the motor is depicted in Fig. 4.

Substituting (19) into (3) gives:

$$V_{dc} = \left(R_a + \frac{L_a}{T_s}\right) i_a(t_k) - \frac{L_a}{T_s} i_a(t_{k-1}) + K\omega(t_k) \quad (20)$$

Equation (20) corresponds to the switch S is closed. When the switch S is opened, the equation (20) yields:

$$0 = \left(R_a + \frac{L_a}{T_s}\right) i_a(t_k) - \frac{L_a}{T_s} i_a(t_{k-1}) + K\omega(t_k) \quad (21)$$

Equation (20) and (21) can be combined to give:

$$V_{dc}u = \left(R_a + \frac{L_a}{T_s}\right) i_a\left(t_k\right) - \frac{L_a}{T_s} i_a\left(t_{k-1}\right) + K\omega\left(t_k\right) \quad (22)$$

where u is the binary control signal for the switch S

- if u = 1, S is closed.
- if u = 0, S is opened.

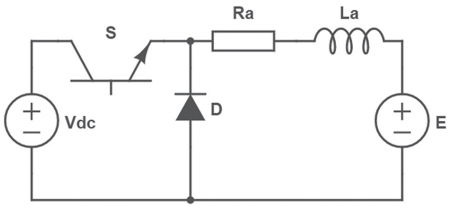

Fig. 2. The principle circuit of DC motor fed by a DC chopper

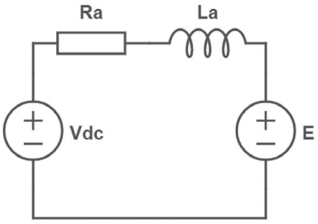

Fig. 3. The armature circuit when the switch S is closed

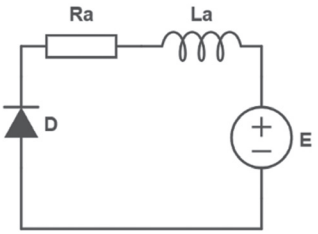

Fig. 4. The armature circuit when the switch S is opened

Equation (22) can be re-written as follows:

$$i_a\left(k\right) = \frac{uT_sV_{dc}}{R_aT_s + L_a} - \frac{KT_s\omega\left(t_k\right)}{R_aT_s + L_a} + \frac{L_a i_a\left(t_{k-1}\right)}{R_aT_s + L_a} \quad (23)$$

Applying the two-step-ahead prediction for equation (23) gives:

$$i_a\left(t_{k+1}\right) = \frac{uT_sV_{dc}}{R_aT_s + L_a} - \frac{KT_s\omega\left(t_{k+1}\right)}{R_aT_s + L_a} + \frac{L_a i_a\left(t_k\right)}{R_aT_s + L_a} \quad (24)$$

Re-arranging (24) results in:

$$\omega\left(t_{k+1}\right) = \frac{V_{dc}u}{K} - \frac{\left(R_aT_s + L_a\right) i_a\left(t_{k+1}\right)}{KT_s} - \frac{L_a i_a\left(t_k\right)}{KT_s} \quad (25)$$

Equation (24) and (25) are used to design a MPC controller for the speed control of the motor. A cost function is defined according to the difference of the reference and future speeds as follows:

$$g = \left|\omega^* - \omega\left(t_{k+1}\right)\right|$$

In every sampling interval, there are two possible switching states of the switch S: the switch S is closed, and the switch S is opened. The optimal state of the switch S will be selected corresponding to the minimum value of the cost function. Fig. 5 is a flowchart of the algorithm of the MPC controller.

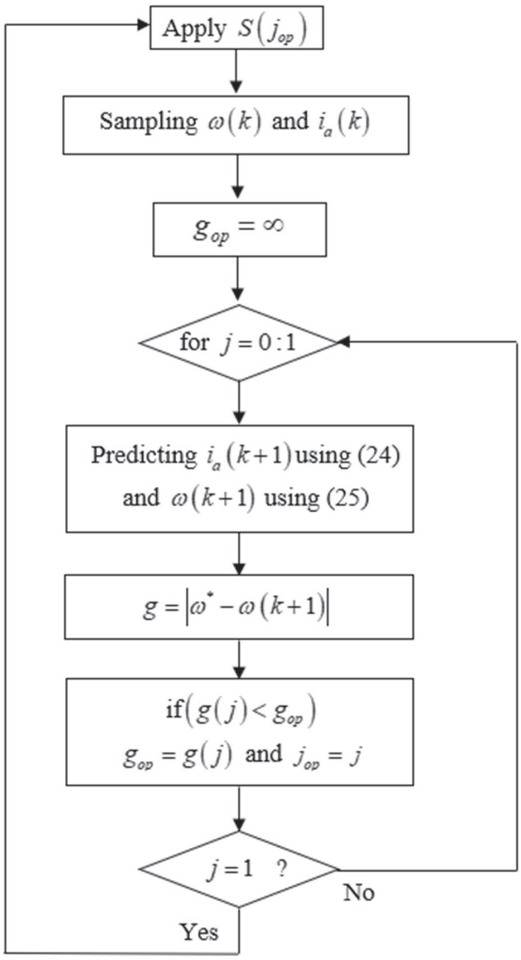

Fig. 5. Flowchart of the MPC control algorithm.

5. SIMULATION AND EXPERIMENTAL RESULTS

This section describes the procedure for deploying an experimental system for the MPC-based speed control of a brushed DC motor. The whole system is shown in Fig. 6. Table 1 is the specification of the experimental system.

Table 1. Specification of the experimental syste.

No	Items
1	An excited-separately 175W DC motor
2	An IGBT-based DC chopper can be controlled by an external signal
3	A dynamometer is used to adjust the load torque
4	An isolated current measurement module is used to measure the armature current
5	Speed measurement and load torque modules are integrated with the dynamometer
6	A laptop is used to monitor the performance of the system
7	An Arduino MEGA 2560 board
8	A STM32F4 Discovery board

A. Motor Parameter Estimation

Fig. 7 is a Simulink diagram for acquiring the output speed response according to the step input voltage in the no-load regime. The motor speed and armature current were acquired by using a Simulink diagram as shown in Fig. 8. The output speed response according to the step input voltage in the no-load regime is illustrated in Fig. 9.

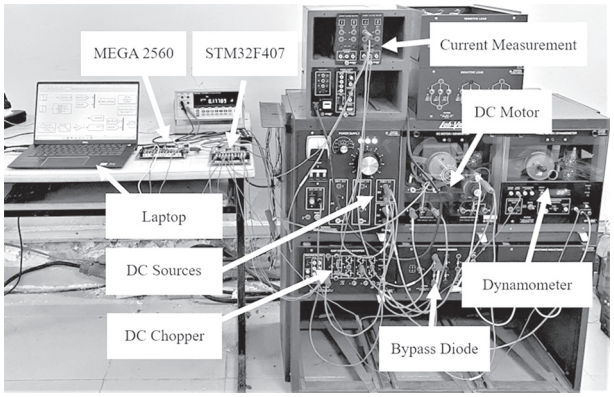

Fig. 6. The whole experimental system

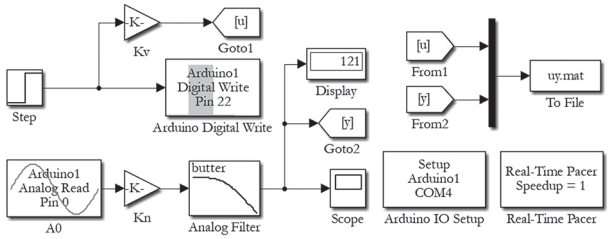

Fig. 7. Simulink diagram for acquiring the output speed response according to the step input voltage

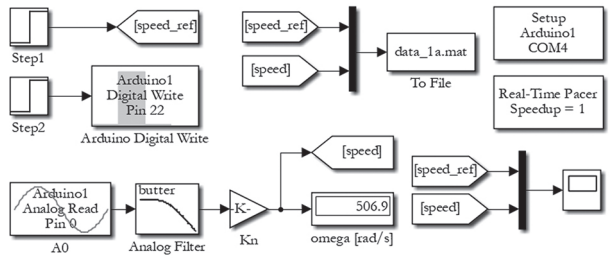

Fig. 8. Simulink diagram for acquiring the motor speed and the armature current

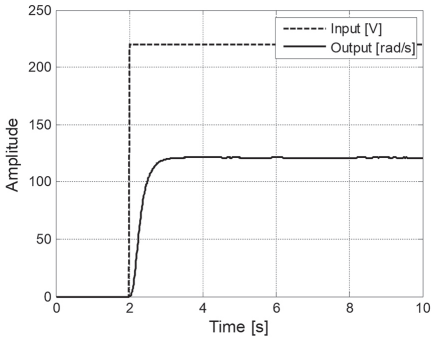

Fig. 9. The output speed response according to the step input voltage of the motor in the no-load regime

The data acquired from the no-load experiment including the step input voltage and the rotor angular velocity as shown in Fig. 9 was then used to estimate the transfer function of the motor. By using the MATLAB System Identification Toolbox [19], the transfer function of the motor in the no-load regime has the following form:

$$\frac{\omega(s)}{V_a(s)} = \frac{18.34}{s^2 + 10.36s + 33.62} \tag{27}$$

Therefore

$$a = 18.34; b = 10.36; c = 33.62 \tag{28}$$

The back-EMF coefficient is calculated as:

$$K = \frac{V_a}{\omega_0} = \frac{228}{126} = 1.8095\left[V / ras / s\right] \tag{29}$$

If applying T_L= 2.5 [N.m] to the rotor shaft and the measurements are $\omega 1$ = 108[rad/s] and I_a=1.397 [A], then the resistance of the armature circuit is computed as:

$$R_a = \frac{V_a - K\omega}{I_a} = \frac{220 - 1.8095 \times 108}{1.397} = 17.5887\left[\Omega\right] \tag{30}$$

The damping constant is determined as:

$$\begin{aligned} D &= \frac{1}{R_a}\left(\frac{cK}{a} - K^2\right) \\ &= \frac{1}{17.5887}\left(\frac{33.62 \times 1.8095}{18.34} - 1.8095^2\right) \\ &= 24 \times 10^{-4}\left[N.m.s\right] \end{aligned} \tag{31}$$

The armature inductance is computed as:

$$L_a = \frac{bK - \sqrt{(bK)^2 - 4aDKR_a}}{2aD} = 1.7047\left[H\right] \tag{32}$$

Finally, the moment of inertia is given by:

$$J = \frac{K}{aL_a} = \frac{1.8095}{18.34 \times 1.7047} = 0.0579\left[kg.m^2\right] \tag{33}$$

B. Simulation Results

Fig. 10 shows a Simulink diagram for investigating the performance of the PI controller. The simulated speed step increment with the PI controller is illustrated in Fig. 11 and the simulated speed step decrement with the PI controller is depicted in Fig. 12.

Fig. 13 displays a Simulink diagram for investigating the performance of the MPC controller. The MPC algorithm is developed using a user-defined function as follows:

---

function S = MPC(speed_ref,speed,ia)
R_a = 17.5887;
L_a = 1.7047;
K = 1.8095;
V_{dc} = 230;
T_s = 0.2;
$omega_{ref}$ = $speed_{ref}$*pi/30;
$omega$ = $speed$*pi/30;
g_{opt} = inf;

$S_{opt} = 0$;
for $S = 0{:}1$
$ia_1 = T_s*V_{dc}/(R_a*T_s + L_a)*S + L_a/(R_a*T_s + L_a)*ia - K*T_s/(R_a*T_s + L_a)*omega$;
$omega_1 = V_{dc}/K*S - (R_a*T_s + L_a)/K/T_s*ia_1 + La/K/Ts*ia$;
$g = abs(omega_{ref} - omega_1)$;
if $(g < g_{opt})$
$g_{opt} = g$;
$S_{opt} = S$;
end
end
$S = S_{opt}$;

The simulated speed step increment with the MPC controller is shown in Fig. 14. Lastly, the simulated speed step decrement with the MPC controller is illustrated in Fig. 15.

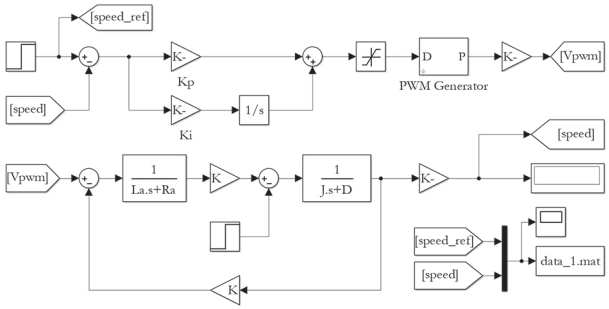

Fig. 10. Simulink diagram for investigating the performance of the PI controller

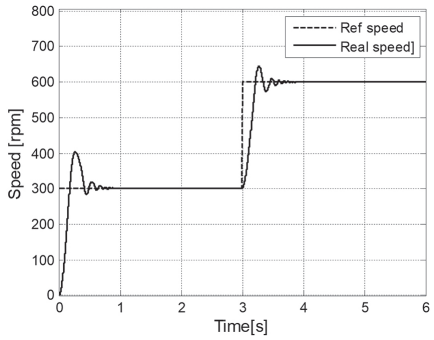

Fig. 11. Simulated speed step increment with the PI controller

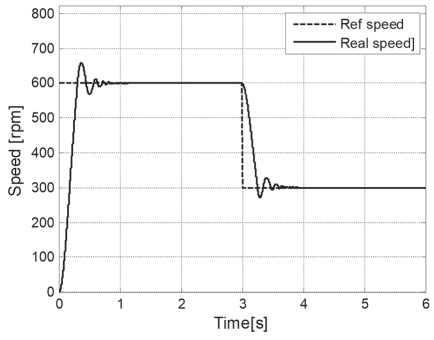

Fig. 12. Simulated speed step decrement with the PI controller

The simulated speed step increment with the MPC controller is shown in Fig. 14. Lastly, the simulated speed step decrement with the MPC controller is illustrated in Fig. 15.

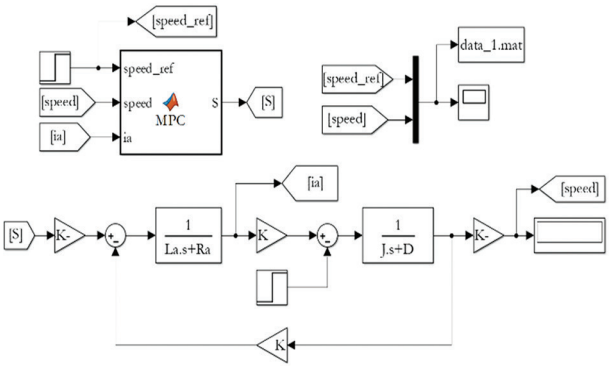

Fig. 13. Simulink diagram for investigating the performance of the MPC controller

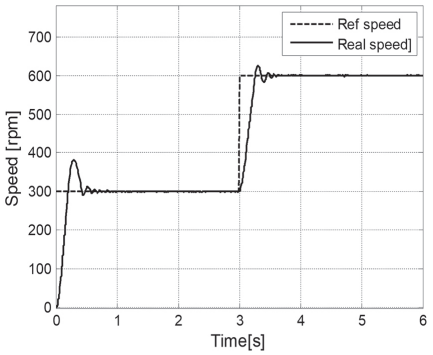

Fig. 14. Simulated speed step increment with the MPC controller

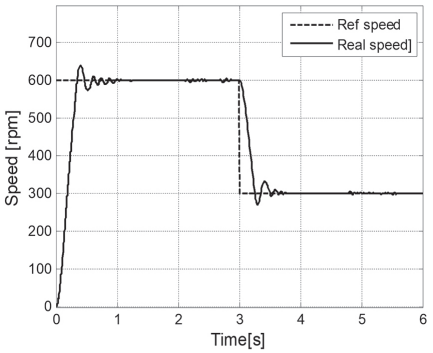

Fig. 15. Simulated speed step decrement with the MPC controller

C. Experimental Results

Fig. 16 is a Simulink diagram using the Waijung Blockset for deploying a discrete-time PI controller on the STM32F4 board [20]. The change of the reference speed is controlled by an external signal at pin PA1 of the board. The PI controller has the proportional constant K_P = 100 and the integral constant K_I = 0,1. The sampling period is 0,0001[s]. Fig. 17 is a Simulink diagram using the Waijung Blockset for deploying the MPC controller on the STM32F4 Discovery board.

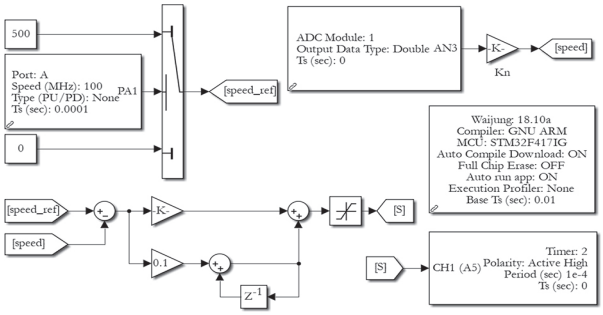

Fig. 16. Simulink diagram of the PI controller using the Waijung Blockset

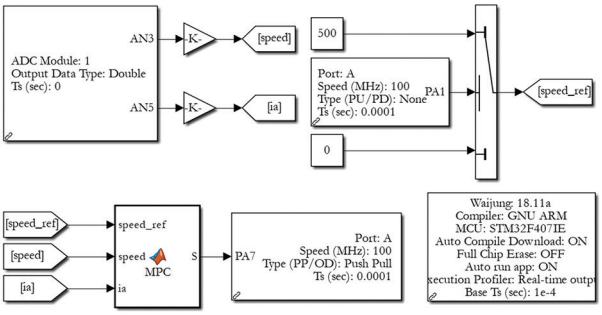

Fig. 17. Simulink diagram of the MPC controller using the Waijung Blockset.

Fig. 18 is the real speed step increment with the PI controller. Fig. 19 is the real speed step decrement with the PI controller. The real speed step increment with the MPC controller is depicted in Fig. 20. Finally, the real speed step decrement with the MPC controller is illustrated in Fig. 21.

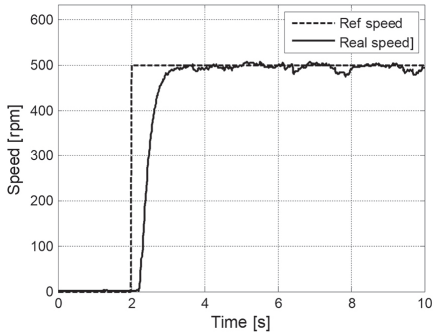

Fig. 18. Real speed step increment with the PI controller

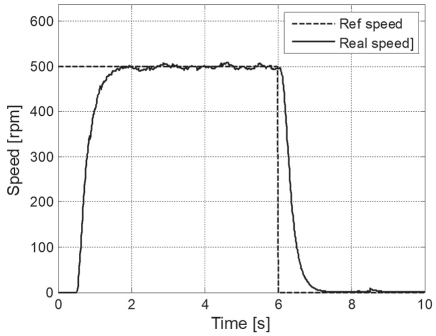

Fig. 19. Real speed step decrement with the PI controller

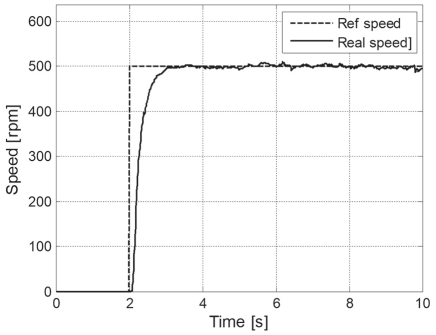

Fig. 20. Real speed step increment with the MPC controller

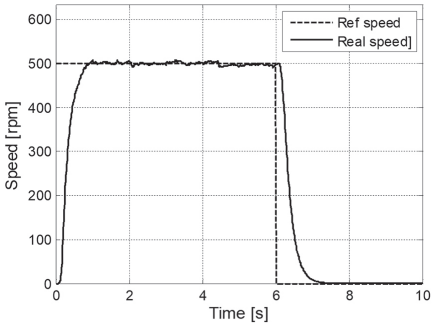

Fig. 21. Real speed step decrement with the MPC controller

The data of the motor speed steps in Figs. 19 and 21 are used to investigate the performances of the PI and MPC controllers. Table 2 is a comparison between the performances of the real PI and MPC controllers. The rise time, settling time and overshoot are considered. Compared to the PI controller, the use of the MPC controller can result in all the reduction of the rise time, settling time and overshoot. Therefore, the MPC controller can outperform the PI controller.

Table 2. Comparison between the performances of the PI and MPC controllers

Controller	Rise Time (s)	Settling Time (s)	Overshoot (%)
PI Controller	0.5599	2.2675	1.4714
MPC Controller	0.4340	2.1093	1.2005

6. CONCLUSION

This study shows that FCS-MPC can be successfully applied to the speed control of brushed DC motors. This control algorithm does not require the use of PWM techniques and conventional PI controllers. The procedure for developing the MPC controller needs the model of the motor. The motor parameters can be conveniently estimated using the measured data and the MATLAB System Identification Toolbox. Finally, with the high performance of the whole system has been given by the proposed control method, the FSC-MPC method can be seen as the most powerful model-based control approach. The future work of this research is to deploy effective MPC controllers for other types of controlled objects such as popular power electronic converters and electric drives.

7. REFERENCES

[1] M. Li, Y. Ma, "Parameter Identification of DC Motor based on Compound Least Square Method", Proceedings of the IEEE 5th Information Technology and Mechatronics Engineering Conference, Chongqing, China, 12-14 June 2020, pp. 1108-1111.

[2] Rubaai, R. Kotaru, "Online identification and control of a DC motor using learning adaptation of neural networks", IEEE Transactions on Industry Applications, Vol. 36, No. 3, 2000, pp. 935-942.

[3] H. Zhou, "DC Servo Motor PID Control in Mobile Robots with Embedded DSP", Proceedings of the International Conference on Intelligent Computation Technology and Automation, Changsha, China, 20-22 October 2008, pp. 332-336.

[4] J. J. Muoz-Cesar, E. A. Merchan-Cruz, L. H. Hernandez-Gomez, E. Guerrero-Guadarrama, A. Jimenez-Ledes, "Speed Control of a DC Brush Motor with Conventional PID and Fuzzy PI Controllers", Proceedings of the Electronics, Robotics and Automotive Mechanics Conference, Cuernavaca, Mexico, 2008, pp. 344-349.

[5] M. S. Qureshi, P. Swarnkar, S. Gupta, "Assessment of DC servo motor with sliding mode control approach", Proceedings of the IEEE First International Conference on Control, Measurement and Instrumentation, Kolkata, India, 8-10 January 2016, pp. 351-355.

[6] H.-P. Ren, R. Zhou, J. Li, "Adaptive backstepping sliding mode tracking control for DC motor servo system", Proceedings of the Chinese Automation Congress, Jinan, China, 20-22 October 2017, pp. 5090-5095.

[7] Munadi, M. A. Akbar, "Simulation of fuzzy logic control for DC servo motor using Arduino based on MATLAB/Simulink", Proceedings of the International Conference on Intelligent Autonomous Agents, Networks and Systems, 2014, pp. 42-46.

[8] J. O. Jang, "A deadzone compensator of a DC motor system using fuzzy logic control", IEEE Transactions on Systems, Man, and Cybernetics, Part C, Vol. 31, no, 1, 2001, pp. 42-48.

[9] M. A. Rahman, M. A. Hoque, "On-Line Self-Tuning ANN-Based Speed Control of a PM DC Motor", IEEE Transactions on Mechatronics, Vol. 2, No. 3, 1997, pp. 169-178.

[10] Z. Runjing, Y. Waiting, Zhangfei, "Application of NN-PI Controller in Direct Current Motor Servo System", Proceedings of the 8th International Conference on Electronic Measurement and Instruments, 2007, pp. 468-471.

[11] J. Pongfai, W. Assawinchaichote, "Self-tuning PID parameters using NN-GA for brush DC motor control system", Proceedings of the 14th International Conference on Electrical Engineering/Electronics, Computer, Telecommunications and Information Technology, Phuket, Thailand, 27-30 June 2017, pp. 111-114.

[12] S. D. Sahputro, F. Fadilah, N. A. Wicaksono, F. Yusivar, "Design and implementation of adaptive PID controller for speed control of DC motor", Proceedings of the 15th International Conference on Quality in Research (QiR): International Symposium on Electrical and Computer Engineering, Nusa Dua, Bali, Indonesia, 24-27 July 2017, pp. 179-183.

[13] E. Afjei, A. Nadian Ghomsheh, A. Karami, "Sensorless speed/position control of brushed DC motor", Proceedings of the International Aegean Conference on Electrical Machines and Power Electronics, Bodrum, Turkey, 10-12 September 2007.

[14] R. M. Ramli, N. Mikami, H. Takahashi, "Adaptive filters for rotational speed estimation of a sensorless DC motor with brushes", Proceedings of the 10th International Conference on Information Science, Signal Processing, and their Applications, Kuala Lumpur, Malaysia, 10-13 May 2010, pp. 562-565.

[15] D. Ertl, L. Weber, "A Method for Real-Time Sensorless Speed Control of Brushed DC Motors in Cost Constrained Systems", Proceedings of the 2nd Global Power, Energy and Communication Conference, Izmir, Turkey, 20-23 October 2020, pp. 152-157.

[16] S. Kouro, P. Cortes, R. Vargas, U. Ammann, J. Rodriguez, "Model Predictive Control—A Simple and Powerful Method to Control Power Converters", IEEE Transactions on Industrial Electronics, Vol. 56, No. 6, pp. 1826-1838.

[17] J. Baek, S. Kim, S. Kwak, "Predictive control method for load current of single-phase voltage source inverters", Proceedings of the IEEE Applied Power Electronics Conference and Exposition, Charlotte, NC, USA, 15-19 March 2015.

[18] R. E. Pérez-Guzmán, M. Rivera, N. Vicencio, P. Wheeler, "Model-based Predictive Control in Three-Phase Inverters", Proceedings of the IEEE International Conference on Industrial Technology, Buenos Aires, Argentina, 26-28 February 2020.

[19] MATLAB System Identification Toolbox, https://www.mathworks.com/products/sysid.html (accessed: 2023)

[20] Waijung Blockset, https://waijung1.aimagin.com (accessed: 2023)

Artificial Intelligent Maximum Power Point Controller based Hybrid Photovoltaic/Battery System

Original Scientific Paper

Aymen Kadhim Mohaisen
Southern Technical University, Amara Technical Institute, Department of Electrical Power
Amara, Iraq
aymenks@stu.edu.iq

Abstract *– Photovoltaic (PV) cells have non-linear properties influenced by environmental factors, including irradiation and temperature. As a result, a method known as maximum power point tracking (MPPT) was implemented to boost the PV cells' efficiency and make the most of the energy they could provide. The traditional perturb and observe (P&O) approach for determining the maximum power point tracking (MPPT) has various drawbacks, including poor steady-state performance, increased oscillation around the MPP point, and delayed reaction. As a result, this work aims to present a hybrid fuzzy logic (FL) and P&O MPPT approach to improve the PV system's performance coupled to the lithium battery storage system. Matlab/Simulink is used to bring the suggested technique to life, after which its efficacy is evaluated in the context of rapid changes in the irradiance level. According to the findings of the simulations, the suggested strategy has the potential to enhance the steady-state performance of PV systems in terms of oscillation and time response. Finally, the proposed results are compared with that obtained by the conventional P&O technique, and the stress of PV power is limited to ΔP=1kW and the overshoot power is limited to 5%.*

Keywords*: Artificial Intelligent Maximum Power Point Controller, photovoltaic/ battery system, fuzzy P&O controller, power management, hybrid power system*

1. INTRODUCTION

Photovoltaic (PV) cells, also known as solar cells, have several non-linear characteristics that can impact their performance and behavior. These include the Current-Voltage (I-V) Curve, which describes the relationship between current and voltage across the cell, which is non-linear and typically follows a characteristic shape. The I-V curve consists of four regions: open circuit, short circuit, maximum power point, and reverse bias. The non-linearity arises from factors like recombination, series and shunt resistances, and temperature effects [1, 2]. Temperature dependence is another non-linear characteristic of PV cells, as temperature influences performance. As temperature increases, the output voltage decreases while the current increases, decreasing overall power output. The temperature coefficient of a PV cell quantifies this non-linear relationship.

Non-uniform illumination, such as shading or partial coverage, can significantly reduce a cell's overall power output due to bypass diodes and current mismatch. The diode junction exhibits non-linear behavior, acting like a diode but not perfectly ideal due to non-zero idealist factors and series resistance [2]. These effects can introduce non-linear behavior in response to high-frequency light intensity or voltage variations.

Hysteresis is the phenomenon where the I-V curve of a PV cell depends on the history of the previous operation, which can be observed during rapid changes in light intensity or dynamic operating conditions. This implies that the same voltage may generate distinct currents depending on whether the voltage is rising, falling, or staying the same. Understanding and modeling these non-linear characteristics is crucial for accurately predicting and optimizing PV system performance, designing efficient power converters, maximum power point tracking (MPPT) algorithms, and overall system integration [3]. The classification of the MPPT methods can be shown in Fig.1.

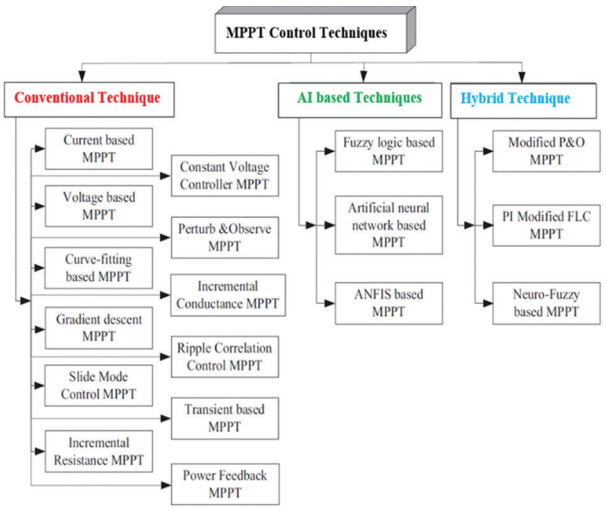

Fig.1. Classification of the most used MPPT techniques

The authors of [4] suggested using a constant voltage controller, sometimes known as a CVC, to maximize the peak power output of PV panels. This technique required little in the way of resources and was easy to put into practice experimentally; nevertheless, the results were less accurate and productive. Despite this, several researchers have suggested and evaluated techniques that are straightforward and inexpensive, such as the perturb and observe (P&O) and incremental conductance (IC) techniques [5-8]. Even though these methods were uncomplicated and straightforward to put into practice, they had a great deal of drawbacks.

When using a P&O approach, there is a greater amount of oscillation around the MPPT, which increases power loss and a drop in the control efficiency. In addition, the IC technique has several limitations, the most notable of which are oscillation and transitory response in the face of rapid change in solar irradiance [9]. Because of this, the variable size incremental conductance approach has been proposed as a solution to the problems currently facing the CVC, P&O, and IC procedures [9, 10].

In addition, the authors in [11, 12] offered the AI approaches based on MPPT to overcome the major difficulties in classical techniques such as fuzzy logic (FL) and neural networks (ANN). These methods based on nonlinear theory also contribute to the increased number of benefits they present compared to more traditional approaches. Consequently, they regarded a robust MPPT and had higher performance in calculating the PV module's operational point under various atmosphere conditions [13, 14]. A hybrid MPPT approach is also used to augment AI techniques such as proportional-integral (PI) with FL or ANN. This technique is used to improve AI techniques by increasing convergence speed.

A fuzzy logic-based MPPT approach was presented by Yaqoob et al. [15] to increase the dynamic response of a PV module connected to pure DC load and subjected to a rapid shift in the amount of solar irradiation. Mat lab/Simulink is used to evaluate the performance of the suggested approach and verify it. Compared to the traditional IC and P&O methods, the use of FL MPPT yields superior results in terms of output quality. Also, Fapi et al. [16] reported a real-time experiment with FL-based MPPT utilizing a digital signal processing (DSP) microcontroller. The findings demonstrate that the suggested method is less complicated, efficient, and reliable than the other common approaches.

Creating a Neuro-Fuzzy MPPT controller is the subject of the study [17]. Initially, the suggested MPPT control is constructed in a state of offline operation, which is necessary for testing various ANN designs and variables. The goal of this method is to design an efficient hybrid technique. The results of the proposed MPPT controller are excellent in obtaining the optimal voltage of the module to track the MPP with a fast time response. The authors in [18] proposed a novel coordinated MPPT method for a grid-connected PV system's inverter. Both the DC boost converter, which is responsible for MPPT of the PV plant, and the inverter, which is responsible for DC voltage set-point management, specialized reactive current injection on demand, and decreased harmonic content of AC grid currents, work together to achieve the system's control goals.

A hybrid FL-P&O-based MPPT is utilized in this article to optimize the output power of the PV system regardless of the weather conditions. The main goal of this work is to provide a variable step size for the P&O using the FL method. In addition, the suggested approach for MPPT analysis is also modeled, and simulated with the help of the MATLAB simulation program. Additionally, the performance of the FL-P&O MPPT is evaluated using a variety of solar irradiances, and these results are compared to those obtained using the more traditional P&O MPPT method.

This research is organized as follows: section 2 presents photovoltaic cell modeling. Section 3 introduces a hybrid PV/battery system. Section 4 presents the proposed MPPT controller. Section 5 indicates the results and discussion, while the conclusion of this paper is presented in section 6.

2. PHOTOVOLTAIC CELL MODELLING

The equivalent circuit of a PV cell, also known as a solar cell, is a simplified representation that models the cell's electrical behavior [17]. It consists of several components, including the single-diode model, which includes photocurrent (Iph), diode current (Id), switch resistance (Rsh), and series resistance (Rs). The photocurrent (Iph) is proportional to the intensity of incident light, while the diode current (Id) is modeled by the p-n junction diode's behavior. The series resistance (Rs) represents resistive losses in the cell's electrical connections and materials, representing the overall resistance in series with the diode and load [19, 20].

However, the PV cell or module current can be written from the semiconductors theory as follows [21, 22].

$$I = I_{PH} - I_o \left[exp\left(\frac{q\,V}{\alpha\,V_t}\right) - 1 \right] - \frac{V + R_s\,I}{R_p} \quad (1)$$

where I is the PV current, V is the PV voltage, V_t (=$N_s\,K\,T/q$) is the thermal voltage (25.7 mV at 25°C) with N_s cells of module, T is the temperature in °C, R_p and R_s are the shunt and series resistances, I_{PH} is the source of photocurrent, I_o is saturation current, α is the constant factor, q is the electron's charge (1.60217646×10^{-19} C), K is the Boltzmann constant (1.3806503×10^{-23} $J/°K$). Fig. 2 shows a model PV cell.

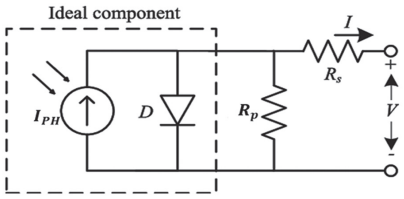

Fig. 2. Single–diode PV cell model

The I_{PH} can be expressed as follows [22].

$$I_{PH} = (I_{PHn} + K_i \Delta T)\frac{G}{1000} \quad (2)$$

Where the change in temperature ΔT, G represents the solar irradiance. To model the PV module, the diode saturation current can be determined as in (3),

$$I_o = I_{on}\left(\frac{T_n}{T}\right)^3 exp\left[\frac{qE_g}{\alpha K}\left(\frac{1}{T_n} - \frac{1}{T}\right)\right] \quad (3)$$

Where Ion is the reverse saturation, temperature (T=25°C), and E_g is the band-gap energy (E_g=1.12). moreover, this current can be written as [20,21],

$$I_{on} = \frac{I_{scn}}{exp\left[\frac{V_{ocn}}{\alpha\,V_{th}}\right] - 1} \quad (4)$$

This study uses the KC200GT PV panel technology to form the required PV system. The electrical parameters under STC conditions of this panel are listed in Table 1.

Table 1. The electrical parameters of the KC200GT PV panel in STC conditions

Parameter	Value
P_{mp}	200W
V_{oc}	32.9 V
V_{mp}	26.3 V
I_{sc}	8.21 A
I_{mp}	7.61 A
K_i	0.0032 A/K
K_v	-0.123 V/K
α	1.3
N_s	54

3. HYBRID PV/BATTERY SYSTEM

The PV-battery system is most used in PV applications, which is used in its configuration. The PV system offers the required power at the sun's availability. At the same time, the battery devices are used as a backup energy storage system at night or in partial shading effect conditions. In recent years, different control strategies have been used to control the power-sharing between the PV system and the battery [23].

Power management or power sharing control is very important to increase efficiency, and the proposed system structure is shown in this paper.

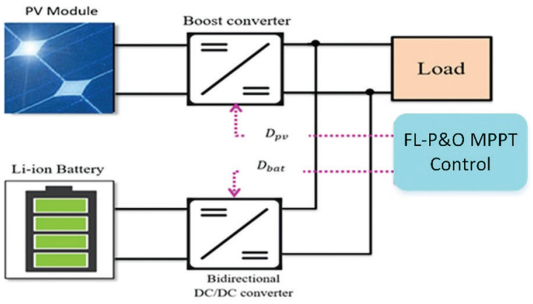

Fig. 3. Proposed PV/battery system structure

In Fig.3, the hybridization between the PV module and battery is considered to share the optimal power between them and the DC load side.

3.1. BATTERY CONTROL MANAGEMENT

Battery management control (BMC) systems offer numerous benefits in various applications, including extended battery life, enhanced safety, optimal performance, increased efficiency, state-of-charge (SOC) monitoring, cell balancing, data logging and analysis, integration and compatibility, remote monitoring and control, scalability, and expandability. These systems help maximize battery life by monitoring and regulating charging and discharging processes, preventing overcharging, over-discharging, and overheating [24]. They also ensure safe operation by incorporating safety features like overcurrent protection, overvoltage protection, and short-circuit protection. Optimal performance is maintained by actively managing charging and discharging processes, ensuring consistent and reliable power delivery. Increased efficiency is achieved by optimizing charging algorithms, reducing power losses, and improving energy conversion efficiency. State-of-Charge (SOC) monitoring provides real-time information about remaining capacity, enabling users to accurately estimate battery runtime and plan activities accordingly. Cell balancing ensures equal charge levels in multiple cells, preventing overcharging or over-discharging [25].

In conclusion, battery management control systems are crucial for optimizing battery performance, extending battery life, ensuring safety, and improving energy

efficiency in various applications. The hybrid PV/battery system used in this paper depends on the lithium-battery model that is presented in Matlab/Simulink, as shown in Fig.4. The output voltage of the battery V_{btt} can be expressed as [25].

$$V_{btt} = E_0 - K\,\frac{Q}{Q-i_t} - R_b i + A_b\, e^{(-Bi_t)} K\,\frac{Q}{Q-i_t} i^* \qquad (5)$$

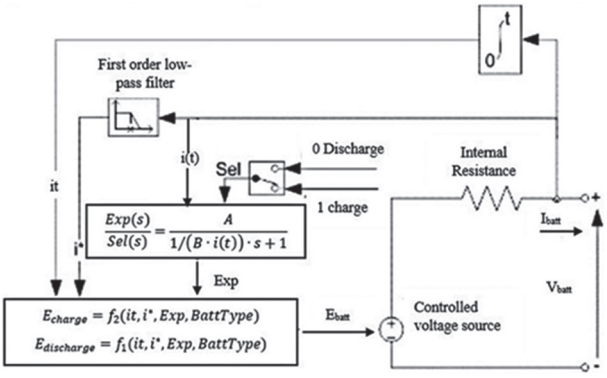

Fig. 4. The Battery electrical circuit module

Where E_0 is the battery constant voltage (V), K is the constant of the polarization (V/Ah), Q is the capacity of the battery (Ah), i_t is the actual charge of the battery (Ah), R_b is the battery internal resistance (Ω), A_b is the exponential zone amplitude (V), B is the time constant inverse of the exponential zone (Ah^{-1}), i^* is the filtered battery current (A). Also, the polarization resistance, Pol_{res} can be written as in Eq. (6), where it presents in the battery charging mode.

$$Pol_{res} = K\,\frac{Q}{i_t - 0.1Q} \qquad (6)$$

In this paper, the reference power of the battery is controlled using a PI controller to feed the optimum duty cycle value for the DC-DC bidirectional converter, as seen in Fig. 5. The DC bus voltage is stabilized to achieve optimal performance under different loads and weather conditions. The PWM frequency of this converter is 5kHz. the indicator(L_{bat}) 20 mH , input capacitor (C_1) 220 µF and output capacitor(C_2) 470 µF.

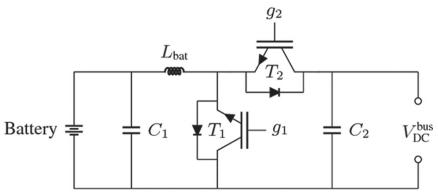

Fig. 5. Battery energy storage with DC/DC bidirectional converter

3.2. MODELLING OF BOOST CONVERTER

DC/DC boost converters offer several advantages in various applications, including voltage boost, efficient power conversion, compact size, regulated output, versatility, power source flexibility, ripple reduction, and control and protection features. These converters enable step-up voltages, high efficiency, compact size, and regulated output, making them ideal for low input voltage systems like battery-powered devices [26, 27]

They are also compact and lightweight, making them suitable for space constraints and integrating into various devices. Regulatory output ensures a stable power supply, especially in sensitive electronic circuits. Boost converters can operate with various power sources, such as batteries, solar panels, or fuel cells, ensuring efficient power management in renewable energy systems and electric vehicles. The circuit consists of an input inductor, a single diode, a semiconductor switch like MOSFET or IGBT, and input and output capacitors [23, 27]. The switching frequency of this converter is 20 kHz.

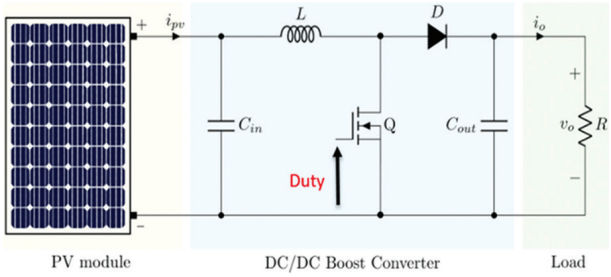

Fig. 6. Boost converter circuit used in MPPT controller

Managing the duty cycle D while the PWM generator executes is how the switch on the boost should be managed so that the MPPT algorithm can be implemented via the boost converter. Because of this, if the switch is in the ON state, the current travels via the inductor and the switch. After that, the energy is stored in the inductor. In contrast, when the PWM signal is withdrawn from the switch, the switch will function in an OFF state. After that, the electrical power stored via the inductor will be supplied to the output.

Furthermore, the continuous conduction mode (CCM) is mostly used in designing and finding the entire parameters of the boost circuit. Because of its low peak current, low switching device conduction losses, low turn-off losses, and high-frequency ripple amplitude, continuous conduction mode is chosen over critical conduction mode and discontinuous conduction mode in boost converters. Therefore, the theoretical equations of the boost converter can be obtained based on this mode [27]. The output voltage (v_o) from the boost converter can be expressed as follows [27]

$$v_o = \frac{1}{1-D}\,v_{pv} \qquad (7)$$

Based on the above equation, the output current can be written as [26]

$$i_o = i_{pv}\,(1-D\,) \qquad (8)$$

To determine the parameters of the boost converter at CCM mode, Eq. 9 should be utilized to calculate the inductor value (L) as [27],

$$L = \frac{v_{PV}\, D}{f_s\, \Delta i_{PV}} \tag{9}$$

where f_s is the switching frequency and Δi_{pv}=0.3. In addition, the output capacitance C_{out} can be calculated as

$$C_{out} = \frac{i_o\, D}{f_s\, \Delta v_o} \tag{10}$$

where Δv_o=0.02v_o. The input capacitor C_{in} size can be determined from (11) [26, 27]:

$$C_{in} \geq \frac{D}{8 \times {f_s}^2 \times L \times 0.01} \tag{11}$$

4. PROPOSED MPPT CONTROLLER

An adaptive fuzzy P&O MPPT approach is utilized in this work to extract the best amount of energy from the PV panel under various irradiance changes. The proposed technique mixes both advantages of the fuzzy logic and the P&O method to solve the problem oscillation that occurred with using P&O alone and increase the time response for gating maximum power under fast solar irradiance. The block diagram of the proposed system is shown in Fig. 7. This figure includes the PV system, proposed MPPT method, boost converter circuit, and the Li-ion battery module.

Fig.8 shows the block of the FL MPPT used in this research. As observed, the change in the power ΔP_{PV} and the change in the voltage ΔP_{PV} are represented as the inputs of the presented FL-MPPT while the duty ratio (D) represents the output.

The membership functions for the output and inputs are done based on a triangular shape with five linguistic variables: negative big (NB), negative small (NS), zero (ZE), positive small (PS), and positive big (PB). As a result, the FL has 25 different rules.

In addition, the center of gravity method is used in this work as the defuzzification method based on the following equation.

$$Y_{COG} = \frac{\sum_{i=1}^{n} Y_i(X_i) X_i}{\sum_{i=1}^{n} Y_i(X_i)} \tag{12}$$

Where Y_{COG} is the output, Y_i is the inference result of rule i, X_i is the output's corresponding rule i.

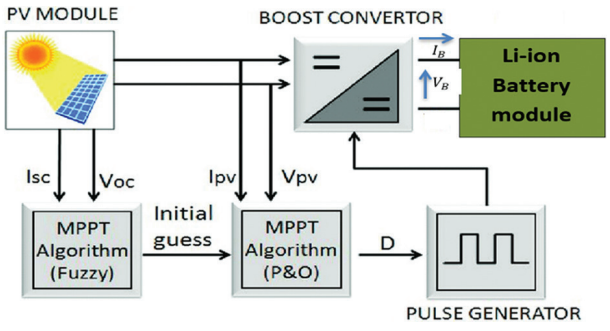

Fig. 7. The Proposed entire system

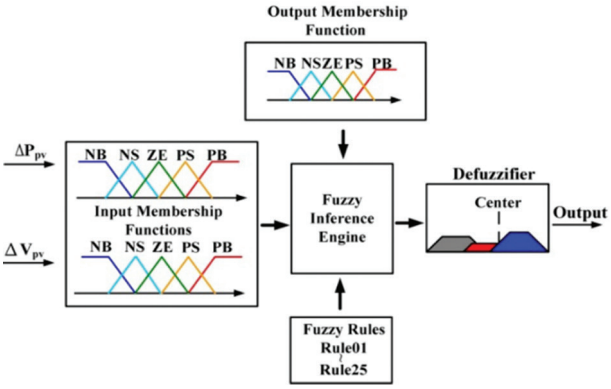

Fig. 8. Block diagram of the proposed FL MPPT controller

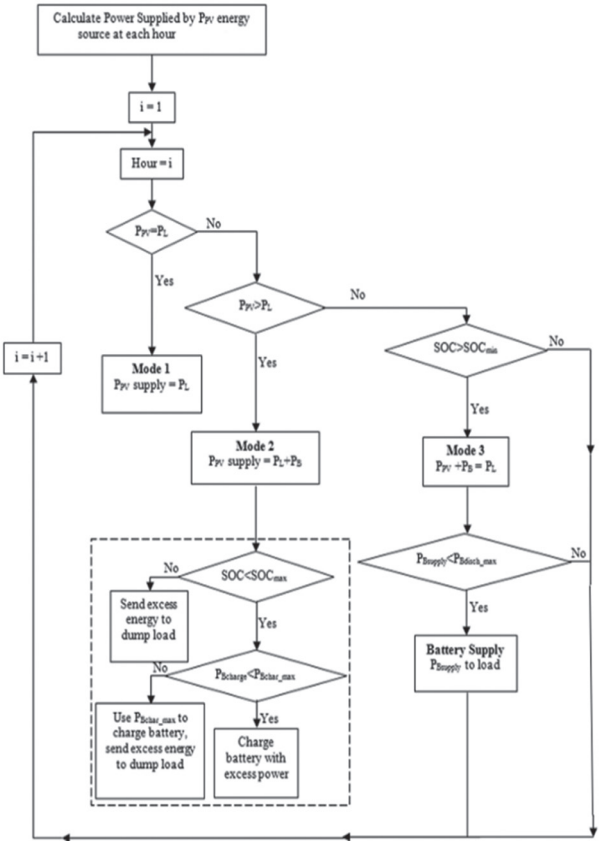

Fig. 9. Flowchart of the power management used in this study

The flowchart of the power management control is presented in **Fig. 9.** In this algorithm, the charge/discharge of the Li-ion battery is controlled and then the optimal duty cycle for the bidirectional is obtained. When the optimum power of the PV system is achieved, and the PV power is equal to the load power, the PV system will supply the DC demand load at the corresponding solar irradiance. The PV system will supply both the battery and load at the case of P_{PV}>P_L, and the system will operate with mode 2, and the battery will charge mode if its SOC is less than the required value. In mode 3, when P_{PV}+P_b=P_L, all generated power from the battery and PV system will convert to the load to cover the increase in the demand side.

5. RESULTS AND DISCUSSION

To validate the proposed method in simulation, Mat lab/Simulink 2019b has been used in this work. The PV system with a rated power of 20KW is used based on the KC200GT PV panel technology with electrical parameters, as observed in Table 1.

Based on the different 25 rule base used for the design of the proposed FL controller, the rule viewer for these rules are shown in Fig. 10. Also, the quiver plot of power and voltage of the fuzzy logic controller is seen in Fig. 11 It clear the relationship between the inputs of power and voltage for the proposed FL controller used to generate the optimal duty cycle for the boost converter.

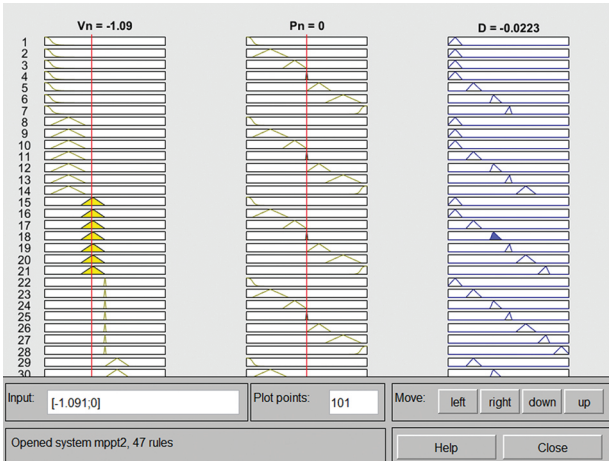

Fig. 10. Rule viewer of the proposed fuzzy logic controller

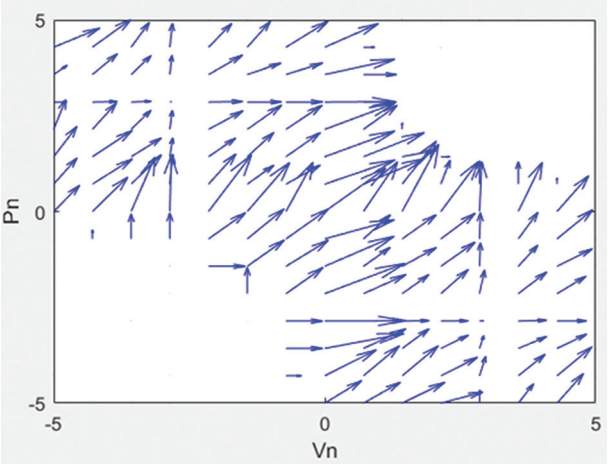

Fig. 11. Quiver plot of power and voltage using fuzzy logic

Furthermore, the proposed method is tested under a fast irradiance level to show the performance and compare it with the conventional technique (P&O) results. Fig. 12 shows the PV power with theoretical maximum power using the conventional P&O technique. The simulation is done for 9 seconds, and the solar irradiance is changed step by step from 250 W/m^2, 500 W/m^2, and 1000 W/m^2. The irradiance is set to 250 W/ m^2 from t=0 to 3 sec.

In this case, the conventional P&O is responded to during response time t=0.8 sec. So, the conventional P&O takes more time to reach the MPP. When the irradiance is changed from 250 to 500 W/m^2 at time t=3 sec, the conventional P&O is reached to the MPP with a fast response but the oscillation across this point is large, (ΔP=2.5 kW) and these issues are repeated during the high irradiance level and cause more power losses. On the other hand, the proposed FL-P&O shows good results regarding fast response and oscillation. As seen in Fig. 13, the proposed method is tested under fast irradiance levels for the same case as the conventional method. As observed, the proposed method is faster than the P&O regarding response, which is reached to MPP at time t=0.1sec at lower level irradiance. The proposed method presents low oscillation issues across the high-level irradiance, where the maximum overshot (ΔP=1kW) leads to minimizing the power loss in the electrical system.

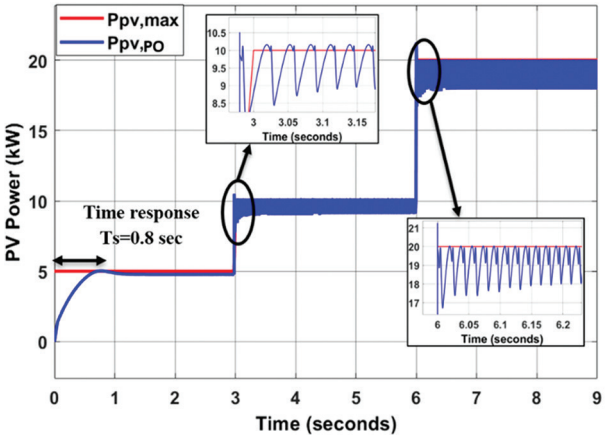

Fig.12. PV Power with theoretical value using the conventional P&O method

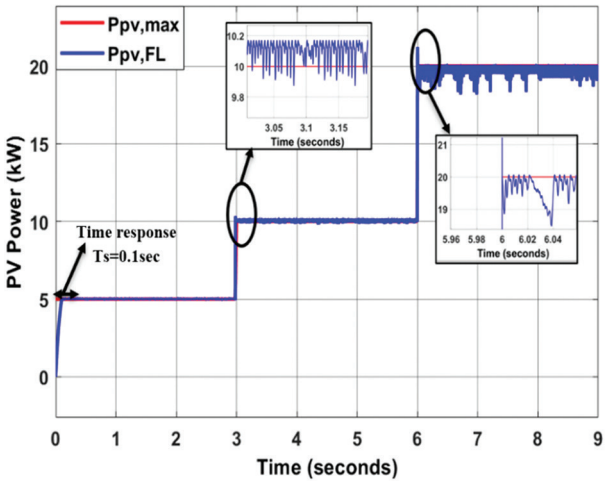

Fig.13. PV Power with theoretical value using the proposed FL-P&O method

Fig. 14 presents the simulation results of the PV system, including PV voltage, current, and power in the case of different irradiance levels for conventional and proposed MPPTs.

As seen, Fig. 14 a) and b) show the PV voltage and current results of FL-P&O MPPT, where voltage is little affected by the change in the irradiance, and this is because the open circuit voltage of the PV system depends strongly on the change in the temperature, not irradiance according to its mathematical equation which has a negative sign coefficient for the temperature term. The PV current is proportional to the irradiance value entered in its equation, as seen in section 2. In the conventional method (Fig. 14 c) and d)), the high ripple in the PV voltage occurs while this ripple is canceled by the proposed method, which means that robust control is achieved using the FL-MPPT. Also, when the solar irradiance is increased from 250 to 500 and then to 1000 W/m^2, the proposed methods reach the maximum PV current with fast response and low harmonic oscillation in the current.

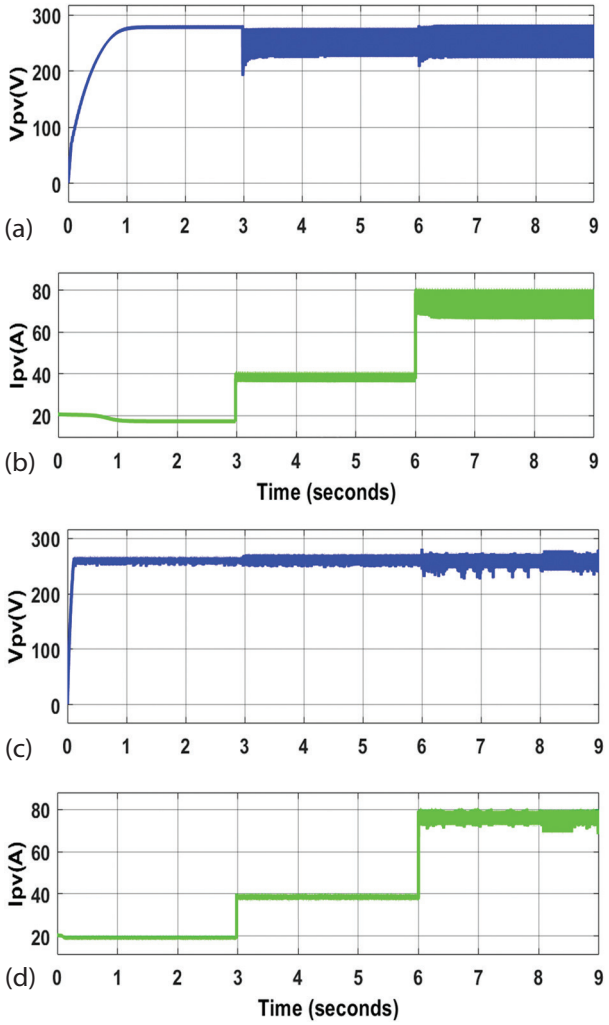

Fig.14. (a) PV Voltage at P&O (b) PV Current at P&O (c) PV Voltage at the proposed FL-P&O technique and (d) PV Current at the proposed FL-P&O technique

Fig. 15. shows the simulation results of the battery during a fast change in irradiance level. The SOC, voltage, and current are shown when the battery works with charging mode from the initial SOC of 50%.

At a low irradiance level, the power management system makes the proposed system work in mode 3 ($P_{PV}+P_B=P_L$) where the output PV power is low and cannot cover all DC load. As a result, to supply the required demand power, both the battery and PV are operated. As seen, the battery is operated in discharge mode from t=0 to t=3 sec, and when the irradiance becomes high (500 and 1000 W/m^2), the SOC of the battery is increased, and then the battery becomes in the charging mode, and the power management system switches the system to work with mode 2($P_{PV}=P_B+P_L$).

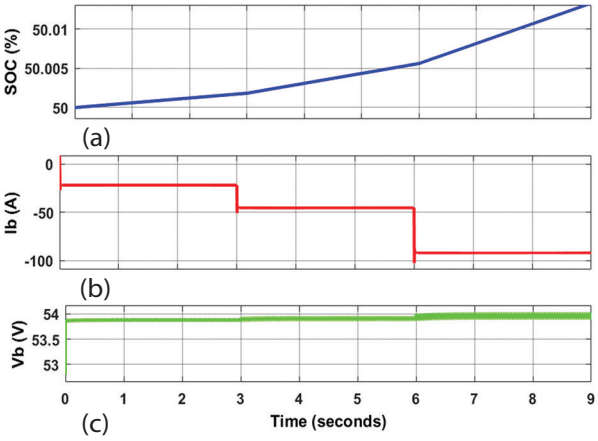

Fig.15. (a) The SOC of the battery, (b) the battery's current, and (c)the voltage's battery

To clear the novelty of the presented study, table 2 was added to show the comparison between the proposed method and the classical P&O in terms of the extracted power from the PV system, tracking time or time response, and the oscillation in the power. This table shows that the presented study has excellent performance under different irradiance values. As observed, the suggested method presents a high dynamic response, less oscillation, and high extracted power.

Table 2. Comparison between the proposed method and conventional P&O

Irradiance (W/m2)	Method	Extracted power (kW)	Time response (sec)	Oscillation (W)
200	P&O	3.7	0.99	3400
	FL-P&O	4.2	0.2	1700
400	P&O	8.7	0.87	2800
	FL-P&O	9.5	0.12	1300
600	P&O	11	0.94	3000
	FL-P&O	12	0.12	1210
800	P&O	15	0.9	2600
	FL-P&O	17	0.13	1100
1000	P&O	18	0.84	2500
	FL-P&O	20	0.11	1000

6. CONCLUSION

This study presents the hybrid fuzzy logic-perturb and observes (FL-P&O) maximum power point tracker (MPPT) for hybrid photovoltaic/battery systems. In

the beginning, the mathematical analysis for the model of the PV cell, the Li-ion battery, and the DC/DC boost converter are investigated. Second, the FL-P&O MPPT approach that has been presented is intended to optimize the output power of the PV system even when the irradiance is subject to rapid change. The suggested FL is modeled in Mat lab/Simulink using five distinct language variables, including ones for the derivative power (P), derivative voltage (V), and duty ratio (D). Additionally, the membership functions (MFs) for the output and inputs are carried out based on a triangle form, and the approach that is used for defuzzification is the center of gravity method. To validate the performance of the suggested technique, it is evaluated under various irradiance conditions. According to the findings of the simulations, the suggested technique performs much better than the traditional P&O method in terms of oscillation, power loss, and time response. The PV system robustness is improved, and the overshoot power is limited to 5% for irradiancies step by 250 W/m^2.

7. REFERENCES

[1] S. J. Yaqoob, S. Ferahtia, A. A. Obed, A. H. Rezk, N.T. Alwan, M. H. Zawbaa, S. Kamel, "Efficient Flatness Based Energy Management Strategy for Hybrid Supercapacitor/Lithium-ion Battery Power System", IEEE Access, Vol. 10, No. 6, 2022, pp. 132153-132163.

[2] S. R. Sinsel, R. L. Riemke, V. H. Hoffmann, "Challenges and solution technologies for the integration of variable renewable energy sources—a review", Renewable energy, Vol. 145, 2019, pp. 2271-2285.

[3] R. Bisht, A. Sikander, "An improved method based on fuzzy logic with beta parameter for PV MPPT system", Optik, Vol. 259, 2022, p. 168939.

[4] D. Baimel, S. Taguchi, Y. Levron, J. Belikov, "Improved fractional open circuit voltage MPPT methods for PV systems", Electronics, Vol. 8, No. 3, 2019, p. 1-20.

[5] S. J. Yaqoob, A. R. Hussein, A. L. Saleh, "Low Cost and Simple P&O-MPP Tracker Using Flyback Converter", Solid State Technology, Vol. 63, No. 6, 2020, pp. 9676-9689.

[6] X. D. Liu, "Photovoltaic MPPT Control Strategy Based on Improved Conductance Increment Method", In Journal of Physics: Conference Series, IOP Publishing Vol. 2527, No. 1, 2023, p. 012040.

[7] S. Motahhi, A. El Ghzizal, S. Sebti, A. Derouich, "Modeling of a photovoltaic system with modified incremental conductance algorithm for fast changes of irradiance", International Journal of Photoenergy, Vol. 2018, 2018, pp. 1-13.

[8] A. L. Saleh, A. A. Obed, Z. A. Hassoun, S. J. Yaqoob, "Modeling and Simulation of A Low-Cost Perturb& Observe and Incremental Conductance MPPT Techniques In Proteus Software Based on Flyback Converter", IOP Conference Series: Materials Science and Engineering, Vol. 881, 2020.

[9] L. Shang, H. Guo, W. Zhu, "An improved MPPT control strategy based on incremental conductance algorithm", Protection and Control of Modern Power Systems, Vol. 5, No. 1, 2020, pp. 1-8.

[10] H. A. Sher, A. F. Murtaza, A. Noman, K. E. Addoweesh, K. Al-Haddad, M. Chiaberge, "A new sensorless hybrid MPPT algorithm based on fractional short-circuit current measurement and P&O MPPT", IEEE Transactions on Sustainable Energy, Vol. 6, No. 4, 2015, pp. 1426-1434.

[11] M. Kermadi, E. Berkouk, "Artificial intelligence-based maximum power point tracking controllers for Photovoltaic systems: Comparative study", Renewable and Sustainable Energy Reviews, Vol. 69, 2017, pp. 369-386.

[12] C. L. Liu, J. H. Chen, Y. H. Liu, Z. Z. Yang, "An asymmetrical fuzzy-logic-control-based MPPT algorithm for photovoltaic systems", Energies, Vol. 7, No. 4, 2014, pp. 2177-2193.

[13] R. Bisht, A. Sikander, "A novel hybrid architecture for MPPT of PV array under partial shading conditions", Soft Computing, 2023, pp. 1-15.

[14] R. Bisht, N. Kumar, A. Sikander, "Fuzzy Logic Based Improved Control Design Strategy for MPPT of Solar PV Systems", Soft Computing: Theories and Applications: Proceedings of SoCTA 2019, Vol. 1154, 2020, pp. 1093-1106.

[15] S. J. Yaqoob, K. W. Nasser, Z. A. Hassoun, "Improved dynamic performance of photovoltaic panel using fuzzy logic-MPPT algorithm", Indonesian Journal of Electrical Engineering and Computer Science, Vol. 21, No. 2, 2021, pp. 617-624.

[16] C. B. N. Fapi, P. Wira, M. Kamta, B. Colicchio, "Design and hardware realization of an asymmetrical fuzzy logic-based MPPT control for photovoltaic

applications", Proceedings of the 47th Annual Conference of the IEEE Industrial Electronics Society, Toronto, Canada, 13-16 October 2021, pp. 1-6.

[17] A. Harrag, S. Messalti, "IC-based variable step size neuro-fuzzy MPPT improving PV system performances", Energy Procedia, Vol. 157, 2019, pp. 362-74.

[18] M. H. Larrode, A. A B. Rújula, "A coordinated control hybrid MPPT algorithm for a grid-tied PV system considering a VDCIQ control structure", Electric Power Systems Research, Vol. 221, 2023, p. 109426.

[19] F. A. Abbas, A. A. Obed, S. J. Yaqoob, "A comparative study between the most used MPPT methods and particle swarm optimization method for a standalone PV system under a fast change in irradiance level", AIP Conference Proceedings, Vol. 2804, No. 1, 2023.

[20] S. J. Yaqoob, A. L. Saleh, S. Motahhir, E. B. Agyekum, A. Nayyar, B. Qureshi, "Comparative study with practical validation of photovoltaic monocrystalline module for single and double diode models", Scientific Reports, Vol. 11, No. 1, 2021, pp. 1-14.

[21] L. P. N. Jyothy, M. R. Sindhu," An artificial neural network based MPPT algorithm for solar PV system", Proceedings of the 4th International Conference on Electrical Energy Systems, Chennai, India, 7-9 February 2018, pp. 375-380.

[22] L. Wang, Z. Wang, H. Liang, C. Huang, "Parameter estimation of photovoltaic cell model with Rao-1 algorithm", Optik, Vol. 210, 2020, p. 163846.

[23] S. Ferahtia, A. Djeroui, T. Mesbahi, A. Houari, S. Zeghlache, H. Rezk, T. Paul, "Optimal Adaptive Gain LQR-Based Energy Management Strategy for Battery–Supercapacitor Hybrid Power System", Energies, Vol. 14, No. 6, 2021 pp. 1-16.

[24] Y. Wang, Z. Sun, Z. Chen, "Development of energy management system based on a rule-based power distribution strategy for hybrid power sources", Energy, Vol. 175, 2019, pp. 1055-1066.

[25] S. Ferahtia, A. Djerioui, S. Zeghlache, A. Houari," A hybrid power system based on fuel cell, photovoltaic source and supercapacitor", SN Applied Sciences, Vol. 2, No. 5, 2020, pp. 1-11.

[26] T. A. Chandel, M. Y. Yasin, M. A. Mallick, "Modeling and simulation of photovoltaic cell using single diode solar cell and double diode solar cell model", International Journal of Innovative Technology and Exploring Engineering, Vol. 8, No. 10, 2019.

[27] W. Jiang, Y. F. Zhou, J. N. Chen, "Modeling and simulation of a boost converter in CCM and DCM", Proceedings of the 2nd International Conference on Power Electronics and Intelligent Transportation System, Shenzhen, China, 19-20 December 2009, pp. 288-291.

Active and Reactive Power loss Minimization Along with Voltage profile Improvement for Distribution Reconfiguration

Original Scientific Paper

Ola Badran
Palestine Technical University – Kadoorie (PTUK),
Faculty of Engineering and Technology, Department of Electrical Engineering-Industrial Automation
Al-Kadoorie Street, Tulkarm, Palestine
o.badran@ptuk.edu.ps

Jafar Jallad
Palestine Technical University – Kadoorie (PTUK),
Faculty of Engineering and Technology, Department of Electrical Engineering-Industrial Automation
Al-Kadoorie Street, Tulkarm, Palestine
j.jallad@ptuk.edu.ps

Abstract *– Optimal distribution network reconfiguration (DNR), distributed generations location and sizing (DGs-LS), tap changer adjustment (TCA), and capacitors bank location and sizing (CAs-SL) are different methodologies used to reduce loss and enhance the voltage profile of distribution systems. DNR is the process of changing the network topography by changing both sectionalized and tie switch states. The optimal location looks to find the optimal setting of the DG and CA within the distribution network. Optimal size seeks to find the optimal output generation of both DG and CA. The TCA looks to find the optimal position for TC. These methods are challenging optimization problems and resort to meta-heuristic techniques to find a globally optimal solution. This paper presents a new methodology with which to simultaneously solve the problem of DNR, DGs-LS, TCA, and CAs-SL in distribution networks. This work aims to minimize active and reactive power losses, including voltage profile improvement using a multi-objective decision approach. The firefly algorithm (FA) and analytic hierarchy process (AHP) are used to optimize the fitness function and determine the function weight factors through the use of MATLAB software. Several scenarios were considered on the IEEE 69-bus network. In terms of active power and reactive losses, reductions in the test system of 96.16% and 92.7%, respectively, were achieved, evidencing the positive impact of the proposed methodology on distribution networks.*

Keywords*: Weight factors, power loss, reconfiguration, DG allocation and sizing, Capacitor location and sizing, Tap changer adjustment*

1. INTRODUCTION

Minimizing energy consumption is important for ensuring power quality and system efficiency [1, 2]. This has led researchers to study the operation and design of power systems using different supply sources in the network. Therefore, different methods have been used to reduce energy consumption in the distribution power system by reducing power loss. The most famous methods are network reconfiguration, DG location and sizing, tap changer adjustment position, and capacitor location and sizing [3-5]. The distribution network reconfiguration (DNR) process can be defined as the process of changing the network topography structures according to changing the status of both tie and sectionalizing switches [6]. This improves specific conditions such as reducing power loss, enhancing the reliability of the network, and improving the voltage profile [7, 8]. In [9], PSO with a discrete version was used for load balancing during DNR. Moreover, in [10], the DNR problem was solved using GA to reduce power losses as well as improve the load index and voltage profile. In [11], NR was used to maximize loadability and improve the voltage profile of the radial network, which led to an increase in network reliability. In [12], NR was applied to reduce reactive power loss to improve both voltage stability and loadability using a two-stage algorithm.

One of the most well-known methods to minimize loss is combining both DNR and DG location and sizing methods [13]. DG location means the best sitting of the DG within the distribution network, while DG sizing expresses the best output generation from the DG [14, 15]. The authors in [16] dealt, simultaneously, with DNR

and DG sizing and location problems in order to optimize power loss. In [17], the authors used a firework algorithm to find the optimal DG sizing and location integrated with optimal network configuration based on minimum power loss. Similar objectives were achieved in [18] using EP and GA. In [19, 20], a discrete artificial bee colony method was used based on the continuation power flow methodology in order to achieve the maximum loadability of the network. In [21, 22], NR integrated with DG through a two-stage hierarchical optimization methodology was proposed to trade between reducing power loss and maximum loadability.

Another well-known method to minimize loss is combining both DNR and CA location and sizing methods [23]. CA location means the best sitting of the CA within the distribution network, while CA sizing expresses the best output generation from the CA [24]. This method aims to reduce power loss, voltage fluctuations, and the operating cost since the capacitor output is reactive power that improves the voltage profile [25]. A lot of optimization techniques have been presented for network reconfiguration considering CA sizing and location. In [26], the authors solved this problem using harmony search and simulated annealing algorithms. In [27, 28], the authors also solved this problem using the ant colony algorithm, Big Bang method, and genetic algorithm. In [29], grey wolf optimization integrated with the PSO method was presented to solve the same problem. The main objectives within these studies were reduced investment cost, annual loss of energy cost, maintenance and operation cost, and switching cost. In [30], GA was used to optimize the CA location and size and optimize the sequence of loop selection for minimizing energy losses. The presented methodology was tested on a real 77-bus system with different load patterns.

Another different method that is also presented in the published works is tap changer adjustment (TCA). TCA is a mechanism that allows transformers to find the best position of the transformer's turn ratios that achieve the best voltage profile [31]. The work in [32] addressed the reconfiguration problem after the power cut caused by the cut of a branch of the system. The work presented an approach that handled the reconfiguration process simultaneously with transformer tap changer adjustments. The presented approach considered the AC power model, network operation topology, and both voltage and load limitations. The results obtained showed that the presented approach could find the best solution; it presents the overloaded branches and the minimum number of buses that were outside of operation. The authors in [33] proposed network reconfiguration with TCA integrated into the DG sizing method to minimize network power loss using the imperialist competitive algorithm. The proposed method indicated an improvement in the voltage profile and power loss reduction compared to other algorithms. In [34], a simultaneous method combined with DNR with DGs-LS, including TCA, was presented. The method proposed a multi-objective decision methodology that obtained the maximum loadability and best voltage profile as well as minimum power loss using the FA.

The main contribution of this paper is the simultaneous combination of the most famous methods used to improve the performance of a distribution system. The methods represent network reconfiguration, DG location and sizing, tap changer adjustment, and capacitor location and sizing. The remainder of this paper is organized as follows: Section II presents the mathematical modeling proposed; Section III presents the proposed approach; Section IV presents the test system and results in detail; and Section V presents the conclusions.

2. MATHEMATICAL MODELING

This section presents the proposed fitness function that solves the optimal DNR problem and optimal DGs-LS, including optimal TCA, along with optimal CAs-LS. In addition, we also present all the constraints and limitations the fitness function fulfills. The function looks to minimize both active and reactive power losses simultaneously while improving the voltage profile index.

2.1. FITNESS FUNCTION

The fitness function is described as follows:

$$\text{Minimize } \mathrm{F} = (\omega_1 \, \mathrm{P_{loss}} + \omega_2 \, \mathrm{Q_{loss}} + \omega_3 \, \mathrm{IVD}) \quad (1)$$

where ω_1, ω_2, and ω_3 are the fitness function (F) weight factors. P_{loss} is the active power loss. Q_{loss} is the reactive power loss. The fitness function is set to be unity to minimize all the function terms. The active power loss (P_{loss})is taken as the ratio of the active power loss after and before optimization, as follows [35]:

$$\mathrm{P_{loss}} = \frac{\mathrm{P_{loss}^{opt}}}{\mathrm{P_{loss}^{0}}} \quad (2)$$

where P_{loss}^{opt} is the active power loss after optimization. P_{loss}^{0} is the active power loss before optimization.

$$\mathrm{P_{loss}} = \sum_{\mathrm{N=1}}^{\mathrm{M}} (\mathrm{R_N} \times |\mathrm{I_N}|^2) \quad (3)$$

where R_N is the resistance in the branch N, I_N is the branch current, and M is the branch number.

Moreover, the reactive Power loss (Q_{loss})is taken as the ratio of the reactive Power loss after and before optimization, as follows [35]:

$$\mathrm{Q_{loss}} = \frac{\mathrm{Q_{loss}^{opt}}}{\mathrm{Q_{loss}^{0}}} \quad (4)$$

where Q_{loss}^{opt} is the reactive power loss after optimization. Q_{loss}^{0} is the reactive power loss before optimization.

$$\mathrm{Q_{loss}} = \sum_{\mathrm{N=1}}^{\mathrm{M}} (\mathrm{X_N} \times |\mathrm{I_N}|^2) \quad (5)$$

where X_N is the reactance in branch N.

Voltage profile index (IVD): this index penalizes the size location pair, which gives higher voltage deviations from the nominal voltage. In this way, the closer the index is to zero, the better the network performance is.

The IVD is addressed as follows:

$$IVD = \max_{i=2}^{n}\left(\frac{|\overline{V_1}|-|\overline{V_i}|}{|\overline{V_1}|}\right) \quad (6)$$

Where V_i is the bus voltage; V_1 is the nominal voltage; and n is the bus number.

2.2. LIMITATIONS AND CONSTRAINTS

All limitations and constraints that the fitness function should satisfy are as follows:

Distributed generator and Capacitor capacity

$$P_i^{min} \le P_{DG,i} \le P_i^{max} \quad (7)$$

$$Q_i^{min} \le Q_{CAP,i} \le Q_i^{max} \quad (8)$$

where $P_{DG,i}$ is the DG size at bus i; P_i^{max} and P_i^{min} are the higher and the lower DG capacities, respectively. $Q_{CAP,i}$ is the capacitor size at bus i; Q_i^{max} and Q_i^{min} are the higher and the lower capacitor capacities, respectively.

- Power injection

$$\sum_{i=1}^{k} P_{DG,i} < \sum_{n}^{nbus}\left(P_{Load_n}\right) + P_{loss} \quad (9)$$

$$\sum_{i=1}^{k} Q_{CAP,i} < \sum_{n}^{nbus}\left(Q_{Load_n}\right) + Q_{loss} \quad (10)$$

where k is the DG number; $nbus$ is the bus number; P^{n}_{Load} is the active power load at bus n; and Q^{n}_{Load} is the reactive power load at bus n. This means that there are no active or reactive powers flowing from DGs or capacitors to the grid.

- Power balance

$$\sum_{i=1}^{k} P_{DG,i} + P_{Substation} = P_{Load} + P_{loss} \quad (11)$$

$$\sum_{i=1}^{k} Q_{CAP,i} + Q_{Substation} = Q_{Load} + Q_{loss} \quad (12)$$

where $Q_{CAP,i}$ is the capacitor size at bus i; $S_{Substation}$ is the main substation apparent power supplied. Total power must fitful the principle of equilibrium. Thus, the supply of power must be equal to its demand.

- Voltage magnitude

$$0.95 \le V_{bus} \le 1.05 \quad (13)$$

where V_{bus} is the bus voltage, which is within the voltage limits (0.95 to 1.05) p.u.

- Radial configuration

At all times, the network must save the radiality configuration.

- Load connection

After the reconfiguration, all distribution buses must be connected to a power source.

3. PROPOSED APPROACH

This section presents the proposed simultaneous methodology to solve the optimal DNR problem and optimal DGs-LS, including optimal TCA, integrated with optimal CAs-LS using the AHP and FA techniques. The proposed methodology looks to minimize both active and reactive power losses and minimize the voltage profile index.

3.1. ANALYTIC HIERARCHY PROCESS

The main fitness formula is controlled by an AHP multi-objective decision approach that determines the weights of the formula factors. The AHP is an effective and practical approach used to solve multicriteria decision-making problems, and it was introduced by Thomas L. Saaty in [36, 37]. The AHP seeks to simplify complex problems by deconstructing them into simple parts. This occurs by taking a fraction of the overall decision problem that allows the decision maker to focus on different criteria based on the importance of said criteria. There are three stages in the AHP: determining the decision-making problem by constructing the hierarchy and finally evaluating the factors in the stairway. The evaluation of the factors of the stairway is then compared using a scale of numbers from one to nine [38]. Table 1 shows the relative importance matrix used in the AHP for various indices.

Table 1. Matrix of relative importance

Standard	Numeric-Rating	Reciprocal
Equality–Importance	1	1
Equality to Moderately	5	0.2
Moderately Important	7	0.143

Table 2 shows the weights obtained from the AHP method. The details of the AHP are illustrated in Fig. 1. For more explanation, this work focuses on different criteria, namely active power loss, reactive power loss, and voltage profile. The relative importance of the active power loss is equal to one (equality–importance), reactive power loss is equal to five (equality to moderately), and the voltage profile is equal to seven (moderately important). Based on these values, the weights obtained are 0.632819 for active power loss, 0.301806 for reactive power loss, and 0.065375 for voltage profile. This means that if the relative importance of the different criteria differs, the weight values directly differ.

Table 2. AHP approach weight factors

Criteria	Active Power Loss	Reactive Power Loss	Voltage profile	Total =ΣRow	Weights = Total/ Sum
Active power loss	1	5	7	13	0.632819
Reactive power loss	0.2	1	5	6.2	0.301806
Voltage profile	0.143	0.2	1	1.343	0.065375
		Sum		20.543	1

3.2. TAP CHANGER ADJUSTMENT

In the presented methodology, there are 17 values representing the TC positions, as shown in Fig. 2. These positions correspond to bus voltage, which changes from -5 to +5 % [39]. This makes the lower and upper bus voltage limits 0.95 p.u and 1.05 p.u, respectively [40].

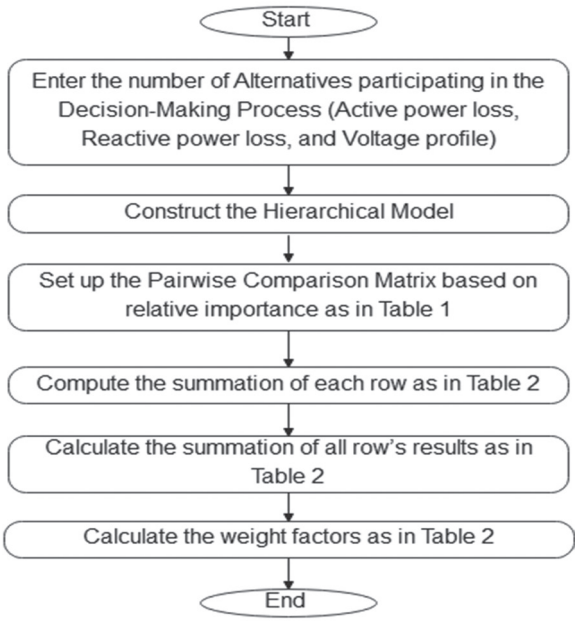

Fig. 1. Flow chart of AHP

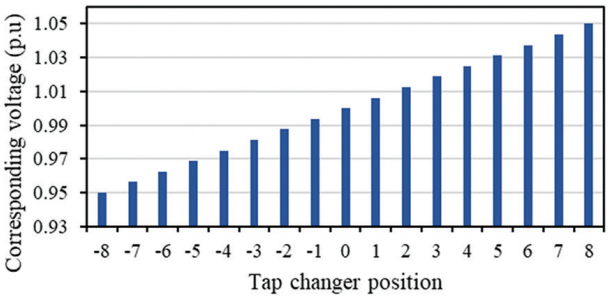

Fig. 2. Tap changer position corresponding to bus voltage (p.u)

3.3. FIREFLY ALGORITHM (FA)

The firefly algorithm is a nature-inspired meta-heuristic method that has gained popularity due to its capability to be involved in transactions with global non-linear optimization problems [41]. The FA is a method inspired by the attitude of fireflies and their different shining types [41]. All fireflies are attracted to flies that achieve strong flashing brightness. Therefore, the flashing brightness is exactly proportional to attraction. Moreover, attraction is proportional inversely to the space between fireflies. Flies will move to a specific location in the case where all fireflies have the same brightness intensity. The steps to implement the FA to solve the OP-DNR problem and OPDGs-LS, including TCA integrated with OPCAs-LS, are proposed as follows:

- Determine the constant values of the FA, population, and iteration size.
- Set the data input, such as the resistance and reactance values of the lines, active and reactive load of the buses, initial values of the bus voltages, and TCA locations.
- Define the weight factors based on the AHP technique, as in Table 2.
- Generate initial FA populations randomly (Y) that achieved all the constraints and imitations that present the tie switches of the distribution (S), DG sizing (DGS), DG location (DGL), CA sizing (CAS), CA location (CAL), and TCA position (TP). All FA elements are set simultaneously, as is presented in the following equation:

$$Y = \begin{bmatrix} S_{11}\ S_{12}\cdots S_{1n}\ DG_{S11}\ DG_{S12}\cdots DG_{S1k}\ DG_{L11}\ DG_{L12}\cdots DG_{L1k}\ CA_{S11}\ CA_{S12}\cdots CA_{S1k}\ CA_{L11}\ CA_{L12}\cdots CA_{L1k}\ T_{P1} \\ S_{21}\ S_{22}\cdots S_{2n}\ DG_{S21}\ DG_{S22}\cdots DG_{S2k}\ DG_{L21}\ DG_{L22}\cdots DG_{L2k}\ CA_{S21}\ CA_{S22}\cdots CA_{S2k}\ CA_{L21}\ CA_{L22}\cdots CA_{L2k}\ T_{P2} \\ \vdots\ \vdots\cdots\vdots\ \vdots\ \vdots\cdots\vdots\ \vdots\ \vdots\cdots\vdots\ \vdots\ \vdots\cdots\vdots\ \vdots \\ S_{m1}S_{m2}\cdots S_{mn}DG_{Sm1}DG_{Sm2}\cdots DG_{Smk}DG_{Lm1}DG_{Lm2}\cdots DG_{Lmk}CA_{Sm1}CA_{Sm2}\cdots CA_{Smk}CA_{Lm1}CA_{Lm2}\cdots CA_{Lmk}T_{Pm} \end{bmatrix} \quad (14)$$

where n is the NO of tie switch; k is the NO of DGs and CAs; and m is the size of the population.

- The iteration process is started by analyzing the distribution load flow using Newton–Raphson methodology to compute the distribution active and reactive power loss values, as well as the values of minimum and maximum bus voltage.
- The value of the fitness function is estimated for all populations of matrix Y related to Equation (1).
- Populations are sorted based on their light intensity in ascending order, and then the lower value is kept, which presents the top light intensity.
- The elements of the Y matrix related to the FA technique are updated, taking into account the constraints and limitations. In addition, the motion is arranged and updated in ascending form related to the following formulas:

$$\beta(r) = \beta_0 e^{-\gamma r^2} \quad (15)$$

where γ is the light absorption coefficient, and β_0 is the attractiveness when r=0 ; r is the 2 FAs' space.

$$r_{lj} = \|y_l - y_j\| = \sqrt{\sum_{k=1}^{d}(y_{l,k} - y_{j,k})^2} \quad (16)$$

where r_{lj} is the Cartesian space between l and j FAs, which presents the Y matrix rows; d is the optimized numbers of the parameters; and $y_{l,k}$ and $y_{j,k}$ represent the k_{th} component of the Cartesian coordinates y_l and y_j of FAs l and j, respectively.

$$y_{l,k} = \beta_0 e^{-\gamma r_{lj}^2}(y_{j,k} - y_{l,k}) + \alpha(\text{rand} - 0.5) + y_{l,k} \quad (17)$$

where the first equation term $x_{l,k}$ presents influence by attractiveness (when γ=1); the second equation term presents the random item related to α; and the third term presents the motion of FAs that FA l is attracted to brighter FA j. The random number rand (1) presents a random number [0, 1].

- The prior operation from steps (5 to 8) is repeated until the maximum iteration number is reached.

- The loop is ended, and the optimal solution is kept that presented the distribution final configuration, CA's location and size, DG's location and size, and TCA location. This optimal solution obtained:
    1. Minimum active power loss.
    2. Minimum reactive power loss.
    3. Best voltage profile index.
- The previous process is re-run one hundred times to check the FA's robustness.

Fig. 3 illustrates the previous methodology in a simple flow chart that summarizes the function of both the FA and AHP methods in solving the optimal DNR and optimal DGs-LS, including optimal TCA integrated with the optimal CAs-LS problem.

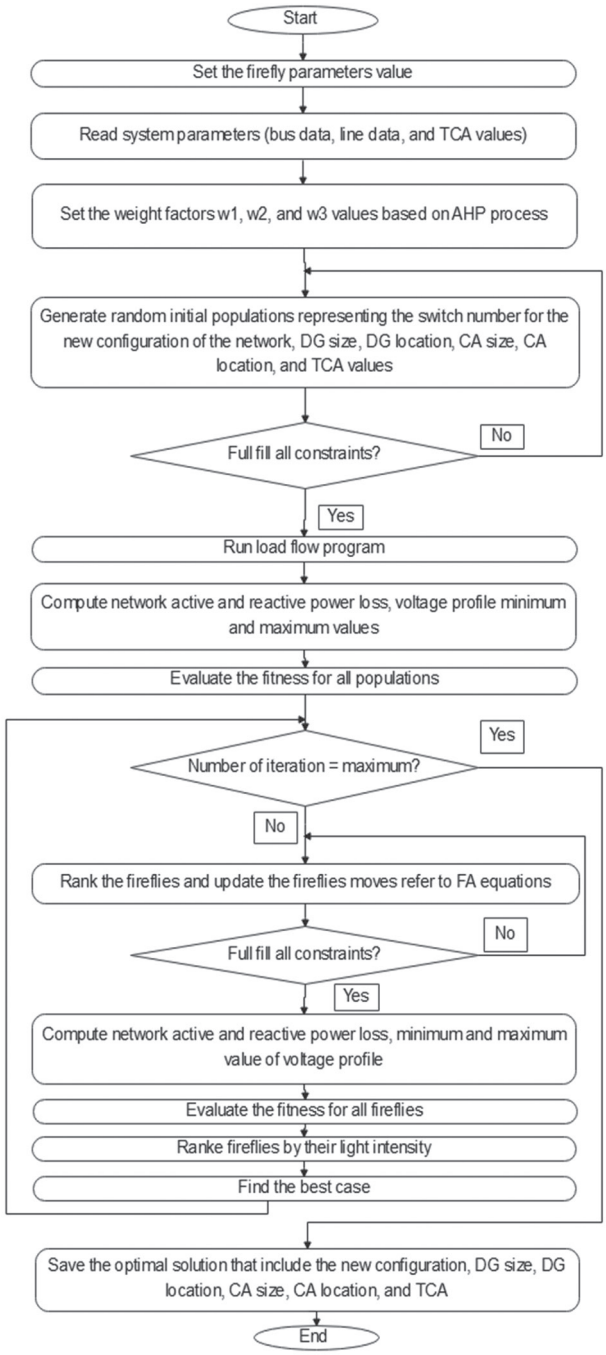

Fig. 3. Flowchart of the proposed approach

4. TEST SYSTEM AND RESULTS

The proposed methodology in this work was implemented and solved using MATLAB software. Simulation codes were carried out on a laptop with an Intel CORE i7 processor. Each code was run 100 times for 100 population sizes and 300-time iterations.

To test the approach's superiority, different scenarios were considered:

Scenario 1: Represent the initial form. The original network system without any modifications.

Scenario 2: Represent the optimal simultaneous distribution network reconfiguration (DNR) and DG location and sizing.

Scenario 3: Represent the optimal DNR simultaneously with DGs-LS, including tap changer adjustment (TCA).

Scenario 4: Represent the optimal DNA simultaneously with DGs-LS, including TAP, and incorporating capacitor bank location and sizing CAs-SL.

The IEEE 69-bus distribution network was used to test the power of the proposed methodology, as shown in Fig. 4 [35].

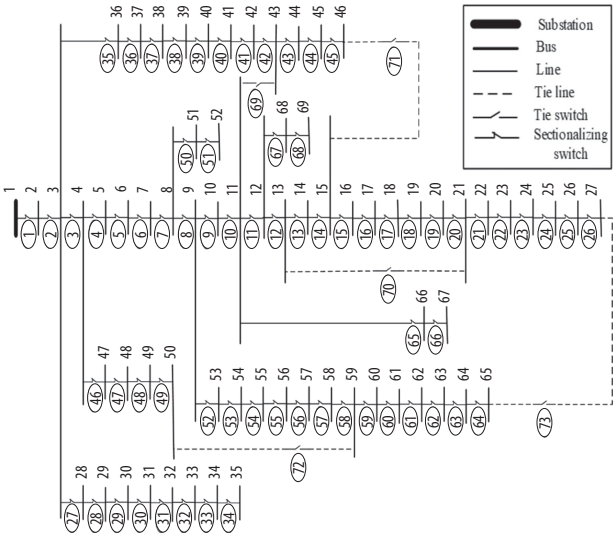

Fig. 4. IEEE 69-bus distribution system

The system data are available in [42]. This system consists of 73 branches, 5 tie switches, and 68 sectionalizing switches. In the initial form (Scenario 1), switches 69 to 73 are open. The system nominal voltage is 12.66 kV, with a minimum voltage magnitude of 0.9092 p.u. The system's apparent power demand is (3, 802.19+j2, 694.6) kVA. The active and reactive power losses are 224.99 kW and 39.16 kVAR, respectively. The DG in this work was assumed to be a mini-hydro generation. The maximum capacity for DG was 2 MW. Furthermore, the maximum capacity for the capacitor was 2 MVAR. The obtained optimal solutions were proposed to be the tie switch, DG location and size, capacitor location and size, and tap changer adjustment position. These were all simultaneously determined.

4.1. IMPACT OF THE PROPOSED METHODOLOGY ON POWER LOSSES

This section of the paper focuses on reductions in active and reactive power loss and improvement in bus voltage. Table 3 summarizes the results obtained from all of the scenarios.

Table 3. Distribution network system features

Optimization technique	Scenario 1	Scenario 2	Scenario 3	Optimization technique
Tie switch	69, 70, 71, 72, 73	13, 12, 62, 10, 57	69, 70, 13, 55, 63	21, 20, 7, 13, 55
DG location (DG sizing (MW))	-------	22 (0.5005) 16 (0.3991) 61 (1.5016)	22 (0.405) 16 (0.213) 61 (1.489)	62(0.7858) 61(1.1103) 51(0.7280)
CA location (CA sizing (MVAR))	-------	-------	-------	51(0.5153) 27(0.2634) 61(0.9992)
Tap changer	-------	-------	1.0194	1.04092
Fitness	-------	0.22785	0.20233	0.046091
Active power loss(kW)	224.557	39.16	36.58	8.621
Reactive power loss (kVAR)	102	38.64	33.315	7.445
Active power reduction (%)	-------	82.56	83.71	96.16
Reactive power reduction (%)	-------	62.12	67.34	92.7
Minimum bus voltage	0.9093	0.980353	1.019367	1.033656
Maximum bus voltage	1	1	1.037505	1.041507

Scenario 1 represents the initial form. The tie switches were 69, 70, 71, 72, and 73. The active and reactive power losses were 224.557 kW and 102 kVAR, respectively. The minimum and maximum bus voltages were 0.9093 and 1.038 pu, respectively. Scenario 2 represents the optimal distribution network reconfiguration of DNR simultaneously with DG location and sizing, where better results were obtained than those in Scenario 1. In Scenario 2, the tie switches changed to 13, 12, 62, 10, and 57. The DG locations were set on buses 22, 16, and 61 with DG sizes of 0.5005 kW, 0.3991 kW, and 1.5016 kW, respectively. The fitness value was 0.22785. Both active/reactive power loss was reduced to 39.16 kW and 38.64 kVAR, respectively, compared to the initial form. The reductions in both active/reactive power loss were 82.56% and 62.12%, respectively. The bus voltages minimum and maximum values improved to 0.980353 and 1 pu, respectively.

Scenario 3 represents the optimal DNR simultaneously with DGs-LS integrated with tap changer adjustment (TCA). In Scenario 3, the tie switches changed to 69, 70, 13, 55, and 63. The DG locations were set on buses 22, 16, and 61 with DG sizes of 0.405 kW, 0.213 kW, and 1.489 kW, respectively. The fitness value was 0.20233 with a tap changer adjustment position of 1.0194. The reductions in active and reactive power losses were reduced to 36.58 kW and 33.315 kVAR, respectively. Both active/reactive power loss reductions were 83.71% and 67.34%, respectively. The bus voltages minimum and maximum values improved to 1.019367 and 1.037505 pu, respectively. This means that Scenario 3 obtained better results than those achieved in Scenarios 1 and 2.

Scenario 4 represents the optimal DNA simultaneously with optimal DGs-LS, including optimal TAP, and incorporating optimal capacitor bank location and sizing CAs-SL. In Scenario 4, the tie switches changed to 21, 20, 7, 13, and 55. The DG locations were set on buses 62, 61, and 51 with DG sizes of 0.78581 kW, 1.11037 kW, and 0.72809 kW, respectively. The capacitor's locations were set on buses 51, 27, and 61 with capacitor sizes of 0.51531 kVAR, 0.26349 kVAR, and 0.99929 kVAR, respectively. The fitness value was 0.046091 with a TCA position of 1.04092. Both active/reactive power losses were reduced to 8.621 kW and 7.445 kVAR, respectively. The reductions in active and reactive power losses were 96.16 % and 92.7 %, respectively. The bus voltages minimum and maximum values improved to 1.033656 and 1.041507 pu, respectively.

4.2. IMPACT OF THE PROPOSED METHODOLOGY ON VOLTAGE PROFILE

Fig. 5 illustrates the IEEE 69-bus network voltage profile for all scenarios. In the initial form, some buses violated the voltage borders. After applying the proposed methodology, the bus's voltage was enhanced to be under the limitations for all scenarios. These limitations mean that the voltage for each bus of the distribution network must be between 0.95 p.u and 1.05 p.u, as mentioned in Equation 13. The best scenario was Scenario 4, where all the bus voltages closed to one.

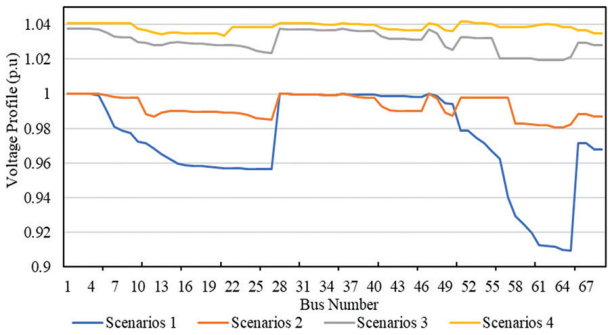

Fig. 5. IEEE 69-bus network of all scenario's voltage profile

4.3. ANALYSIS OF FA'S OVERALL PERFORMANCE

The presented methodology code was run one hundred times. Each time, a local solution was saved. The minimum value between these local solutions is called the global solution, which represents the best solution. The best solution presented the optimal configuration, optimal DG sizing and location, optimal capacitor sizing and location, and optimal TCA. The convergence of the global solutions for all scenarios was drawn and is

compared in Fig. 6. From the convergence performances analyzed, Scenario 4 obtained the best fitness.

Fig. 7 illustrates the robustness test of the proposed methodology. The FA was strongly robust since all fitness values were close together for all runs in Scenario 4. The robustness of the FA is also evaluated in Table 4 by calculating the standard deviation for all scenarios. The minimum, maximum, and average values are also calculated for all scenarios. Scenario 4 achieved the best values, obtaining the best standard deviation of 0.010504. The value of standard deviation should be close to zero for the robustness method. That means that the FA was effective and robust in determining the optimal solutions for a complex problem.

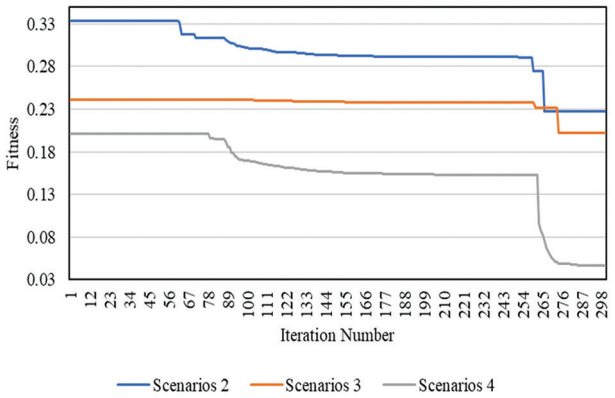

Fig. 6. Convergence curve of all scenarios

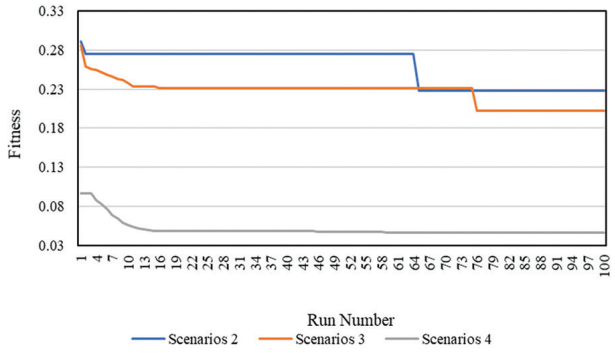

Fig. 7. Robustness curve of all scenarios

Table 4. Robustness test statistical analysis for all scenarios

Scenario	Min value	Max value	Average value	Standard deviation
Scenario 2	0.22785	0.291004	0.258075	0.022726
Scenario 3	0.20233	0.285469	0.226285	0.01566
Scenario 4	0.046091	0.096183	0.050388	0.010504
Scenario 5	0.22785	0.291004	0.258075	0.022726

Table 5 outlines our results compared with those obtained in other published works. From the results, it can be seen that the power loss obtained from the proposed method using the FA and AHP is 39.16 kW, while when using other methods, the power loss obtained is greater than 39.16 kW. Thus, the reduction in the power loss using the FA is 82.56 %, meaning that the maximum value was achieving using this method compared to others. The proposed methodology using the FA and AHP was the best as this obtained minimum power loss and maximum loss reduction.

Table 5. Results comparative

Scenario 2	Open switch	DG outputs (MW)	Weaker Bus voltage (pu)	Power loss (kW)	Loss reduction (%)
GA [43]	10, 55, 45, 15, 62	2.02920	0.97270	46.500	73.380
RGA [43]	10, 55, 14, 16, 62	2.06540	0.97420	44.230	80.320
HSA [43]	69, 58, 13, 17, 61	1.87180	0.97360	40.300	82.080
FWA [44]	69, 70, 13, 55, 63	1.8182	0.9796	39.25	82.55
MPSO [8]	14-58-61-69-70	2.2736	0.98994	42.2	81.1
ISCA [45]	12, 9, 57, 63, 69	1.8731	-	39.73	82.34
The proposed method by FA	13, 12, 62, 10, 57	2.4012	0.98035	39.16	82.56

5. CONCLUSIONS

Different methods like network reconfiguration, distributed generation location and sizing, tap changer adjustment, and capacitor location and sizing play an important role in distribution networks because they reduce power losses and improve voltage profile. This paper proposed a new methodology that combined the FA and AHP to tackle these methods simultaneously. The proposed methodology can perform optimal network reconfiguration, distributed location and sizing, tap changer adjustment, and capacitor location and sizing simultaneously. Several scenarios were performed on the IEEE 69-bus network. In this work, Scenario 4 showed higher active and reactive power loss reduction when all methods were considered simultaneously compared to the other scenarios. Furthermore, the voltage profile index was improved in all scenarios, especially in Scenario 4. Moreover, the results proved that the FA is strongly robust and accurate when finding global solutions for complicated problems and comparing them to other published works. Finally, we compared part of our results to those obtained in other reported works. On the whole, our results showed that we obtained better active power loss than other reported studies have. Future research could focus on the switching sequence order that changes the original network form to the optimal network form. Furthermore, dynamic load and renewable energy could be integrated into the distribution network.

6. ACKNOWLEDGMENT

"The authors would like to thank Palestine Technical University-Kadoorie (PTUK) for supporting this research".

7. REFERENCES:

[1] A. Bagheri, H. Monsef, H. Lesani, "Renewable power generation employed in an integrated dynamic distribution network expansion planning", Electric Power Systems Research, Vol. 127, 2015, pp. 280-296.

[2] J. Yan et al. "Clean, efficient and affordable energy for a sustainable future", Applied Energy, Vol. 185, 2017, pp. 953-962.

[3] B. Mukhopadhyay, D. Das, "Multi-objective dynamic and static reconfiguration with optimized allocation of PV-DG and battery energy storage system", Renewable and sustainable energy reviews, Vol. 124, 2020, p. 109777.

[4] M. V. dos Santos, G. A. Brigatto, L. P. Graces, "Methodology of solution for the distribution network reconfiguration problem based on improved harmony search algorithm", IET Generation, Transmission & Distribution, Vol. 14, 2020, pp. 6526-6533.

[5] T. P. Mtonga, K. K. Kaberere, G. K. Irungu, "Optimal shunt capacitors' placement and sizing in radial distribution systems using multiverse optimizer", IEEE Canadian Journal of Electrical and Computer Engineering, Vol. 44, 2021, pp. 10-21.

[6] R. Pegado, Z. Naupari, Y. Molina, C. Castillo, "Radial distribution network reconfiguration for power losses reduction based on improved selective BPSO", Electric Power Systems Research, Vol. 169, 2019, pp. 206-213.

[7] A. Onlam et al. "Power loss minimization and voltage stability improvement in electrical distribution system via network reconfiguration and distributed generation placement using novel adaptive shuffled frogs leaping algorithm", Energies, Vol. 12, 2019, p. 553.

[8] S. Essallah, A. Khedher, "Optimization of distribution system operation by network reconfiguration and DG integration using MPSO algorithm", Renewable Energy Focus, Vol. 34, pp. 37-46, 2020.

[9] S. Sivanagaraju, J. V. Rao, P. S. Raju, "Discrete particle swarm optimization to network reconfiguration for loss reduction and load balancing", Electric power components and systems, Vol. 36, 2008, pp. 513-524.

[10] A. Eldurssi, R. O'connell, "A Fast Nondominated Sorting Guided Genetic Algorithm for Multi-Objective Power Distribution System Reconfiguration Problem", Power Systems, IEEE Transactions on, Vol. 30, 2015, pp. 593-601.

[11] K. M. Muttaqi, V. Ganapathy, G. G. Jasmon, "Network reconfiguration for enhancement of voltage stability in distribution networks", IEE Proceedings - Generation, Transmission and Distribution, Vol. 147, 2000, pp. 171-175.

[12] A. Tyagi, A. Verma, P. R. Bijwe, "Reconfiguration for loadability limit enhancement of distribution systems", IET Generation, Transmission & Distribution, Vol. 12, 2018, pp. 88-93.

[13] S. D. Saldarriaga-Zuluaga, J. M. Lopez-Lezama, N. Munoz-Galeano, "Hybrid harmony search algorithm applied to the optimal coordination of overcurrent relays in distribution networks with distributed generation", Applied Sciences, Vol. 11, 2021, p. 9207.

[14] L. A. Wong et al. "Review on the optimal placement, sizing and control of an energy storage system in the distribution network", Journal of Energy Storage, Vol. 21, 2019, pp. 489-504.

[15] O. S. W. Badran, "IEEE-69 Distribution Network Performance Improvement by Simultaneously Optimal Distributed Generation Sizing and Location Using PSO Algorithm", Palestine Technical University Research Journal, Vol. 1, No. 1, 2023, pp. 1-15.

[16] O. Badran et al. "Multi-Objective network reconfiguration with optimal DG output using meta-heuristic search algorithms", Arabian Journal for Science and Engineering, Vol. 43, 2018, pp. 2673-2686.

[17] A. M. Imran, M. Kowsalya, D. P. Kothari, "A novel integration technique for optimal network reconfiguration and distributed generation placement in power distribution networks", International Journal of Electrical Power & Energy Systems, Vol. 63, 2014, pp. 461-472.

[18] W. M. Dahalan, H. Mokhlis, R. Ahmad, A. H. A. Bakar, I. Mursirin, "Simultaneous network reconfiguration and DG sizing using evolutionary programming and genetic algorithm to minimize power losses", Arabian Journal for Science and Engineering, Vol. 39, 2014, pp. 6327-6338.

[19] M. Aman, G. B. Jasmon, A. H. A. Bakar, H. Mokhlis, "Optimum network reconfiguration based on maximization of system loadability using continuation power flow theorem", International Journal of Electrical Power & Energy Systems, Vol. 54, 2014, pp. 123-133.

[20] M. M. Aman, G. B. Jasmon, H. Mokhlis, A. H. A. Bakar, "Optimum tie switches allocation and DG placement based on the maximization of system loadability using discrete artificial bee colony algorithm", IET Generation, Transmission & Distribution, Vol. 10, 2016, pp. 2277-2284.

[21] M. H. Hemmatpour, "Optimum interconnected islanded microgrids operation with high levels of renewable energy", Smart Science, Vol. 7, 2019, pp. 47-58.

[22] M. Hemmatpour, M. Mohammadian, M. Rashidinejad, "A novel reconfiguration mixed with distributed generation planning via considering voltage stability margin", AUT Journal of Electrical Engineering, Vol. 43, No. 1, 2011, pp. 23-34.

[23] L. A. Gallego, J. M. Lopez-Lezama, O. G. Carmona, "A Mixed-Integer Linear Programming Model for Simultaneous Optimal Reconfiguration and Optimal Placement of Capacitor Banks in Distribution Networks", IEEE Access, Vol. 10, 2022, pp. 52655-52673.

[24] M. R. Babu, C. V. Kumar, S. Anitha, "Simultaneous reconfiguration and optimal capacitor placement using adaptive whale optimization algorithm for radial distribution system", Journal of Electrical Engineering & Technology, Vol. 16, 2021, pp. 181-190.

[25] Y. Gebru, D. Bitew, H. Aberie, K. Gizaw, "Performance enhancement of radial distribution system using simultaneous network reconfiguration and switched capacitor bank placement", Cogent Engineering, Vol. 8, 2021, p. 1897929.

[26] R. S. Rao, "An hybrid approach for loss reduction in distribution systems using harmony search algorithm", International Journal of Electrical and Computer Engineering, Vol. 4, 2010, pp. 557-563.

[27] L. W. de Oliveira et al. "Optimal reconfiguration and capacitor allocation in radial distribution systems for energy losses minimization", International Journal of Electrical Power & Energy Systems, Vol. 32, 2010, pp. 840-848.

[28] M. Kasaei, M. Gandomkar, "Loss reduction in distribution network using simultaneous capacitor placement and reconfiguration with ant colony algorithm", Proceedings of the Asia-Pacific Power and Energy Engineering Conference, Chengdu, China, 28-31 March 2010, pp. 1-4.

[29] P. S. Prasad, M. Sushama, "Distribution Network Reconfiguration and Capacitor Allocation in Distribution System Using Discrete Improved Grey Wolf Optimization", Proceedings of Innovations in Electrical and Electronic Engineering, Springer, 2022, pp. 602-617.

[30] V. Farahani, B. Vahidi, H. A. Abyaneh, "Reconfiguration and capacitor placement simultaneously for energy loss reduction based on an improved reconfiguration method", IEEE Transactions on Power Systems, Vol. 27, 2011, pp. 587-595.

[31] K. G. Ing, J. J. Jamian, H. Mokhlis, H. A. Illias, "Optimum distribution network operation considering distributed generation mode of operations and safety margin", IET Renewable Power Generation, Vol. 10, 2016, pp. 1049-1058.

[32] A. Mendes, N. Boland, P. Guiney, C. Riveros, "Switch and tap-changer reconfiguration of distribution networks using evolutionary algorithms", IEEE Transactions on Power Systems, Vol. 28, 2012, pp. 85-92.

[33] G. I. Koong, J. J. Jamain, H. A. Illias, W. M. Dahalan, M. M. Aman, "Simultaneous network reconfiguration with distributed generation sizing and tap changer adjustment for power loss reduction using imperialist competitive algorithm", Arabian Journal for Science and Engineering, Vol. 43, 2018, pp. 2779-2792.

[34] O. Badran, J. Jallad, "Multi-Objective Decision Approach Integrated with Loadability and Weight Factor Analysis for Reconfiguration with DG Sizing and Allocation Including Tap Changer", Arabian Journal for Science and Engineering, Vol. 48, 2023, pp. 6797-6818.

[35] O. Badran, J. Jallad, "Multi-Objective Decision Approach for Optimal Real-Time Switching Sequence of Network Reconfiguration Realizing Maximum Load Capacity", Energies, Vol. 16, 2023, p. 6779.

[36] T. L. Saaty, "How to make a decision: the analytic hierarchy process", European Journal of Operational Research, Vol. 48, 1990, pp. 9-26.

[37] R. W. Saaty, "The analytic hierarchy process—what it is and how it is used", Mathematical modelling, Vol. 9, 1987, pp. 161-176.

[38] T. L. Saaty, L. G. Vargas, "The analytic network process", Springer, 2013.

[39] R. Azimi, S. Esmaeili, "Multiobjective daily Volt/VAr control in distribution systems with distributed generation using binary ant colony optimization", Turkish Journal of Electrical Engineering and Computer Sciences, Vol. 21, 2013, pp. 613-629.

[40] M. N. A. Rahim et al. "Protection coordination toward optimal network reconfiguration and DG sizing", IEEE Access, Vol. 7, 2019, pp. 163700-163718.

[41] X.-S. Yang, "Firefly algorithm, Levy flights and global optimization", Proceedings of Research and development in intelligent systems XXVI: Incorporating applications and innovations in intelligent systems XVII, 2010, pp. 209-218.

[42] J. Savier, D. Das, "Impact of network reconfiguration on loss allocation of radial distribution systems", IEEE Transactions on Power Delivery, Vol. 22, 2007, pp. 2473-2480.

[43] R. S. Rao, K. Ravindra, K. Satish, S. V. L. Narasimham, "Power loss minimization in distribution system using network reconfiguration in the presence of distributed generation", IEEE Transactions on Power Systems, Vol. 28, 2012, pp. 317-325.

[44] A. M. Imran, M. Kowsalya, D. P. Kothari, "A novel integration technique for optimal network reconfiguration and distributed generation placement in power distribution networks", International Journal of Electrical Power & Energy Systems, Vol. 63, 2014, pp. 461-472.

[45] U. Raut, S. Mishra, "An improved sine–cosine algorithm for simultaneous network reconfiguration and DG allocation in power distribution systems", Applied Soft Computing, Vol. 92, 2020, p. 106293.

INTERNATIONAL JOURNAL OF ELECTRICAL AND COMPUTER ENGINEERING SYSTEMS

Published by Faculty of Electrical Engineering, Computer Science and Information Technology Osijek,
Josip Juraj Strossmayer University of Osijek, Croatia.

About this Journal

The International Journal of Electrical and Computer Engineering Systems publishes original research in the form of full papers, case studies, reviews and surveys. It covers theory and application of electrical and computer engineering, synergy of computer systems and computational methods with electrical and electronic systems, as well as interdisciplinary research.

Topics of interest include, but are not limited to:

- Power systems
- Renewable electricity production
- Power electronics
- Electrical drives
- Industrial electronics
- Communication systems
- Advanced modulation techniques
- RFID devices and systems
- Signal and data processing
- Image processing
- Multimedia systems
- Microelectronics
- Instrumentation and measurement
- Control systems
- Robotics
- Modeling and simulation
- Modern computer architectures
- Computer networks
- Embedded systems
- High-performance computing
- Parallel and distributed computer systems
- Human-computer systems
- Intelligent systems
- Multi-agent and holonic systems
- Real-time systems
- Software engineering
- Internet and web applications and systems
- Applications of computer systems in engineering and related disciplines
- Mathematical models of engineering systems
- Engineering management
- Engineering education

Paper Submission

Authors are invited to submit original, unpublished research papers that are not being considered by another journal or any other publisher. Manuscripts must be submitted in doc, docx, rtf or pdf format, and limited to 30 one-column double-spaced pages. All figures and tables must be cited and placed in the body of the paper. Provide contact information of all authors and designate the corresponding author who should submit the manuscript to https://ijeces.ferit.hr. The corresponding author is responsible for ensuring that the article's publication has been approved by all coauthors and by the institutions of the authors if required. All enquiries concerning the publication of accepted papers should be sent to ijeces@ferit.hr.

The following information should be included in the submission:

- paper title;
- full name of each author;
- full institutional mailing addresses;
- e-mail addresses of each author;
- abstract (should be self-contained and not exceed 150 words). Introduction should have no subheadings;
- manuscript should contain one to five alphabetically ordered keywords;
- all abbreviations used in the manuscript should be explained by first appearance;
- all acknowledgments should be included at the end of the paper:
- authors are responsible for ensuring that the information in each reference is complete and accurate. All references must be numbered consecutively and citations of references in text should be identified using numbers in square brackets. All references should be cited within the text;
- each figure should be integrated in the text and cited in a consecutive order. Upon acceptance of the paper, each figure should be of high quality in one of the following formats: EPS, WMF, BMP and TIFF;
- corrected proofs must be returned to the publisher within 7 days of receipt.

Peer Review

All manuscripts are subject to peer review and must meet academic standards. Submissions will be first considered by an editor-in-chief and if not rejected right away, then they will be reviewed by anonymous reviewers. The submitting author will be asked to provide the names of 5 proposed reviewers including their e-mail addresses. The proposed reviewers should be in the research field of the manuscript. They should not be affiliated to the same institution of the manuscript author(s) and should not have had any collaboration with any of the authors during the last 3 years.

Author Benefits

The corresponding author will be provided with a .pdf file of the article or alternatively one hardcopy of the journal free of charge.

Units of Measurement

Units of measurement should be presented simply and concisely using System International (SI) units.

Bibliographic Information

Commenced in 2010.
ISSN: 1847-6996
e-ISSN: 1847-7003

Published: semiannually

Copyright

Subscription Information

The annual subscription rate is 50€ for individuals, 25€ for students and 150€ for libraries.

Postal Address

Faculty of Electrical Engineering,
Computer Science and Information Technology Osijek,
Josip Juraj Strossmayer University of Osijek, Croatia
Kneza Trpimira 2b
31000 Osijek, Croatia

IJECES Copyright Transfer Form

(Please, read this carefully)

This form is intended for all accepted material submitted to the IJECES journal and must accompany any such material before publication.

TITLE OF ARTICLE (hereinafter referred to as "the Work"):

COMPLETE LIST OF AUTHORS:

The undersigned hereby assigns to the IJECES all rights under copyright that may exist in and to the above Work, and any revised or expanded works submitted to the IJECES by the undersigned based on the Work. The undersigned hereby warrants that the Work is original and that he/she is the author of the complete Work and all incorporated parts of the Work. Otherwise he/she warrants that necessary permissions have been obtained for those parts of works originating from other authors or publishers.

Authors retain all proprietary rights in any process or procedure described in the Work. Authors may reproduce or authorize others to reproduce the Work or derivative works for the author's personal use or for company use, provided that the source and the IJECES copyright notice are indicated, the copies are not used in any way that implies IJECES endorsement of a product or service of any author, and the copies themselves are not offered for sale. In the case of a Work performed under a special government contract or grant, the IJECES recognizes that the government has royalty-free permission to reproduce all or portions of the Work, and to authorize others to do so, for official government purposes only, if the contract/grant so requires. For all uses not covered previously, authors must ask for permission from the IJECES to reproduce or authorize the reproduction of the Work or material extracted from the Work. Although authors are permitted to re-use all or portions of the Work in other works, this excludes granting third-party requests for reprinting, republishing, or other types of re-use. The IJECES must handle all such third-party requests. The IJECES distributes its publication by various means and media. It also abstracts and may translate its publications, and articles contained therein, for inclusion in various collections, databases and other publications. The IJECES publisher requires that the consent of the first-named author be sought as a condition to granting reprint or republication rights to others or for permitting use of a Work for promotion or marketing purposes. If you are employed and prepared the Work on a subject within the scope of your employment, the copyright in the Work belongs to your employer as a work-for-hire. In that case, the IJECES publisher assumes that when you sign this Form, you are authorized to do so by your employer and that your employer has consented to the transfer of copyright, to the representation and warranty of publication rights, and to all other terms and conditions of this Form. If such authorization and consent has not been given to you, an authorized representative of your employer should sign this Form as the Author.

Authors of IJECES journal articles and other material must ensure that their Work meets originality, authorship, author responsibilities and author misconduct requirements. It is the responsibility of the authors, not the IJECES publisher, to determine whether disclosure of their material requires the prior consent of other parties and, if so, to obtain it.

- The undersigned represents that he/she has the authority to make and execute this assignment.
- For jointly authored Works, all joint authors should sign, or one of the authors should sign as authorized agent for the others.
- The undersigned agrees to indemnify and hold harmless the IJECES publisher from any damage or expense that may arise in the event of a breach of any of the warranties set forth above.

_____ _____

Author/Authorized Agent **Date**

CONTACT
International Journal of Electrical and Computer Engineering Systems (IJECES)
Faculty of Electrical Engineering, Computer Science and Information Technology Osijek
Josip Juraj Strossmayer University of Osijek
Kneza Trpimira 2b
31000 Osijek, Croatia
Phone: +38531224600,
Fax: +38531224605,
e-mail: ijeces@ferit.hr